**Two-Dimensional
Time-Dependent Plasma Structures
of a
Hall Effect Thruster**

DISSERTATION

David Liu, Captain, USAF

AFIT/DS/ENY/11-04

**DEPARTMENT OF THE AIR FORCE
AIR UNIVERSITY**

AIR FORCE INSTITUTE OF TECHNOLOGY

Wright-Patterson Air Force Base, Ohio

Two-Dimensional
Time-Dependent Plasma Structures
of a
Hall Effect Thruster

DISSERTATION

Presented to the Faculty

Department of Aeronautics and Astronautics

Graduate School of Engineering and Management

Air Force Institute of Technology

Air University

Air Education and Training Command

In Partial Fulfillment of the Requirements for the

Degree of Doctor of Philosophy

David Liu, BS, MS

Captain, USAF

September 2011

AFIT/DS/ENY/11-04

Two-Dimensional
Time-Dependent Plasma Structures
of a
Hall Effect Thruster

David Liu, BS, MS

Captain, USAF

Approved:

_____   _____
LtCol Richard D. Branam, PhD (Chairman)   Date

_____   _____
LtCol Richard E. Huffman, PhD (Member)   Date

_____   _____
Dr. Mark F.Reeder (Member)   Date

_____   _____
Dr. William F. Bailey (Member)   Date

_____   _____
Dr. William A. Hargus (Member)   Date

Accepted:

_____   _____
M. U. Thomas, PhD   Date
Dean, Graduate School of
Engineering and Management

For my grandparents who raised me and made all of the sacrifices so that each of us could live the lives we wanted.

I will always be grateful . . .

Acknowledgements

Thanks to my advisors Dr. Richard Branam and Dr. Richard Huffman for the sound guidance and endless patience during this process. Without their help and support this would have never been possible. I would also like to thank my other committee members Dr. Mark Reeder, Dr. William Bailey, and Dr. William Hargus for all of the great discussions and insight into this research.

I would like to thank the ENY Laboratory Technicians: Mr. Jay Anderson, Mr. Wilbur Lacy, Mr. Barry Page, Mr. John Hixenbaugh, and Mr. Chris Zickefoose for all their help, dedication, and support throughout the last three years.

Finally, to my family. Thank you all for the support you have shown me throughout this endeavor. Most of all, thank you Megs for all your love, support, understanding, and patience.

David Liu

AFIT/DS/ENY/11-04

Abstract

The Hall thruster is a type of electric propulsion utilized by satellites to perform a wide variety of missions ranging from station keeping, orbital maneuvers, and even deep space propulsion. In order to accommodate the multitude of missions, it also has a wide assortment of sizes and power configurations which can range from approximately an inch in diameter at 20 W to approximately 12 inches in diameter at 1.5 kW. Additionally, this electro-static device provides high specific impulse without the added weight penalty associated with conventional chemical thrusters. It supplies this high specific impulse by ionizing a gas such as xenon or krypton and then accelerating it through the electric field to speeds on the order of kilometers per second depending on the thruster size and power. Although the steady-state outputs such as thrust and specific impulse are measurable, other transient mechanisms within the main discharge are still not well understood.

Previous efforts have focused on measuring the oscillatory behavior within the plasma discharge, however, these diagnostics are made with an intrusive probe which may perturb the plasma characteristics. This work describes the application of a non-intrusive technique, in particular, direct emission measurements of the plasma discharge at sampling rates on the order of one-million frames per second. This ultra-high speed imaging capability provides a two-dimensional description of the plasma field with time-resolved information. Moreover, this technique minimizes the disturbance to the plasma which ensures unperturbed plasma characteristics. Both the 200 W and 600 W Hall thrusters are used in this work in addition to comparative studies with xenon and krypton propellant.

The high speed imaging of the direct emission, or the visible light emission from the main discharge of the Hall thruster, presents a unique illustration of the transient interactions within the plasma. Analysis of the instabilities shows one of the modes

captured through this technique is the "Breathing" mode which is mathematically described by the "Predator/Prey" model. The images also reveal the breathing mode to be the dominate oscillatory mode while operating at the nominal thruster setting.

Other observations include the intensity of the direct emission which follows closely the periodic behavior of the discharge current. Variations in thruster settings such as discharge current, discharge potential, and magnet current also cause deviations in the breathing mode characteristics such as the amplitude of the emission intensity and variations in frequency. Different propellant usage, such as krypton or xenon, maintains the general characteristics of the breathing mode. However, the propellants have different frequencies at the same operating conditions. The variation in krypton versus xenon velocities minimally affects the frequency; rather the main contribution to the frequency dissimilarity is due to the ionization lengths associated with each propellant type.

Operating the thruster at lower discharge potentials allows for the observation of other instabilities within the main discharge. These instabilities move in the azimuthal direction unlike the breathing mode which travels in an axial direction. Previous reports suggest these oscillations can be the result of several types of plasma instability such as the spoke instability, gradient-induced oscillations, non-homogeneous plasma instabilities, and magnetic striations.

Table of Contents

List of Figures

xviii

List of Tables

Two-Dimensional

Time-Dependent Plasma Structures

of a

Hall Effect Thruster

I. Introduction

1.1   Motivation and Objectives

The objective of this research is to provide time-resloved measurements of a Hall Effect Thruster (HET), or Hall thruster, to quantify properties in the discharge plume. Oscillations in the plasma discharge were previously reported. However, a detailed analysis was not done with respect to non-intrusive techniques. Understanding these oscillations is important to determine how different operating conditions will affect the behavior and ultimately affect the performance and efficiency of the thruster.

Detection of these various instabilities or oscillations is usually accomplished by intrusive means where potential, emissive, or Langmuir probes are inserted into main discharge of the thruster. These intrusive techniques may change the dynamics of the plasma causing greater uncertainty in the result. In contrast, this research will use direct photon emission, in the visible and near-infrared spectrum, of the plasma to determine the two-dimensional characteristics of the plasma field, frequency of the instabilities, and the electron temperature. The frequencies of instabilities in a Hall thruster can range from a couple of kHz to MHz, but the scope of this study will be limited to those frequencies less than 500 kHz. There are two reasons to limit this work to 500 kHz. The first reason is interest in frequencies from 10 to 100 kHz include previously observed oscillations and instabilities such as the breathing mode and several azimuthal modes. Second, due to the nature of the low density plasma in the main discharge of a Hall thruster, the weak emission intensity restricts acceptable camera frame rates to less than one-million frame per second (Mfps).

1

Although the power supply for Hall thrusters are from a direct current (DC) source, fluctuations within the main discharge were observed from the beginning. These fluctuations within the plasma vary in direction, frequency, and intensity where the exact origins are not well understood. Furthermore, the impact of such fluctuations on thruster performance has become a greater point of emphasis to satisfy the growing demand for better, cheaper, and more efficient means of space propulsion to accommodate the ever broadening range of space missions [8].

The motivation for this research is to manage Hall thruster fluctuations through either active or passive controls to improve performance and efficiency. Additionally, with the greater competition for available resources and increasing thruster sizes, testing of Hall thrusters has grown more expensive. Test results are vital to computer modeling and simulations as they become more involved and include more detailed physics. Thus, the secondary motivation is to provide the modeling and simulation community with higher fidelity data to improve their modeling ability.

The objectives for this research are:

1. capture and quantify operational modes and instabilities up to 500 kHz to identify the cause and provide potential means to improve thruster performance,

2. develop non-intrusive, time-dependent methods for determining velocity and frequency of plasma instabilities within the main discharge of a Hall thruster,

3. develop methods to investigate the two-dimensional characteristics of the plasma instabilities,

4. determine the effect of thruster parameters on plasma instabilities,

5. determine the possible causes of the azimuthal instabilities.

In order to accomplish the objectives and satisfy the motivation, the physics of the oscillations require further understanding. In this work, the direct emission of the plasma is captured using ultra-high speed imaging to reslove the plasma field in space and time. The images revealed two main types of oscillations when the thruster

2

was operated at specific conditions. The first is the discharge oscillations, where the intensity of the plasma emission is periodic with minimal variations in the azimuthal direction. Oscillations were also compared to electrical parameters of the thruster, such as the discharge current, to determine any potential external drivers.

The second mode observed is best described as small areas of high plasma emission traveling in the azimuthal direction. These plasma structures are particularly visible when the thruster is operated at the lower discharge potentials. Angular velocities of these structures were calculated to determine the frequency and nature of the instabilities. Furthermore, to help explain the origins of these plasma structures the electron temperature within the discharge was determined by using a collision-radiation model (CRM) in conjunction with the near-infrared (NIR) spectrum data.

The dissertation consists of 5 chapters where the remainder of this chapter will concentrate on the history of electric propulsion and its role in today's space program. The next chapter will concentrate on the physics of electric propulsion starting with fundamentals in plasma dynamics, to include plasma formation in the thruster and the motion of charged particles influenced by an electric and/or magnetic field. Operational characteristics of the thruster, such as a description of the parts and the fuel types, will also be discussed. Chapter II will also cover some of the previous work that has lead to the development and greater understanding of the Hall thruster. Diagnostic techniques and the experimental setup will be discussed in detail in Chapter III including the ultra-high speed imaging and electron temperature measurements. Results and discussions are provided in Chapter IV where the use of the BHT-200 and BHT-600 is further discussed. In addition, the use of krypton is compared to xenon data in order to evaluate the effects of using an alternative propellant. Lastly, Chapter V will provide a summary of this study including recommended future work.

1.2 History of Electric Propulsion

No history of astronautics can be fully developed without the mention of Konstantin Eduardovitch Tsiolkovsky and his contribution in the field of space propulsion. In 1903, he published *Investigation of Universal Space by Means of Reactive Devices* where he derives an equation relating the change in velocity to the exit velocity and the ratio of initial to final mass of the spacecraft [13,74]. Today this important equation, governing the design of almost all space propulsion applications, is referred to the Ideal Rocket Equation [74]. Armed with this knowledge, Tsiolkovsky was able to determine the exit velocity of the propulsion device was a critical design parameter in which he sought to improve. Based on laboratory experiments at the turn of the century of cathode tubes and the observations of accelerated electrons, Tsiolkovsky made a mention of a device which could use these accelerated particles for space propulsion. Unknowingly, Tsiolkovsky may have been one of the first people ever to envision a device where electrical energy would supplant the more common means of chemical reaction to propel a spacecraft. As a self-taught schoolteacher, Tsiolkovsky never had much support for his ideas. Much of the scientific community was dominated by the graduate scientists. As such, most of his work was published by himself or not at all [13].

At about the same time, and probably unaware of Tsiolkovsky, a young Robert Hutchings Goddard began his experiments with an electric gas discharge tube. With it, he realized the cathode tube remained relatively cool while the charged particles inside were imparted with very high velocities [74]. Goddard, who experimented with rocket propulsion as an aside from his official research work on electricity, was intrigued with the idea of getting high particle velocities without high temperatures in the chamber. He noted this idea and began recording his thoughts about a new idea of propulsion which would incorporate electricity to accelerate charged particles in a propulsion device. However, with the war looming, Goddard was forced to abandon this train of thought and focus on ideas more relevant to the technologies available in his era for propulsive devices such as chemical propulsion [13].

The third prominent figure to shape the history of electric propulsion is Hermann Julius Oberth [74]. He devoted the last chapter of his book, *Wege zur Raumschiffahrt* (*Ways of Spaceflight*), to the analysis and benefits of using an electric propulsion device for space travel. In it, he advocated the use of electrically charged gases accelerated by an electric potential and about the mass savings when using electric propulsion instead of the conventional propulsion devices [13].

Ernest Stuhlinger was also another pioneer in the field of electric propulsion; he presented comprehensive studies on different components for electric propulsion systems and showed electric propulsion could be another viable option depending on mission needs [77]. For instance, Stuhlinger developed the idea of specific power in which he describes the power per unit mass of the power plant as a performance parameter in which the propulsion was maximized by carefully choosing the exit velocity depending on the specific power, the duration of the propulsion period, and the desired terminal velocity. To his credit, the notion of specific power is still used in modern design of electric propulsion [74].

At this point, electric propulsion as a technology was still at its infancy. Although there was great potential in the idea, the limiting factors to this proposal were actually the subsystems; such as power production including the size and weight, the limited facilities providing the space environment to test electric propulsion, and a mission able to take advantage of the inherent characteristics of low thrust, but high exit velocities [13]. Fortunately, in 1953 electrical propulsion found a niche in space missions with the help of H.S. Tsien and his work on orbital maneuvers. Tsien found having a low thrust propulsion system that could provide thrust on the order of 10^{-5} to 10^{-4} g_o was sufficient to make orbit transfer maneuvers in a period of days or weeks given the thrust vector was approximately tangential to the spiral trajectory.

In the years to follow many more studies were conducted on the feasibility of electric propulsion including its power source (nuclear or solar), lighter electrical power supplies, ion source, and beam neutralization. But it was not until 1957 that

a resurgence of interest sparked progressive companies and the technical community to form teams to investigate and bring forth this technology of which the Air Force Office of Scientific Research (AFOSR) was one of the first to provide contracts to the commercial sector [74]. As the technology of electric propulsion began to mature and assert itself as a real and feasible method for space propulsion, different classes of electric propulsion began to take shape such as electrothermal, electrostatic, and electromagnetic.

First mentioned around 1962 in a series of brief communications by Seikel, Salz, Lary, and coworkers in the Bulletin of the American Physical Society, the Hall thruster was, by all accounts first developed in the United States. However, work on it was set aside in the United States in favor of another electric propulsion device, the ion thruster. In 1968, the first Soviet experiments with the Hall thruster were published in international journals. The United States decided to focus their attention on the ion thruster while the Soviet space program focused on the Hall thruster. After their development of the Hall thruster, the Soviets were able to utilize it on many of their spacecraft [11, 25, 47].

In fact, the Soviets were able to conduct more than 170 hours of operations in 1972 aboard the *Meteor* satellite. This satellite was the first to carry the newly developed thruster system and provided more than 17 km of altitude control whereby the satellite was positioned into a sun-synchronous orbit. From the early success of the Meteor class satellites, the Soviet space program began to use the Hall thruster for orbit correction in 1972, geostationary satellite final positioning and station keeping in the East-West direction in 1982, and after 1994 the Hall thruster was also used for the North-South geostationary station keeping missions. Since then, the Soviet Hall thruster has been used on over 140 missions to include satellites from the European Space Agency [47].

However, in the early 1990's the Unites States resumed Hall thruster research when it realized that the Russian Hall thruster met a significant number of near-

Earth space propulsion applications such as specific impulse, I_{sp}, and thrust-to-power ratio [41]. In December of 2006 the first satellite with a Hall thruster, designed and built in the Unites States, was launched from NASA Wallops Flight Facility on Wallops Island, VA. This successful launch demonstrated the value of electric propulsion, its diversity, and its potential in space propulsion conceived over 45 years ago.

II. Hall Thruster Operation

2.1 General Operation

In order to fully comprehend the dynamics of the Hall thruster, it is important to first understand the basic physics that allow this thruster to perform its mission described in the previous section. Since the Hall thruster is an electrostatic device, it is also important to understand the electrical components which produce the electric and magnetic fields essential to the thrusters operation [24]. It is also prudent at this time to understand plasma generation inside the channel of the thruster and how the resulting fields affect the charged particles. Lastly, this section will delve into the types of fuel which the Hall thruster can use and the effects of fuel type.

Hall thrusters have a couple of different configurations, but the most general case considered here is the axis-symmetric or coaxial geometry thruster, as seen in Figure 2.1. It consists of two concentric cylinders with one side of the cylinders open and the other side closed. At the closed end is the electrically biased anode with a propellant inlet. The walls of the thruster, or the open area inside the concentric cylinders, are insulated with a dielectric material with a low sputtering yield and relatively low electron emission due to the ions in the plasma colliding with the wall. Close to the open end of the thruster, an array of magnets are used to create a radial magnetic field. On the outside of the thruster, a cathode uses a small amount of the propellant to generate the electrons required for the plasma formation within the thruster [24].

2.2 Plasma Formation

Together with an applied electric and magnetic field, the operation of the thruster starts by the cathode emitting electrons, which are accelerated towards the anode at the back of the channel. However, before the electrons reach the anode, they are captured by the magnetic field, near the exit of the thruster, produced by the electromagnets. Trapped in the electric and magnetic field, the electrons are forced to travel along the $E \times B$ direction azimuthally. The electrons cannot leave the magnetic
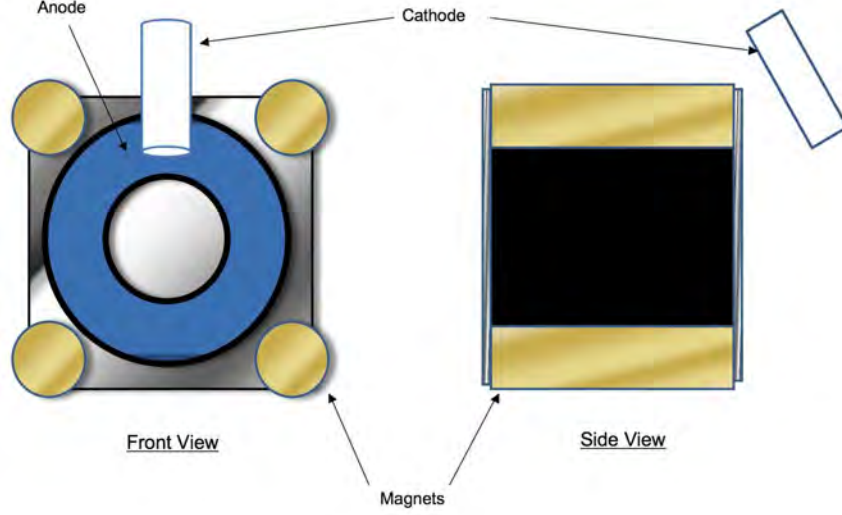
Figure 2.1:   Hall thruster schematic.

field because their Larmor radii, r_L, expressed in equation (2.1) below is less than the characteristic length, L.

$$r_L = \frac{v_{th}}{\omega_c} = \frac{m}{eB}\sqrt{\frac{8kT_e}{\pi m}} = \frac{1}{B}\sqrt{\frac{8m}{\pi e}T_{eV}} \ll L \tag{2.1}$$

where v_{th} is the thermal velocity, ω_c is the electron cyclotron frequency, m is the mass of the propellant, e is the electron charge, B is the magnetic field, k is the Boltzmann constant, and T_e is the electron temperature.

At the same time the electrons are circling in the channel, propellant enters on the opposite side at the anode. While the propellant is traveling towards the exit, they are bombarded by the electron cloud. If an electron within the cloud has sufficient energy and impacts the propellant atom, it will free the electron in the valence shell and the result will be a positively charged particle and two free electrons; thus, the

propellant is ionized by direct electron impact. The singly ionized or simple ionization of the molecule or atom is shown as

$$A + e \rightarrow A^+ + e + e \tag{2.2}$$

where A represents a molecule of neutral propellant, A^+ is a positively charged molecule or ion, and e is a free electron. After the ionization, the charged particle reacts to the electric field, but not the magnetic field due to its large ion Larmor radii, r_i, expressed below, and is accelerated outside the channel and away from the thruster [37].

$$r_i = \frac{v_i}{\omega_c} = \frac{m}{eB}\sqrt{\frac{2ev_b}{m}} = \frac{1}{B}\sqrt{\frac{2m}{e}}v_b \gg L \tag{2.3}$$

where v_i is the ion velocity and v_b is the beam velocity.

As the charged particle passes the cathode, it attracts an electron from the cathode which begins the neutralization process before completely leaving the thruster system. The electron, which balances with the positively charged ion, prevents the ion from colliding back with the spacecraft and causing sputter erosion. Alternatively, some of the electrons generated by the plasma formation and the cathode remain in the magnetic field traveling in the $E \times B$ direction continuing to generate plasma within the thruster channel until they reach the anode.

2.3 Imparting Force

The accelerated particle must act against something to impart a force, in this case thrust. Recall the electrons are confined by the magnetic field and moving in the azimuthal direction. The velocity of those electrons is described by the following

$$\vec{v_e} = \frac{\vec{E} \times \vec{B}}{B^2} \tag{2.4}$$

where E is the electric field and B is the magnetic field.

In addition, the electrostatic force on the electrons, balanced by the Lorentz force, is expressed as equation (2.5), below,

$$\overrightarrow{F_e} = -2\pi \iint qn_e \overrightarrow{E} r \, drdz - 2\pi \iint en_e v_e \times \overrightarrow{B} r \, drdz = 0 \qquad (2.5)$$

where q is the charge of the particle and n_e is the number density of electrons. Given the ions are not magnetized and the charge of the ions are opposite to the charge of the electrons, the force on the ions is expressed as:

$$\overrightarrow{F}_i = 2\pi \iint qn_i \overrightarrow{E} r \, drdz \qquad (2.6)$$

Again assuming the plasma is quasi-neutral, and using the definition of the Hall current given in equation (2.7).

$$\overrightarrow{J}_{Hall} = -en_e \overrightarrow{v_e} \qquad (2.7)$$

The sum of the forces of the ions and the electrons is expressed as

$$\sum F = -2\pi \iint qn_i \overrightarrow{E} r \, drdz + 2\pi \iint \overrightarrow{J}_{Hall} \times \overrightarrow{B} r \, drdz = 0 \qquad (2.8)$$

where n_i is the number density of ions.

Solving equation (2.8), above, shows the electron force is related to the Hall current force such that the force on the electrons is equal and opposite of the Hall current force on the magnets. The force on the ions is equal and opposite to the force on the electrons, thus, the force on the ions acts on the Hall current force of the magnets. Simply speaking, the thrust is transferred from the ions to the body of the thruster through the electromagnetic Lorentz force.

2.4 Ionization Process

The majority of the ionization process for a Hall thruster is direct ionization by electron impact as previously mentioned where an electron, with sufficient energy, collides with a valence electron of a neutral particle. This collision causes the valence electron to separate from the neutral particle leaving a positively charged particle and two free electrons [23]. The electron-neutral collisional ionization rate is given by equation (2.9) [76].

$$R_i(c_{rel}) = n_n n_e \sigma_{n-e}(c_{rel}) dc_{rel} \tag{2.9}$$

where c_{rel} is the relative velocity, n_n is the neutral number density, and σ_{n-e} is the electron-neutral collisional cross section.

Although this process depicts the dominant ionization processes within the thruster, other types of ionization also occur. For instance, a charged particle can collide with an additional electron before or while it is accelerated in the electric field. In this case, the singly ionized particle is doubly ionized. This particle phenomenon is considered as a loss in the system, since the energy required to doubly ionize a particle is not used to ionize a neutral particle. Furthermore, a doubly ionized particle is not accelerated twice as fast as the singly charged particle. The doubly ionized particle is only accelerated $\sqrt{2}$ times faster than the singly ionized particle, thus, the energy it took to create this slightly faster ion will not equal to the amount of energy imparted to thrust.

2.5 Charged Particle Motion in Electric and Magnetic Field

Consider one particular charged particle in the plasma field, the force exerted on the particle, $\overrightarrow{F}$, ignoring relativistic effects, is described by the Lorentz equation [76]:

$$\overrightarrow{F} = q \left[\overrightarrow{E} + \overrightarrow{v} + \overrightarrow{B} \right] \tag{2.10}$$

12

In the following analysis, the magnetic and electric fields are discussed to understand the dynamics of the charged particle leading to the dynamics of the bulk plasma in the Hall thruster [26].

For the simplest case, consider a particle in a static uniform magnetic field. The Lorentz force is expressed as the following differential equation:

$$\frac{d(m\vec{v})}{dt} = q(\vec{v} \times \vec{B}) \tag{2.11}$$

To find the kinetic energy of the particle, the scalar product of velocity and equation (2.11) yields:

$$\vec{v} \cdot \frac{d(m\vec{v})}{dt} = \frac{d(\frac{1}{2}m\vec{v}^2)}{dt} = \vec{v} \cdot q(\vec{v} \times \vec{B}) = 0 \tag{2.12}$$

As seen in equation (2.12), the kinetic energy is a constant for a particle in the magnetic field. Referring to Figure 2.2, the velocity is separated into orthogonal components parallel, $v_\parallel$, and perpendicular, $v_\perp$, to the direction of the magnetic field. Since the Lorentz force has no component in the parallel direction to the magnetic field, the following set of equations are written for the dynamics of the particle:

$$\frac{dv_\parallel}{dt} = 0 \tag{2.13}$$

$$m\frac{dv_\perp}{dt} = q(v_\perp \times B) \tag{2.14}$$

Using a Cartesian coordinate system, the particle motion in a magnetic field, in the z-direction, is further broken down into three components:

$$m\frac{\partial v_x}{\partial t} = qBv_y \tag{2.15}$$
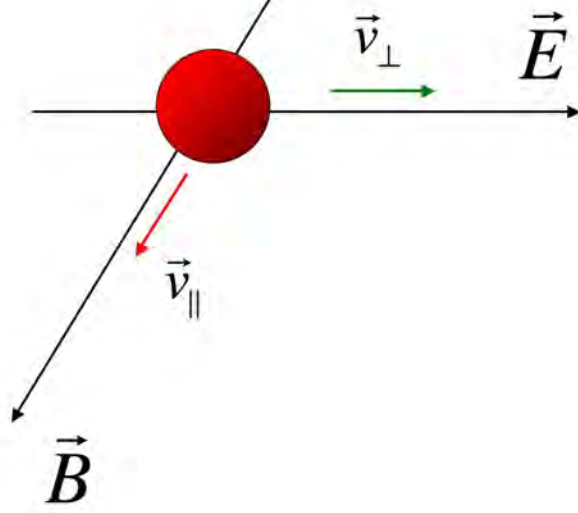
Figure 2.2:   Coordinates of the electric field and the magnetic field.

$$m\frac{\partial v_y}{\partial t} = qBv_x \tag{2.16}$$

$$m\frac{\partial v_z}{\partial t} = 0 \tag{2.17}$$

Now taking the time derivative of the above equations, (2.15), (2.16), and (2.17) and solving for the velocity in each direction gives

$$\frac{\partial^2 v_x}{\partial t^2} = \frac{qB}{m}\frac{\partial v_y}{\partial t} = -\left(\frac{qB}{m}\right)^2 v_x \tag{2.18}$$

$$\frac{\partial^2 v_y}{\partial t^2} = -\frac{qB}{m}\frac{\partial v_y}{\partial t} = -\left(\frac{qB}{m}\right)^2 v_y \tag{2.19}$$

14

The equations of motion for the particle in a static uniform magnetic field now reduce to two linear ordinary differential equations, which are solved in closed form:

$$v_x = v_\perp \cos(\omega_c t + \phi) \tag{2.20}$$

$$v_y = \mp v_\perp \sin(\omega_c t + \phi) \tag{2.21}$$

Furthermore, equations (2.20) and (2.21), the velocity components of particle motion in a magnetic field, was integrated again, which expresses the displacements of the particles as

$$x - x_o = \frac{v_\perp}{\omega_c} \sin(\omega t + \phi) \tag{2.22}$$

$$y - y_o = \frac{v_\perp}{\omega_c} \cos(\omega t + \phi) \tag{2.23}$$

From equations (2.22) and (2.23), above, the radius of the charged particles, in this case electrons, orbiting the magnetic field lines can be determined as

$$r = r_L = \frac{v_\perp}{\omega_c} \tag{2.24}$$

where r_L is the Larmor radius seen in Figure 2.3, below.

In these derivations, the velocity in the z-component was left out. However, in reality the charged particles travel axially in the direction of the magnetic field as shown in Figure 2.4 due to diamagnetism. This phenomenon causes an induced magnetic field opposite to the applied magnetic field thus forcing the particle along the direction of the magnetic field in a helix with a radius given by the Larmor radius.

Furhtermore, the electric field in a Hall thruster is perpendicular to the magnetic field. The electric field is separated into orthogonal components in which the parallel

15
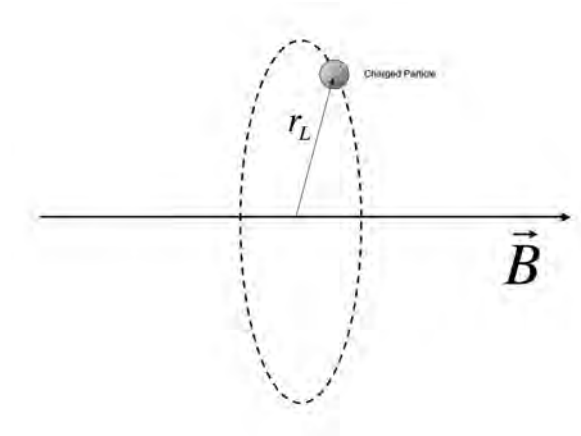
Figure 2.3:   Diagram of the Larmor radius, r_L
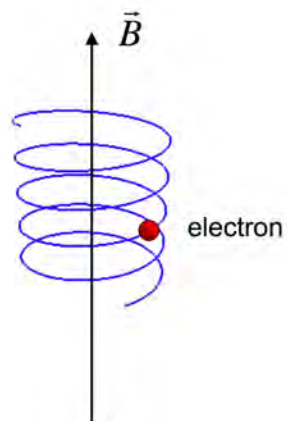
Figure 2.4:   Electron motion in the magnetic field

component of the electric field is in the same direction as the perpendicular component of the magnetic field and the perpendicular component of the electric field is aligned with the parallel component of the magnetic field. Coupled with elementary physics of which a charged particle in an electric field is accelerated along the electric field lines, in this case along the perpendicular magnetic field direction, the equations of motion now becomes:

$$\frac{\partial v_{\parallel}}{\partial t} = 0 \tag{2.25}$$

$$m\frac{\partial v_{\perp}}{\partial t} = q\left(E + v_{\perp} \times B\right) \tag{2.26}$$

Having previously discussed the motion of a charged particle in a magnetic and electrical field separately, the remaining discussion will focus on the motion of the charged particle subject to both electric and magnetic fields simultaneously. Again, using the magnetic field as a reference direction, the components of acceleration of a charged particle are separated into a parallel component and a perpendicular component as shown in equation (2.27) and (2.28):

$$\frac{\partial v_{\parallel}}{\partial t} = \frac{q}{m}E_{\parallel} \tag{2.27}$$

$$\frac{\partial v_{\perp}}{\partial t} = \frac{q}{m}\left(E_{\perp} + v_{\perp} \times B\right) \tag{2.28}$$

Once more, transforming these coordinates to the more convenient Cartesian coordinates in which the magnetic field is parallel to the z-direction, the following equations are formed:

$$\frac{\partial v_x}{\partial t} = \frac{q}{m}(E_x + v_y B) \tag{2.29}$$

17

$$\frac{\partial v_y}{\partial t} = \frac{q}{m}(E_y - v_x B) \qquad (2.30)$$

These two non-homogeneous linear ordinary differential equations, similar to previous sections, are solved to yield:

$$v_x = v_\perp \cos\left(\omega t + \phi\right) + \frac{E_y}{B} \qquad (2.31)$$

$$v_y = \pm v_\perp \sin\left(\omega t + \phi\right) - \frac{E_x}{B} \qquad (2.32)$$

where the positive sign denotes a positively charged particle and the negative sign denotes a negatively charged particle.

Another phenomenon commonly observed is the $E \times B$ drift velocity denoted by u_d. This velocity occurs when the charged particle, in this case an electron, is accelerated in the direction of $-E$ while on the other half of its orbit around the magnetic field line it is decelerated in the direction of $+E$. Consequently, this elongates one half of the electrons orbit while it curtails the other half resulting in a motion in the $E \times B$ direction. From the Lorentz equation, the drift is assumed as steady state where:

$$E = -v \times B = -u_d \times B \qquad (2.33)$$

To solve for the drift velocity, u_d, and knowing the resultant is an $E \times B$ product, the cross product of the above equation is taken to give:

$$E \times B = (-u_d \times B) \times B = vB^2 - B(B \cdot u_d) \qquad (2.34)$$

Given the dot product of the last term is equal to zero since the drift velocity is the resultant of a cross product term, the drift velocity is now expressed as equation (2.35) [24, 31]:

$$u_d = \frac{E \times B}{B^2} \tag{2.35}$$

2.6 Hall Thruster Instability

Much of the discussion until now is based on single particle motion with an assumed velocity, temperature, or other parameter of the charged particle. In the bulk plasma perspective, it is important to emphasize these parameters are based on distributions and not every particle is the same. As such, these variations result in different gradients within the plasma altering the electric and magnetic fields. Some of the oscillations are inherent to the ionization, particle diffusion, and acceleration processes of the Hall thruster and considered natural modes of the plasma intended to self-regulate the charged particle production and diffusion within the system.

Several oscillations or instabilities arise with such gradients of which several different bands are categorized. The Hall thruster frequencies are observed from the low kHz regime all the way up to the MHz regime and range from narrow band, coherent waves to broadband, non-coherent wave structures. The amplitude and frequencies of these oscillations have been attributed by the Russian literature to have a strong dependence on operating conditions such as mass flow rate, propellant type, applied voltage, initial and time evolving geometry, degree of contamination in the discharge chamber, cathode characteristics (mass flow rate and location), PPU characteristic and configuration. The breathing mode is also highly dependent on the magnetic field profile and magnitude. The axial location inside the chamber also has a significant role in the frequencies of these oscillations [12, 14, 46].

2.7 Breathing Mode

Several types of oscillations were reported and characterized in the literature. The most commonly observed are the "breathing mode" oscillations. This mode is identified by the azimuthally uniform increase in exhaust plume density along the axial direction of the thruster. Utilizing a 1-D hybrid model, where the electrons are treated as a fluid and the ions are described by a collisionless kinetic equation, Boeuf and Garrigues were able to determine the frequency of the oscillations present in the main discharge of an SPT-100. Their calculations yielded results close to those found experimentally of 15-22 kHz. In addition, their model predicted the frequency of the breathing mode would increase as the discharge potential of the thruster was increased. The authors associated the oscillations with the periodic depletion of neutral atoms at the exit plane of the thruster.

In order to maintain the current continuity in the region of high magnetic field near the exit of the channel, the electric field requires an increase to match the low electron conductivity at the same location. Thus at the exit plane, large electron temperatures and ionization rates exist in which the neutral atoms eventually traveling to the exit are quickly ionized. As the neutral density suddenly decreases, the neutral/ionized front begins to retreat upstream towards the anode where the electron temperatures and ionization rates are much lower, resulting in a decrease in the plasma density as the neutral atom density decreases. Together with a corresponding decrease in electron flux at the exhaust, the neutral atoms begin to re-populate the region since there are not as many electrons to ionize them. With a high neutral density in the exhaust where a large electric field exists, the probability of ionization is again increased leading to the depletion of plasma in the exhaust region and so on [4].

This breathing mode described by Boeuf and Garrigues is synonymous to the "predator-prey" model derived by Fife *et al* where the species conservation equations is written as:

$$\frac{\partial n_i}{\partial t} = \xi(T_e) n_i n_n - n_i \frac{v_i}{L} \tag{2.36}$$

$$\frac{\partial n_n}{\partial t} = -\xi(T_e) n_i n_n + n_i \frac{v_n}{L} \tag{2.37}$$

where $\xi(T_e)$ is the ionization rate coefficient, v_i is the fluid velocity of the ions, v_n is the fluid velocity of the neutrals, and L is the characteristic length of the ionization/acceleration zone.

Applying the linear perturbation on the number densities of both the ions and neutrals gives equations (2.38) and (2.39):

$$n_i = n_{i,0} + \epsilon n_i' \tag{2.38}$$

$$n_n = n_{n,0} + \epsilon n_n' \tag{2.39}$$

where ϵ is the ionization energy. At ϵ^0, equations (2.36) and (2.37) become:

$$\xi n_{n,0} = \frac{v_i}{L} \tag{2.40}$$

$$\xi n_{i,0} = \frac{v_n}{L} \tag{2.41}$$

and at ϵ^1 the equations become

$$\frac{\partial n_i'}{\partial t} = \xi(T_e) n_{i,0} n_n' \tag{2.42}$$

21

$$\frac{\partial n'_n}{\partial t} = -\xi(T_e)n'_i n_{n,0} \tag{2.43}$$

Taking the derivative of equation (2.42) and then substituting equation (2.43) gives

$$\frac{\partial^2 n'_i}{\partial t^2} + \xi(T_e)^2 n_{i,0} n_{n,0} n'_i = 0 \tag{2.44}$$

Equation (2.44) is now solved as an undamped harmonic oscillator with a frequency, f, given by:

$$f \approx \sqrt{\xi(T_e)^2 n_{i,0} n_{n,0}} \tag{2.45}$$

Substituting in equations (2.40) and (2.41) gives the frequency of the oscillator as:

$$f \approx \frac{1}{L}\sqrt{v_i v_n} \tag{2.46}$$

From the predator-prey model derived in Equation (2.46), the frequency of the oscillations are inversely proportional to the ionization length and only depends on the square-root of the velocities [22]. Additionally, other theoretical models have developed building upon these relationships [43].

Many studies with different intrusive techniques have shown the frequency of the breathing mode is accurately described with this model. For many instances, the breathing mode was found in the 15-30 kHz regime for a variety of thruster sizes. In addition, the frequency of the breathing modes was also found as a function of the thruster operating conditions. For instance, numerous studies show increases in discharge potential also increased the breathing mode frequency in addition to changes in the mass flow rate. Manipulation of the breathing mode is also accomplished by changing the magnetic field since it plays an important role in this phenomenon. Moreover, the frequency was also sensitive to the power supply [2,3,6,8,12,33,61,65].

Non-intrusive measurements, such as laser-induced fluorescence, (LIF) and direct emission measurements, were also able to substantiate the breathing mode [30,62, 63]. In particular, the research in direct emission studies show a correlation between the light emission intensity and the periodic discharge current [15–17,68]. Other works which correlate the discharge current to the emission intensity were also able to associate plasma properties, such as electron temperature and density to the discharge current as well [55–60].

The breathing mode was observed in different sizes of Hall thrusters as evidenced by Ito *et al*. They were able to identify a breathing mode in the 35 to 70 kHz regime for a micro-Hall thruster configuration in which they were testing. Their results suggests a correlation to the breathing mode frequency which was derived by Fife *et al* in equation (2.46). Furthermore, they reported the frequency of the oscillations decreased as the discharge potential was decreased [39].

Alternative designs such as the cylindrical Hall Thruster (CHT) also exhibits the breathing mode in the kHz regime. In Raitses *et al*, the CHT measured in their work showed a breathing frequency of 14 kHz, similar to the the frequency ranges which were reported for standard Hall thrusters. In addition, measurements of the breathing mode were also observed in the discharge oscillations where dimming and brightening of the emission was detected in the images [70].

Other measurements of the breathing mode include magnetic field studies. Electric coils were positioned in which the force lines cross the coil surface was used to detect the non-stationary magnetic field lines which generate a voltage drop. Correlating the magnetic field with the current discharge, the two frequencies were the same and showed for this setup and measuring technique the frequency was 25 kHz [48].

The breathing mode for Hall thrusters was measured extensively in recent studies where frequencies of these modes were found consistent for a given thruster. This consistent frequency within the main discharge can provide time-dependent measurements of the plasma properties by correlating the measurements to a reference time

in the breathing mode oscillation. Since the measurements of the plasma properties were referenced in time, an average of the data was made to provide averaged, time-dependent data. The utilization of this technique can also extend into 2-D by translating the measurement point about the face of the thruster. An example of this technique was demonstrated utilizing an emissive probe on a 200 W Hall thruster where the probe was translated about the face of the thruster to provide an averaged 2-D, time-correlated map of the plasma properties [72].

Emission measurements captured with high-speed cameras and utilizing the the time-correlation technique have also shown the breathing mode oscillations on traditional Hall thrusters as well. Since the direct emission signal from the plasma was low, a concave mirror was used outside of the vacuum chamber to maximize light collection. After the light was focused by the mirror, it was sent through fiber optics to a photomultiplier where the signal was displayed and analyzed by an oscilloscope and spectrum analyzer, respectively. The result of the experiment provided a breathing mode frequency of 33 kHz for a SPT-100 type thruster. By placing the two probes along the thruster axis, the ions in the plume were found to have a phase velocity of 20 km/s. Additionally, high speed images were taken with an image intensifier and CCD camera. Although the frames per second capability of the camera was not reported, sequential images of the plasma ring inside the channel was given at 2 μs apart with an exposure time of 1 μs [15, 17].

Further work in high speed imaging included the use of multiple optical fibers implanted within the outer wall of the thruster to determine the behavior of the plasma at pre-exit and exit conditions [16]. Another improvement to the high speed imaging was the incorporation of broadband spectral filters to determine the species (i.e excited neutrals or ions) within the image. However, the technique was not able to show the 2-D image of where the different species exists in the plume [68, 75].

2.8 Azimuthal Modes

In contrast to the breathing mode, which is characterized by waves moving in the axial direction and uniform azimuthally, the azimuthal modes tend to travel in the $E \times B$ direction and are similar to spokes on a wheel spinning about its axis [12, 46]. Like the breathing mode, azimuthal instabilities were also well documented experimentally.

In Hargus et. al., experimental data showed as the anode potential was decreased the azimuthal modes of the thruster became more dominate. For instance, when the potential was decreased from 100 V to 85 V, frequencies in the azimuthal mode, 27 kHz, begin to emerge from the breathing mode, 17 kHz. An increase in mass flow rate which corresponded to an increase in frequency was also observed. Determination of the azimuthal mode velocity was accomplished with two probes separated by $45°$ in the azimuthal direction. The data from the probes were then cross-correlated to give an average phase shift of 4.1 μs yielding a wave speed of 8.6 km/s. From their experiments, Hargus et al were able to determine there was weak, but coherent azimuthal wave near the exit plane when the thruster was operated in the current saturated regime of the I-V curve. The azimuthal wave near the exit plane became much more intense as the potential is decreased while maintaining the higher current regime (know as the "knee" of the I-V curve). In addition, operating the thruster in the ionization region of the I-V curve close to the knee, the azimuthal wave were observed to become even more pronounced, seemingly to extend further into the channel with increasing frequency. Lastly, at the low potential regime of thruster operation, the azimuthal waves were still distinct but seemed to only exist in the region very near the anode [33].

The azimuthal waves were again observed in the experimental data provided by Chesta et al. Two electrostatic probes, low-impedance Langmuir probes biased negatively, were placed in the plume of the Hall thruster separated azimuthally by

30°. Assuming the plasma was quasi-neutral (i.e. $n_n = n_e$) the current density was given as:

$$J = 0.61 e n_e \sqrt{\frac{kT_e}{m_i}} \qquad (2.47)$$

where e is the electron charge, n_e is the electron number density, k is the Boltzmann constant, T_e is the electron temperature, and m_i is the mass of the propellant ion. For operational conditions at low potentials, the azimuthal modes was relatively the most prominent modes. It had a frequency in the range of 5-10 kHz and had a phase velocity of 1.0 to 4.0 km/s which was near the critical propellant velocities reported in Janes and Lowder [8].

Time correlation results from Smith and Cappelli were not only able to identify the breathing mode but were capable of determining the azimuthal mode in a 200 W Hall thruster as well. In their findings for the plasma potential properties, the azimuthal wave frequency was resolved at approximately 25 kHz with an azimuthal velocity of 1.8 km/s. The authors also determined the azimuthal fluctuation was a single wave which rotates about the channel [72].

Alternatively with Laser Induce Fluorescence (LIF), the azimuthal ion velocity for a SPT 100 was determined as 0.25 km/s. Although Smith and Cappelli reported azimuthal wave velocities seven times higher than others, it is important to understand they were not looking at the same thing. Smith and Cappelli were looking at the plasma potential at a specific location whereas LIF determines parameters based on the ions themselves [62].

In comparison, Hargus and Pote were able to determine the azimuthal velocity by employing LIF on the thruster plume. For a BHT-600 thruster, they were able to show the ions, and not the plasma potential, were traveling in the azimuthal direction and had a velocity of 0.475 km/s [72]. Based on other LIF studies of various thrusters, they were also able to determine the ion azimuthal velocity was inversely related to the outer diameter of the acceleration channel [62]. Incorporating the notion of

Hall thruster scaling in which the magnetic field decreases as the thruster geometry increases, the azimuthal ion velocity was shown proportional to the applied magnetic field [32].

Although abundant experimental data on the azimuthal instability in the low to mid kHz regime exists, the cause of these instabilities are not well understood. Since several of the azimuthal modes of thruster exists in this frequency band, the measured azimuthal instabilities are attributed to either one or a combination of the following causes.

Descriptions of anomalous diffusion across a magnetic field were first reported by Yoshikawa and Rose. They were able to show in a magnetic field the diffusion of electrons in a plasma field was proportional to $1/B$ [79].

Subsequently, Janes and Lowder were able to further build on the anomalous electron transport research by investigating a Hall accelerator. Utilizing two Langmuir probes, separated by a known angle, they were able to measure density variations within the plasma. Since the angle between the two probes was known, the delay in the signal from probe 1 to probe 2 was used to determine the velocity of the fluctuating plasma. Janes and Lowder were able to correlate the experimentally determined velocity of the azimuthal wave (or spoke) to the ionization process through a critical velocity given by equation (2.48):

$$v_{cr} = \sqrt{\frac{2\phi}{M}} \tag{2.48}$$

where ϕ was the ionization potential and M was the atomic weight of the propellant. The correlation between the critical velocity was found true even with different propellants such as xenon, krypton, and argon where their critical velocities are given in Table 2.1 [40].

Quantitatively, the formation of the spoke was attributed to a coupling between the non-uniformity of the density and the process of ionization. A tilt to the azimuthal

Table 2.1:   Critical velocity for multiple propellants taken from Janes and Lowder

Propellant	Critical Velocity, v_{cr} [km/s]
xenon	4.2
krypton	5.7
argon	8.7

wave was also discovered by Janes and Lowder in which they explained it as a function of the propagation distance traveled by the ionization wave along the anode while an ion is accelerated through the exhaust [12, 40].

Another azimuthal instability is the result of gradient-induced oscillations. Unlike the spoke instabilities, these oscillations are not directly related to the ionization process, rather, they are electrostatic waves which propagate in the azimuthal direction. [12, 64]

Studying these gradient-induced oscillations requires the application of the linearized equations of two-fluid magneto hydrodynamics (MHD) of a cold, collisionless plasma. The MHD equations are written as:

$$\frac{\partial n_i}{\partial t} + v_0 \frac{\partial n_i}{\partial x} + n_0 \nabla \cdot \vec{v} = 0 \tag{2.49}$$

$$\frac{\partial n_e}{\partial t} + u_0 \frac{\partial n_e}{\partial y} + \nabla \cdot (n_o \vec{u}) = 0 \tag{2.50}$$

$$\frac{\partial \vec{v}}{\partial t} + v_0 \frac{\partial \vec{v}}{\partial x} = \frac{e}{m_i} \vec{E} \tag{2.51}$$

$$\frac{\partial \vec{u}}{\partial t} + u_0 \frac{\partial \vec{u}}{\partial y} = -\frac{e}{m_e} \left[\vec{E} + \frac{1}{c} \left(\vec{u} \times \vec{B_0} \right) + \frac{1}{c} \left(\vec{u_0} \times \vec{B} \right) \right] \tag{2.52}$$

$$\nabla \times E = -\frac{1}{c} \frac{\partial \vec{B}}{\partial t} \tag{2.53}$$

$$\nabla \times B = \frac{1}{c}\frac{\partial \vec{E}}{\partial t} + \frac{4\pi e}{c}\left[n_0\left(\vec{v} - \vec{u}\right) + \vec{v_0}n_i - \vec{u_0}n_e\right] \tag{2.54}$$

where n_0 is the plasma density, u_0 is the electron drift velocity, v_0 is the ion drift velocity, $\vec{u}$ is the electron velocity, $\vec{v}$ is the ion velocity, e is the elementary charge, c is the speed of light, $\vec{E}$ is the electric field, and $\vec{B}$ is the magnetic field.

Following Esipchuk and Tillin, the dispersion relation has the roots:

$$\omega = k_x v_0 - \frac{k^2 v_0^2}{2k_y\left(u_0 - u_B\right)} \pm \frac{k v_0^2}{2\left(u_0 - u_B\right)}$$
$$\times \sqrt{\left(\frac{k_x}{k_y}\right)^2 - 4\frac{k_x\left(u_0 - u_B\right)}{k_y v_0} + 4\frac{u_0\left(u_0 - u_B\right)}{v_0^2} + 1} \tag{2.55}$$

where k was the wave vector with components k_x and k_y along the applied electric field and along the azimuthal direction, respectively. Eq. 2.55 is rewritten in the form of:

$$\omega = \omega_{az} + i\eta \tag{2.56}$$

where the real part, ω_{az}, is the azimuthal frequency and the imaginary part, η, is the growth rate of the oscillations [20].

For the first mode instabilities where $k = 2\pi/\lambda = 1/r$ and choosing azimuthal propagation where $k_y = 10k_x$, the frequencies of gradient-induced oscillations were found in the 25 - 55 kHz regime and was shown as a strong function of the magnetic field and not a strong function of the ionization process [12, 64].

Other possible causes of the azimuthal instability are the magnetic striation within the plasma caused by crossed electric and magnetic fields. These striations were first theoretically considered by Velikhov and Dykhne and by Kerrebrock in low

temperature plasmas where the state of the plasmais described by the generalized
Ohm's Law:

$$\sigma \left[E + T_e \frac{\nabla n_e}{n_e} + \left(\delta - \frac{3}{2} \right) \nabla T_e \right] = j + j \times \frac{eB}{mc} \tau \tag{2.57}$$

the energy conservation equation for electrons:

$$\phi \frac{\partial n_e}{\partial t} + \frac{3}{2} \frac{\partial}{\partial t} (n_e T_e) - \delta \nabla T_e \frac{j}{e} = \frac{Ej}{e} - \kappa \frac{n_e T_e}{\tau} \tag{2.58}$$

and the Saha equation:

$$\frac{n_e^2}{n - n_e} = A T_e^{3/2} e^{-\phi/T_e} \tag{2.59}$$

where σ is the conductivity, δ is a number determined by the dependence of the mean
free path of the electrons on the velocity and by the form of their velocity distribution
function, j is the current, τ is the mean free path time, and A is a known constant.
The term with the thermal conductivity was left out of Equations (2.58) and for
simplicity, the electron temperature was assumed greater than the gas temperature
$(T_e \gg T_g)$.

Under the condition of $\nabla \times E = 0$ and $\nabla \cdot j = 0$, the linearized equations of
(2.57),(2.58), and (2.59) for small amplitude waves in the form of $e^{i(kZ - \omega t)}$ yield the
dispersion relation:

$$i\omega = \frac{j^2 \left(-2\omega\tau \sin\varphi\cos\varphi - 2\cos^2\varphi + 2\sin^2\varphi \frac{\partial ln\tau}{\partial lnn_e} - \frac{\partial lnT}{\partial lnn_e} \right)}{n\sigma\phi \left[1 + \frac{3}{2v} \left(1 + \frac{\partial ln\tau}{\partial lnn_e} \right) \right]}$$

$$+ \frac{i \left(kj \right) \left(\nu - \frac{3}{2} - x\nu \right)}{en \left(\nu + \frac{3}{2} \right)^2 (1 - x) + \frac{3}{2} (2 - x)} \tag{2.60}$$

where φ is the angle between the current j and the front of the wave, $\nu = \frac{\phi}{T_e}$, and $x = \frac{n_e}{n}$. More importantly, the velocity of the magnetic striations is given as:

$$v \approx \frac{T_e}{\phi}\sqrt{\frac{T_e}{M}} \tag{2.61}$$

The calculated velocity of the magnetic striations provide a means to compare observed values which will aid in the determination of instability type in later sections [67, 69].

In previous experimental work, the striation tended to have a *tilt* due to boundary conditions in which the plasma was contained. The angle of the tilt, φ, was due to the short-circuit of the external electric circuit of the container and altered the wave formation and traveling direction [42]. Although the magnetic striations were observed in tubes or discharge columns, this tilt was also observed in the experimental data of Janes and Lowder, Esipchuk *et al*, and Chesta *et al* and may be the result of the magnetic striations [8, 19, 40, 67].

2.9 Higher Frequency Modes

In the lesser known and understood oscillation regimes of 20-100 kHz, the instabilities here are further divided into two categories. The first of these categories include instabilities related to inhomogeneous and weakly ionized plasma. The second instabilities are related to ionization. Both cases show instabilities within the regime and further study is required to understand the causes.

For frequency ranges in the 70-500 kHz regime, referred to as "transient-time" oscillations, the instabilities often correspond to the ion in-chamber residence time scale. They are usually observed to travel axially and are described as quasi-axial electrostatic waves. They are broadband type oscillations of mixed bands and tend to play an important role in regulating the plasma transport.

The final and least understood oscillations reside in the 0.5-5 MHz regime. These higher frequency oscillations seem more like broadband noise, but upon further examination were predicted in models by Esipchuck and Tilinin as azimuthal in nature [8, 48, 49, 53].

In conclusion, some of these oscillations are natural modes of the Hall thruster and inherent in the design of such electrostatic devices. They are either azimuthal waves or travel in the axial direction. In most cases, these oscillations have a strong dependence or correlation with the magnetic field while the remaining are functions of the inhomogeneous plasma or weak ionization rates in specific regions [12].

III. Diagnostic Technique and Experimental Apparatus

This chapter will cover the diagnostic technique used in this study to include the optical emission and the CRM model which was used to gather the time-dependent, two-dimensional data and the electron temperature of the main discharge. In addition, this chapter will describe the types of Hall thrusters used and the facility in which the experiment was completed. Lastly, the multiple test matrices are discussed for the different types of experiments which was performed for this study.

3.1 Plasma Emission and the Collisional-Radiation Model

The emission from the main discharge of the Hall thruster is the result of excited particles moving to a lower energy level by means of releasing a photon. For the Hall thruster, several such mechanisms occur due to the different species within the plasma. The most common mechanism which contributes to the optical radiation is given as:

$$e^- + A \rightarrow A^* + e^- \tag{3.1}$$

$$e^- + A \rightarrow A^{+k*} + (k+1)\,e^- \tag{3.2}$$

$$e^- + A^* \rightarrow A^{+k*} + k e^- \tag{3.3}$$

$$e^- + A^m \rightarrow A^* + e^- \tag{3.4}$$

$$e^- + A^m \rightarrow A^{+k*} + (k+1)\,e^- \tag{3.5}$$

where the * represents excited species which either lead to optical emission or have sufficient lifetime to transfer the excitation in subsequent atomic or electronic col-

lisions. The variable k represents the charge state of the ion while m indicates a metastable state of the generic atom or molecule A [9].

Since the plasma produced by the Hall thruster has low density, it is reasonable to assume the plasma is optically thin, where photons are allowed to escape rather than be reabsorbed. Without the re-absorbtion, the upward radiative transitions are negligible compared to the downward transitions. Conversely, all upward transition or excitation in this assumption is the result of collisions since the radiation density is low. The resultant is the simple model of corona equilibrium so named for its applicability to the solar corona [37].

The intensity per unit volume of the plasma radiation for a specific wavelength, λ is approximated by:

$$I_\lambda = \frac{hc}{4\pi\lambda} N_0 N_e \left[\sum_j \frac{N_j}{N_0} \int_0^\infty f_e\left(E_e\right) \sigma_{ej}^\lambda\left(E_e\right) v_e dE_e \right] \tag{3.6}$$

where N_0, N_e, and N_j, are the number densities of the gas, electrons, and gas in the state j. The terms $f_e\left(E_e\right)$ and $\sigma_{ej}^\lambda\left(E_e\right)$ are the electron energy distribution function and the cross section for an electron with energy, E_e, to excite an atom or ion from state j to produce radiation at the wavelength, λ. In addition, the electron energy distribution is

$$f_e\left(E_e\right) = \frac{2}{\pi} \sqrt{\frac{2}{\pi\left(kT_e\right)^3 m_e}} e^{-E_e/kT_e} \tag{3.7}$$

and the cross section is

$$\sigma_{ej}^\lambda\left(E_e\right) = \left(\frac{bh^2}{8\pi m_e kT_e}\right) \left(\frac{\Omega}{g}\right) \tag{3.8}$$

where b is a correction coefficient, g is the atomic degeneracy and Ω is the collision strength. From Equation (3.6), (3.7), and(3.8), the emission of the plasma is a func-

tion of several factors such as the number densities (of different populations) and the electron temperature, T_e [44, 73, 78].

Individual wavelengths of the emission were also studied to provide additional properties of the plasma. For the strong emission lines of the Hall thruster, the corona radiation model is considered a strong starting point for a CRM. However, the assumptions used in the corona model does not fully resolve some of the complex processes which take place in the Hall thruster main discharge. Some of the deficiencies of the initial models were the non-inclusion of stepwise excitation by means of the metastable states, the inability to describe some plasma emissions in the ionization region, and the neglect of heavy particle interactions.

For xenon in a Hall thruster discharge, the mechanisms which cause an optical radiation is due mainly to the following collision processes in the CRM:

$$e^- + Xe \rightarrow Xe^* + e^- \tag{3.9}$$

$$e^- + Xe \rightarrow Xe^{+k*} + (k+1)\,e^- \tag{3.10}$$

$$e^- + Xe^* \rightarrow Xe^{+k*} + ke^- \tag{3.11}$$

$$e^- + Xe^m \rightarrow Xe^* + e^- \tag{3.12}$$

$$e^- + Xe^m \rightarrow Xe^{+k*} + (k+1)\,e^- \tag{3.13}$$

$$Xe^+ + Xe \rightarrow Xe^{+*} + Xe^* \tag{3.14}$$

$$Xe^{+2} + Xe \rightarrow Xe^{+2*} + Xe^* \tag{3.15}$$

$$Xe^{+2} + Xe \rightarrow Xe^{+*} + Xe^{+*} \tag{3.16}$$

With the inclusion of the heavier particles, the plasma radiation intensity for xenon per unit volume emitting in the wavelength, λ is given as:

$$I_\lambda = \frac{hc}{4\pi\lambda} N_0 N_e \sum_p \frac{N_p}{N_0} \int_0^\infty f_e(E_e) \sigma_{ep}^\lambda(E_e) v_e dE_e +$$

$$\frac{hc}{4\pi\lambda} N_0 N_e \sum_q \frac{N_q}{N_0} \int_0^\infty f_q(E_q) \sigma_q^\lambda(E_q) v_i dE_q \tag{3.17}$$

where N_0, N_e, N_p, and N_i are the number densities for xenon atoms, electrons, xenon atoms in the p state and ions. The terms $f_e(E_e)$ and $f_q(E_q)$ are the electron and ion distribution functions. The expression $\sigma_{ep}^\lambda(E_e)$ and $\sigma_q^\lambda(E_q)$ are the cross sections for an electron with energy, E_e, to excite a xenon atom or ion from state p and the cross section of an ion with charge q and energy, E_q, to produce radiation at the wavelength, λ. The velocity of the electrons and ions are expressed as v_e and v_i.

However, equation (3.17) assumes the states excited by electron and ion collisions are only depopulated through radiation decay which is not justifiable for all xenon atomic and ionic transitions. Nevertheless, experimental measurements and analysis conducted by Karabadzhak *et al* of the electron and ion distribution functions in addition to collisional cross sections provided a model for determining intensity [44]. For specific NIR lines of XeI, the intensity of the optical emission can be modeled as:

$$I_\lambda(XeI) = \frac{hc}{4\pi\lambda} N_0 N_e \left(k_{e0}^\lambda + \frac{N_m}{N_0} k_{em}^\lambda + \alpha k_1^\lambda + \frac{1-\alpha}{2} k_2^\lambda \right) \tag{3.18}$$

where k_{e0}^λ is the ground state electron-atom impact line emission excitation rate coefficient and is defined as:

$$k_{e0}^\lambda = \int_0^\infty 2E_e \sqrt{\frac{2}{\pi (kT_e)^3 m_e}} \exp\left(-\frac{E_e}{kT_e}\right) \sigma_{e0}^\lambda (E_e)\, dE_e, \qquad (3.19)$$

k_1^λ is the singly charged ion collision emission excitation rate coefficient and has the form:

$$k_1^\lambda \approx \sigma_1^\lambda (eV) \sqrt{\frac{2eV}{M}}, \qquad (3.20)$$

k_2^λ is the doubly charged ion collision emission excitation rate coefficient and has the form:

$$k_2^\lambda \approx \sigma_2^\lambda (2eV) \sqrt{\frac{4eV}{M}}, \qquad (3.21)$$

and α is the ratio of the first ion number density to the electron number density [9,18].

With analytical and experimental results from Chiu *et al* and Sommerville *et al*, the ratio of select emission lines can provide electron temperatures measurements throughout the xenon plasma produced by a Hall thruster [9,45,73]. The importance of such a technique provides a means to determine plasma properties without disturbance to the flowfield. Additionally, the Karabadzhak, Chiu, and Dressler (KCD) method can be applied to other thrusters given some additional information which is provided by simulations such as HPHall [44]. One unique application of the KCD method was applied to the BHT-200 to determine the electron temperature of the plasma plume [10,78].

The selection of emission lines in the NIR are based on the emission excitation cross section measure by Chiu *et al*. The specific lines of interest are 823.2, 828.0, and 834.7 nm. Ratio of the lines 823/828 nm and 834/828 nm provide a strong measure, over a wide range, of electron temperatures with each ratio uncoupled from

the other [18]. For the BHT-200, the ratio of intensities was calculated and provided in Figure 3.1.
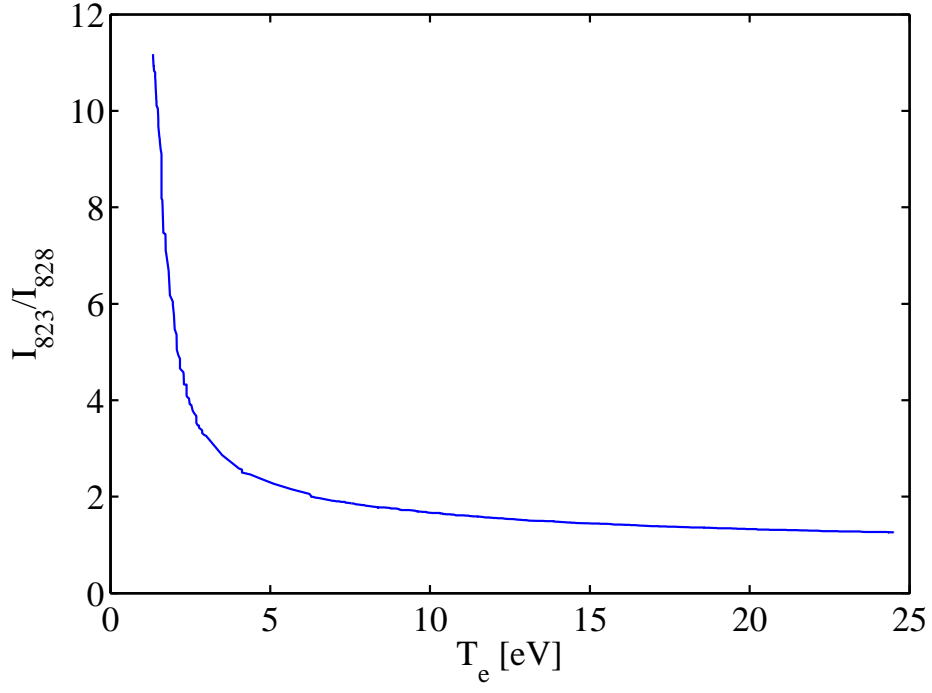
(a) Electron Temperature dependence on I_{823}/I_{828}
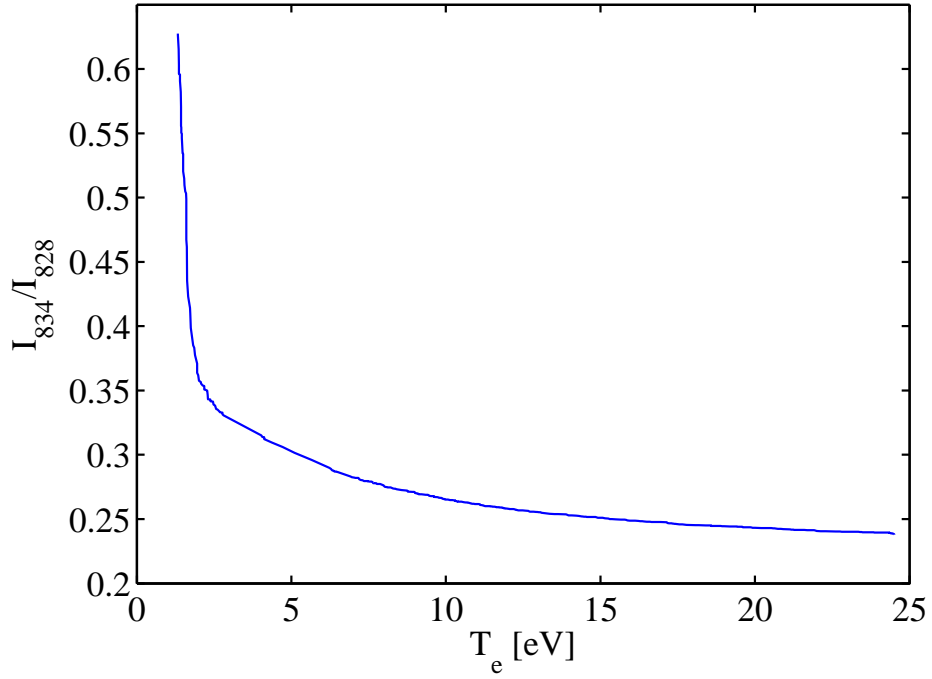
(b) Electron Temperature dependence on I_{834}/I_{828}

Figure 3.1:   The computed electron temperature dependence on the intensity ratios of I_{823}/I_{828} (a) and I_{834}/I_{828} (b) for the BHT-200.

Figure 3.2:   Photo of the BHT-200 Hall thruster.

3.2   Experimental Apparatus

The BHT-200 and BHT-600 were used for this experiment. Both of the Hall thrusters were manufactured by Busek Co. Inc. based out of Natick, MA. The BHT-200, shown in Figure 3.2, was designed to operate at a nominal discharge potential of 250 V with a discharge current of 0.8 A which equates to an operating discharge power of 200 W. It requires a propellant mass flow rate of 0.94 mg/s of xenon and provides a thrust of 12.8 mN at a specific impulse of 1390 seconds with propulsive efficiency of 43.5% [36].

Conversely, the BHT-600, shown in Figure 3.3, was designed to operate at a nominal discharge potential and current of 300 V and 2.0 A, respectively, with a propellant mass flow rate of 2.6 mg/s of xenon. It is capable of providing 39.1 mN of thrust while supplying 1530 s of specific impulse with a propulsive efficiency of 49%
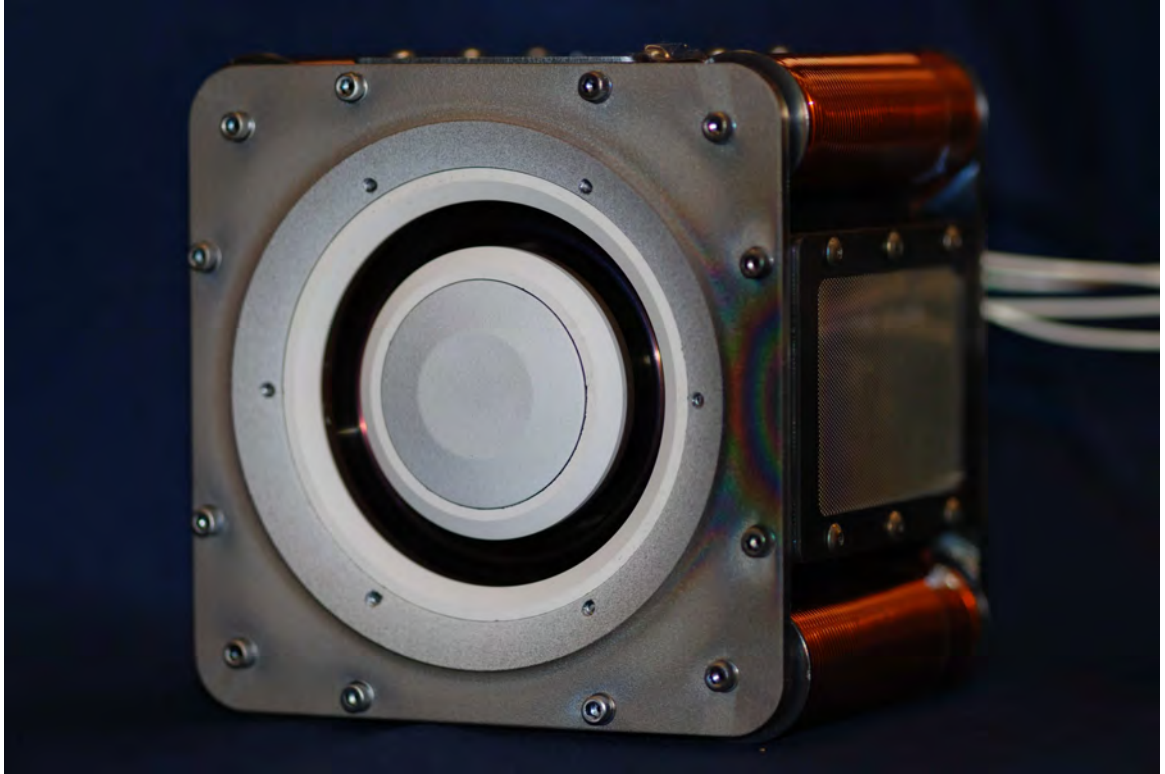
Figure 3.3:   Photo of the BHT-600 Hall thruster.

[29]. A comparison of the two thrusters nominal operating conditions and nominal performance characteristics is shown in Table 3.1 and Table 3.2, respectively.

Both the 200 W and 600 W Hall thruster are currently operated by the Busek BPU-600 PPU, Power Processing Unit, and is powered by a Sorensen model DCS55-55 which is capable of suppling a potential range of 0-55 V at 0-55 A at 3 kW maximum output. The PPU, contains separate power processing cards for the anode, cathode heater, cathode keeper, and magnets.

As seen in Figure 3.4, the anode, cathode keeper, cathode heater, and magnets all have different input potential and current requirements but they all have a common ground, and in this case, they are grounded to the vacuum tank. In addition, the power supplies to the anode, cathode keeper, and magnets have a shunt resistor placed in series for a National Instruments SCXI-1321 to measure the current of each component in real-time.

41
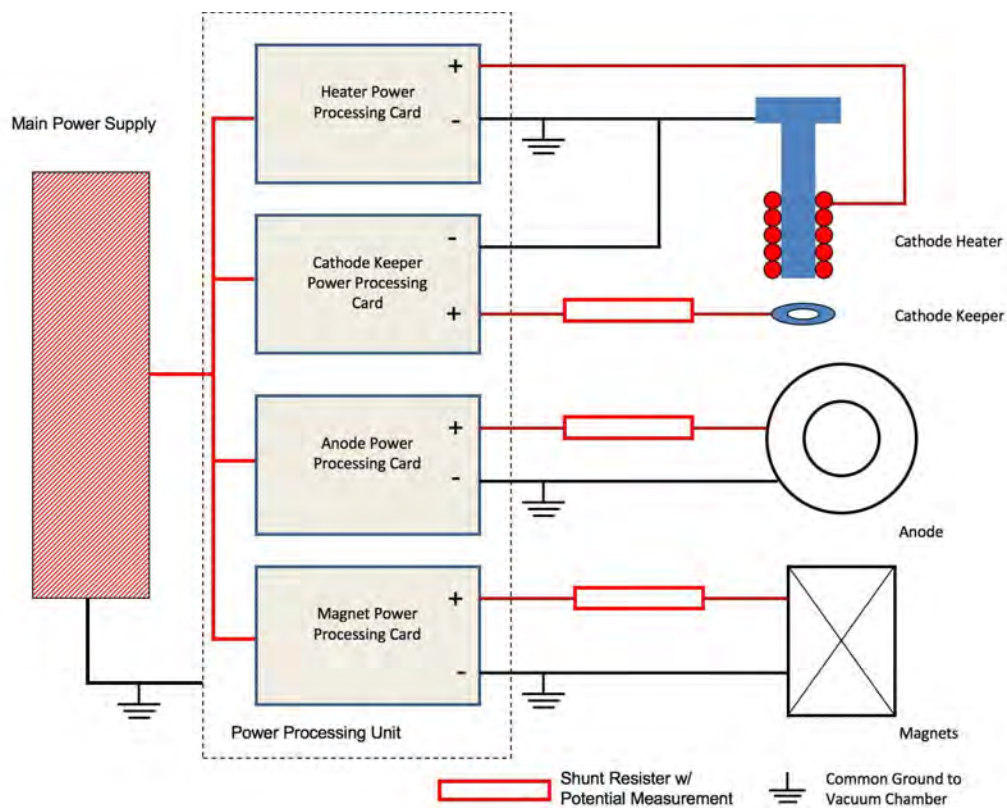
Figure 3.4:   Electrical diagram of Hall thruster components. Each component of the BPU-600 is powered by the main power supply and share a common ground. Shunt resisters are placed in series with each component to provide real-time electrical parameters to the user.

Table 3.1:   Comparison of nominal operating conditions for BHT-200 and BHT-600 Hall thrusters.

Properties	BHT-200	BHT-600
Discharge Potential [V]	250	300
Discharge Current [A]	0.8	2.0
Discharge Power [W]	200	600
Magnet Current [A]	1.0	1.75
Propellant Mass Flow [mg/s]	0.94	2.6

Table 3.2:   Comparison of nominal performance parameters for BHT-200 and BHT-600 Hall thrusters.

Properties	BHT-200	BHT-600
Thrust [mN]	12.8	39.1
Specific Impulse [s]	1390	1530
Efficiency [%]	43.5	49.0

The Space Propulsion Application Simulation System (SPASS) Laboratory located at the Air Force Institute of Technology (AFIT) on Wright-Patterson AFB provided the high capacity vacuum chamber in which the 200 W and 600 W thrusters were tested. The chamber measures 1.8 m in diameter with a length of 2.5 m having a volume of approximately 6.5 m^3 and is capable of pumping 16,000 liters per second of xenon. The vacuum chamber is capable of reaching and maintaining 3×10^{-8} torr of base pressure by means of a two-stage pump down system and is fully automated by an Allen-Bradley Automation Control System. The integration of the two-stage pump down system, Allen Bradley control unit, and the vacuum chamber was integrated by PHPK of Columbus, Ohio. The first stage of pumping down the vacuum chamber, from atmospheric pressure to 80 mtorr, is accomplished by a Leybold-Trivac rotary van vacuum pump and the second stage is completed by four 20 in CVI Torrmaster TM 500 cryogenic pumps. Gases inside the vacuum chamber are condensed on the cryo-head assembly reaching temperatures in the range of 16-22 K and acts like a cold trap inside of the chamber.

The pressure of the vacuum chamber from atmosphere to 80 mtorr is measured by a Lester 300 series mini-convectron gauge which also supports the switch-over from roughing pump to cryogenic pumping operations. An ExTorr XT 100 Residual Gas Analyzer (RGA) measures pressures below 80 mtorr by measuring the partial pressures of each atomic mass and calculating the total pressure via Dalton's Law of Partial Pressures.

The vacuum chamber is also equipped with three optical windows to allow for data collection in the visible and infrared (IR) spectrum. The material used for the IR window is zinc selenide (ZnSe) due to its high transmissivity in the near IR spectrum of 700 nm to 1400 nm. The IR window itself is 12.7 cm in diameter and 10 mm thick however the viewport which contains the IR window and mounts it to the vacuum chamber has a viewing diameter of 11.4 cm [5].

The other two optical viewing ports are optimized in the visible spectrum. It is made of optical quality glass and has a transmissivity in the range of the visible spectrum. The windows measure 12.7 cm and are 10 mm thick. They are attached to view ports that allow for a viewing diameter of 11.4 cm.

Propellant flow to the anode of the Hall thruster is provided by a MKS model 180A flow control valve with a range of 0 to 50 SCCM while the cathode propellant line is controlled by MKS model 180A with a range of 0 to 10 SCCM. In total, the lab has four control valves, three in the 0-10 SCCM range and one in the 0-50 SCCM range controlling a combination of cathodes and anodes in support of multiple testing. All of the flow control valves are managed by the MKS flow controller Type 247 which has the capability to regulate four channels. Flow control valves to both the anode and cathode are calibrated at the factory for xenon and are accurate to $\leq 0.01\%$. The two types of propellants being used in the SPASS Lab are 99.99% pure xenon and 99.99% pure krypton. The propellant feed system can be seen in Figure 3.5, below [71].
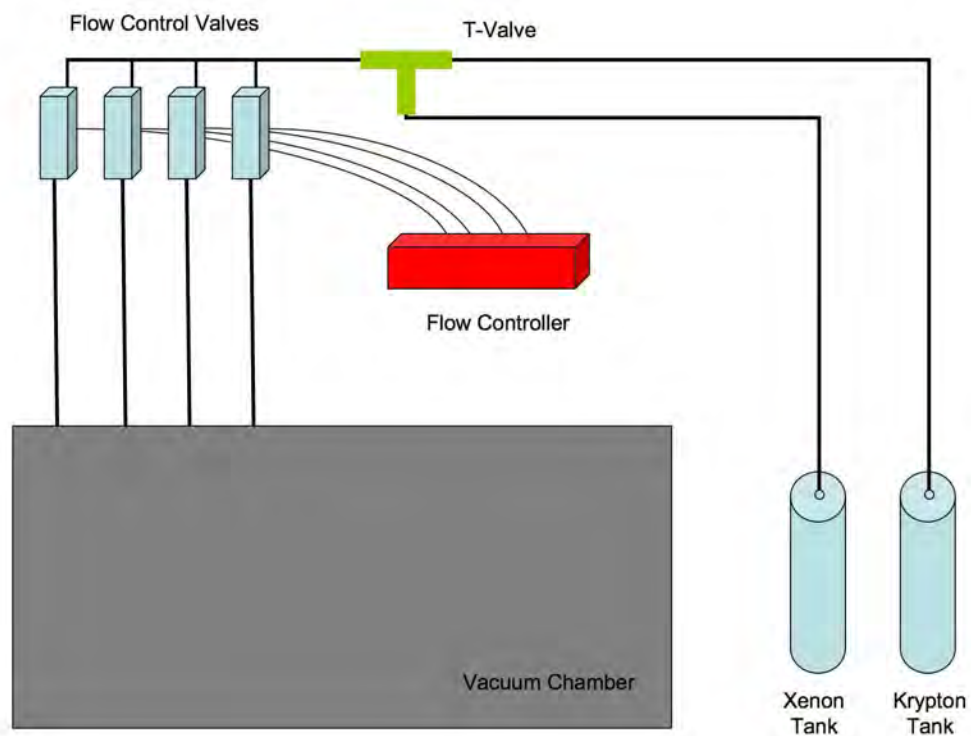
Figure 3.5:   Propellant flow diagram for the Hall thrusters. Xenon and krypton propellant tanks are attached to a T-valve to allow the user to switch between either propellant while the vacuum chamber is pumped down. Four flow control valves, all controlled by the same flow controller, allow for precise flow rates to the anode and the cathode.

The Hall thrusters were mounted on an Aerotech three-axis translational stage inside the SPASS Lab vacuum chamber, as seen in Figure 3.6. The translational stage provided over 60 cm of range in each axis which is controlled independently at sub-millimeter accuracy. Although it is fully automated, the translational stage was used in the manual setting to align the thruster. A visible spectrum window was used for optical access during this experiment.

The direct emission data was collected with a Shimadzu HyperVision HPV-2 high-speed camera which is able to record at one-million frames per second (Mfps) by using an In-Situ-Charged Coupled Device (IS-CCD) as its sensor. The spectral sensitivity of the camera was optimized for the visible spectrum as shown in Figure 3.7 [1]. With the given spectral sensitivity, the optical emission of both excited neutrals and ions were captured by the camera, consequently limiting the understanding of how each species behaved independently. However, this technique still provided abundant information on the behavior of the plasma field in space and time.

The camera has a 312 by 260 pixel resolution and has a maximum storage capacity of 100 images at 1 Mfps. Three exposure times of 250, 500, and 750 ns can be set manually on the camera at the 1.0 Mfps frame rate. Attached to the camera is a Sigma 300 mm telephoto lens with a maximum aperture f/stop of 2.8. It has a focus distance of 2.5 m, magnification of 7.5, and a view angle of 8.2 degrees. Even with the telephoto lens, the outer wall diameter of the thruster, approximately 32 mm for the 200 W thruster and 64 mm for the 600 W thruster, only encompassed 70 by 70 pixels or 120 by 120 pixels in the image frame, respectively. After the thrusters were started and allowed to stabilize at the various conditions, the Aerotech translational stage was used to align the thruster plume through the optical access window (i.e. the thruster plume was centered on the IS-CCD sensor of the camera).

Electrical parameters, such as the discharge potential and discharge current of the thruster, were recorded using a two-channel oscilloscope. The probe used to measure the discharge potential was a high voltage probe, which has a potential limit
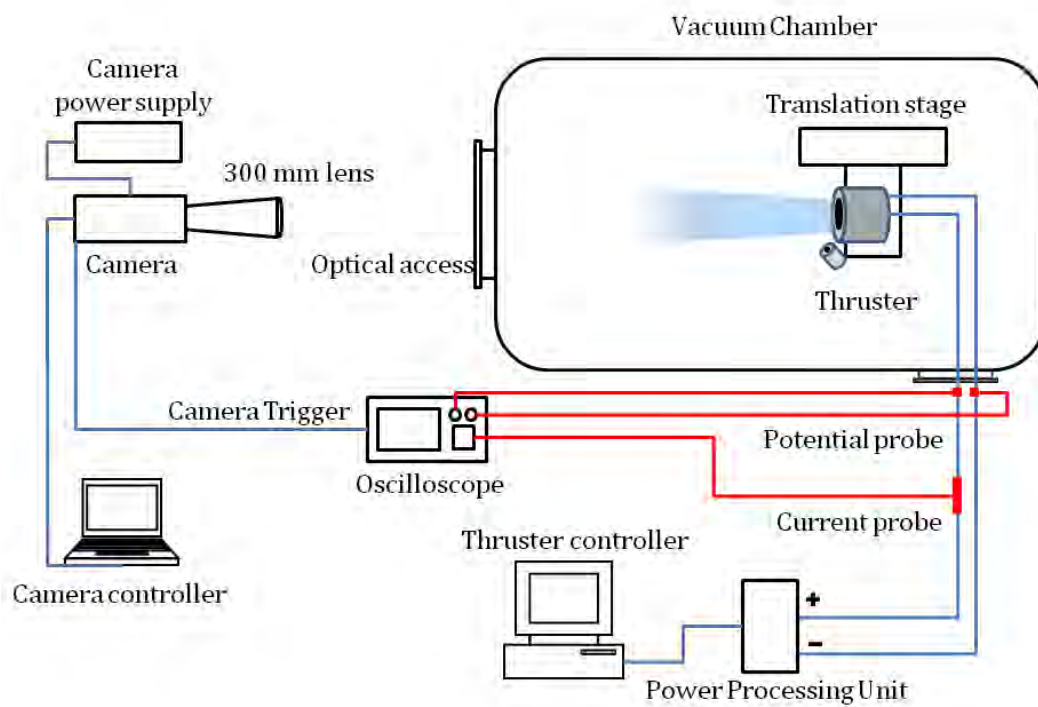
Figure 3.6:   Direct emission experimental setup. The ultra-high speed camera was triggered by the oscilloscope which also measured the discharge current and potential. The camera was placed directly in front of the thruster along the centerline.
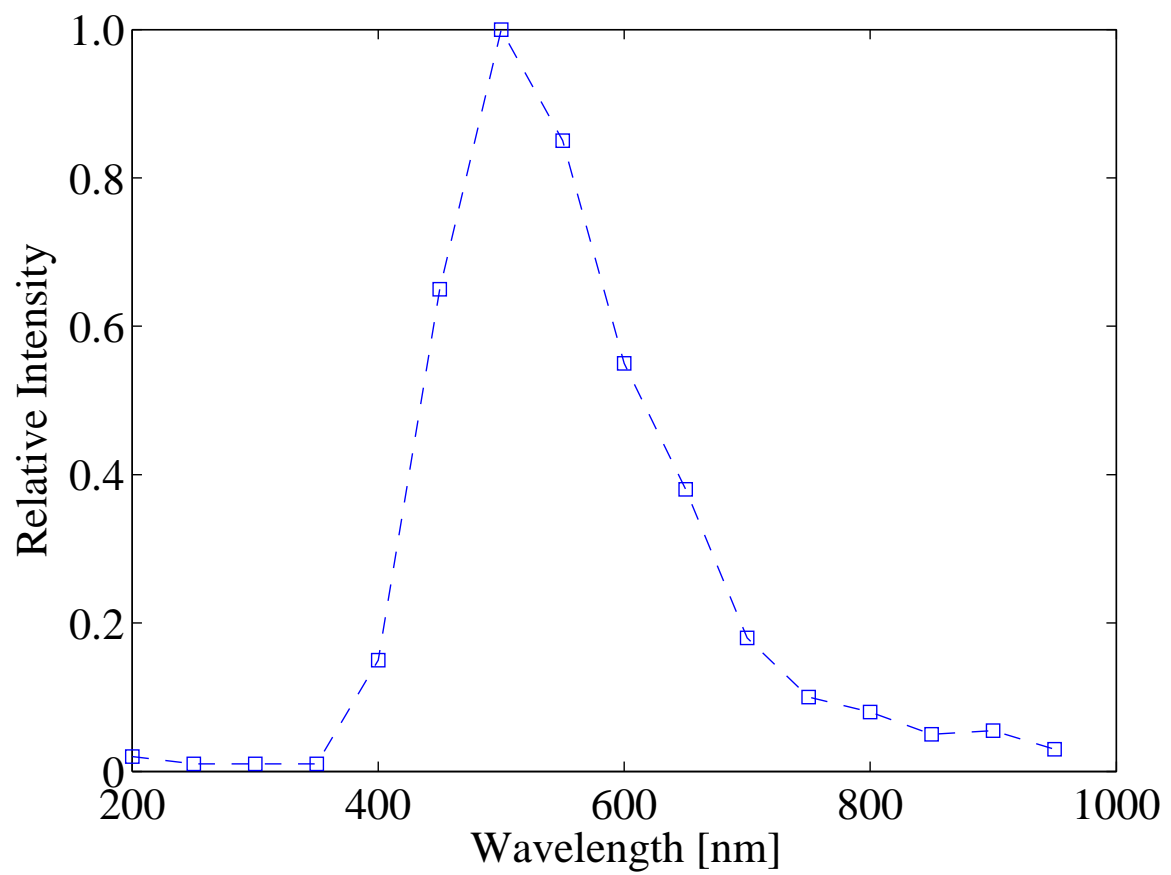
Figure 3.7: Relative spectral response of the Shimadzu HPV-2 ultra-high speed camera taken from Shimadzu HPV-2 Spectral Response
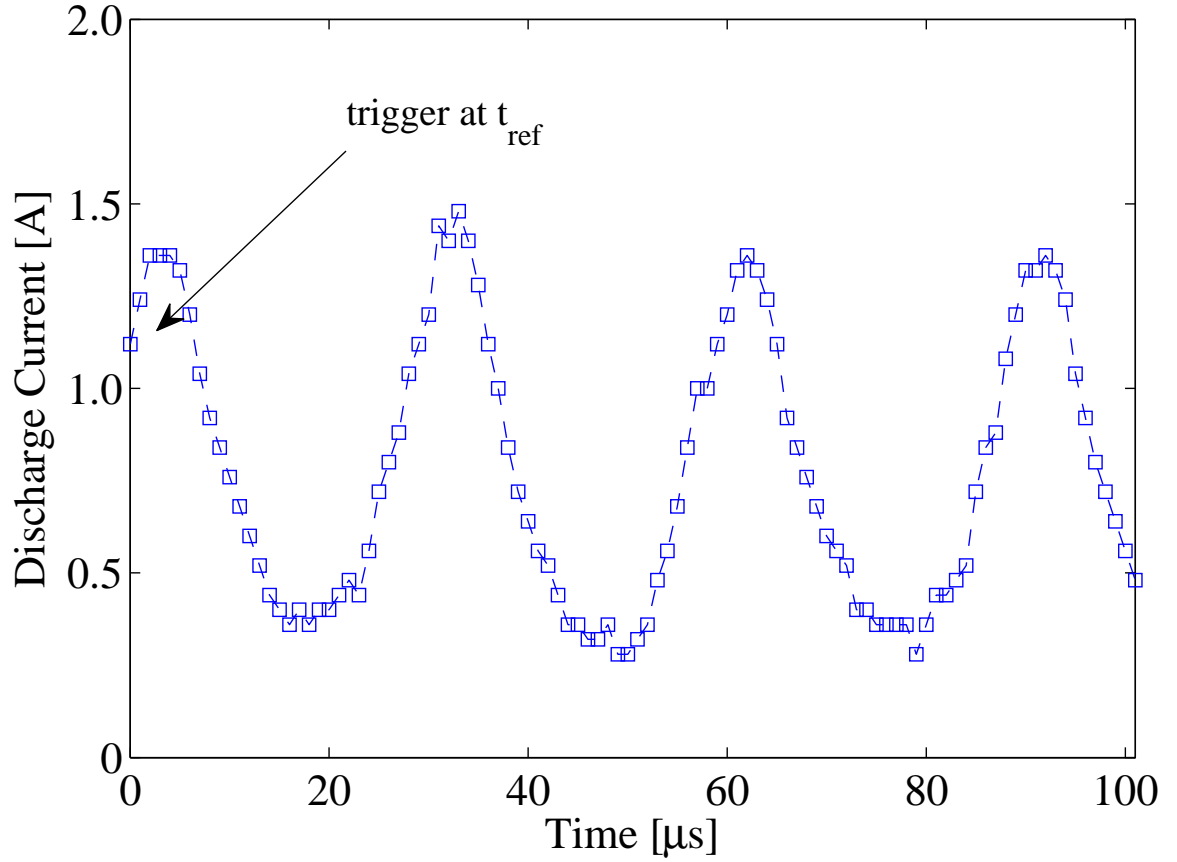
Figure 3.8: Sample discharge current of 200 W Hall thruster operated at nominal conditions. $V_d = 250$ V, $I_d = 0.8$ A, $\dot{m} = 0.94$ mg/s of xenon. The trigger for the high-speed camera and the oscilloscope data acquisition was initiated by this signal at the indicated time, t_{ref}.

of 5600 V with a maximum sampling rate of 100 MHz. An inductive current probe was used to measure the discharge current. It was capable of measuring up to 50 A peak pulse current and could sample up to 50 MHz. Since the maximum frame rate of the camera was 1 Mfps, the oscilloscope was also set with a sampling frequency of 1 MHz.

As shown in Figure 3.8, the discharge current of the thruster was observed oscillating periodically. The recurrent feature of this signal was exploited by triggering the camera when the value of the discharge current rose to a set value in which the external trigger of the oscilloscope would start the camera, while simultaneously

recording the discharge current and potential. Using this technique, the current, potential, and ultra-high speed video was synchronized to a reference time, t_{ref}.

The BHT-200 was operated at different discharge potentials to characterize different instabilities within the plasma discharge. For the BHT-200 operating with xenon propellant, the discharge potential was set at the nominal value of 250 V and reduced incrementally to 80 V. In addition, at the lower discharge potentials, the discharge current and magnet current were also varied independently to determine their effects on the observed instabilities. Table 3.3 shows the test matrix for the BHT-200 operating with xenon.

In cases 1-10 the discharge potential was varied while maintaining the the nominal discharge current and magnet current of 0.8 and 1.0 A, respectively. Consequently, as the discharge potential was decreased, the discharge current of the thruster would also vary. In order to maintain the constant discharge current, the mass flow of the thruster was varied. However, cases 24-29 were performed to investigate the effects of the oscillations when the discharge potential was varied while the mass flow rate and magnet current were held constant.

In cases 11-14 the discharge potential and current were held constant at 90 V and 0.8 A, respectively, while magnet current was varied. In comparison, cases 20-23 also have constant discharge potential and discharge current, however, in these test cases the discharge potential was set to 80 V while the discharge current was still maintained at 0.8 A. These two sets of cases were examined to determine if the effects of the magnet current changed at various discharge potentials. For cases 15-19, the discharge potential and magnet current was held constant while the discharge current were varied from 0.5 A to 1.6 A.

Furthermore, experimental data for the BHT-200 was also gathered at different operating conditions utilizing krypton. As with the xenon case, the test matrix can be found in Table 3.4 where the discharge potential was varied from 250 V to 80 V to

Table 3.3:   Test matrix of BHT-200 operating with xenon. Variations of different thruster parameters were explored to determine its effects on the plasma oscillations and instabilities.

Case	Discharge Potential [V]	Discharge Current [A]	Magnet Current [A]	Mass Flow Rate [mg/s]
1	250	0.80	1.0	0.94
2	230	0.80	1.0	0.94
3	210	0.80	1.0	0.90
4	190	0.80	1.0	0.90
5	170	0.80	1.0	0.86
6	150	0.80	1.0	0.84
7	130	0.80	1.0	0.81
8	110	0.80	1.0	0.81
9	90	0.80	1.0	0.94
10	80	0.80	1.0	1.11
11	90	0.80	0.2	0.77
12	90	0.80	0.4	0.85
13	90	0.80	0.6	0.87
14	90	0.80	0.8	0.92
15	80	0.50	1.0	0.89
16	80	0.60	1.0	0.95
17	80	1.00	1.0	1.13
18	80	1.20	1.0	1.26
19	80	1.60	1.0	1.53
20	80	0.80	0.2	0.86
21	80	0.80	0.4	0.95
22	80	0.80	0.6	1.00
23	80	0.80	0.8	1.07
24	210	0.83	1.0	0.95
25	170	0.86	1.0	0.95
26	130	0.97	1.0	0.95
27	110	0.96	1.0	0.95
28	90	0.83	1.0	0.95
29	80	0.50	1.0	0.95

induce different oscillations within the thruster. In addition, the discharge current and magnet current were also varied to determine their effects on the observed oscillations.

In cases 1-9 the discharge current and magnet current were held constant while the discharge potential was varied. Again, the mass flow rate was adjusted throughout the discharge potential test regime to maintain the constant discharge current. In contrast, in cases 19-23 the discharge current was allowed to vary in order to keep the mass flow rate constant while the magnet current was held constant at 1.0 A.

Cases 10-13 maintained the discharge potential and current at 90 V and 0.8 A, respectively, while varying the magnet current. For cases 14-18 the discharge potential and magnet current were held constant at 90 V and 1.0 A, respectively, while the discharge current was allowed to vary.

For the BHT-600, the test matrix is similar to the matrix discussed for the BHT-200. Different oscillations of the plasma discharge were observed when the discharge potential was allowed to vary. Other parameters of the thruster, such as the discharge current and magnet current, were also allowed to vary to determine their effects on the oscillations and instabilities. Table 3.5 shows the test matrix for the BHT-600 utilizing xenon.

The discharge current and magnet current were held constant at 2.0 A and 1.75 A, respectively, while the discharge potential was allowed to vary from 300 V to 90 V for cases 1-12. Alternatively, the remaining cases held the discharge potential constant while varying either the magnet current, cases 13-17 and cases 23-27, or the discharge current as seen in cases 18-22.

This process was then repeated for the BHT-600 when operated with krypton as shown in Table 3.6. Cases 1-9 maintained the discharge current and magnet current constant at 2.0 A and 1.75 A, respectively, while varying the discharge potential from 250 V to 90 V. The remaining cases held the discharge potential constant at either 100 V, cases 10-13 and 14-18, or 90 V, cases 19-23, similar to the xenon cases. However, in cases 10-13 and 19-23 the magnet current was varied while maintaining

Table 3.4:   Test matrix of BHT-200 operating with krypton. Variations of different thruster parameters were explored to determine its effects on the plasma oscillations and instabilities.

Case	Discharge Potential [V]	Discharge Current [A]	Magnet Current [A]	Mass Flow Rate [mg/s]
1	250	0.80	1.0	0.67
2	230	0.80	1.0	0.66
3	210	0.80	1.0	0.66
4	190	0.80	1.0	0.66
5	170	0.80	1.0	0.66
6	150	0.80	1.0	0.70
7	130	0.80	1.0	0.76
8	110	0.80	1.0	0.93
9	90	0.80	1.0	1.26
10	90	0.80	0.2	0.88
11	90	0.80	0.4	1.18
12	90	0.80	0.6	1.18
13	90	0.80	0.8	1.24
14	90	0.50	1.0	1.15
15	90	0.60	1.0	1.19
16	90	1.00	1.0	1.37
17	90	1.20	1.0	1.45
18	90	1.60	1.0	1.56
19	230	0.80	1.0	0.67
20	210	0.81	1.0	0.67
21	190	0.82	1.0	0.67
22	170	0.81	1.0	0.67
23	150	0.72	1.0	0.67

Table 3.5:   Test matrix of BHT-600 operating with xenon. Variations of different thruster parameters were explored to determine its effects on the plasma oscillations and instabilities

Case	Discharge Potential [V]	Discharge Current [A]	Magnet Current [A]	Mass Flow Rate [mg/s]
1	300	2.00	1.75	2.60
2	280	2.00	1.75	2.54
3	260	2.00	1.75	2.54
4	240	2.00	1.75	2.51
5	220	2.00	1.75	2.51
6	200	2.00	1.75	2.48
7	175	2.00	1.75	2.48
8	150	2.00	1.75	2.33
9	125	2.00	1.75	2.32
10	120	2.00	1.75	2.32
11	110	2.00	1.75	2.32
12	90	2.00	1.75	2.33
13	100	2.00	0.25	1.81
14	100	2.00	0.50	2.09
15	100	2.00	1.00	2.28
16	100	2.00	1.25	2.28
17	100	2.00	1.50	2.28
18	100	1.60	1.75	2.03
19	100	2.00	1.75	2.26
20	100	2.20	1.75	2.44
21	100	2.50	1.75	2.66
22	100	3.00	1.75	3.04
23	90	2.00	0.25	1.81
24	90	2.00	0.50	2.05
25	90	2.00	1.00	2.24
26	90	2.00	1.25	2.24
27	90	2.00	1.50	2.30
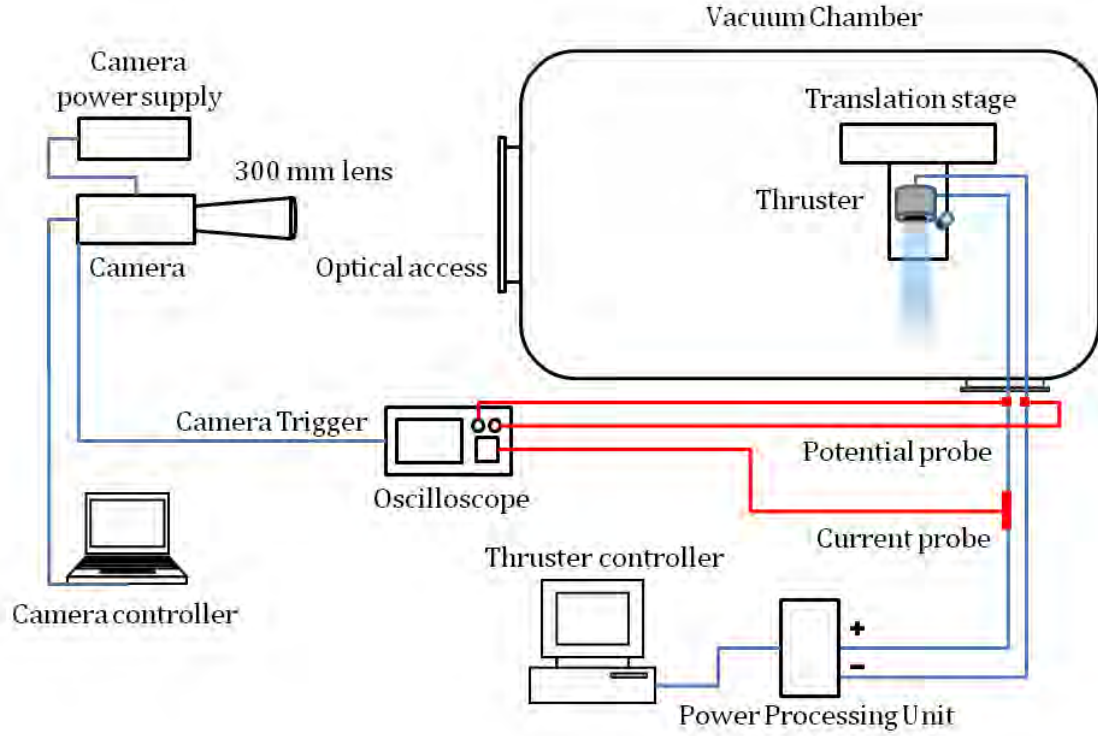
Figure 3.9: Direct emission experimental setup for the side views of the plasma discharge. The ultra-high speed camera was triggered by the oscilloscope which also measured the discharge current and potential. The camera was placed to capture the plasma plume from the side or 90-degrees from the face of the thruster.

a constant discharge current. Conversely, cases 14-18 held a constant magnet current while varying the discharge current.

In addition to the images from the zero-aspect or front view, high speed images of the thruster rotated 90-degrees were also taken as seen in Figure 3.9. Alignment of the plasma plume to the camera was accomplished with the 3-axis translational stage to ensure the image pixels were maximized. These side images of the thruster were taken at much lower frame rates compared to the zero-aspect view since the low density plasma did not provide sufficient direct emission in this orientation.

Table 3.7, 3.8, 3.9, and 3.10 shows the test matrices for direct emission of the plasma plume with the thruster positioned 90-degrees to the high speed camera. In

55

Table 3.6:   Test matrix of BHT-600 operating with krypton. Variations of different thruster parameters were explored to determine its effects on the plasma oscillations and instabilities

Case	Discharge Potential [V]	Discharge Current [A]	Magnet Current [A]	Mass Flow Rate [mg/s]
1	250	2.00	1.75	1.90
2	225	2.00	1.75	1.91
3	200	2.00	1.75	1.90
4	175	2.00	1.75	1.90
5	150	2.00	1.75	1.91
6	125	2.00	1.75	2.14
7	120	2.00	1.75	2.18
8	110	2.00	1.75	2.32
9	90	2.00	1.75	3.24
10	100	2.00	0.50	1.91
11	100	2.00	1.00	2.23
12	100	2.00	1.25	2.44
13	100	2.00	1.50	2.55
14	100	1.60	1.75	2.48
15	100	2.00	1.75	2.66
16	100	2.25	1.75	2.78
17	100	2.70	1.75	2.94
18	100	3.20	1.75	3.28
19	90	2.00	0.25	1.47
20	90	2.00	0.50	2.04
21	90	2.00	1.00	2.38
22	90	2.00	1.25	2.55
23	90	2.00	1.50	3.01

Table 3.7: Test matrix of BHT-200 for side view imaging operating with xenon. Only the discharge potential was varied while the discharge current and magnet current was held constant at 0.8 A and 1.0 A, respectively.

Case	Discharge Potential [V]	Discharge Current [A]	Magnet Current [A]	Mass Flow Rate [mg/s]
1	250	0.80	1.00	0.90
2	210	0.80	1.00	0.90
3	170	0.80	1.00	0.90
4	150	0.80	1.00	0.87
5	130	0.80	1.00	0.86
6	110	0.80	1.00	0.86
7	90	0.80	1.00	0.92
8	80	0.80	1.00	1.10

these set of images, the discharge current and the magnet current were held constant while the discharge potential was allowed to vary.

Emission spectrum of the BHT-200 was also measured in this study and the schematic of the experiment is shown in Figure 3.10. The spectra of the discharge emission was collected by using an Ocean Optics USB4000 spectrometer with a 42 mm focal length with a wavelength range of 200 to 850 nm. The spectrometer was attached to a SMA 905 to 0.22 numerical aperture single-strand optical fiber which was fed through the vacuum chamber via a fiber optic access hub. Once inside the vacuum chamber, the fiber optic cable connected to the fiber optic access hub which was attached to a wide angle collimator optimized for visible to NIR wavelength. The collimator was placed 60 degrees off-axis from the centerline of the thruster and located approximately 300 mm from the face of the thruster. Alignment of the collimator was accomplished by using a low power laser to position the optical train which was set to investigate the area between the annulus.

Table 3.11 provides the test matrix of the measured emission data. The mass flow rate and magnet current at the various discharge potentials was held constant at 0.94 mg/s of xenon and 1.0 A throughout the test regime.

Table 3.8:   Test matrix of BHT-200 for side view imaging operating with krypton. Only the discharge potential was varied while the discharge current and magnet current was held constant at 0.8 A and 1.0 A, respectively.

Case	Discharge Potential [V]	Discharge Current [A]	Magnet Current [A]	Mass Flow Rate [mg/s]
1	250	0.80	1.0	0.65
2	210	0.80	1.0	0.65
3	170	0.80	1.0	0.65
4	150	0.80	1.0	0.66
5	130	0.80	1.0	0.68
6	110	0.80	1.0	0.91
7	90	0.80	1.0	1.25

Table 3.9:   Test matrix of BHT-600 for side view imaging operating with xenon. Only the discharge potential was varied while the discharge current and magnet current was held constant at 2.0 A and 1.75 A, respectively.

Case	Discharge Potential [V]	Discharge Current [A]	Magnet Current [A]	Mass Flow Rate [mg/s]
1	250	2.00	1.75	2.54
2	200	2.00	1.75	2.39
3	150	2.00	1.75	2.39
4	100	2.00	1.75	2.32

Table 3.10:   Test matrix of BHT-600 for side view imaging operating with krypton. Only the discharge potential was varied while the discharge current and magnet current was held constant at 2.0 A and 1.75 A, respectively.

Case	Discharge Potential [V]	Discharge Current [A]	Magnet Current [A]	Mass Flow Rate [mg/s]
1	250	2.00	1.75	1.86
2	200	2.00	1.75	1.88
3	150	2.00	1.75	1.96
4	100	2.00	1.75	1.96
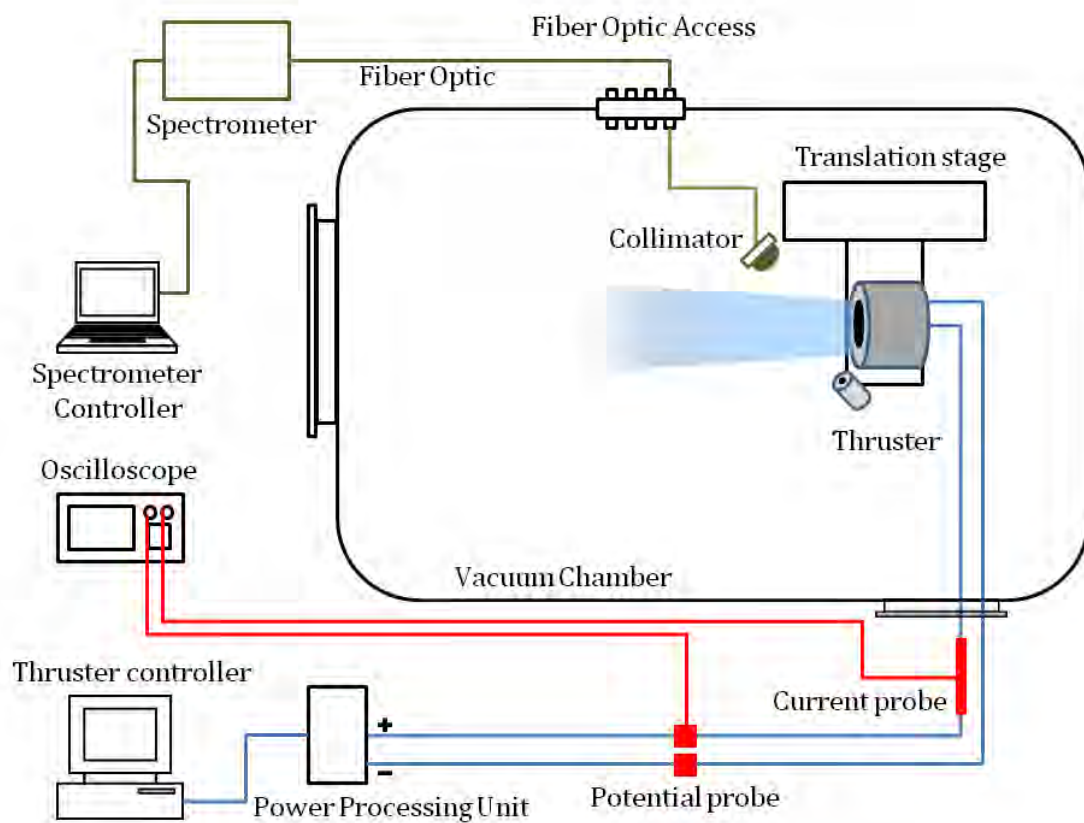
Figure 3.10: Emission spectra of BHT-200 experimental setup. A collimator was used on the end of a optical fiber to collect the emission of the plasma plume. The optical fiber was passed through the wall of the vacuum chamber via the fiber optic access and fed into the spectrometer.

Table 3.11:   Test matrix of BHT-200 emission spectra operating with xenon for a constant mass flow rate of 0.94 mg/s and a magnet current of 1.0 A.

Case	Discharge Potential [V]	Discharge Current [A]	Magnet Current [A]	Mass Flow Rate [mg/s]
1	230	0.80	1.0	0.94
2	210	0.83	1.0	0.94
3	190	0.84	1.0	0.94
4	170	0.86	1.0	0.94
5	150	0.90	1.0	0.94
6	130	0.97	1.0	0.94
7	110	0.96	1.0	0.94
8	100	0.91	1.0	0.94
9	90	0.83	1.0	0.94
10	80	0.50	1.0	0.94

IV. Results and Discussion

Experimental results for the BHT-200 and BHT-600 are presented in this chapter. High speed images of the main discharge were taken for both xenon and krypton feed gas at a zero-aspect view which provides temporal and spatial information in the azimuthal direction of the thruster. In addition to the zero-aspect views of both thrusters, high speed images were also taken at 90-degrees to the thruster face to provide temporal and spatial information in the axial direction.

4.1 Breathing Mode with Xenon

A series of images from the high-speed camera of the BHT-200 with xenon feed gas are shown in Figure 4.1 where the time (in μs) is annotated in the lower right-hand corner of each frame. In the images, the main discharge of the thruster was captured vacillating in intensity where the direct emission started from a minimum value, increasing to a maximum value, and finally returning to the minimum value. In addition, the images in Figure 4.1 are given false color, shown in Figure 4.2, to enhance visualization of the discharge. An advantage for the enhanced coloring is demonstrated in the ability to highlight specific features such as the boron-nitride walls and the plasma *jet* at the center of the image.

For comparison, the color enhanced, high-speed images of the BHT-600 main discharge are also presented in Figure 4.3. Although the two thrusters have different diameters and discharge power, many similarities exists between the two series of high-speed images. In both series of images, the periodic increase and decrease of the intensity is clearly seen in the optical emission. Other features such as the center plasma jet is also observed in the images at $t = 6$ to $t = 9$ during the peak of emission intensity. While it is difficult to see other features, such as the emission of the ceramic insulation, when compared to the BHT-200 images, there are other features which are more dominant in the BHT-600 emission. At the nominal operating conditions, the BHT-600 clearly shows azimuthal plasma structure within the discharge which was not as obvious in the BHT-200 images. A possible reason for the difference in
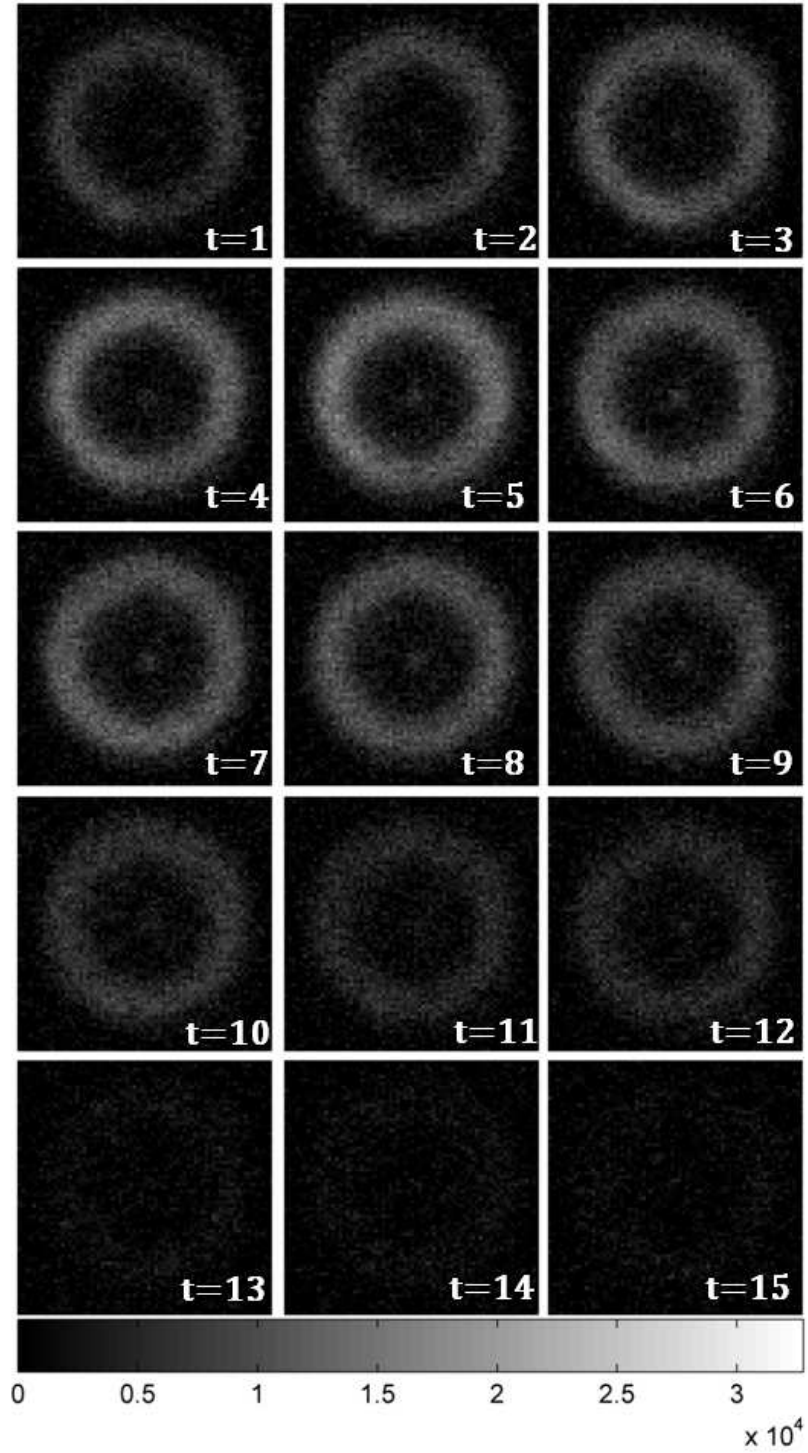
Figure 4.1: Sequential images (gray scale) of BHT-200 discharge oscillation operating at nominal conditions. $V_d = 250$ V, $I_d = 0.8$ A, $I_m = 1.0$ A, $\dot{m} = 0.94$ mg/s of xenon. The time between images was 1 μs with an exposure time of 750 ns. Arbitrary intensity.
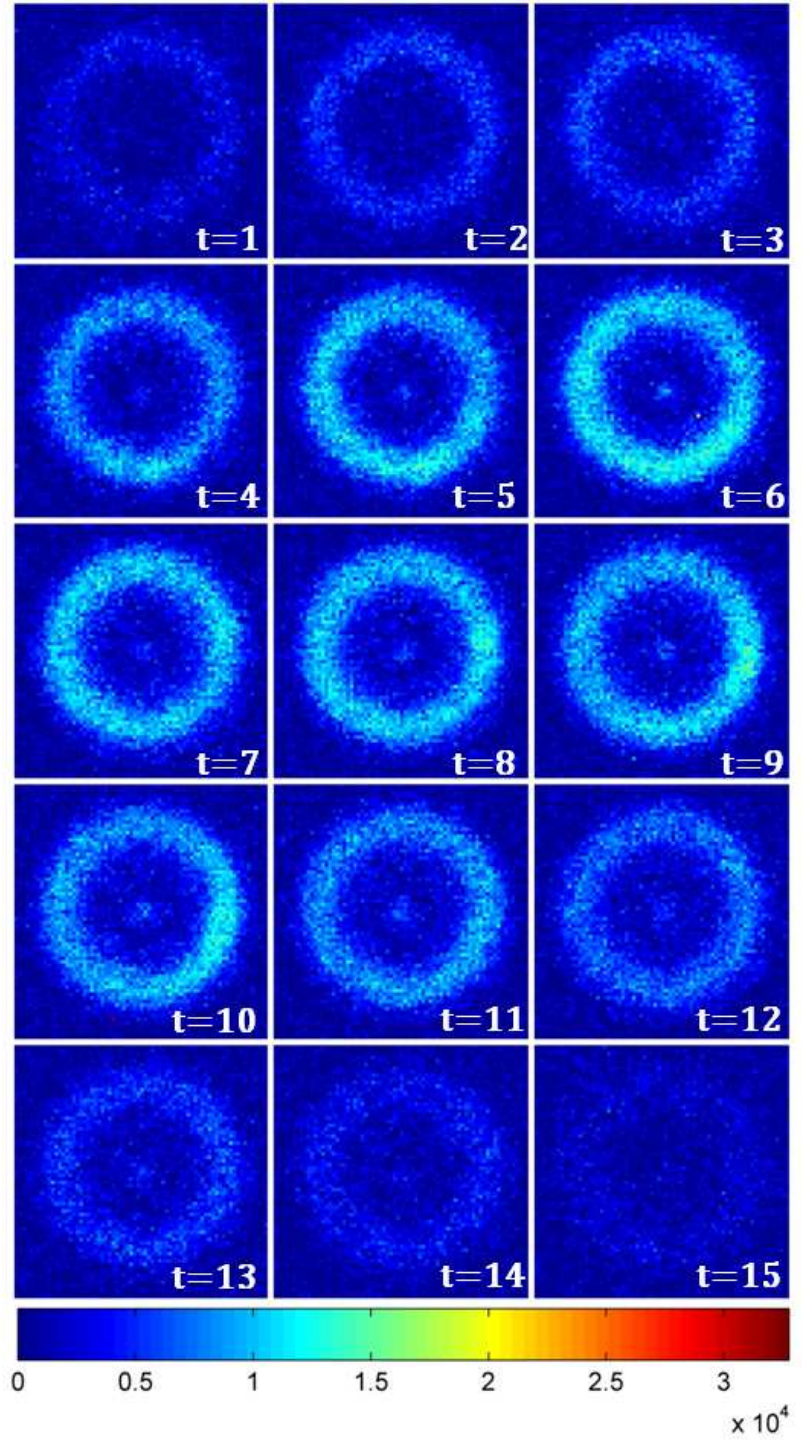
Figure 4.2: Sequential images (color enhanced) of BHT-200 discharge oscillation operating at nominal conditions. $V_d = 250$ V, $I_d = 0.8$ A, $I_m = 1.0$ A, $\dot{m} = 0.94$ mg/s. The time between images was 1 μs with an exposure time of 750 ns. Arbitrary intensity.

the ability to observe the azimuthal plasma structures is related to the difference in number density and electron temperature between the two thrusters.

Although in both series of images, there were azimuthal plasma structures within the main discharge, the predominate mode here is the periodic increase and decrease of the entire discharge channel. This type of behavior was observed in other studies as well. However, the images were usually not observed in sequence, rather reconstructed temporally by referencing the images to a discharge current amplitude spanning a period [15–17, 68].

To verify the optical emission is consistent with the discharge current, the average intensity of each image was determined at the corresponding time. Figure 4.4 shows the average intensity of the images correlates well with the discharge current for the BHT-200.

Additionally, the emission intensity of the BHT-600 was also compared to the discharge current. Figure 4.5 shows the intensity of the emission following closely to the discharge current similar to the BHT-200 data. The close relationship of optical emission to the discharge current was reasonable since the plasma allows for the current to move within the thruster.

The discharge current was also observed to have an amplitude modulation where the maximum value of current was not constant, as seen in Fig. 4.6. The cause of the amplitude modulation is probably related to the propellant mass flow. The delivery of propellant to the ionization region may not be sufficient for continuous flow to match the pumping of the vacuum chamber where observations suggests changes in the mass flow rate to the thruster alters the amplitude of the discharge current. The effects of the mass flow to the discharge oscillations will be discussed in a later section. Since the amplitude of the discharge current changed over time, it was important to determine if the observed emission data accurately represents this variation. Utilizing a discharge current signal with significant amplitude variation, Fig 4.7 shows the plasma emission followed the discharge current accurately throughout. Moreover, the
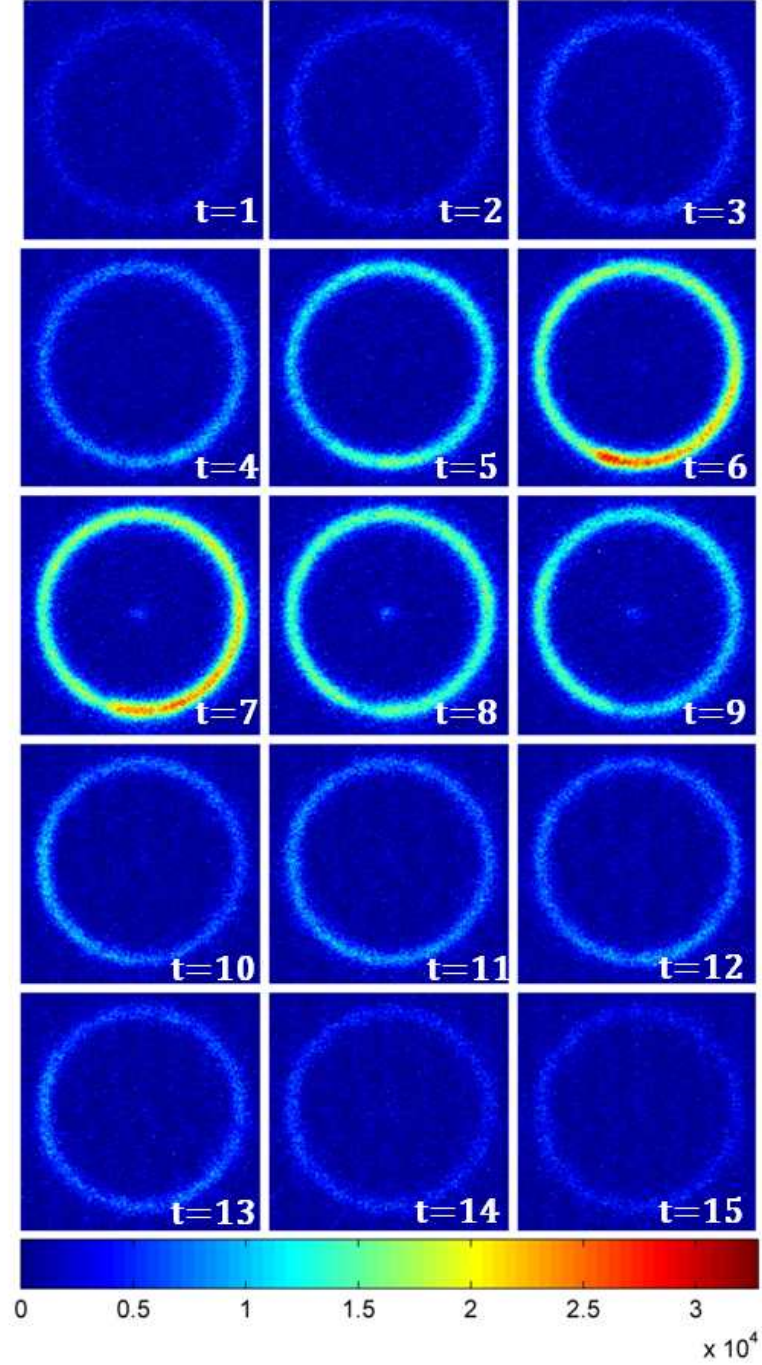
Figure 4.3: Sequential images (color enhanced) of BHT-600 discharge oscillation operating at nominal conditions. $V_d = 300$ V, $I_d = 2.0$ A, $I_m = 1.75$ A, $\dot{m} = 2.6$ mg/s of xenon. The time between images was 1 μs with an exposure time of 750 ns. Arbitrary intensity.
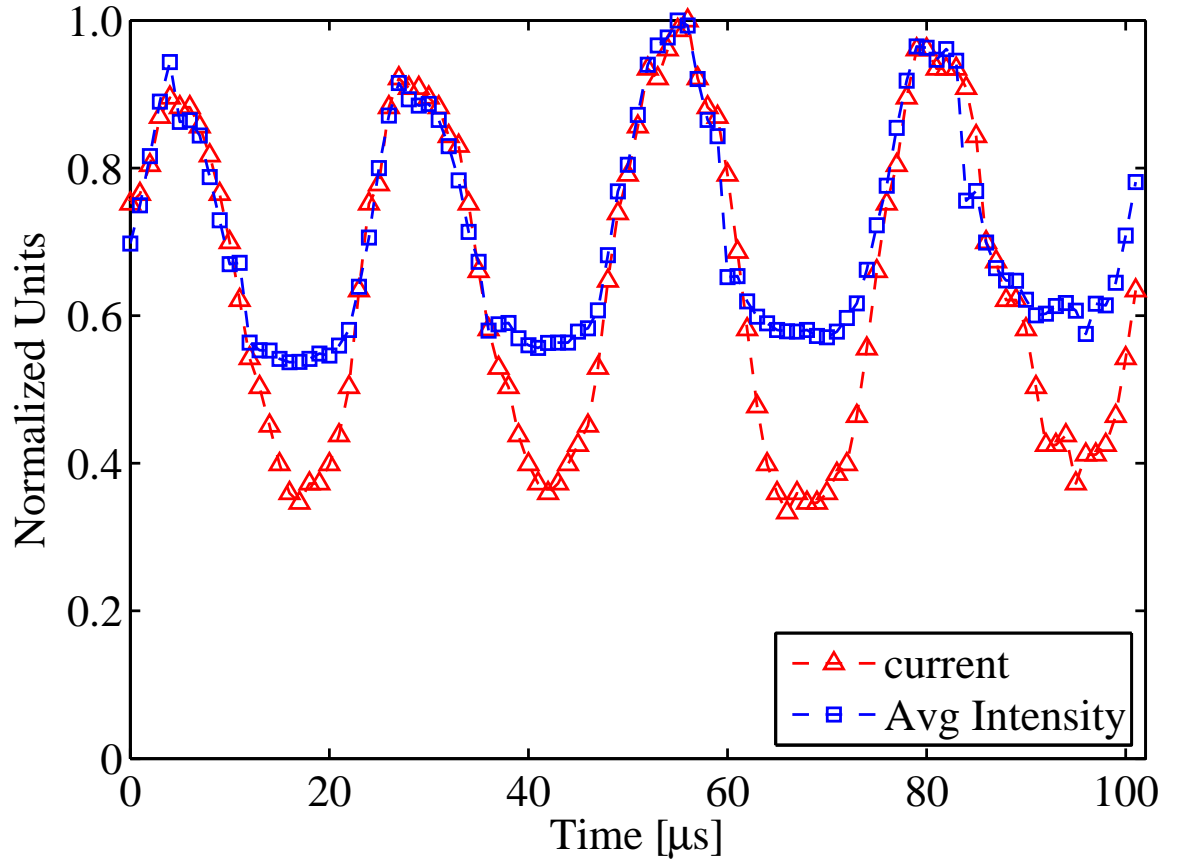
Figure 4.4:   Discharge current (triangles) compared to the average image intensity (square) of the BHT-200. Thruster was operating at nominal conditions. $V_d = 250$ V, $I_d = 0.8$ A, $I_m = 1.0$ A, $\dot{m}= 0.94$ mg/s of xenon.

Figure 4.5: Discharge current (triangles) compared to the average image intensity (square) of the BHT-600. Thruster was operating at nominal conditions. $V_d = 300$ V, $I_d = 2.0$ A, $I_m = 1.75$ A, $\dot{m} = 2.6$ mg/s of xenon.
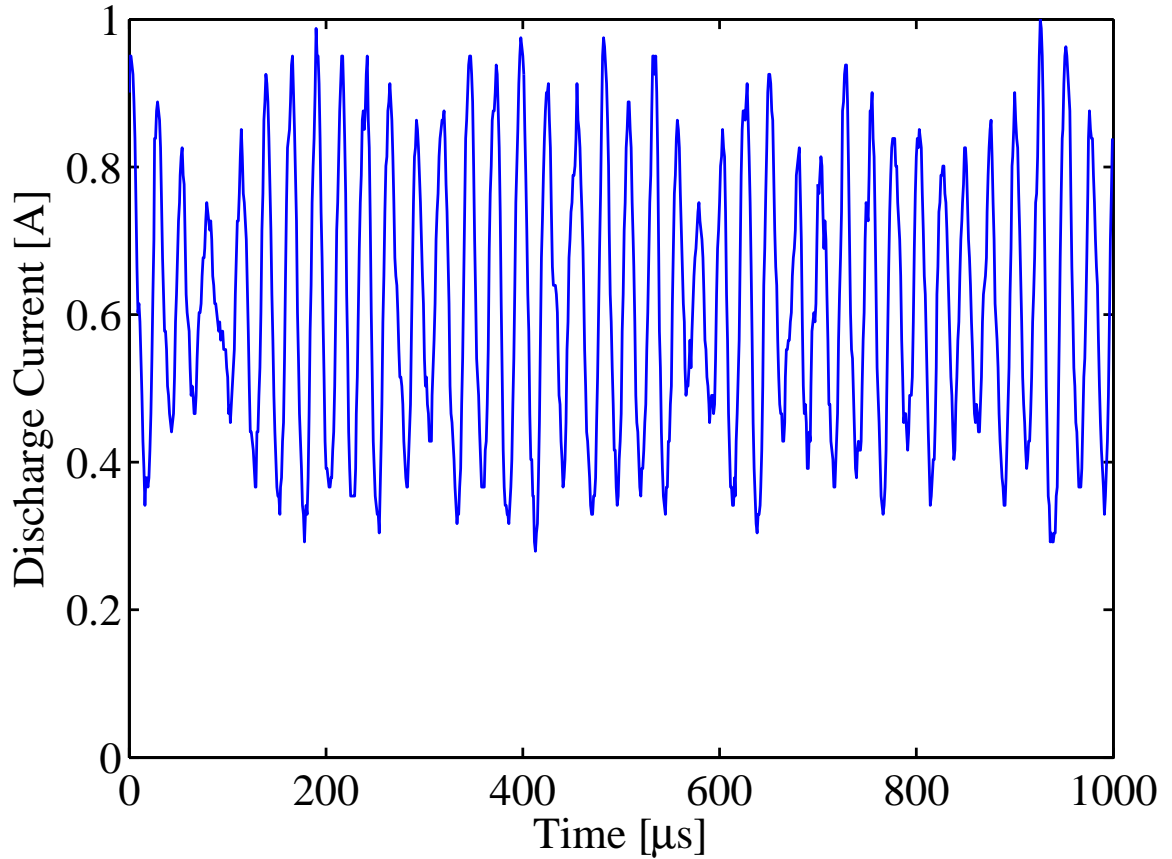
Figure 4.6:   Discharge current of the BHT-200 with observed amplitude modulation. Thruster operating at nominal conditions. $V_d = 250$ V, $I_d = 0.8$ A, $I_m = 1.0$ A, ṁ= 0.94 mg/s of xenon.

large degree of amplitude change provided a benchmark to ensure the algorithm used to determine the average emission intensity was accurate throughout the data.

Alternatively, a radial component of the plasma emission wave can also be determined. Within the high-speed images, the radial component seen as the change in emission ring thickness is denoted as Δr which is schematically shown in Figure 4.8. In this study the boundaries of Δr is defined within 95% of the peak intensity.

Expansion of the plasma emission also follows the discharge current closely as seen in Figure 4.9 for the BHT-200 and Figure 4.10 for the BHT-600. This expansion further suggests the excited neutrals or ions leaving the ionization region is not absolutely perpendicular to the face of the thruster. Instead, the plasma travels in
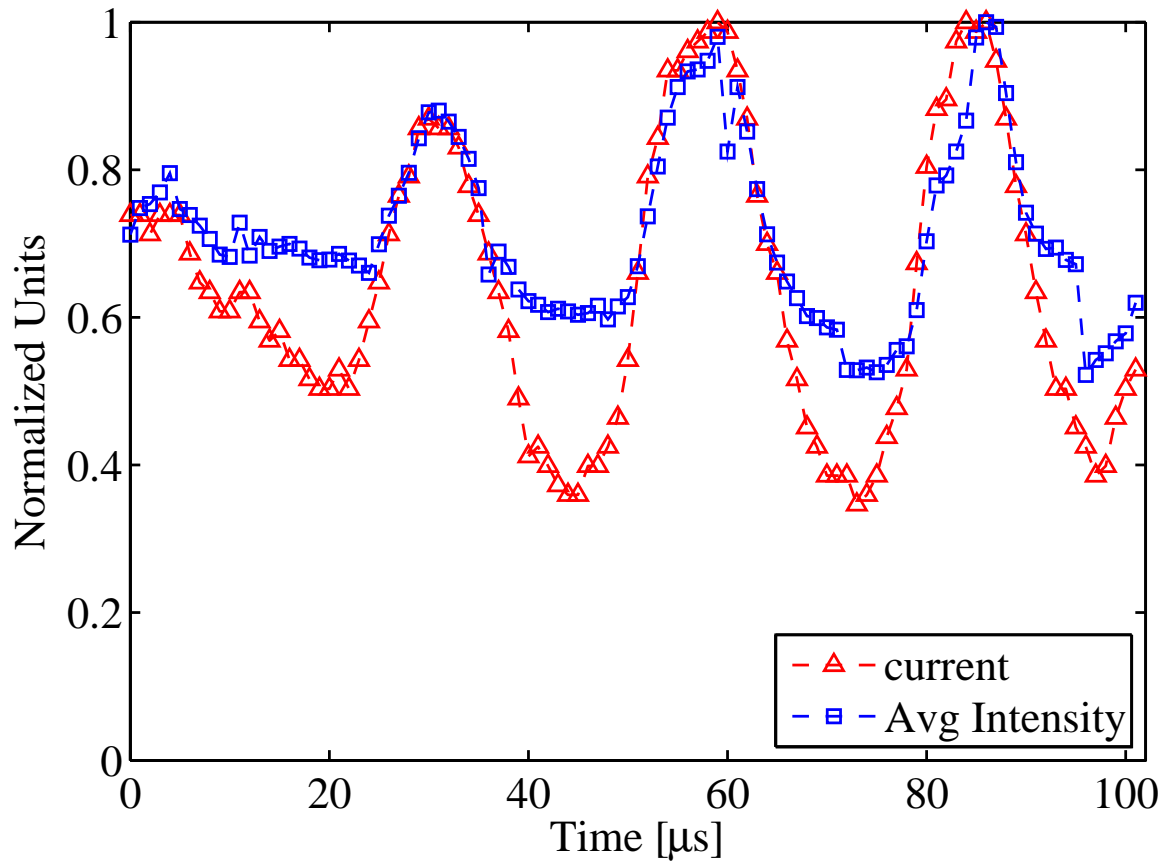
Figure 4.7:   Discharge current with high amplitude variations (triangles) compared to plasma emission thickness (squares) located within the inner and outer walls of the thruster annulus. Thruster was operating at nominal conditions. $V_d = 250$ V, $I_d = 0.8$, $I_m = 1.0$ A, $\dot{m}= 0.94$ mg/s of xenon.
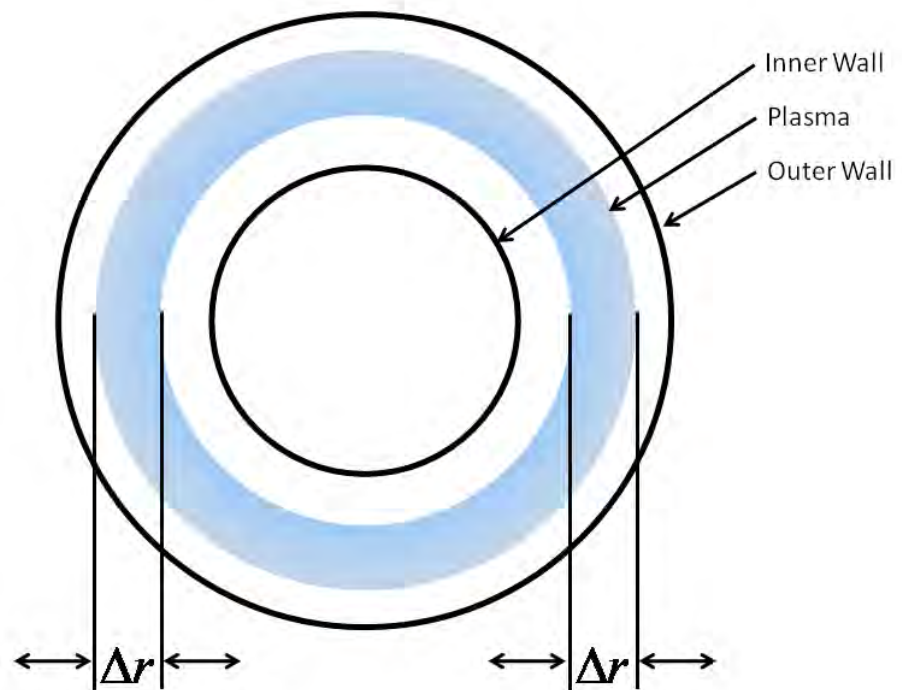
Figure 4.8:   Schematic representation of plasma emission wave traveling in the radial direction within the annulus of the Hall thruster.
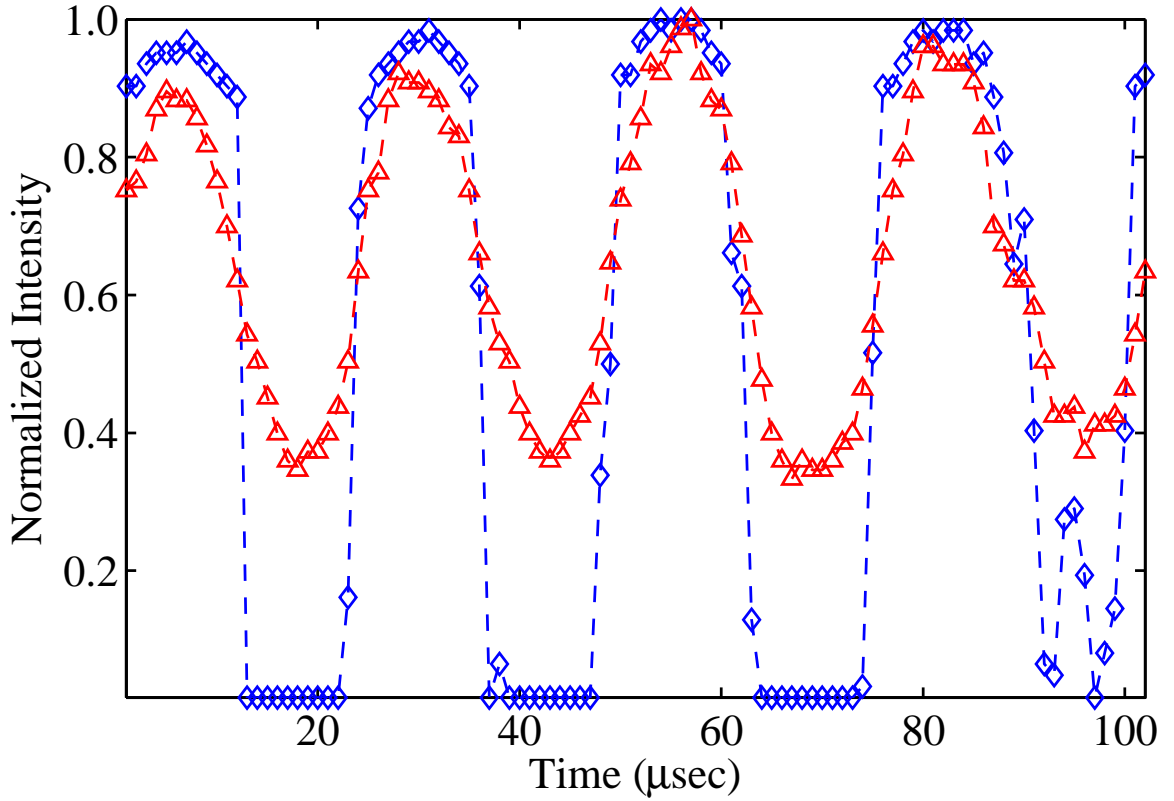
Figure 4.9: Discharge current with high amplitude variation (triangles) compared to plasma emission thickness (diamonds) located within the inner and outer walls of the thruster annulus. Thruster was operating at nominal conditions. $V_d = 250$ V, $I_d = 0.8$ A, $I_m = 1.0$ A, $\dot{m} = 0.94$ mg/s of xenon.

a divergent manner, resulting in an expansion of the plasma traveling towards the observer (the camera in this case) with some radial component which is measured by Δr. Thus, Δr is not a radial expansion in a single plane, rather in multiple planes parallel to the thruster face.

A different method to visualize the discharge oscillation was to show Δr in relation to the inner and outer walls of the thruster in time as seen in Fig. 4.11. In addition, this approach provides spatial information as well as temporal information by illustrating the time-dependent plasma emission in the radial direction.

The data exhibited the periodic increase and decrease in plasma emission consistent with the breathing mode or the predator-prey model [4, 21]. More importantly, the data presented in Figure 4.11 demonstrates the location of initial plasma for-
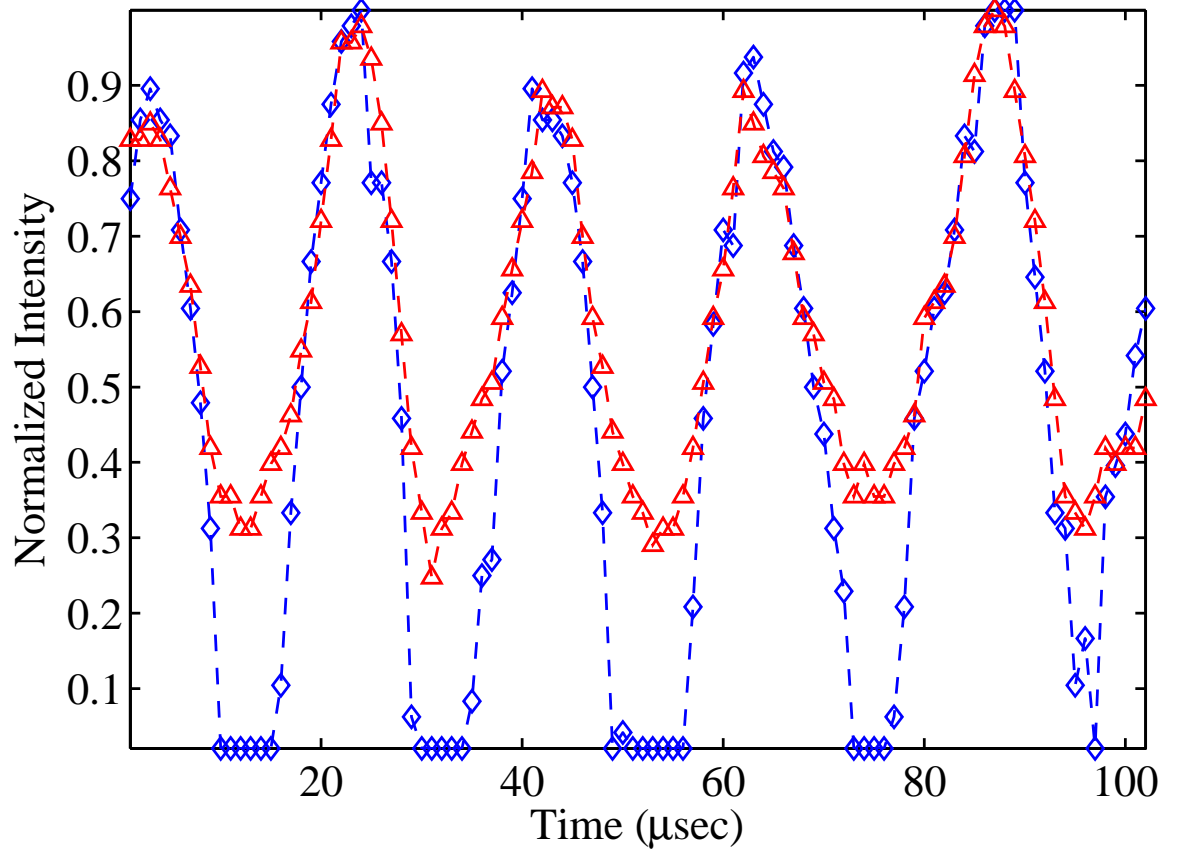
Figure 4.10: Discharge current with high amplitude variation (triangles) compared to plasma emission thickness (diamonds) located within the inner and outer walls of the thruster annulus. Thruster was operating at nominal conditions. $V_d = 300$ V, $I_d = 2.0$ A, $I_m = 1.75$ A, $\dot{m} = 2.6$ mg/s of xenon.
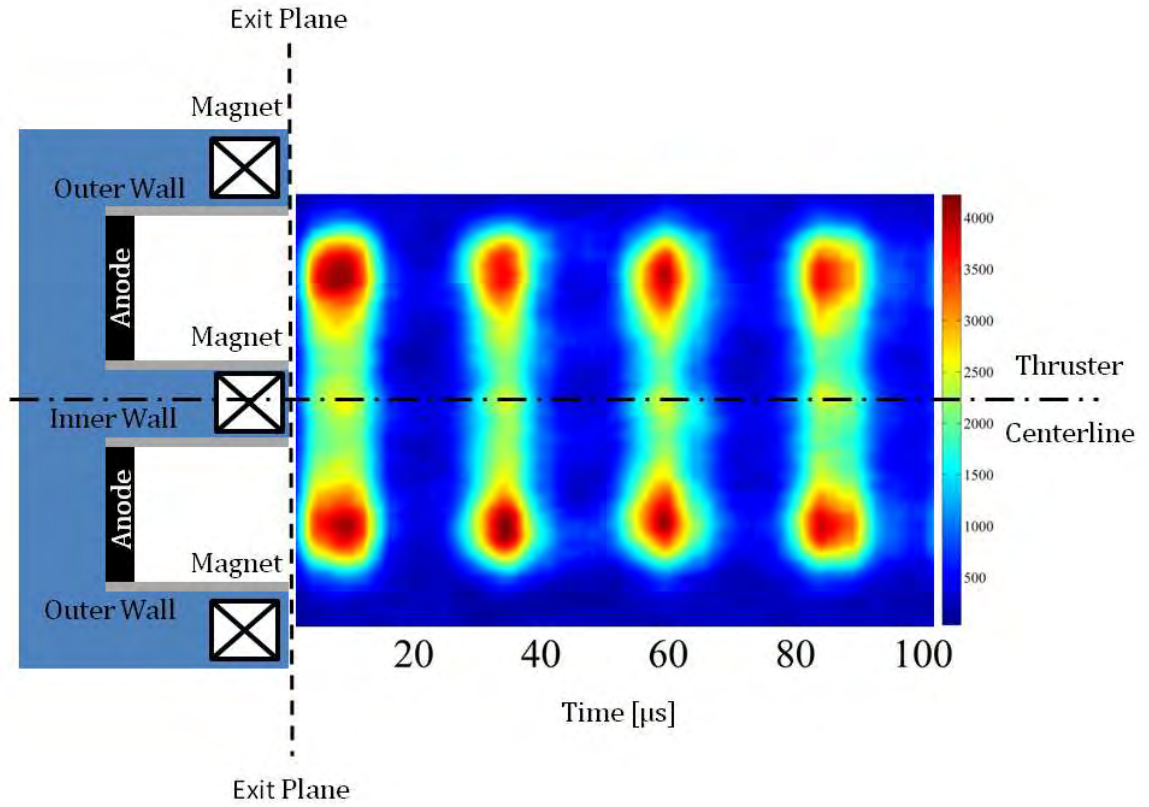
Figure 4.11: Plasma emission (arbitrary intensity) of BHT-200 as a function of space and time. Distance from the inner wall to the outer wall of the thruster was approximately 8 mm. Thruster was operating at nominal conditions. $V_d = 250$ V, $I_d = 0.8$ A, $I_m = 1.0$ A, $\dot{m} = 0.94$ mg/s of xenon.

mation in the center of the channel. As the breathing cycle begins and the plasma travels further away from the thruster face, the plasma begins to spread or diverge from the thruster centerline. When the breathing mode begins to decrease, the traveling plasma returns to more of a parallel path to the thruster centerline until minimal plasma emission exists. This observation is also true for the BHT-600 case. In Figure 4.12, the emission of the main discharge is much smaller representing the thinner discharge channel of the BHT-600 compared to the BHT-200. The periodic nature of the discharge emission was also observed similar to the BHT-200 case. However, detailed examination of Figure. 4.11 and Figure 4.12 shows the intensity and shape of the plasma emission from either side of the thruster is fairly different (top and bottom). This difference is attributed to the azimuthal plasma structures first seen in Figure 4.2 and 4.3.

Additionally, in Figure 4.11 and 4.12, small structures are observed throughout the time interval at the centerline of the thruster which was not observed if only the average image intensity was utilized. This increase of emission intensity is the plasma jet commonly seen in photos of Hall thrusters and as expected it also follows the breathing mode frequency. This jet is the result of interactions of the plasma as they collide towards the center in addition to the beam focusing controlled by the magnetic field. The jet structure was also measured to occur approximately 3 μs after the initial formation of the plasma emission within the thruster annulus further supporting the jet as a result of the discharge colliding in the center. The size of the plasma jet structure is also related to the size and intensity of the plasma emission emanating between the channel. For instance in Figure 4.11, in the first structure (between $t = 0$ and $t = 20$), the intensity and size of the emission originating from the channel is very strong and the resultant jet is also relatively strong compared to the other jet structures.
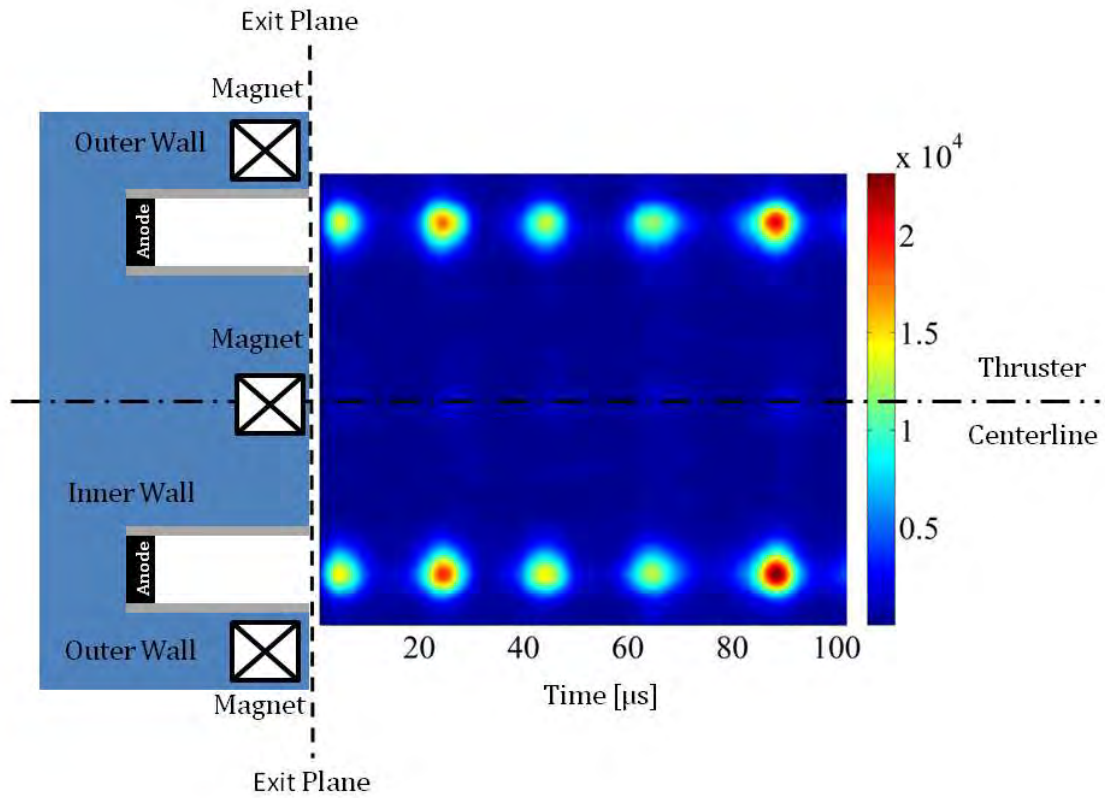
Figure 4.12:   Plasma emission (arbitrary intensity) of BHT-600 as a function of space and time. Distance from the inner wall to the outer wall of the thruster was approximately 7.5 mm. Thruster was operating at nominal conditions. $V_d = 300$ V, $I_d = 2.0$ A, $I_m = 1.75$ A, ṁ= 2.6 mg/s of xenon.

Another advantage of calculating the parameter, Δr, is it provides a dimension in which a velocity is determined. In this case, the instantaneous velocity of the plasma emission wave is calculated and shown in Equation 4.1:

$$\Delta r' = \frac{\Delta r}{\Delta t} * \delta P \tag{4.1}$$

where Δt is the change in time and δP is the pixel-to-mm conversion.

For the nominal condition of the BHT-200, the average maximum radial velocity of the plasma structures was calculated as 6.6 km/s. Although the velocity measured in this case was not inclusive of the ion velocity, it was still similar to the radial ion velocities found by Hargus and Charles [28]. Similarities of the velocity suggest the majority of the captured emission was the result of excited ions with some minor contributions from the neutral emission. The instantaneous velocity of the plasma structures also provides temporal details of the plasma emission. An example of the BHT-200 operating at nominal conditions with xenon is illustrated in Figure 4.13. The instantaneous velocity is shown with the corresponding Δr measurement for completeness.

Frequency for the discharge oscillation was calculated by collecting the current data as a function of time which was analyzed via a Fast Fourier Transform (FFT). The frequency data was collected for 20 samples and the average frequency was calculated at 42 kHz for the BHT-200 operating at the nominal conditions listed in Table 3.1. Fig. 4.14, shows where the average of the peaks occurred at 40 kHz. Utilizing the same method, the frequency of the BHT-600 was also measured. Figure 4.15 shows the average frequency of the larger thruster was approximately 48 kHz, which is 14% greater than the BHT-200 both operating at nomial conditions with xenon.

In Figure 4.14 and 4.15, the peaks of the frequency were broad. Further investigation of the peak broadening is shown in Figure 4.16 where the frequency of the discharge current shifts out of phase. The data collected to make this comparison was from the same day and during continuous operation of the BHT-200 at the nominal
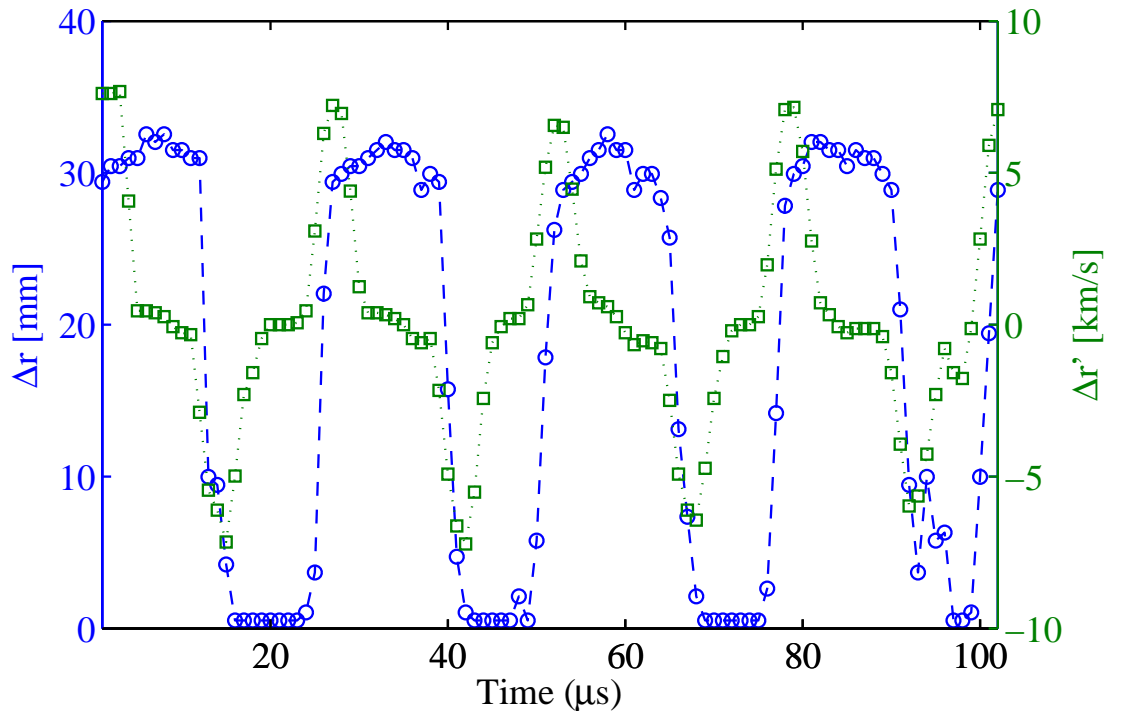
Figure 4.13: Instantaneous velocity profile of the radial component of the plasma emission wave for the BHT-200 operating with xenon. Thruster was operated at nominal conditions. $V_d = 250$ V, $I_d = 0.8$ A, $I_m = 1.0$ A, $\dot{m}= 2.6$ mg/s of xenon.
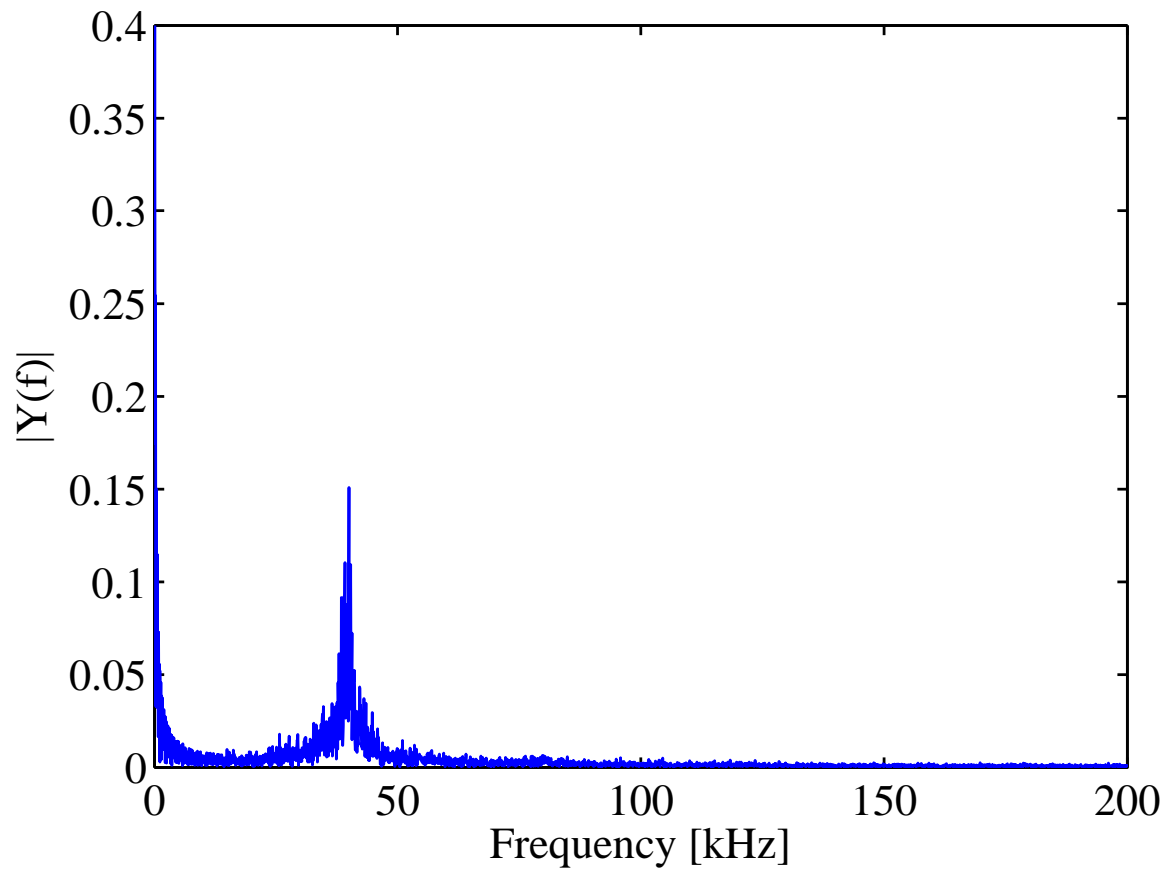
Figure 4.14:   Frequency plot for discharge oscillation of BHT-200 with xenon. Thruster was operating at nominal conditions. $V_d = 250$ V, $I_d = 0.8$ A, $I_m = 1.0$ A, $\dot{m} = 0.94$ mg/s of xenon.
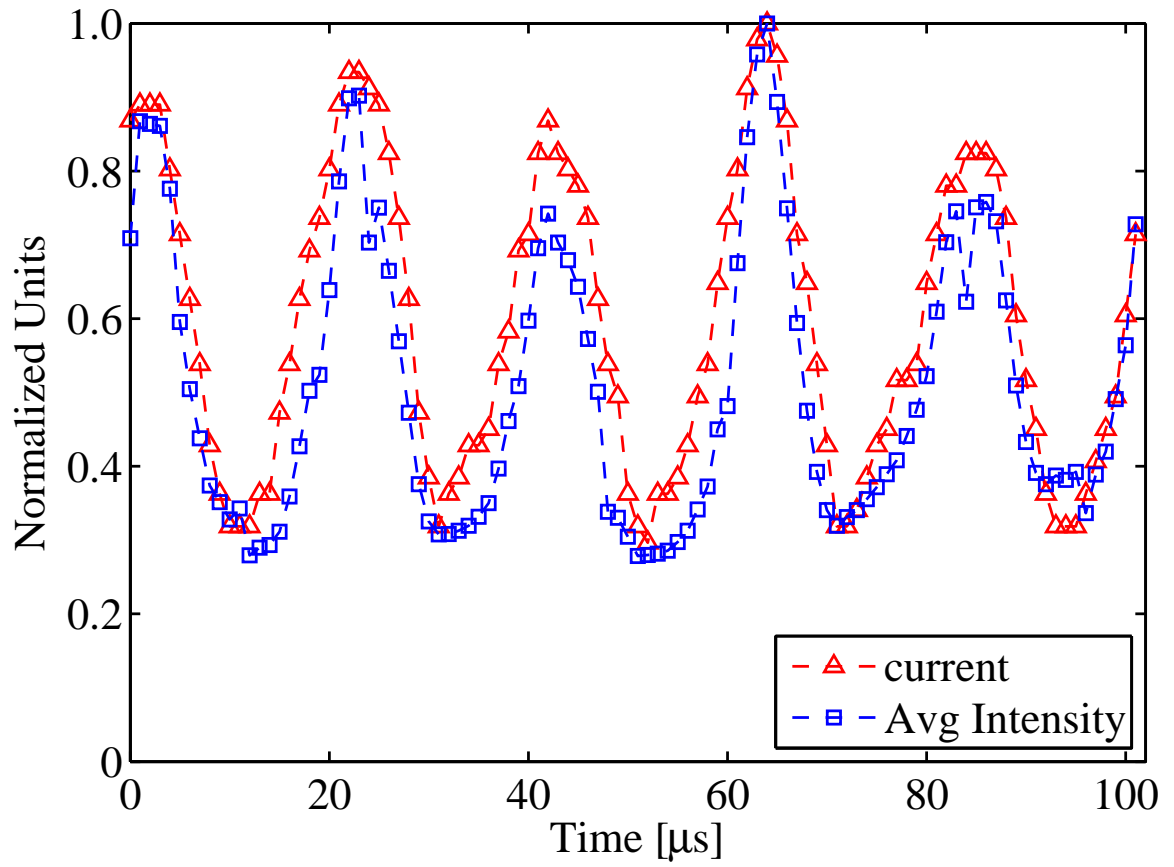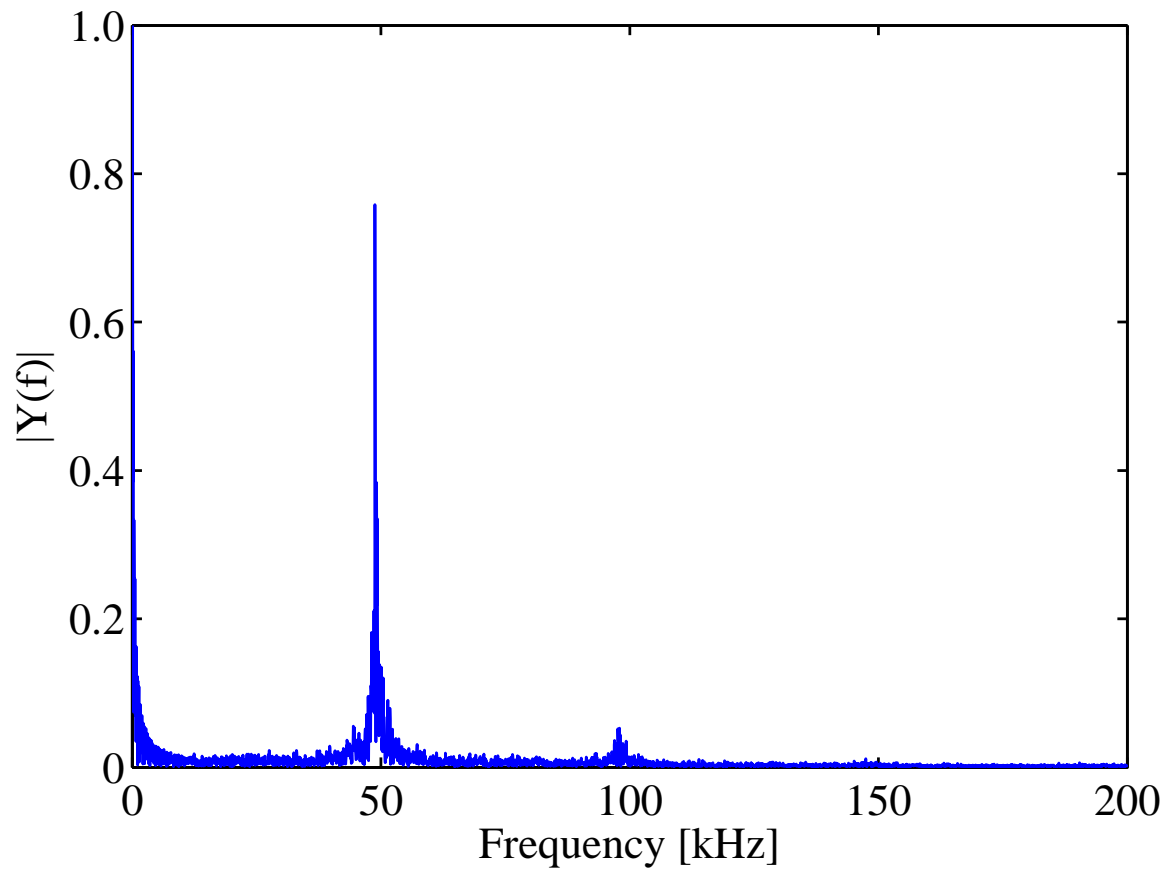
Figure 4.15: Frequency plot for discharge oscillation of BHT-600 with xenon. Thruster was operating at nominal conditions. $V_d = 300$ V, $I_d = 2.0$ A, $I_m = 1.75$ A, $\dot{m} = 2.6$ mg/s of xenon.
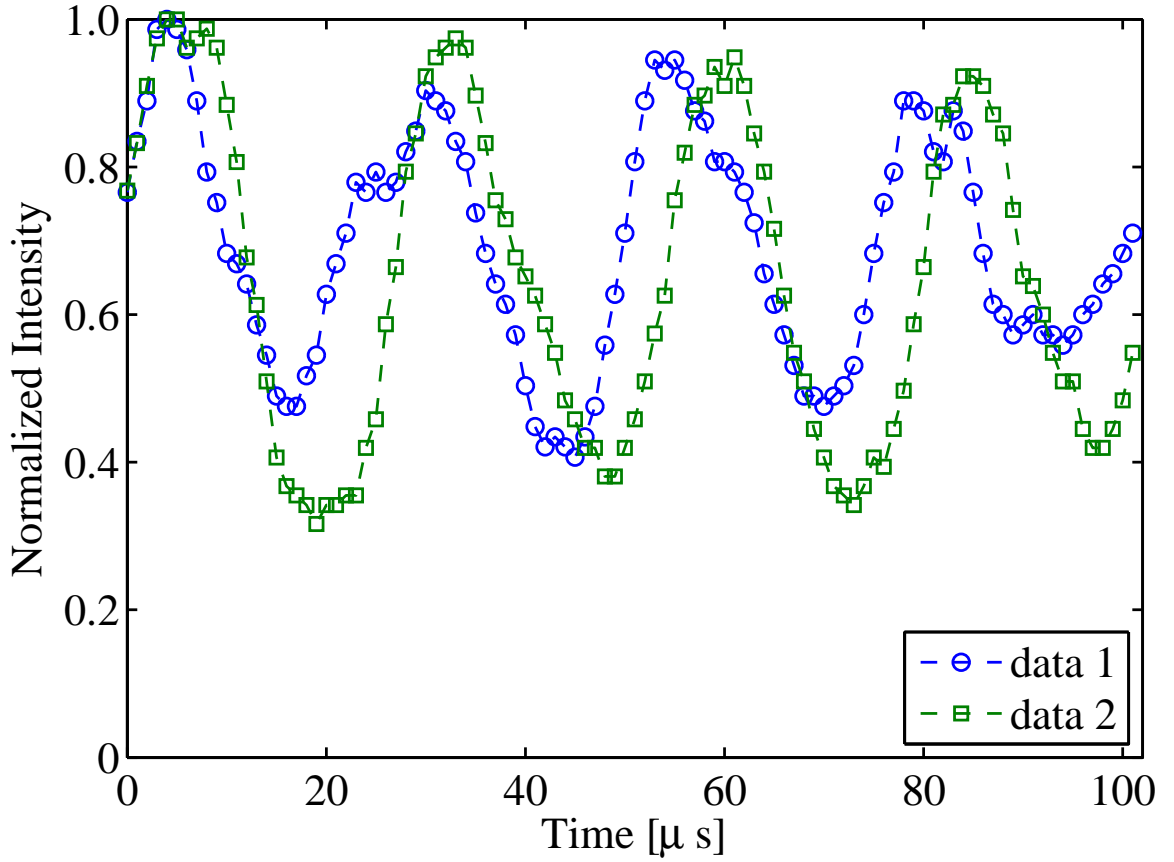
Figure 4.16:   Discharge current trace for BHT-200 for two image series demonstrating variable frequencies in the discharge oscillation. The two discharge currents were collected on the same day during continuous thruster operation at nominal conditions. $V_d = 250$ 'V, $I_d = 0.8$ A, $I_m = 1.0$ A, $\dot{m} = 0.94$ mg/s of xenon.

conditions. Before the data was taken , both thrusters were allowed to stabilize for over one hour to avoid any transient start instabilities which have been reported [35]. Even at *stable* or *steady-state* operation, the BHT-200 thruster still experienced shifts in the discharge frequency.

The periodic decrease and increase of plasma emission shown in the images of the discharge was in qualitative agreement with the oscillatory characteristics predicted by numerical models [4,21,22]. The origins of these oscillations is attributed to the large magnetic field at the exit of the thruster and the resulting low electron conductivity leading to an increased electric field to maintain the current continuity. This region of enhanced ionization decreased the neutral density at the exit which caused the

neutral front to move further up towards the anode where the ionization was much lower. With the decreased ionization rate, the electron flux would also decrease in the region, causing the neutral density to move back towards the exit plane thus completing the cycle.

This "breathing mode" described by Boeuf and Garrigues is also comparable to the "predator-prey" model derived by Fife *et al* [4, 21]. To verify the oscillations measured in this study are consistent with the breathing mode or predator/prey model, experimentally measured values for a 200 W thruster are used in Equation 2.46. For an ion velocity, $v_i \approx 15$ km/s [28], neutral velocity, $v_n \approx 300$ m/s [27], and an ionization zone, $L = O\left(10^{-2}\right)$ m [72], the frequency for the discharge oscillation was estimated at 34 kHz which is in agreement to the observed frequency of 40 kHz for the BHT-200. In addition, the experimentally obtained ion velocities of the BHT-600 was approximately $V_i \approx 20$ km/s [29, 32]. Assuming the neutral velocity and ionization length of the BHT-600 was of the same order, the calculated frequency was estimated at 40 kHz which is also in agreement with the observed value of 48 kHz in this study. In addition, the measured frequency was also comparable to other experimentally observed discharge oscillations in the kHz regime. However, it is important to note the other measurements are not necessarily for the BHT-200 or the BHT-600 [8, 16, 34, 59].

4.2   Xenon Breathing Mode at Various Discharge Potential

One of the attributes of the Hall thruster is its throttling capability. Some missions on-board a satellite may not require as much thrust or I_{sp} while other missions may require more. Thus, a need exists to study the Hall thruster at these different, *off nominal*, operating conditions. In particular, this section looks at the breathing mode oscillations at different discharge potentials.

In order to look only at the effects of discharge potential for the BHT-200, the magnet current was held constant at 1.0 A while the discharge current was also held constant at 0.8 A. However, as the discharge potential was lowered from the nominal value of 250 V, the discharge current would also decrease. Thus, in order to maintain the constant discharge current, the mass flow rate was increased to support the desired discharge current. In addition, the cathode was allowed to operate in the self-heating mode. The parameters of the thruster are given in Table 3.3.

Figure 4.17 and 4.18 show the evolution of the emission intensity as a function of time. At a discharge potential of 250 V, the breathing mode oscillations are periodic in nature and has a clear minima and maxima within the signal. When the discharge potential is lowered to 230 V, some irregularities begin to manifest within the periodic signal (example shown at $t = 175$ μs) in Figure 4.17. Further reductions in the discharge potential seem to dampen the overall current amplitude. The dominant peaks and valleys seen in the 250 V case begins to terminate and is substituted with a more modulated signal.

However, as the discharge potential is further decreased, the signal amplitude begins to increase which is shown in Figure 4.18 at 150 V. Although the amplitude of the discharge current never returns to the 250 V case, the breathing mode oscillations is clearly seen. In addition, as the discharge potential was decreased from 250 V to 80 V the period of the oscillations was also observed to increase. The trend of the breathing mode oscillation is further illustrated in Figure 4.19. Between a discharge potential of 230 V and 250 V, the breathing mode is clearly visible. While the dis-
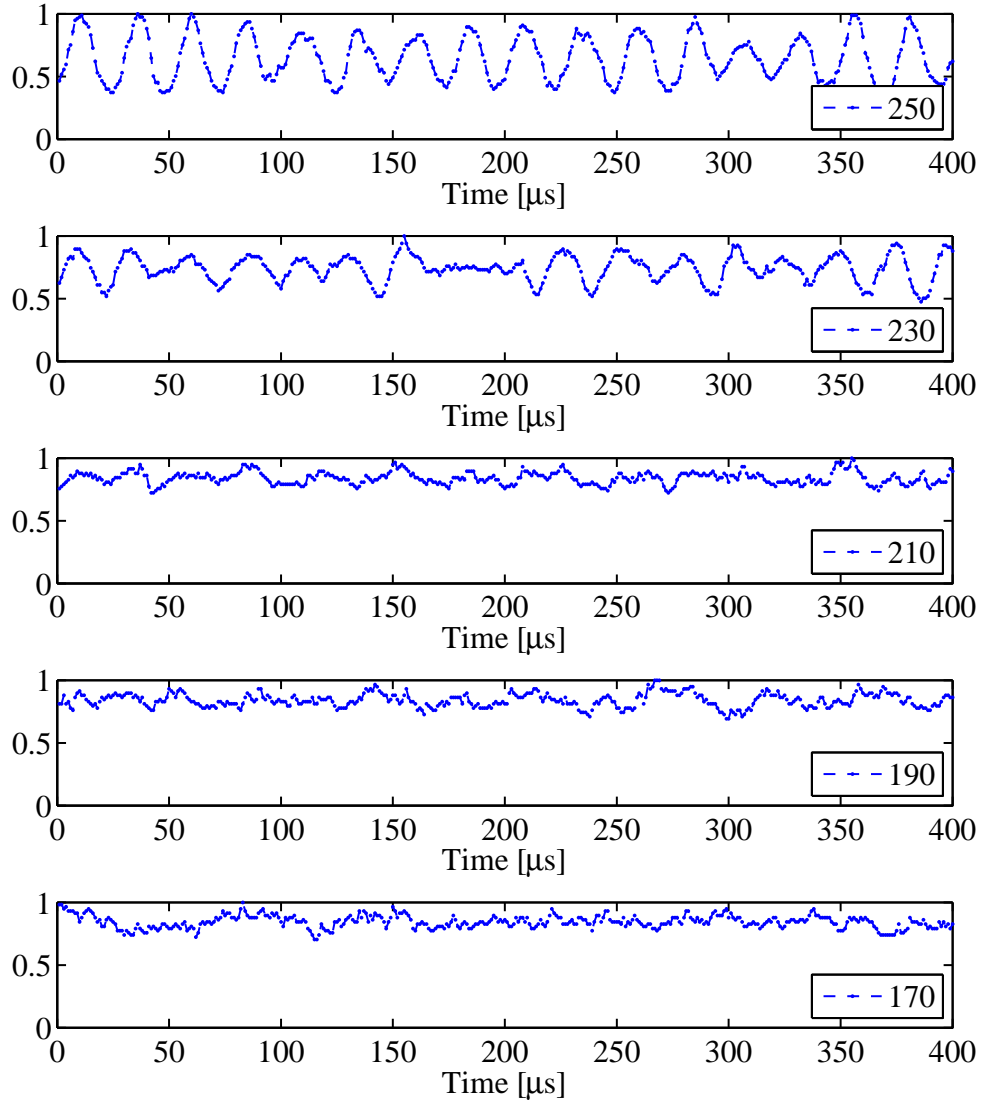
Figure 4.17: Discharge current of BHT-200 operating with xenon at various discharge potentials (denoted in lower right corner). The discharge current and magnet current were held constant at 0.8 A and 1.0 A, respectively.
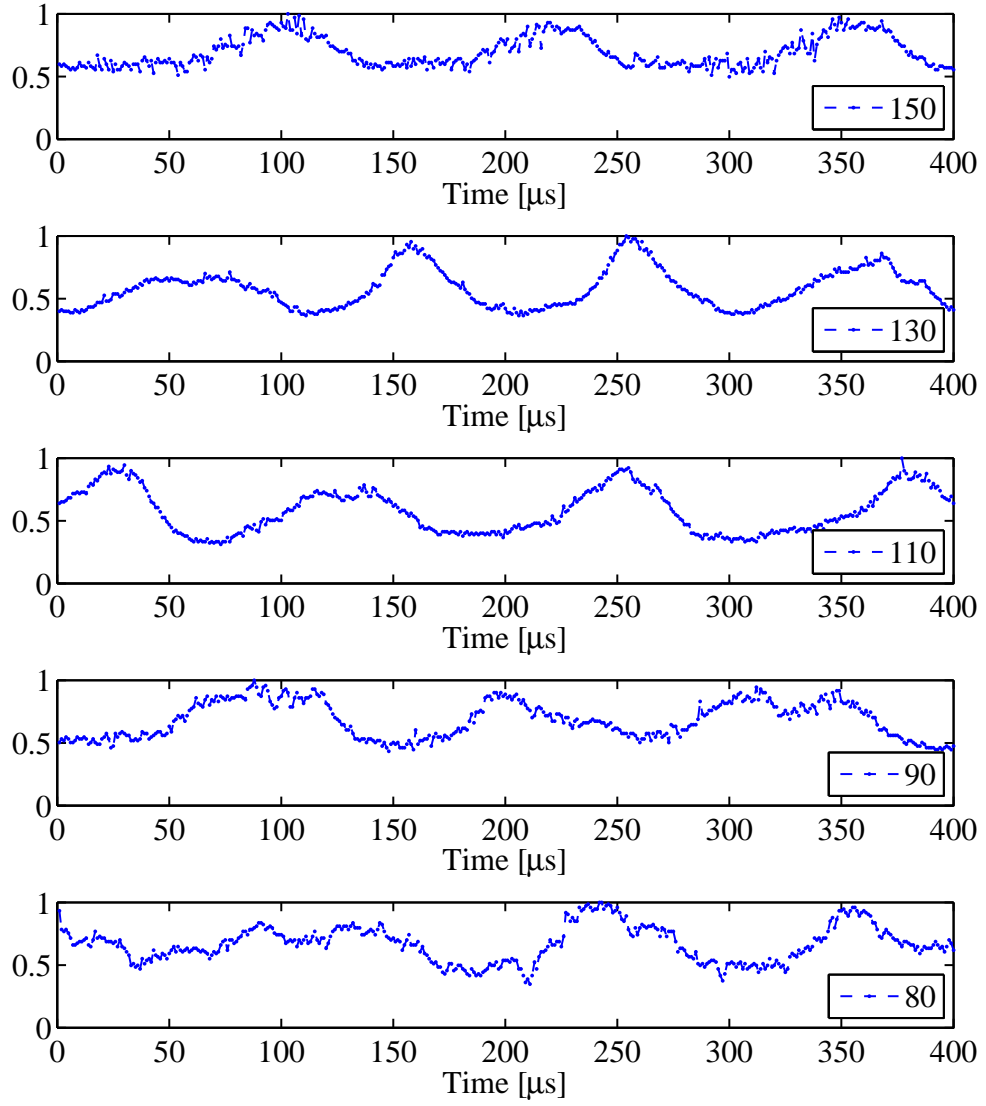
Figure 4.18:   Discharge current of BHT-200 operating with xenon at various discharge potentials (denoted in lower right corner). The discharge current and magnet current were held constant at 0.8 A and 1.0 A, respectively.

charge potentials were in the 170 V to 210 V range, the oscillations are nearly damped out as represented by the solid color in the interval. In the remainder test regimes of 80 V to 150 V, the breathing mode oscillations return to the discharge current signal. However, the amplitude is not as intense and the duration of the breathing is also longer which is represented by the larger contours within the figure.

For the BHT-600, the time-dependent discharge current is given in Figure 4.20 and 4.21. Similar to the BHT-200, the BHT-600 also exhibits the dampening effect on the amplitude of the discharge current as the discharge potential is decreased from the nominal discharge potential of 300 V. The oscillations of the breathing mode also becomes more sporadic in the middle of the test regime at 175 V to 220 V resembling the BHT-200. This result suggests the dampening of the discharge current in the middle of the operation regime is not unique to an individual thruster rather a systematic effect.

A contour plot of the discharge current is given in Figure 4.22 for the BHT-600 using xenon. The evolution of the time-dependent discharge current at various discharge potentials further demonstrates the coherent oscillatory behavior of the breathing mode at high and low discharge potentials. At the lower discharge potential of 90 V to 150 V, another difference persists between the BHT-200 and BHT-600 signal. For the BHT-600 signal, the amplitude of the discharge current starts much lower, approximately 20% of the maximum value, compared to the BHT-200 which stays greater than 50% of the maximum value. Since the main discharge requires some minimal power input to sustain the plasma, the theorized cause is due to the higher power level the BHT-600 operates compared to the BHT-200.

The frequency of the breathing mode oscillations was determined by performing a FFT on the discharge signal as described before. Over the discharge potential range of 80 V to 250 V for the BHT-200, the frequency was found in the range of 7 kHz to 40 kHz. Figure 4.23 shows the frequency of the breathing mode is proportional to the discharge potential and can vary significantly based on the thruster operational
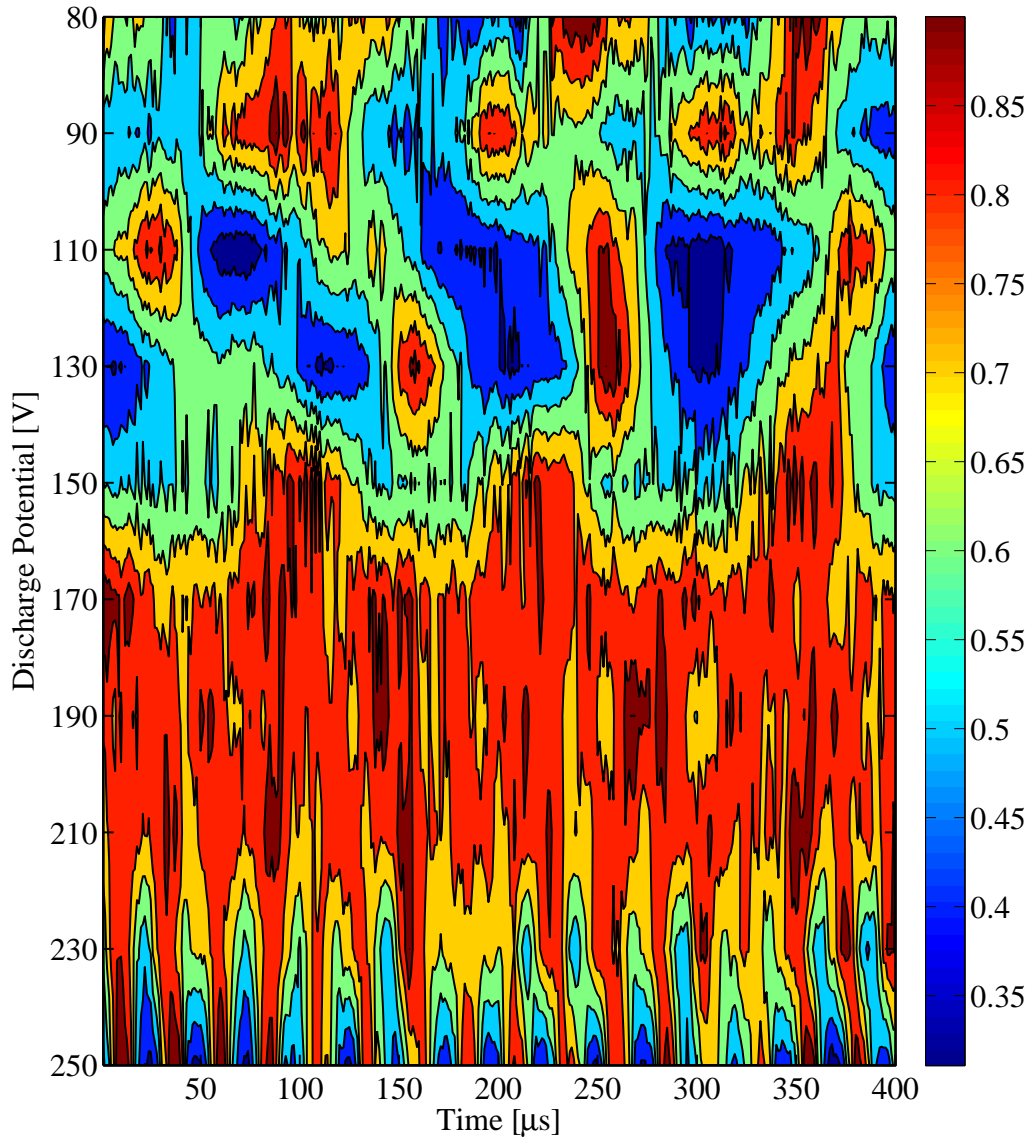
Figure 4.19:   Spectrum of discharge current of BHT-200 operating with xenon at various discharge potentials. The discharge current and magnet current were held constant at 0.8 A and 1.0 A, respectively.
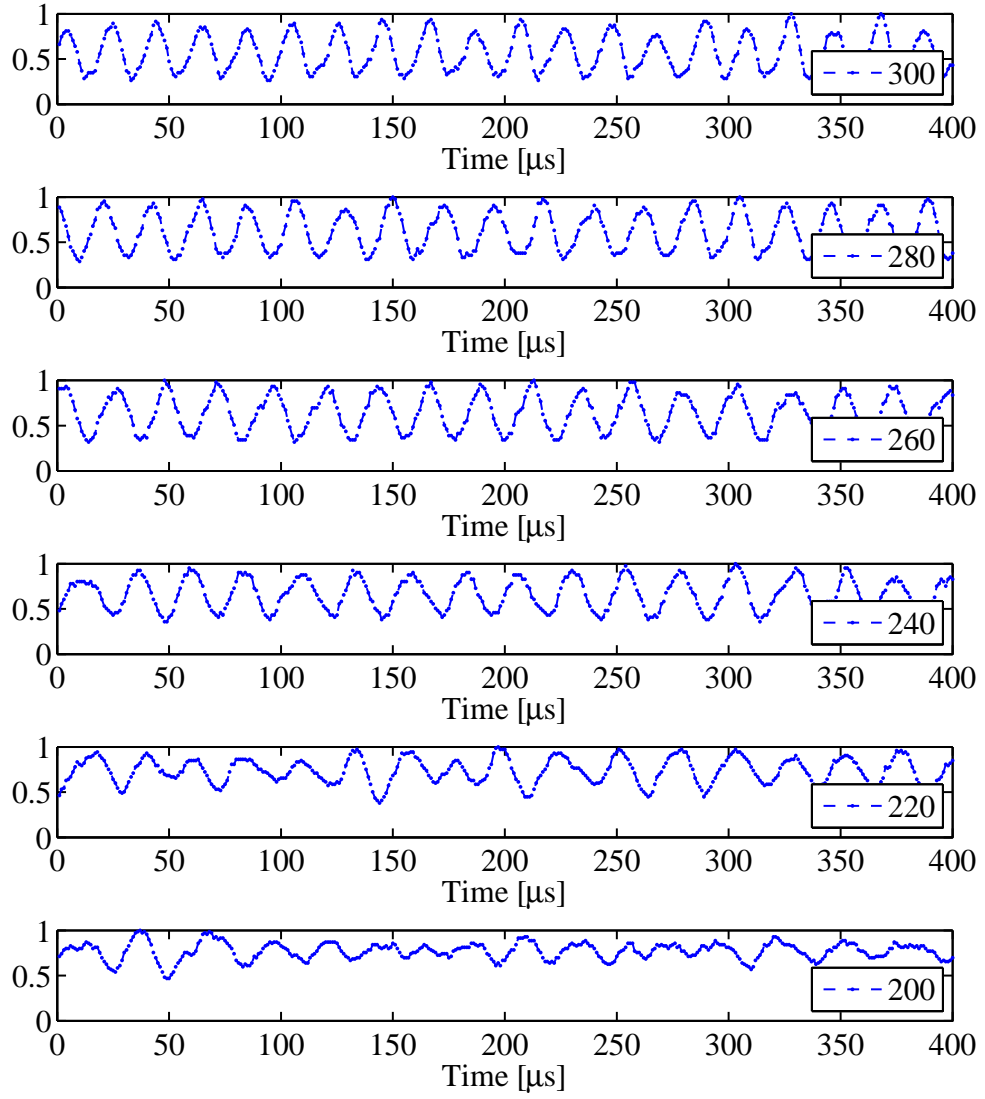
Figure 4.20: Discharge current of BHT-600 operating with xenon at various discharge potentials (denoted in lower right corner). The discharge current and magnet current were held constant at 2.0 A and 1.75 A, respectively.
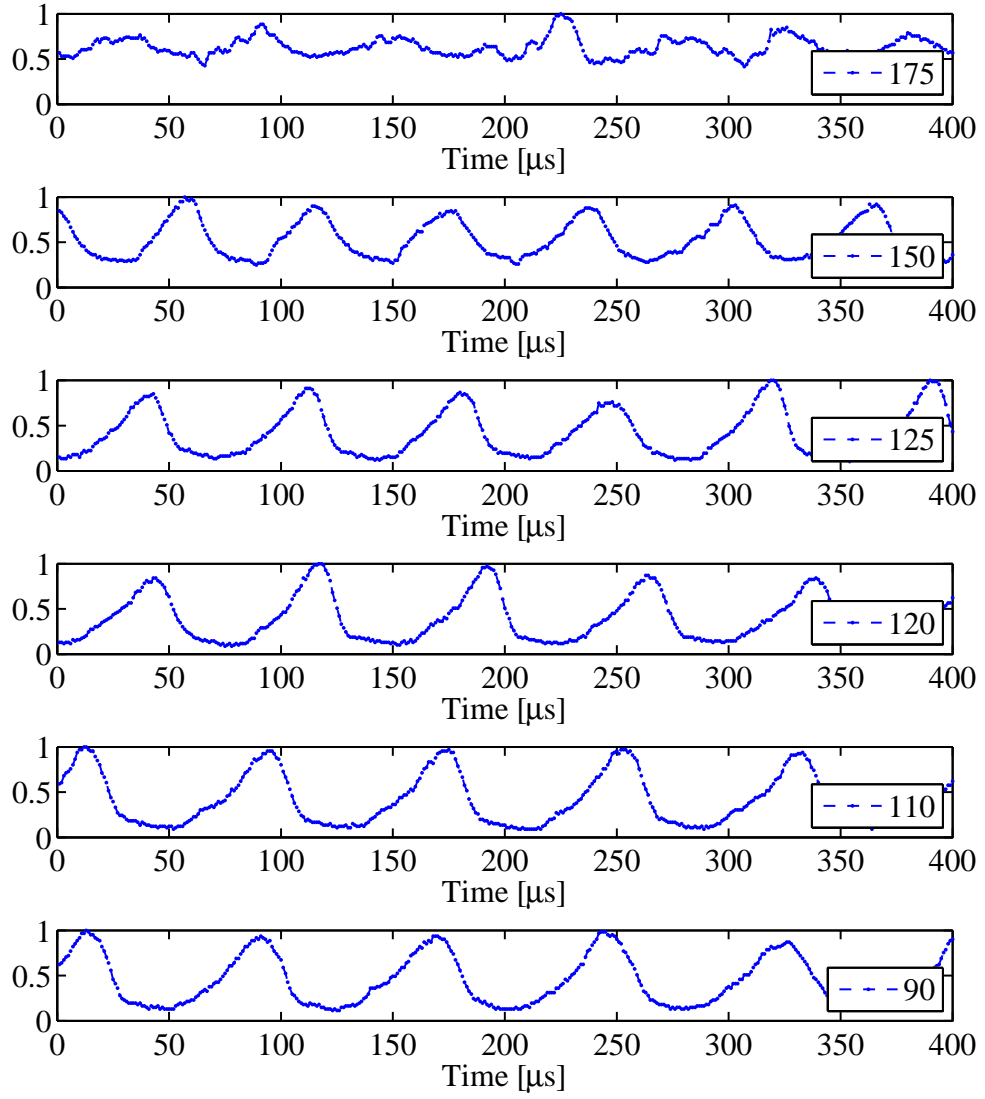
Figure 4.21: Discharge current of BHT-600 operating with xenon at various discharge potentials (denoted in lower right corner). The discharge current and magnet current were held constant at 2.0 A and 1.75 A, respectively.

88
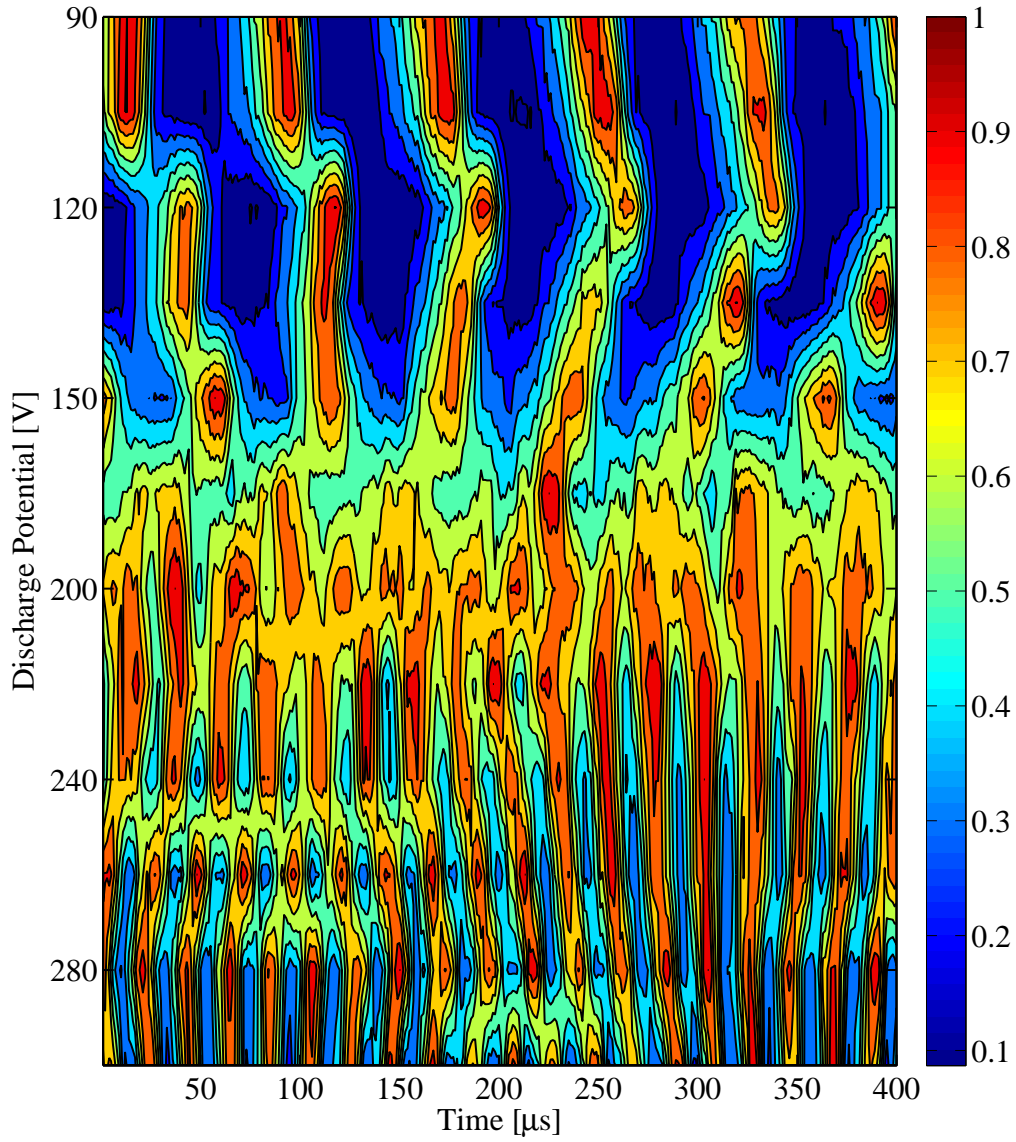
Figure 4.22: Spectrum of discharge current of BHT-600 operating with xenon at various discharge potentials. The discharge current and magnet current were held constant at 2.0 A and 1.75 A, respectively.
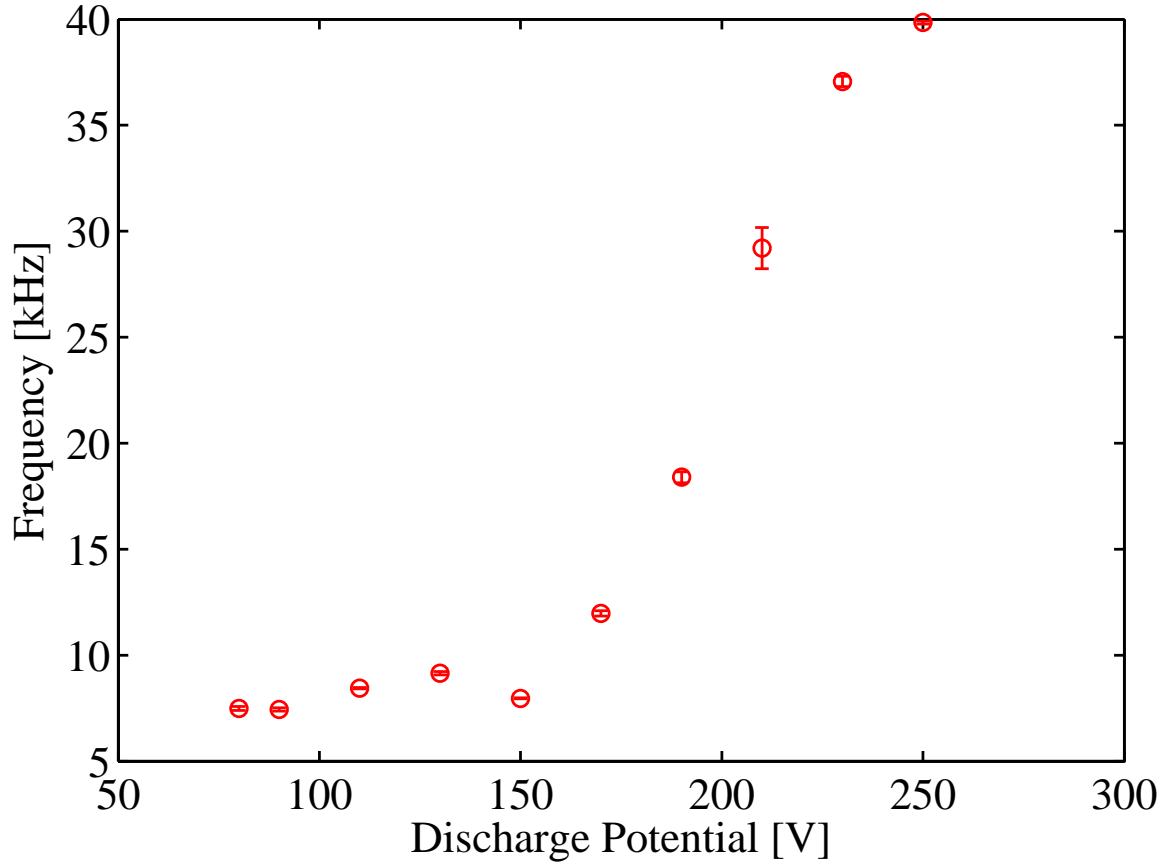
Figure 4.23:   Breathing mode frequency dependence on discharge potential for the BHT-200 operating with xenon. The average discharge current and magnetic current were held constant at 0.8 A and 1.0 A, respectively.

parameters. Although the discharge current in Figures 4.17 and 4.18 did not clearly show oscillations within the signal, due to the relatively small amplitude, the FFT was able to determine the frequency throughout the test regime with minimal standard error.

The breathing mode frequency of the BHT-600 was also investigated as a function of discharge potential. Figure 4.24 illustrates the dependence of the breathing mode frequency to the discharge potential in the large thruster. In comparison to the BHT-200 data, the two frequency trends are very similar, in particular, both thrusters exhibit two different slopes which meet in the middle of the operational regime. The result supports the conclusion both types of thrusters have two breathing modes. It

Figure 4.24:   Breathing mode frequency dependence on discharge potential for the BHT-600 operating with xenon. The average discharge current and magnetic current were held constant at 2.0 A and 1.75 A, respectively.

is possible at the lower discharge potentials, the ionization rate decreases non-linearly which may cause the discontinuous jump in the breathing mode frequency.

Since the predator/prey model, expressed in Equation 2.46, is a function of the neutral velocity, additional experiments were completed at various discharge potentials with a constant mass flow rate instead of a constant discharge current. Recall the discharge current was held constant by adjusting the mass flow rate. Figure 4.25 shows the frequency of the breathing mode when the mass flow rate was held constant at 0.95 mg/s of xenon compared with the data from constant discharge current of 0.8 A. In both experiments the magnet current was held constant at 1.0 A. By holding the mass flow rate constant, the discharge current of the thruster varied as the discharge potential was decreased.
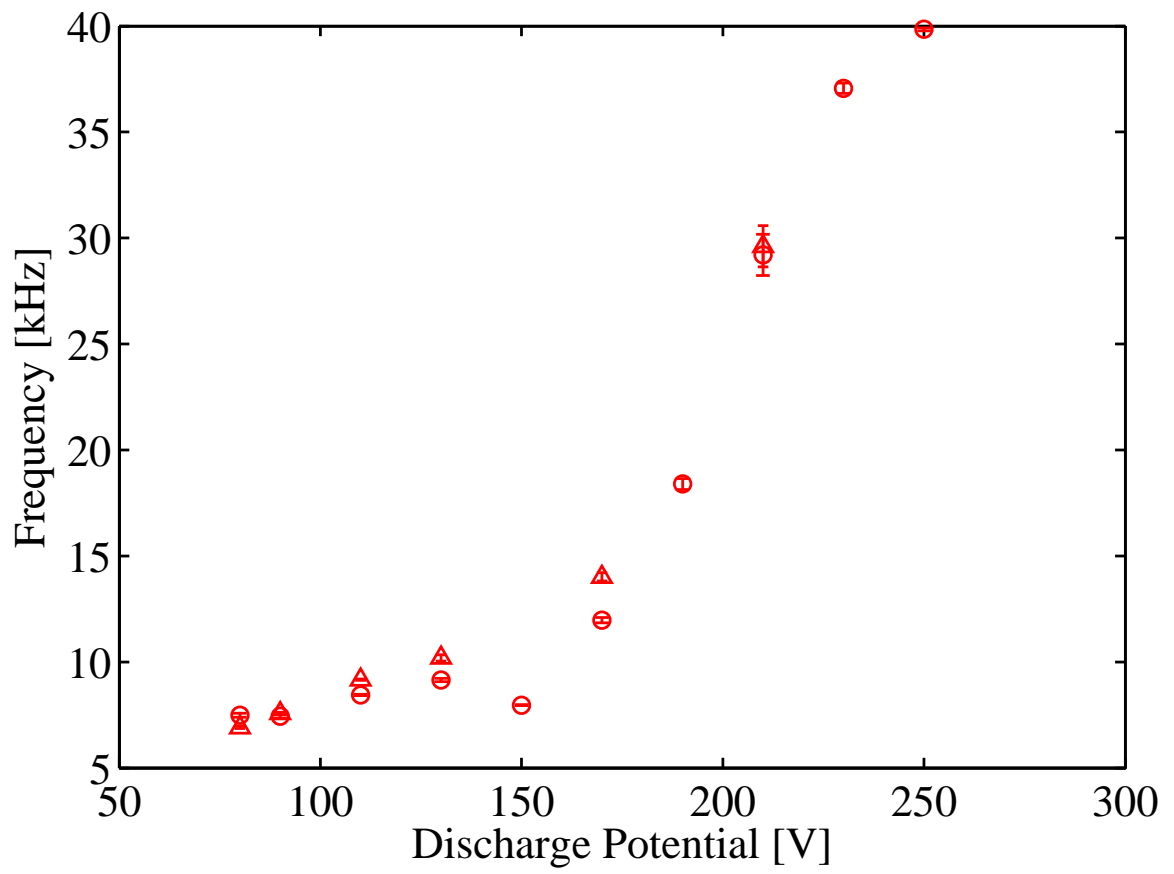
Figure 4.25: Comparison of breathing mode frequency dependence on discharge potential for a constant mass flow rate (circles) and a constant discharge current (triangles) operating with xenon. The magnetic current for the BHT-200 was held constant at 1.0 A.

Data for the discharge potentials of 230 V and 250 V at the constant mass flow rate was not taken since at those potentials the mass flow rate was the same. However, the data shows the breathing mode frequency for the two instances are very similar in trend and nearly identical in value. The only variation was at 150 V where the data was not taken for the constant mass flow case due to time constraints. Variations in the mass flow rates in the two cases were in the range of 14% to 16% with a maximum difference in breathing mode frequency of 14%. This results shows the breathing mode frequency is mostly dependent on the discharge potential with the relation to the mass flow rate nearly linear. Further discussions with regards to the effect of the mass flow rate are presented later.

Recall, minor variations in the mass flow rate only made trivial differences in the frequency as seen in Figure 4.25. The results observed from these test cases support the conclusion contributions from the ion velocity and the ionization length may have made a greater contribution in the frequency. Although the ion velocity will increase with increasing discharge potential, optical emission measurements do not provide a simple, easy-to-interpret relationship between discharge potential and ion velocity. Moreover, the dependence of the ion velocity is only to the one-half power and may not have a significant contribution. Conversely, the ionization length may have a significant influence on the frequency. When the discharge potential is increased, the electron temperature distribution is also increased, causing the ionization zone to decrease; a direct result of more high energy electrons available for ionization. This decrease in the ionization zone could lead to an increase in the breathing mode frequency.
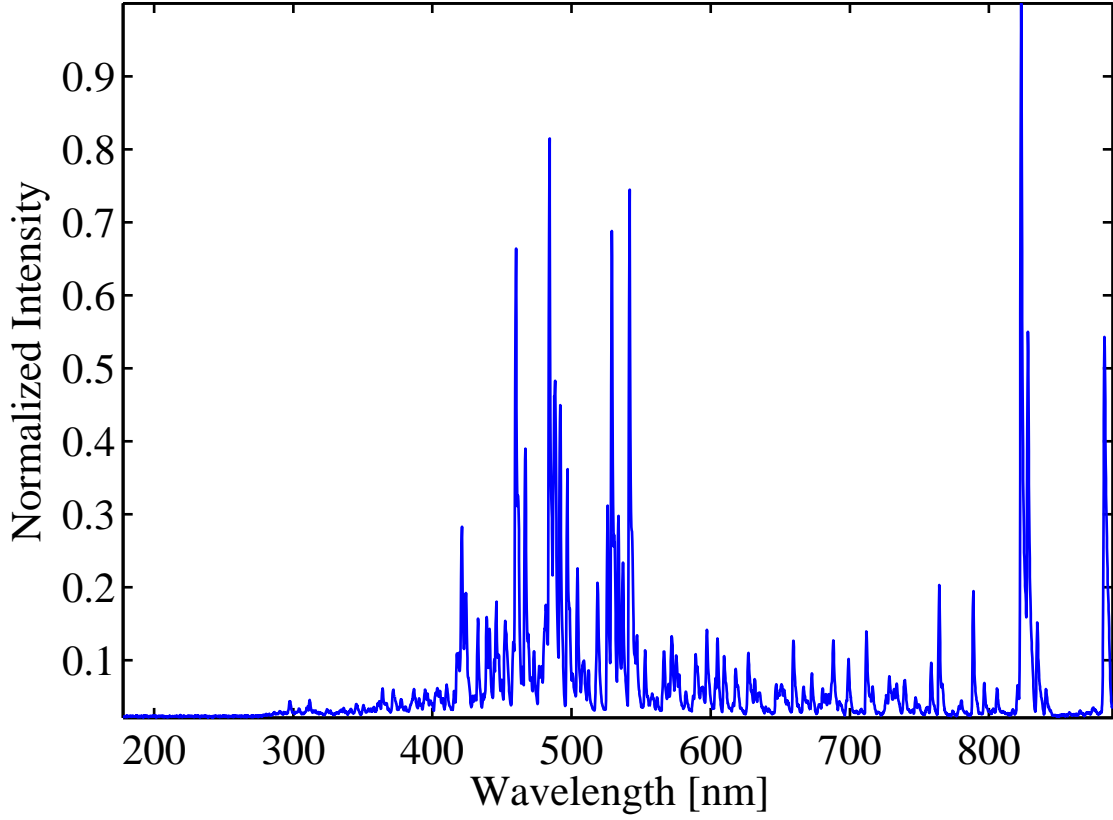
Figure 4.26:   Sample xenon spectra of the BHT-200. The thruster was operating at nominal conditions. $V_d = 250$ V, $I_d = 0.8$ A, $I_m = 1.0$ A, ṁ= 0.94 mg/s of xenon.

4.3   Electron Temperature at Various Discharge Potential

To determine the relationship between the discharge potential and electron temperature, a CRM was applied to the BHT-200 with xenon. Intensities of the 823.2, 828.0, and 834.7 nm line was taken with the spectrometer as depicted in Figure 3.10. A sample spectra of the BHT-200 operating at a discharge potential, discharge current, magnet current, and mass flow rate of 250 V, 0.8 A, 1.0 A, and 0.94 mg/s of xenon, respectively, is given in Figure 4.26.

The intensities of the selected emission lines were taken as a function of discharge potential to create the desired ratio of intensities illustrated in Figure 4.27 and 4.28 . The ratio of intensity was then correlated to the calculated electron temperature profile generated by the CRM and HPHall models to provide Figure 4.27 and 4.28 which shows the relationship of electron temperature and intensity ratios. The

94
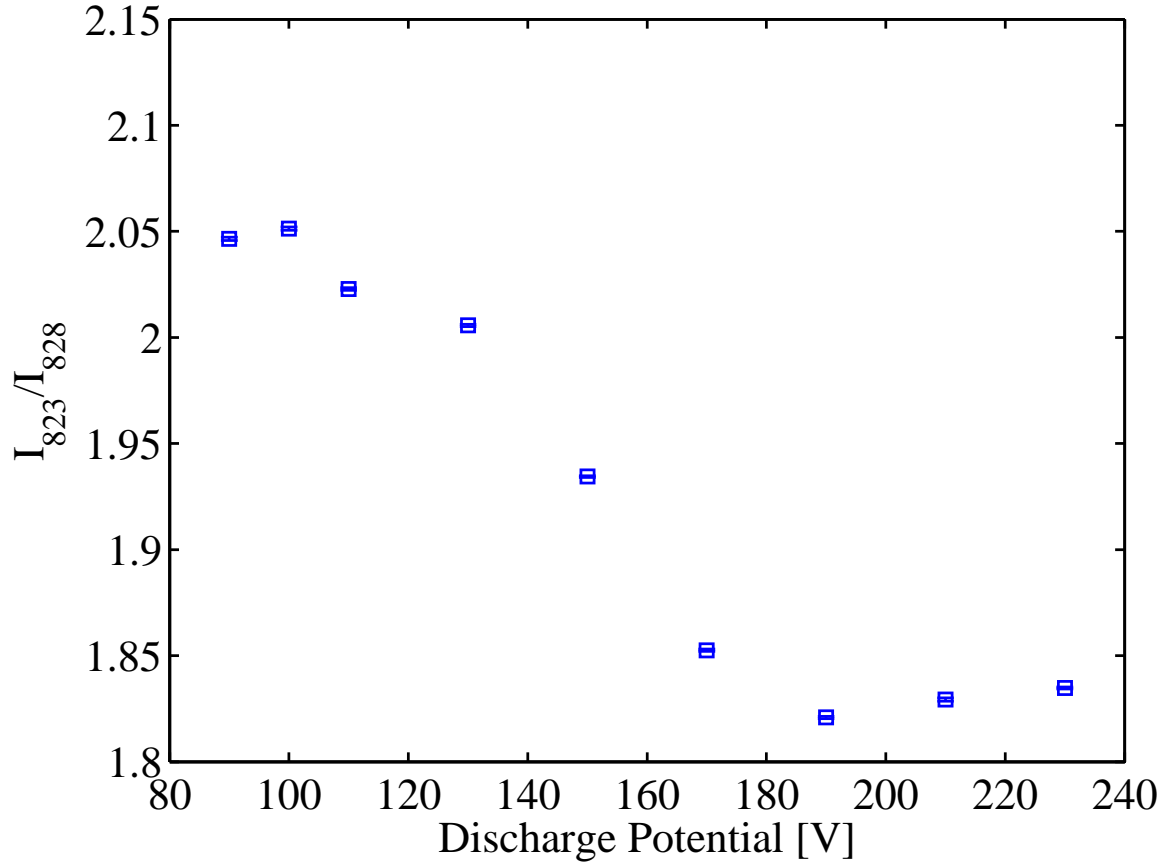
Figure 4.27:   Measured intensity ratio I_{823}/I_{828} for the BHT-200 with xenon at various discharge potentials. The magnet current and mass flow rate were held constant at 1.0 A and 0.94 mg/s of xenon.

intensity ratio data then further correlated to the discharge potential at which the emission spectra was taken to provide Figure 4.29 and 4.30 From Figure 4.29, the intensity ratio of I_{823}/I_{828} suggests the temperature of the ionization zone was in the 5.1 eV to 6.2 eV range. However, the intensity ratio of I_{834}/I_{828}, Figure 4.30, suggests the electron temperature at the same location was in the range of 5.3 eV to 8.4 eV.

Although both ratio of intensities show an increase in the electron temperature as the discharge potential was increased, the value of the temperature was considerably lower than previously measured [63]. Close examination of the data suggests, the cause of the lower electron temperature was due to two factors. The first, was caused by the original design of the experiment. Due to time and budget constraints, the collection optic used to gather the spectra was a large angle collimating lens which fed into the
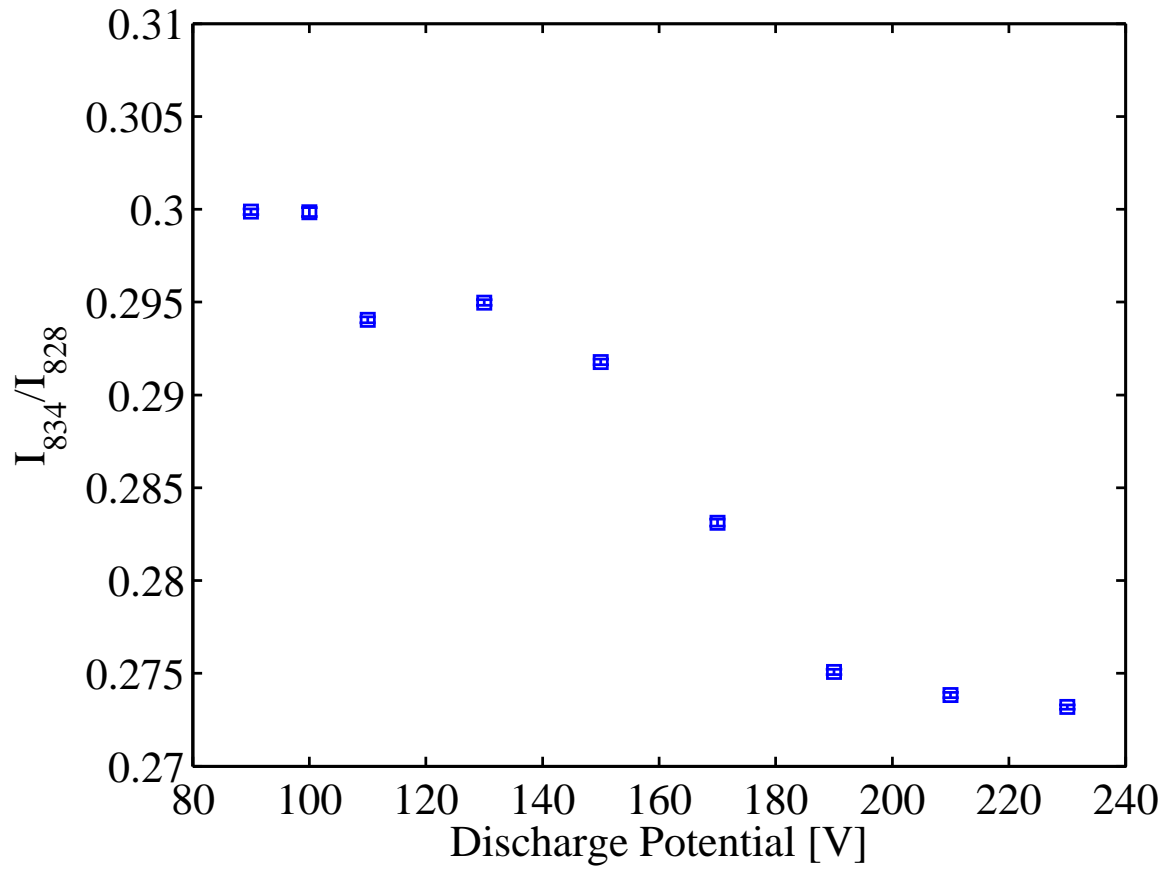
Figure 4.28:   Measured intensity ratio I_{823}/I_{828} for the BHT-200 with xenon at various discharge potentials. The magnet current and mass flow rate were held constant at 1.0 A and 0.94 mg/s of xenon.
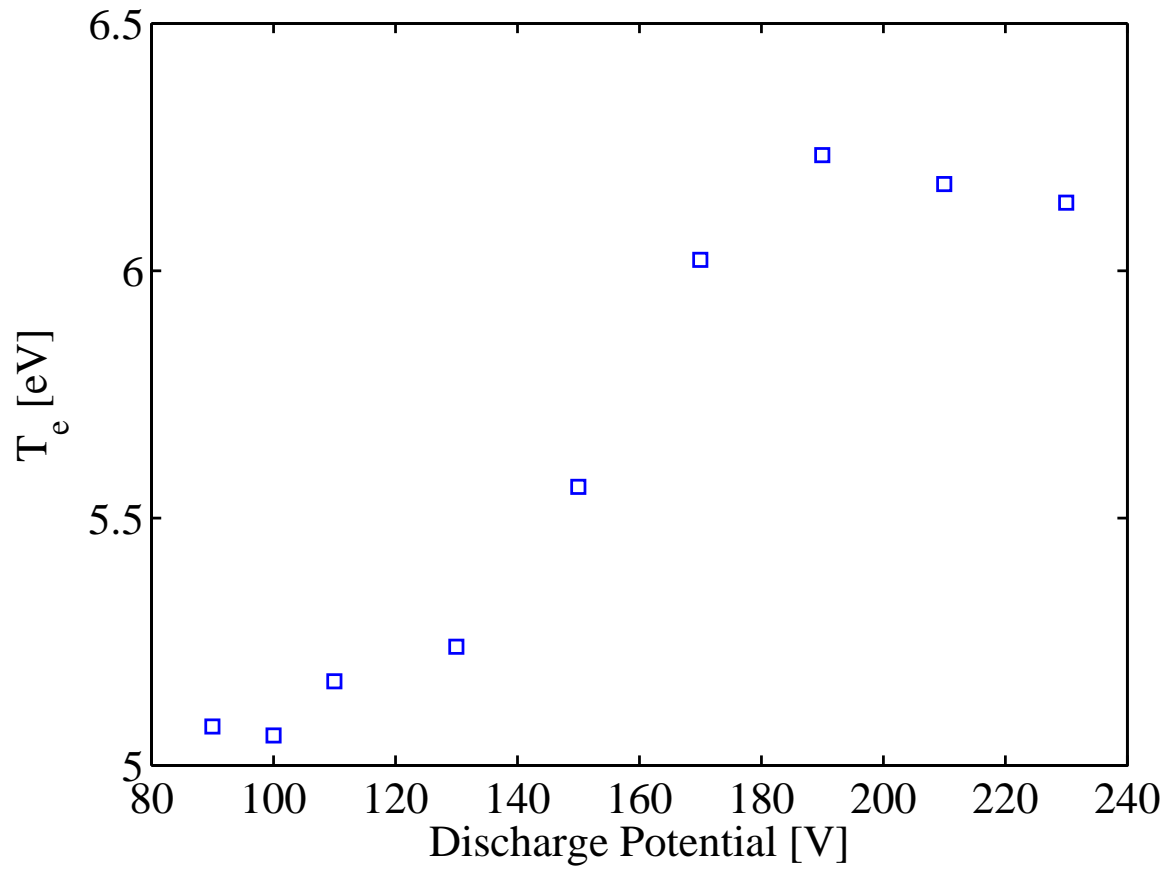
Figure 4.29:   Measured electron temperature of the BHT-200 main discharge with CRM intensity ratio I_{823}/I_{828} at various discharge potentials. The magnet current and mass flow rate were held constant at 1.0 A and 0.94 mg/s of xenon.
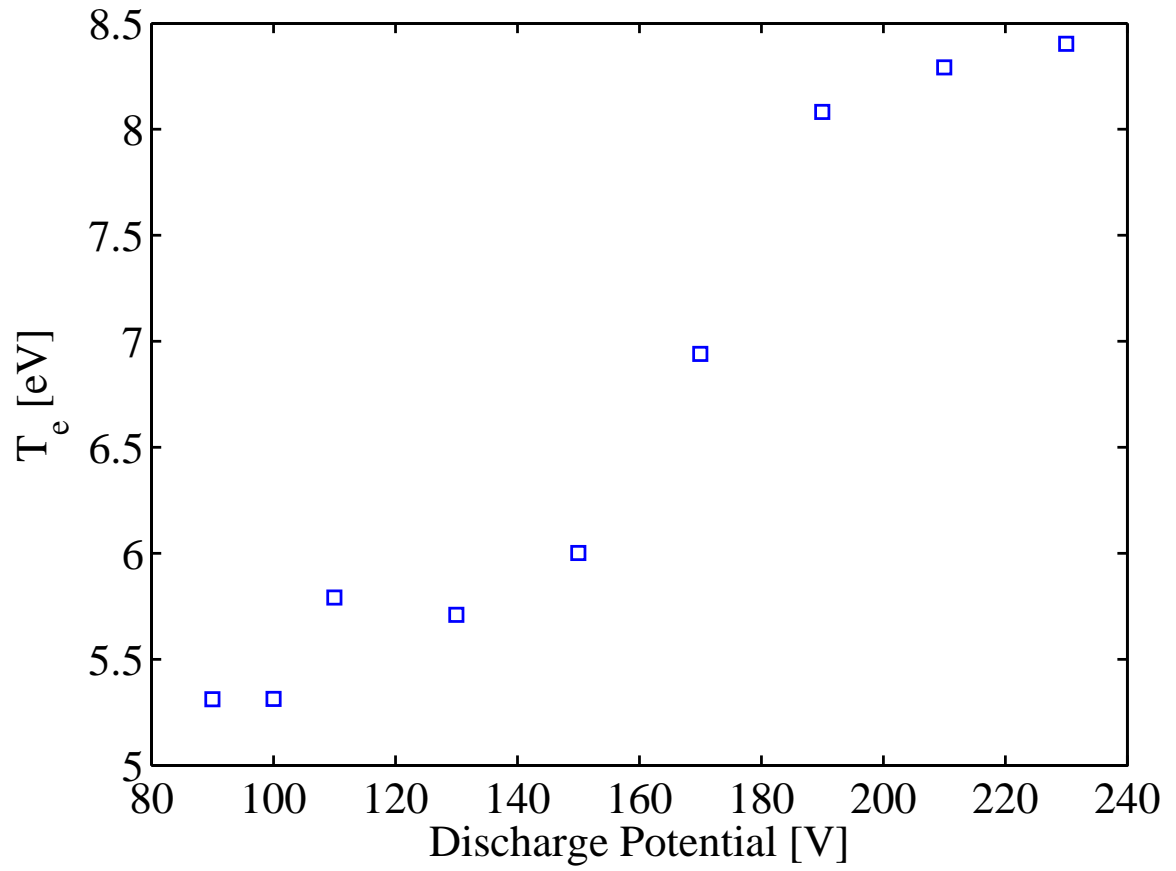
Figure 4.30: Measured electron temperature of the BHT-200 main discharge with CRM intensity ratio I_{834}/I_{828} at various discharge potentials. The magnet current and mass flow rate were held constant at 1.0 A and 0.94 mg/s of xenon.

fiber optic cable. The large field-of-view of the collimator collected a large spatial sample, in turn, causing a spatial averaging effect in the data where cooler regions of the plume were included in the measurement of the ionization zone. Second, the computed electron temperature data was based on parameters generated from the HPHall modeling tool. One limitation of HPHall is it requires experimental data to verify the generated parameters. Since no experimental data for the BHT-200 at various discharge potentials was available, generating the proper parameters to input into the CRM was difficult. Thus, as an approximation tool, the CRM calculated values were from the nominal operating conditions of the BHT-200. Nonetheless, the CRM model, in conjunction with the HPHall simulation, provided the qualitative data which confirmed the electron temperature does increase with discharge potential. Although this result did not provide the anticipated result of electron temperature, it did provide further support to the overall analysis.

4.4 Xenon Breathing Mode at Various Discharge Current and Magnet Current

In order to further understand the breathing mode, other parameters of the thruster such as the discharge current and magnet current were also varied. Although previous sections compared the breathing mode at different discharge currents, this section will provide a more in-depth analysis on the influence of the discharge current. While the title of this section refers to the variation in discharge current, it is actually a variation in the mass flow rate as well. Since the mass flow rate is proportional to the number density of neutrals, the increase in mass injected into the ionization zone relates to a corresponding increase in the discharge current.

A lower discharge potential, 80 V, was specifically chosen to explore the effects of the discharge current on the breathing mode. Recall the breathing mode frequency was not as coherent in the lower discharge potentials and more susceptible to parameter variations. Second, it was difficult to operate the thruster at very high and low mass flow rates in the higher discharge potential regime. Lastly, the middle of the potential regime was not chosen since the amplitude of the signal was very low.

The effect of the discharge current on the breathing mode frequency is shown in Figure 4.31. The results show as the mass flow rate was increased, the frequency increased which is consistent with the predator/prey model. Overall, the breathing mode frequency increased 47% over the span of 0.4 to 1.6 A.

The time-dependent discharge current trace, shown in Figure 4.32, brings to light some characteristics of the breathing mode as the discharge current is increased. When the discharge current is set at 0.4 A, the periodic oscillations were clearly seen. However, as the current is increased, the frequency of the oscillations begins to increase. The additional influx of neutrals to the ionization zone caused an increase in oscillation allowing for the exhaust and replenishment cycle of the neutrals to occur quicker.
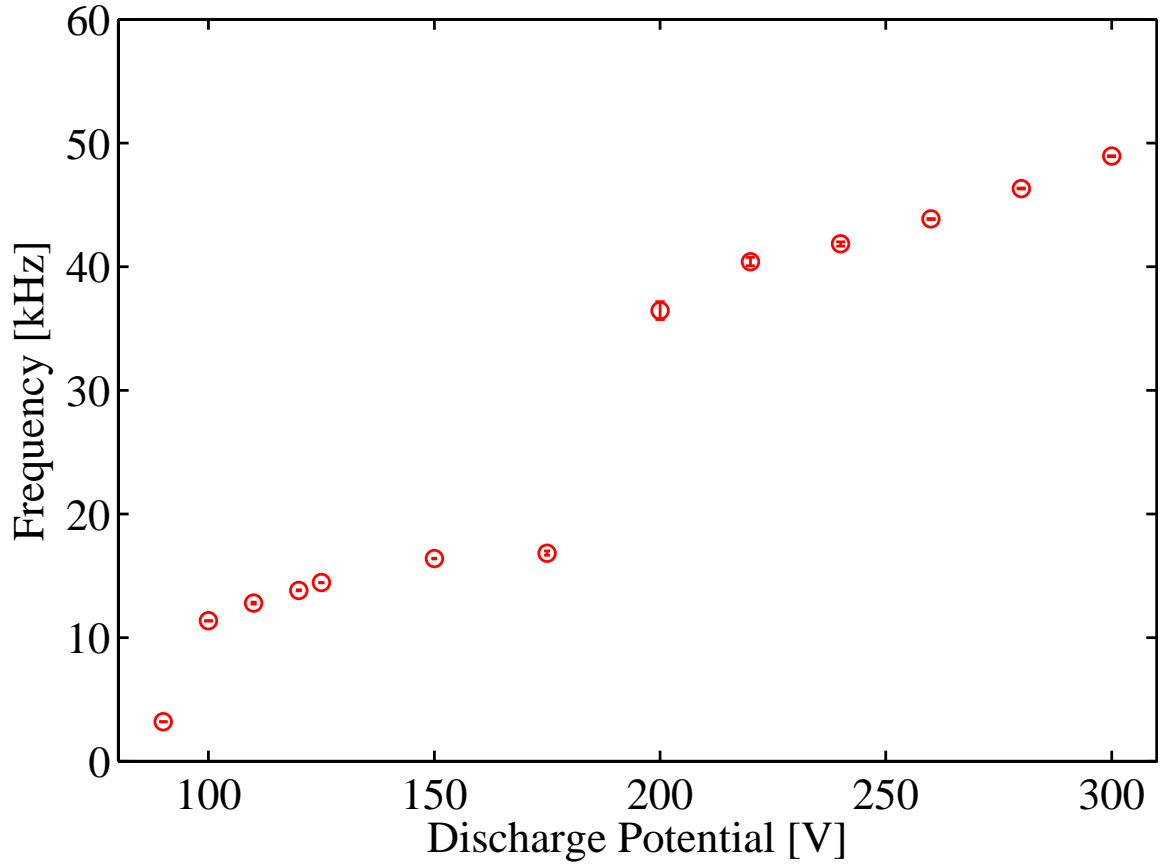
Figure 4.31: Breathing mode frequency dependence on discharge current for the BHT-200 operating with xenon. The average discharge potential and magnetic current were held constant at 80 V and 1.0 A, respectively.

Figure 4.32: Discharge current of BHT-200 with xenon operating at various average discharge currents (denoted in lower right corner). The discharge potential and magnet current were held constant at 80 V and 1.0 A, respectively.
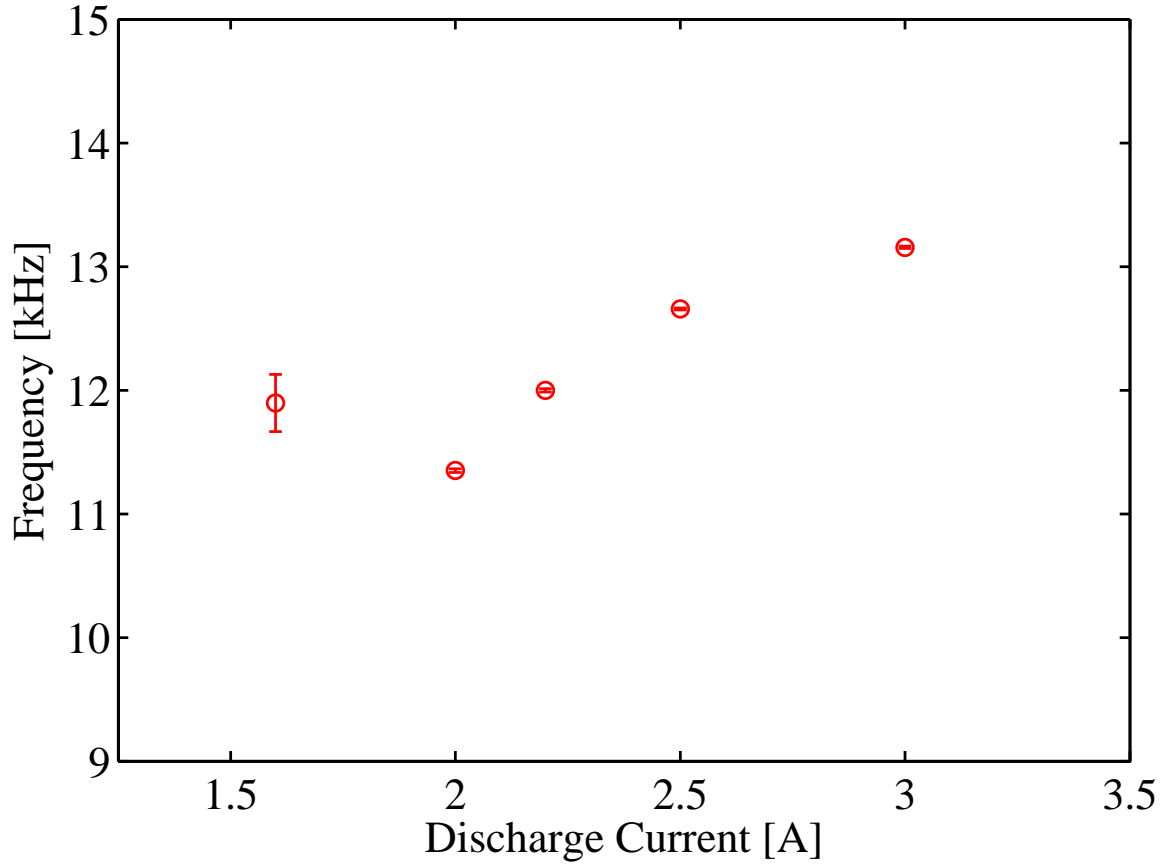
Figure 4.33: Breathing mode frequency dependence on the discharge current for the BHT-600 operating with xenon. The discharge potential and magnet current were held constant at 100 V and 1.75 A, respectively.

The effect of the discharge current was also examined for the BHT-600. Again, the lower discharge potential was used since it had a sufficient amplitude of breathing mode frequency which allowed for a large range of discharge current or mass flow rates. Figure 4.33 shows the dependence of the breathing mode frequency with the discharge current. Similar to the BHT-200 case, a linear relationship between the frequency and the discharge current exists showing a 14% increase in frequency over a 47% increase in discharge current.

Unlike the xenon case, the discharge current trace in Figure 4.34 did not show any significant amplitude dampening. Moreover throughout the test regime, the breathing mode oscillation signal was very coherent even at the lower average discharge current. However, in Figure 4.33, the average frequency at the discharge

current of 1.6 A was greater than expected and does not follow the trend. Although the current trace in Figure 4.34 does not show it, the main discharge of the thruster was difficult to sustain at the low mass flow rates, contributing to a larger percentage of uncertainty and higher than expected frequency values.

The influence of the magnet current on the breathing mode was also explored. In Figure 4.35, the variation of the magnet current from 0.2 A to 1.0 A only resulted in a minor net change in the breathing mode frequency and is constant over the range tested. Further analysis of the individual discharge current signal, in Figure 4.36, gives more insight on the influence of the magnet current. As the magnet current is increased the oscillation of the breathing mode becomes less coherent. This may be due to other instabilities within the main discharge which are discussed in later sections.

In comparison the breathing mode frequency of the BHT-600 was also studied at various magnet currents with the discharge potential held constant at 90 V. Unlike the constant breathing mode frequency seen in the BHT-200 data, Figure 4.37 shows an inverse relationship between the magnet current and the breathing mode frequency. To verify this result, another set of various magnet current data was taken at a higher discharge potential of 100 V and both sets of data seem to agree.

The resulting difference in behavior with respect to the magnetic field and the breathing mode frequency may be due to the variations in magnetic field topology of the BHT-200 and BHT-600 as shown in Cheng [7]. With the length of the ionization zone influenced by the magnetic field topology, the measured breathing mode frequencies provide insight on the dependence of the ionization length to the magnetic field of each thruster [4, 22]. For the BHT-200, the constant breathing mode frequency suggests the ionization length is nearly constant throughout the test regime which shows the magnet current may not influence the magnetic field topology. Conversely, the breathing mode frequency of the BHT-600 shows the ionization length to increase as the magnet current is increased.

104

Figure 4.34: Discharge current of BHT-600 with xenon operating at various average discharge currents (denoted in lower right corner). The discharge potential and magnet current were held constant at 100 V and 1.75 A, respectively.
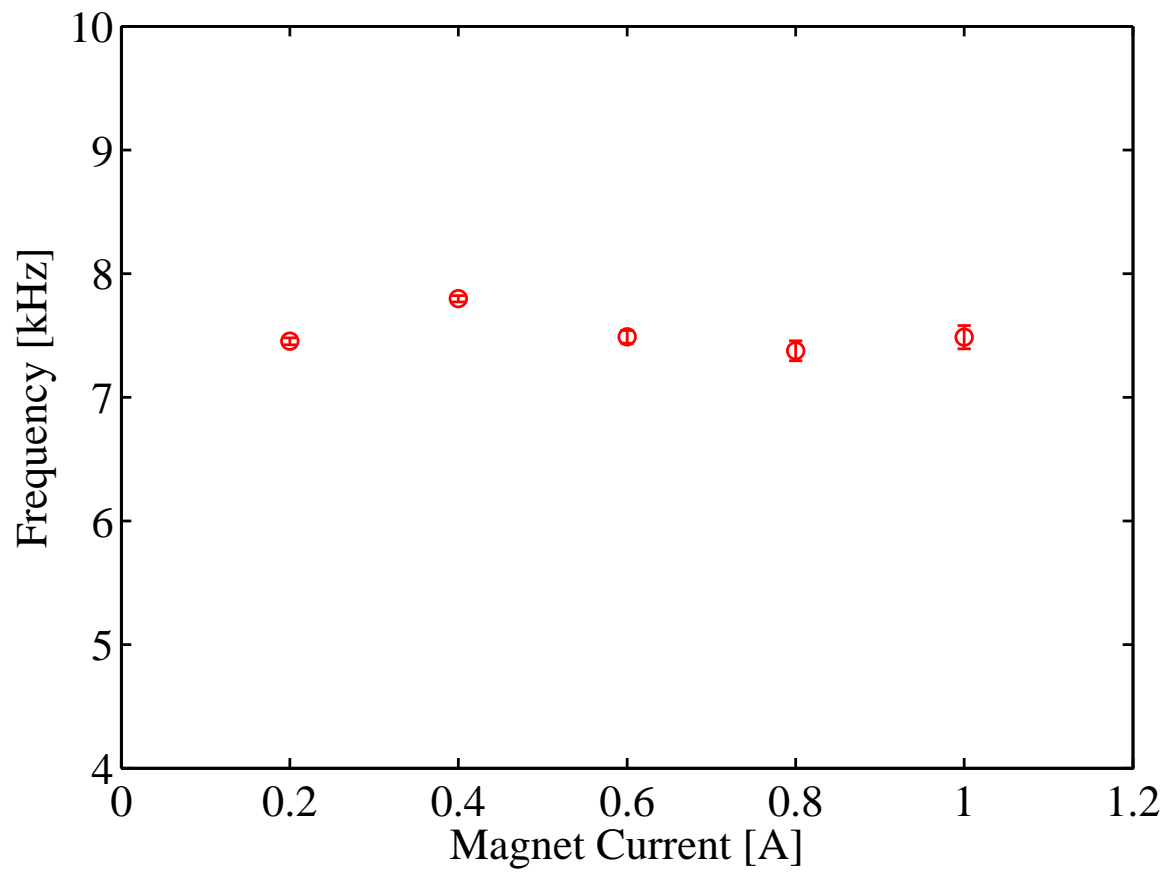
Figure 4.35: Breathing mode frequency dependence on the magnet current for the BHT-200 operating with xenon. The discharge potential and discharge current were held constant at 80 V and 0.8 A, respectively.
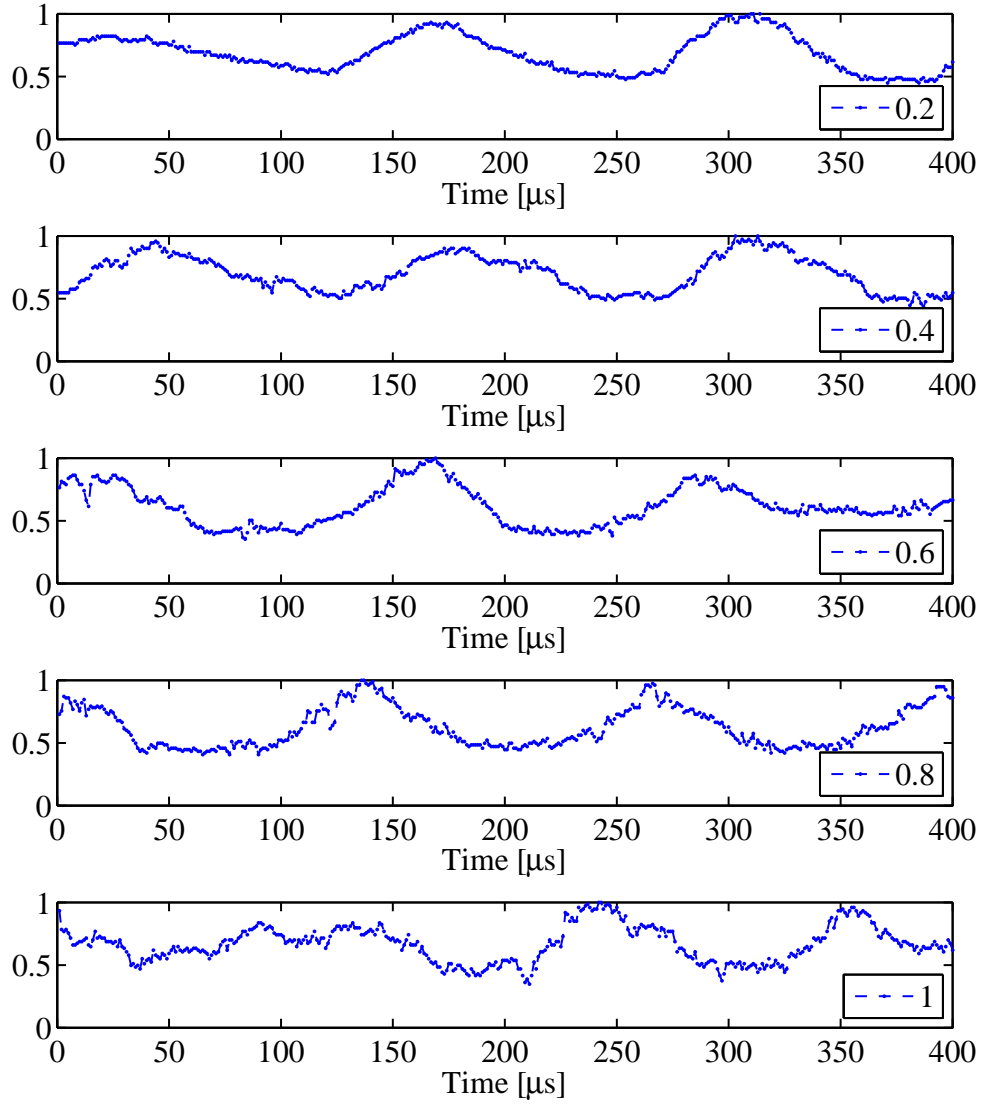
Figure 4.36: Discharge current of BHT-200 with xenon operating at various magnet currents (denoted in lower right corner). The discharge potential and discharge current were held constant at 80 V and 1.0 A, respectively.
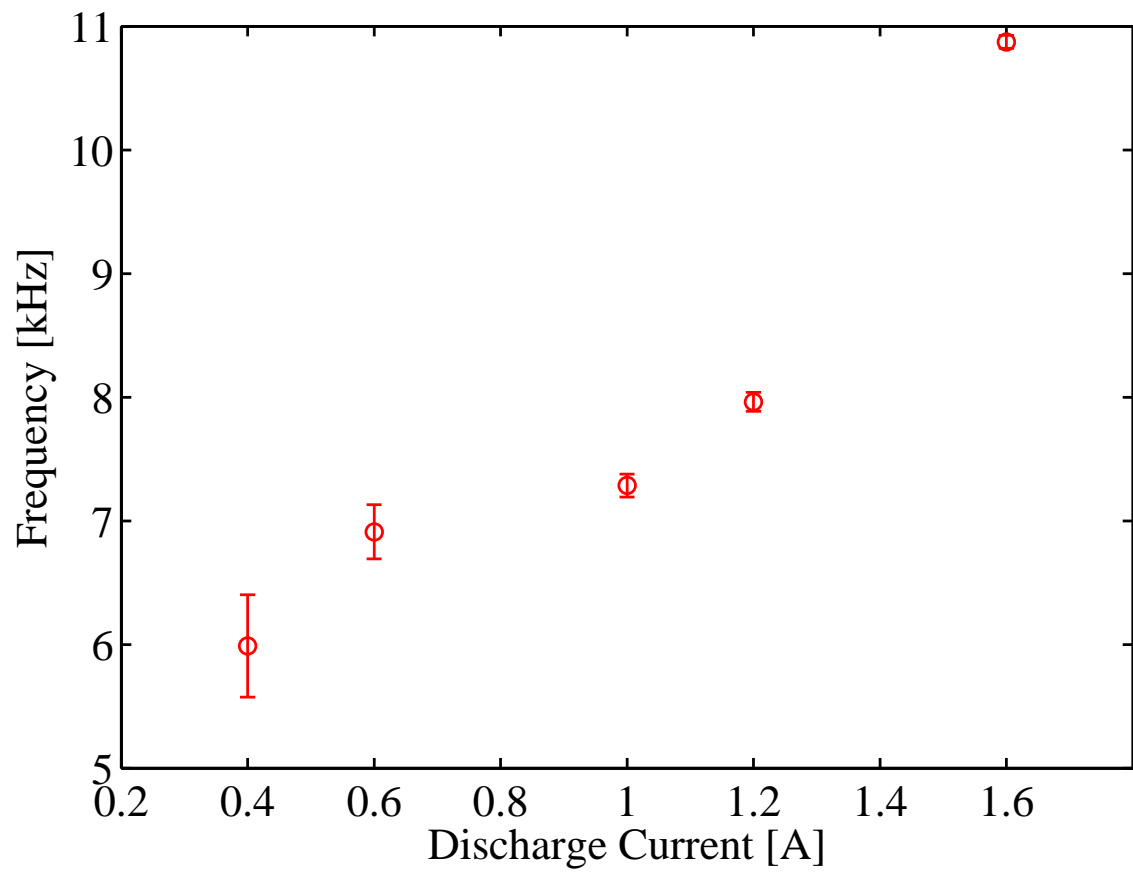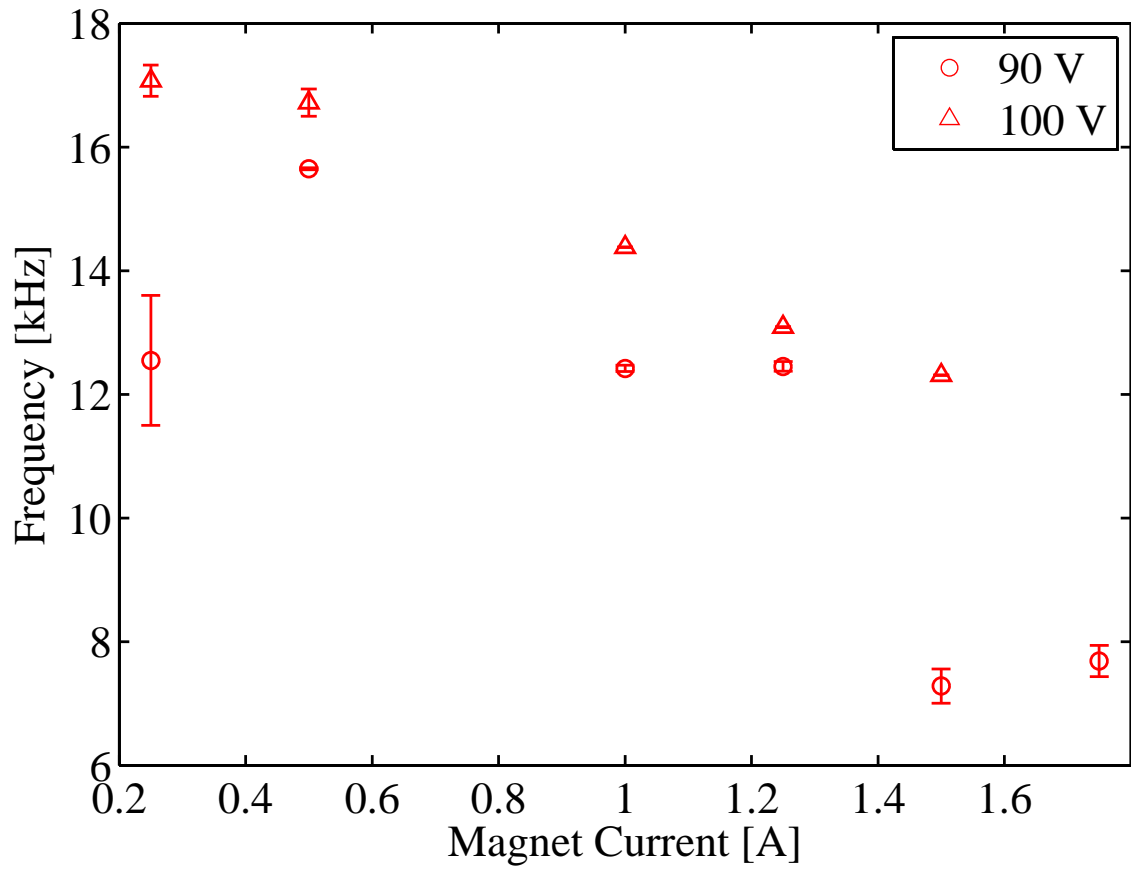
Figure 4.37: Breathing mode frequency dependence on the magnet current for the BHT-600 operating with xenon. The discharge potentials and discharge current were held constant at 90 V (circles)/100 V (triangles) and 0.8 A, respectively.

4.5   Krypton Breathing Mode at Various Discharge Potential

The direct emission of the plasma discharge was also taken for the BHT-200 and BHT-600 with krypton propellant. In the zero-aspect views of the BHT-200, shown in Figure 4.38, the periodic increase and decrease of the breathing mode is not as evident as the xenon case at the same operating condition. Although, the high speed images do show the plasma emission between the annulus of the thruster, the amplitude of the emission has decreased when compared to the high speed images of the xenon discharge.

In order to understand the cause of the intensity decrease and the suppression of the breathing mode, the discharge current trace at the various discharge potentials is presented in Figure 4.39 and 4.40. The discharge current data, Figure 4.39, shows the breathing mode for krypton was damped at the 250 V case in the same way the oscillations of the discharge current was damped for xenon at the the 170 V to 210 V cases shown in Figure 4.17.

Furthermore, the oscillatory behavior returns to the discharge signal at the lower discharge potentials similar to the xenon case. This result suggests the behavior of the thruster for both xenon and krypton are similar and the difference between the two depends on the discharge potential. In other words, the krypton discharge current trace at 250 V is comparable to the xenon discharge current trace at 210 V. Similarly, the krypton discharge current trace at 150 V is comparable to the xenon discharge current trace at 130 V. This *shift* in the average discharge current between xenon and krypton seems consistent throughout the different discharge potentials tested in this study. A possible cause of the shift is due to the difference in ionization potential between xenon and krypton. With krypton having a higher ionization potential, the rate of ionization is not large enough, at 250 V, to fully develop the breathing mode since not enough of the neutrals ionized to create the deficit.

The breathing mode frequency was also calculated at various discharge potentials with a constant mass flow rate and constant discharge current. The results of
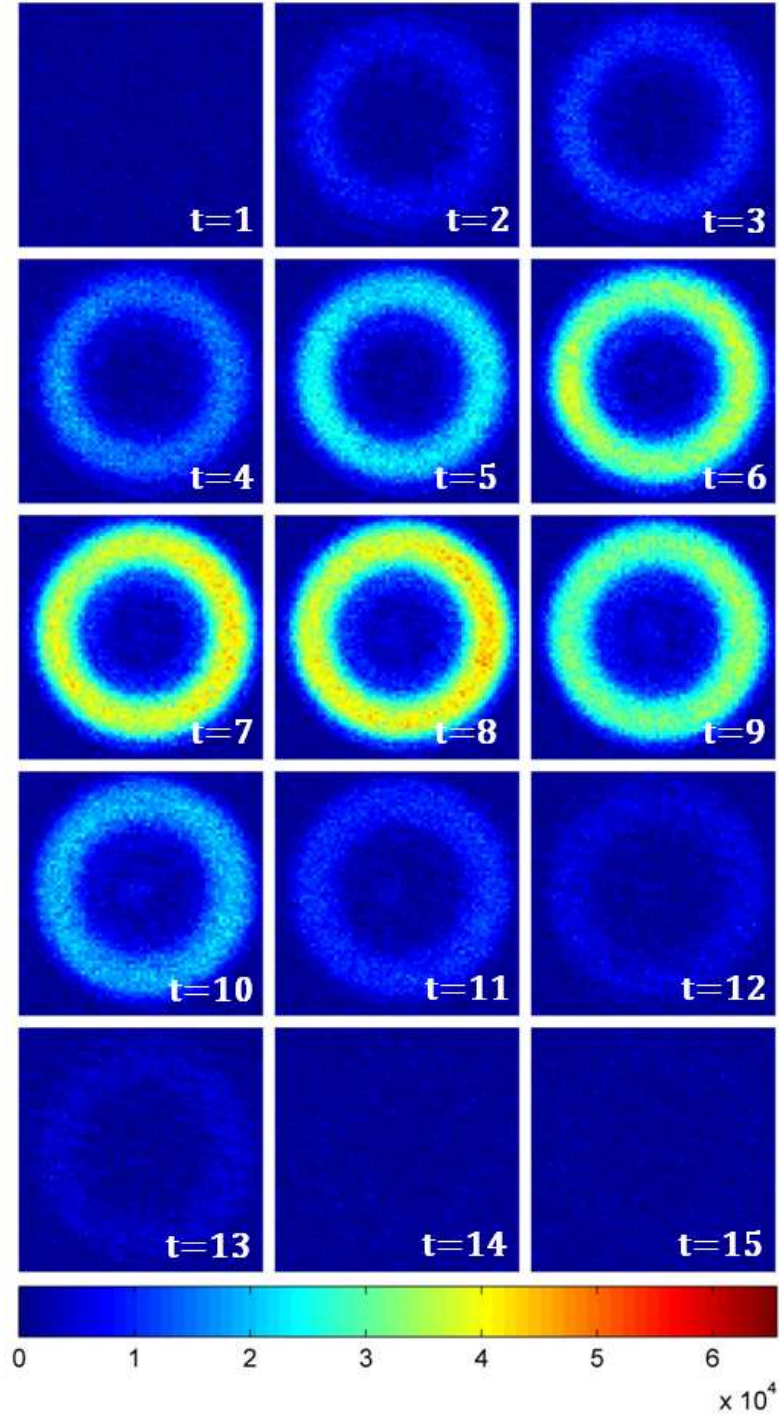
Figure 4.38: Sequential images (color enhanced) of BHT-200 discharge oscillation operating at nominal conditions with krypton. $V_d = 250$ V, $I_d = 0.8$ A, $I_m = 1.0$ A, ṁ= 0.67 mg/s of krypton. The time between images was 1 μs with an exposure time of 750 ns. Arbitrary intensity.
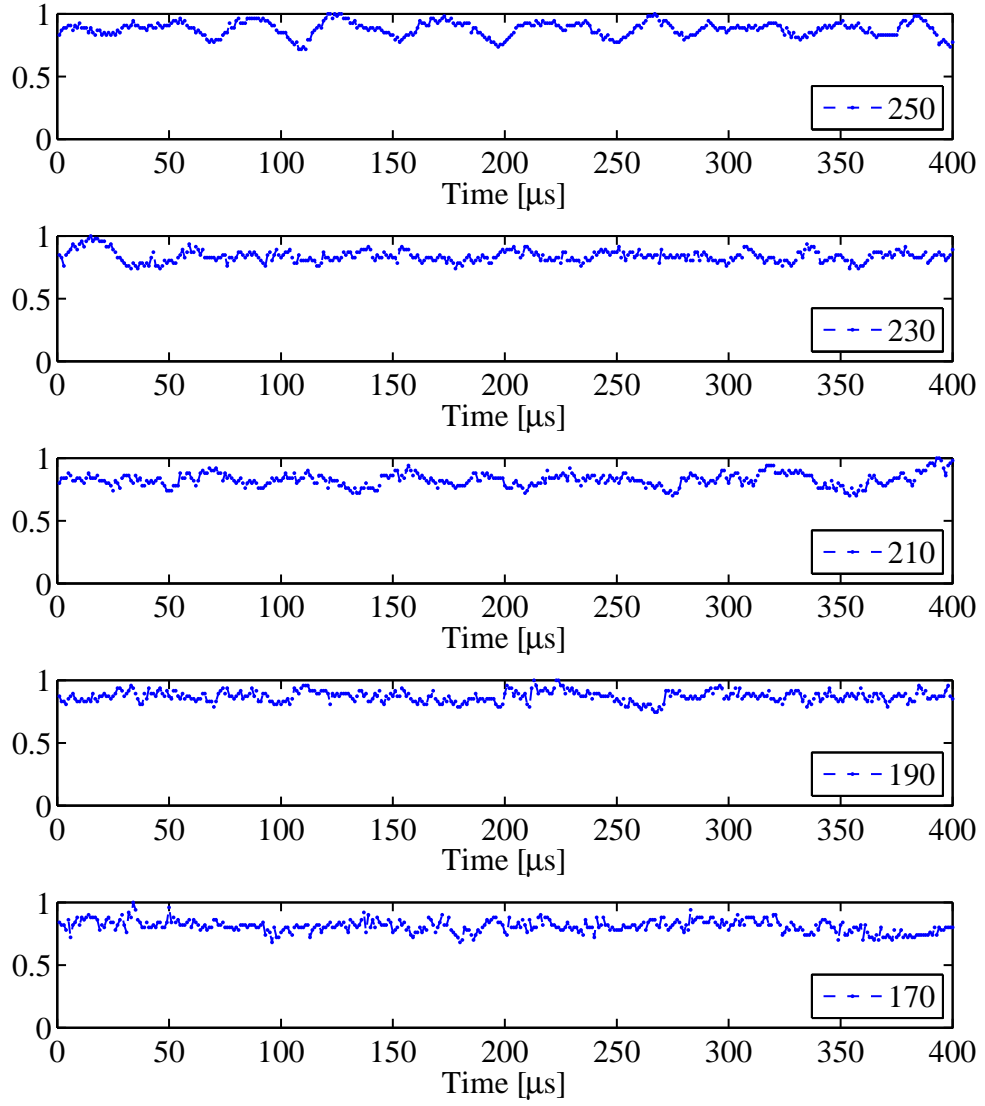
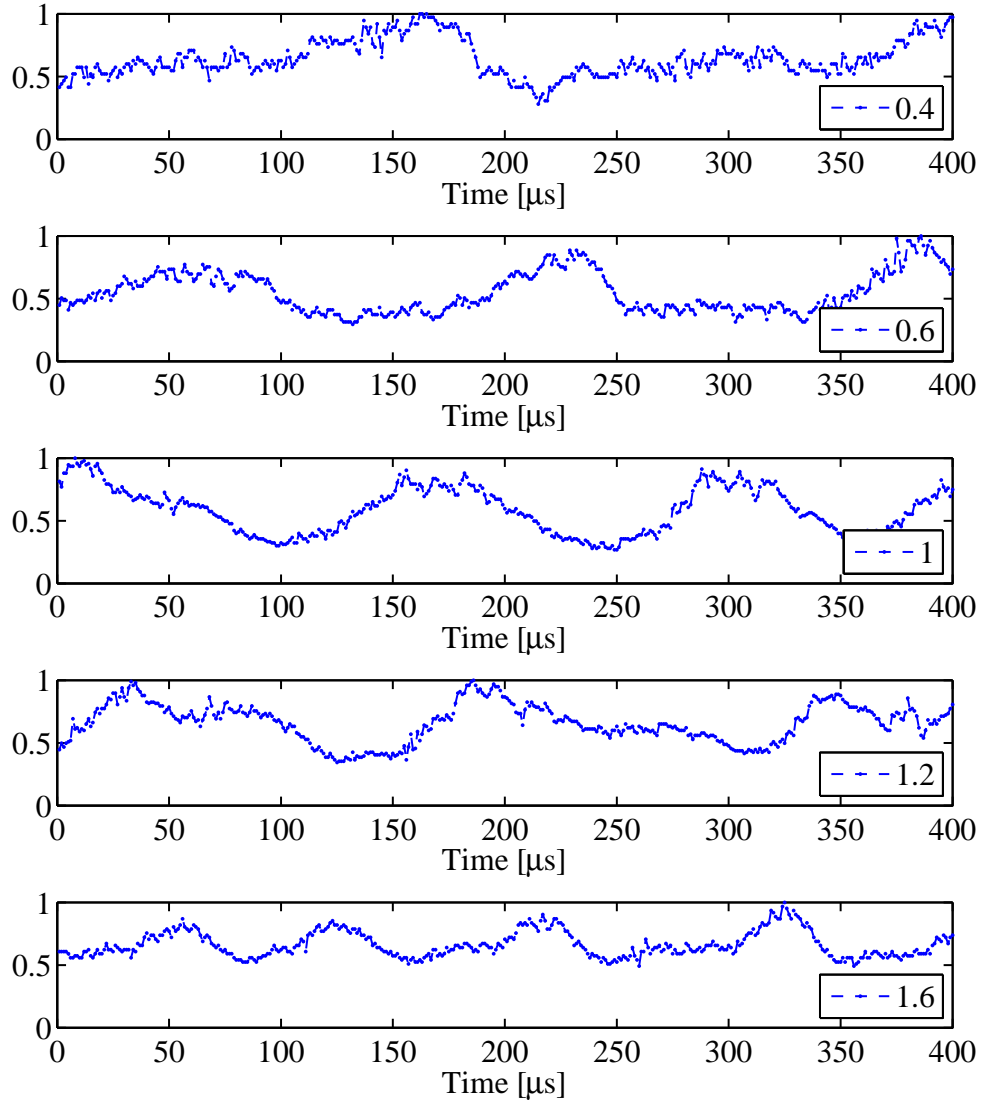Figure 4.39: Discharge current of BHT-200 with krypton and operating at various discharge potentials (denoted in lower right corner). The discharge current and magnet current were held constant at 0.8 A and magnet current 1.0 A, respectively.
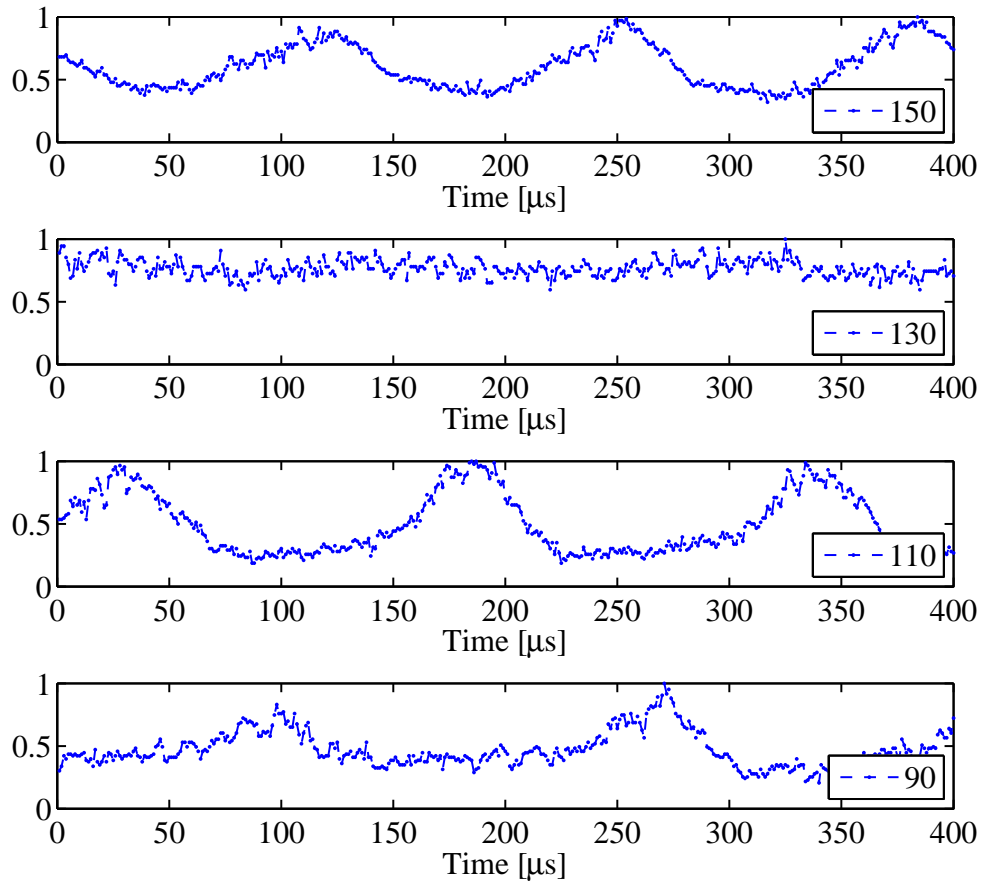
Figure 4.40: Discharge current of BHT-200 with krypton and operating at various discharge potentials (denoted in lower right corner). The discharge current and magnet current were held constant at 0.8 A and magnet current 1.0 A, respectively.

both observations are provided in Figure 4.41. Similarities in frequency suggests the differences in discharge current or mass flow rates were not significant in the influence of the breathing mode frequency, albeit, the differences in discharge current or mass flow rates were small.

Frequencies were also collected for the BHT-600 thruster utilizing krypton as the feed gas. The discharge current traces, Figure 4.42 and 4.43, also show the krypton breathing mode frequency is damped at the higher discharge potentials and not fully develop until the discharge potential was lowered to 200 V which is similar to the BHT-200 utilizing krypton.

Furthermore, using the discharge current trace, it was possible to select high-speed images which illustrate the breathing mode of the BHT-600. In this case, Figure 4.44 shows the krypton breathing mode operating at a discharge potential, discharge current, and magnet current of 200 V, 2.0 A, and 1.75 A, respectively. Similar to the other cases presented, the intensity of the emission increased and decreased periodically within the thruster annulus. It is also possible to see non-uniformities of the emission in the azimuthal direction.

The frequency of the krypton breathing mode was also determined for the BHT-600. Figure 4.45 shows the result of various discharge potentials on the breathing mode frequency and compares the krypton data to the xenon data for the same thruster. For both the BHT-200 and BHT-600, the increase of the breathing mode frequency with increasing discharge potential corresponds with the predator/prey model previously described in equation (2.45). As the discharge potential is increased, the electron temperature also increased leading to an increase in the ionization rate.. Since there was an increase in the ionization rate, the breathing mode frequency also increased.

In addition to having the breathing mode increase with increasing electron temperature, consistent with the predator/prey model, the BHT-600 also shows the krypton data to have a lower frequency at the same discharge potential with an exception
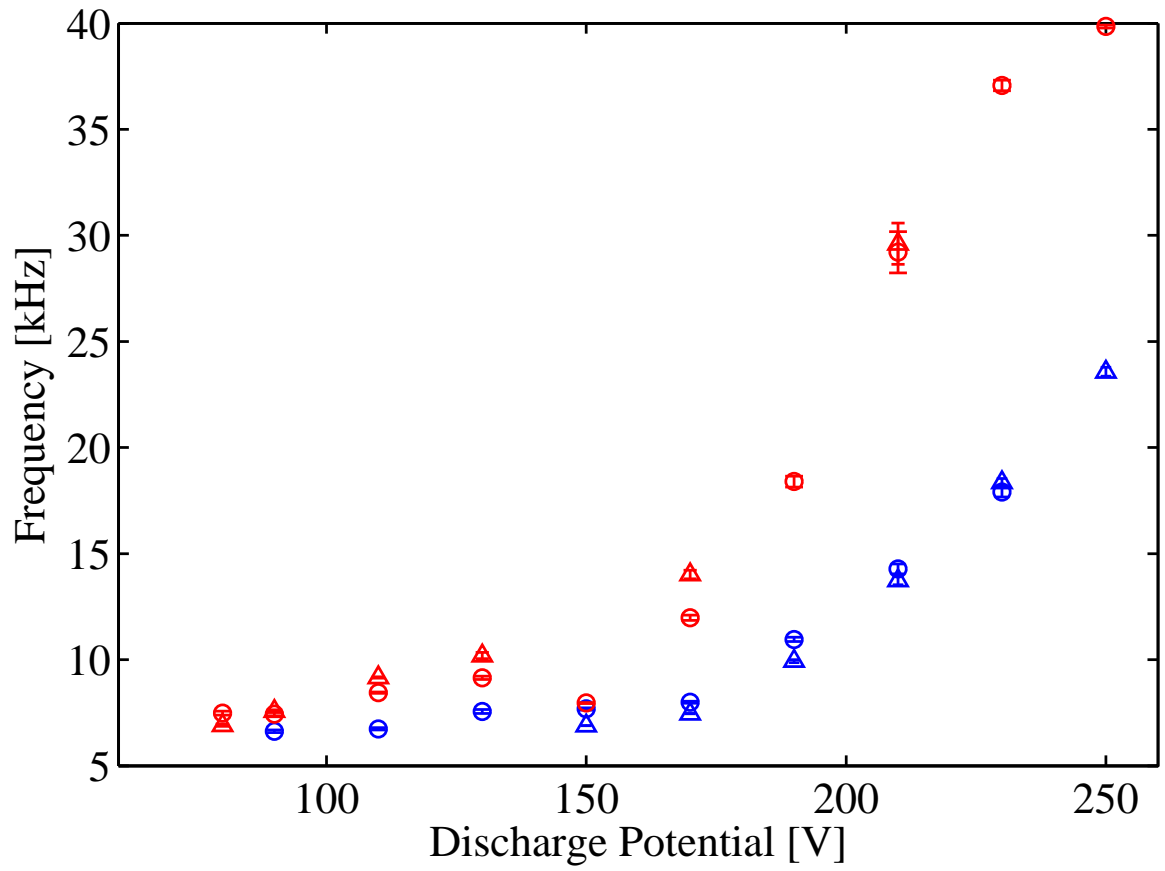
Figure 4.41: Comparison of breathing mode frequency dependence on discharge potential for the BHT-200 utilizing xenon (red) and krypton (blue). The constant mass flow rate (triangles) was also compared to the constant discharge current (circles) case. The magnet current was held constant at 1.0 A.
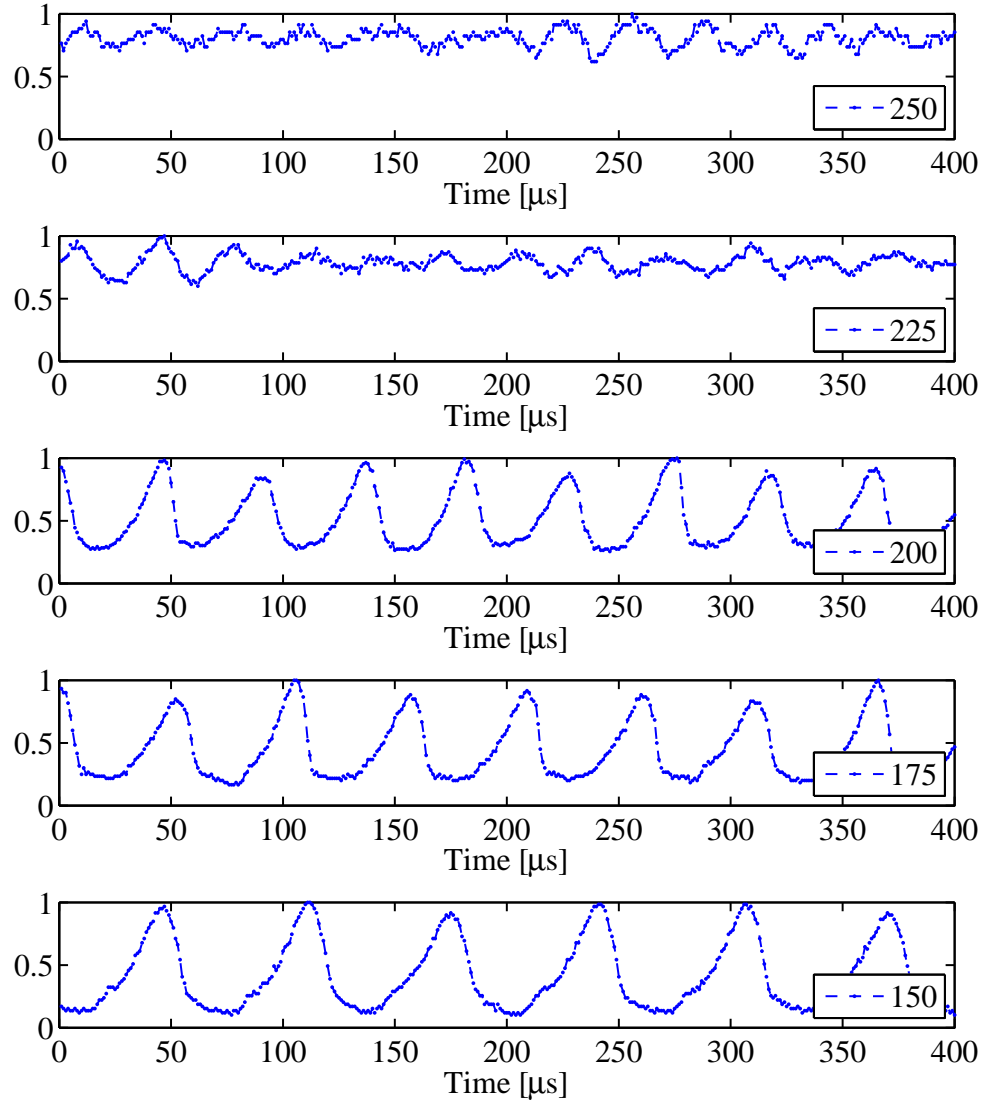
Figure 4.42: Discharge current of BHT-600 with krypton and operating at various discharge potentials (denoted in lower right corner). The discharge current and magnet current were held constant at 2.0 A and magnet current 1.75 A, respectively.
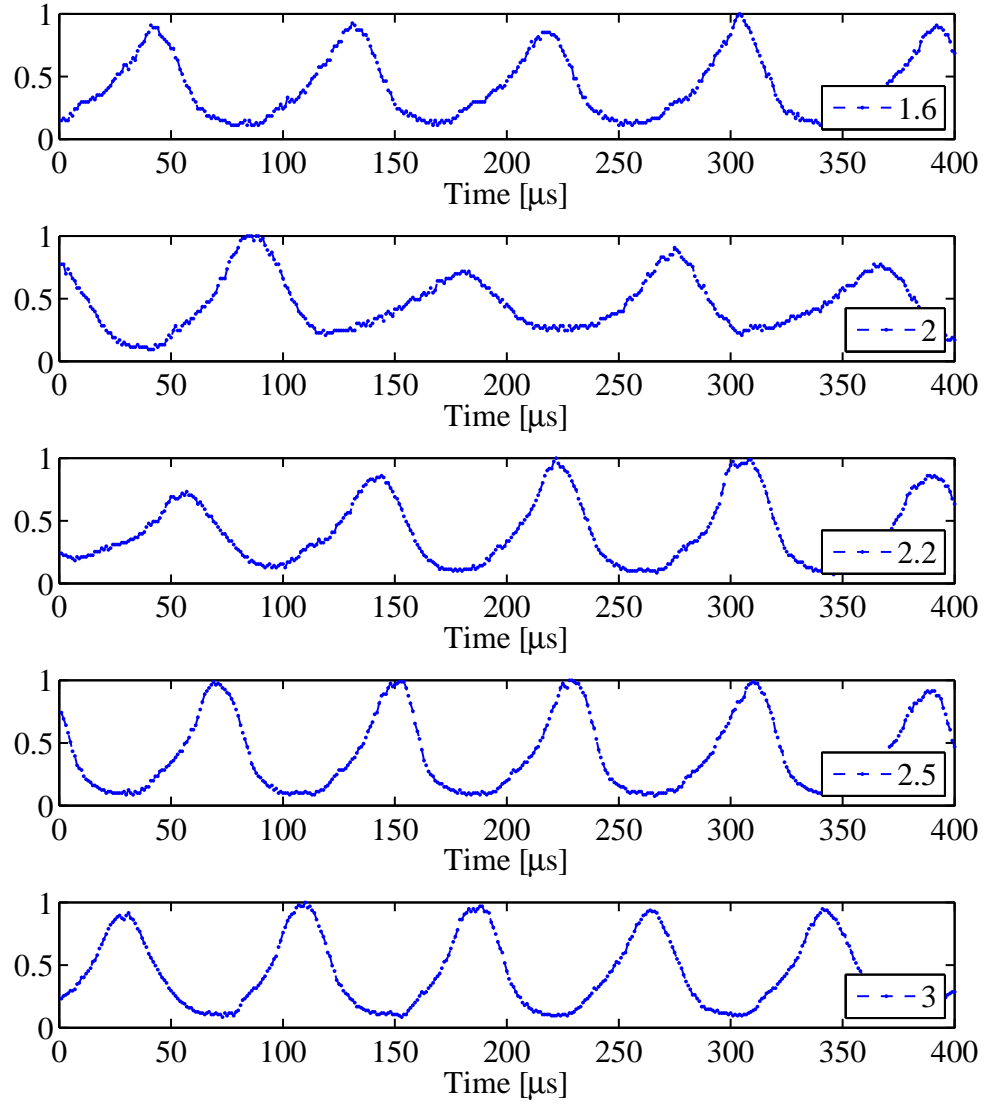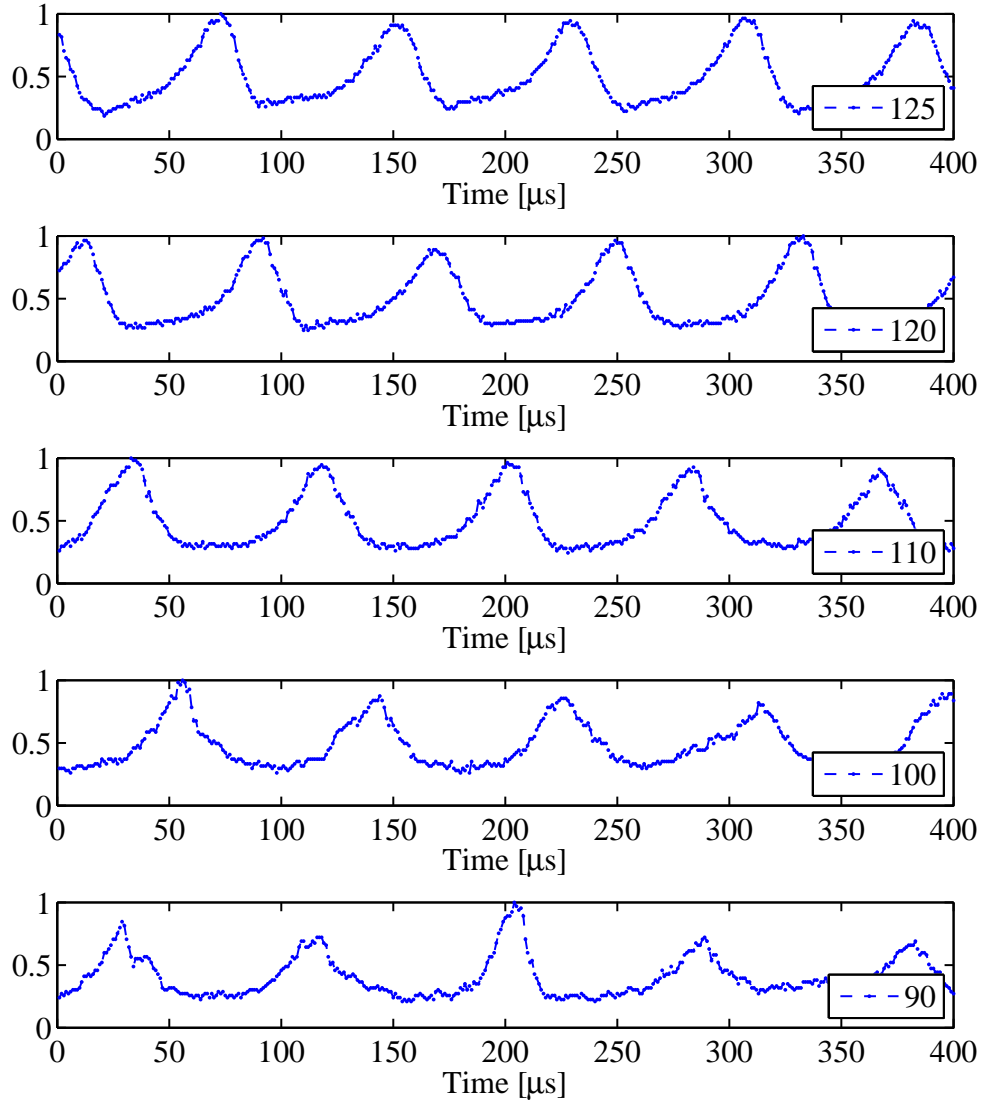
Figure 4.43: Discharge current of BHT-600 with krypton and operating at various discharge potentials (denoted in lower right corner). The discharge current and magnet current were held constant at 2.0 A and magnet current 1.75 A, respectively.
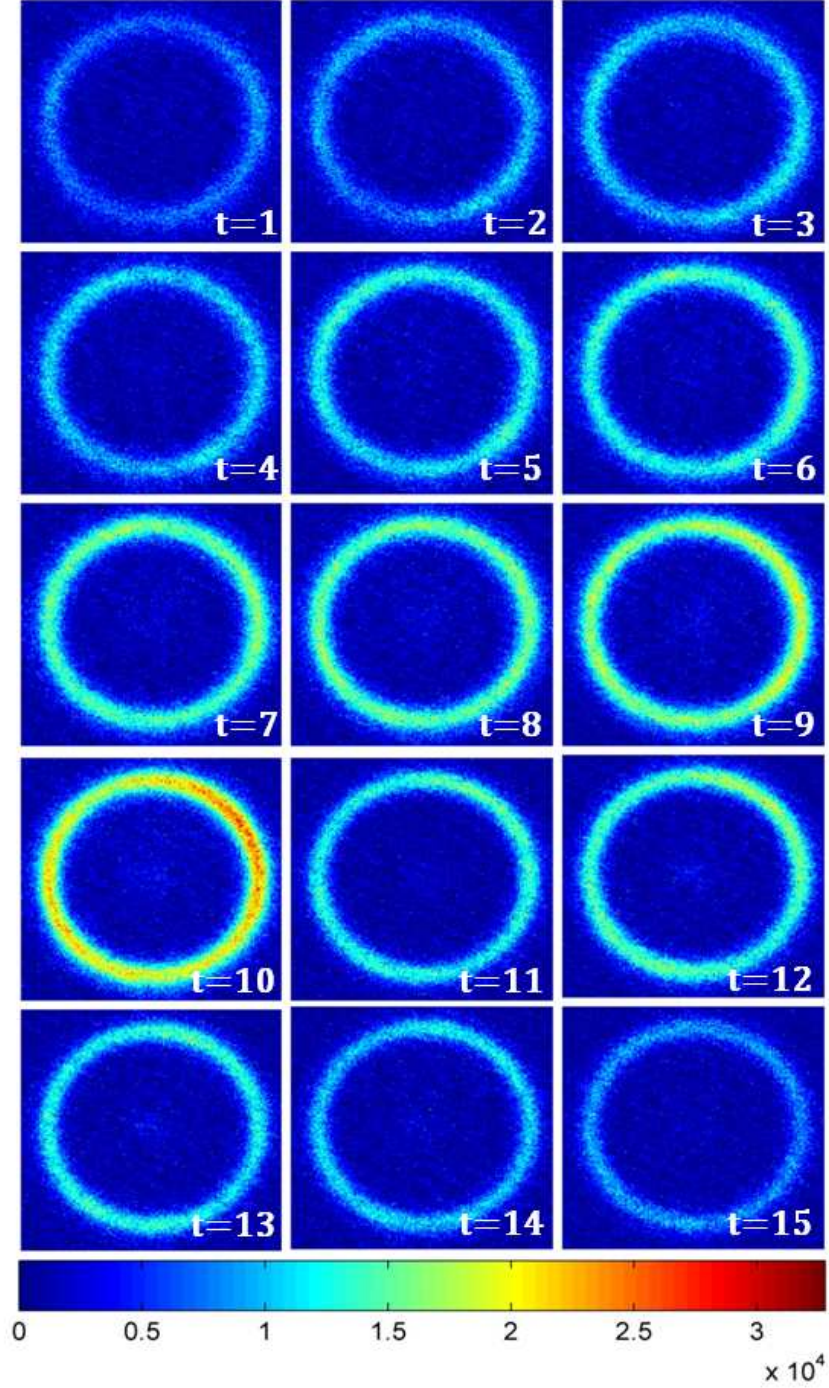
Figure 4.44: Sequential images (color enhanced) of BHT-600 discharge oscillation with krypton operating at $V_d = 200$ V, $I_d = 2.0$ A, $I_m = 1.75$ A and $\dot{m} = 1.9$ mg/s of krypton. The time between images was 1 μs with an exposure time of 750 ns. Arbitrary intensity.
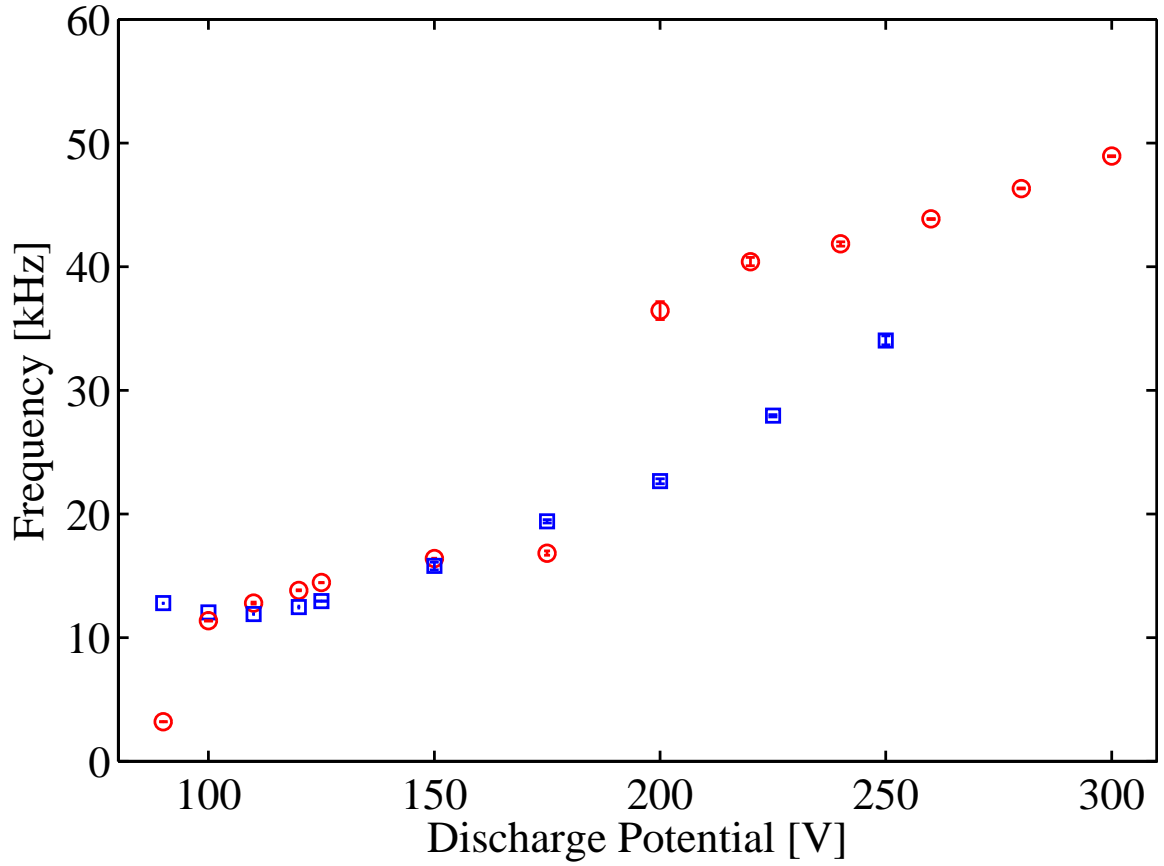
Figure 4.45: Breathing mode frequency dependence on discharge potential for the BHT-600 operating with xenon (circles) and krypton (squares). The discharge current and magnet current were held constant at 2.0 A and 1.75 A, respectively.

at the very low discharge potentials of 90 V and 100 V. At the exception points, the mass flow rate was significantly increased to maintain the discharge. As a result of the increase in the mass flow rate, the krypton breathing mode frequency exceeded the xenon frequency as seen from the previous section. This relationship is also explored in the following sections for krypton.

Comparing the xenon breathing mode frequency to the krypton breathing mode frequency, at the same discharge potentials with constant magnet current and discharge current, the frequency for xenon is consistently greater than krypton for both thrusters. From equation (2.46), several quantities contribute to the breathing mode frequency such as the ionization length, ion velocity, and neutral velocity. With a lower molecular mass compared to xenon, the ion and neutral velocities for krypton

are greater at comparable discharge quantities which should provide a greater krypton breathing mode frequency. However, the measured breathing mode frequencies for xenon and krypton does not support this assertion, which suggests the ionization length may have a greater influence compared to the ion and neutral velocities. Since the xenon breathing mode frequency is larger than a comparable krypton breathing mode frequency, this suggests the ionization length is larger for krypton than xenon. The longer krypton ionization length may be the result of the smaller cross section of krypton compared to xenon which may require a longer residence time before the krypton neutrals are ionized by an electron with sufficient energy. As a result of the increased residence time of krypton, the ionization length would have also increased as compared to xenon [54]. Indeed, measurements of Hall thrusters by Linnell and Gallimore confirms the ionization length is longer for krypton than xenon at comparable thruster parameters [50–52].

4.6 Krypton Breathing Mode at Various Discharge Current and Magnet Current

The breathing mode frequency of the BHT-200 and BHT-600 with krypton was also investigated at different discharge currents and different magnet currents as listed in Table 3.4 and 3.6. For the BHT-200, a low discharge potential of 90 V was set for both propellants. Figure 4.46 illustrates the influence of the discharge current on the krypton breathing mode frequency with the discharge potential and magnet current held constant at 90 V and 1.0 A, respectively. Additionally, Figure 4.46 compares the krypton results with the xenon results.
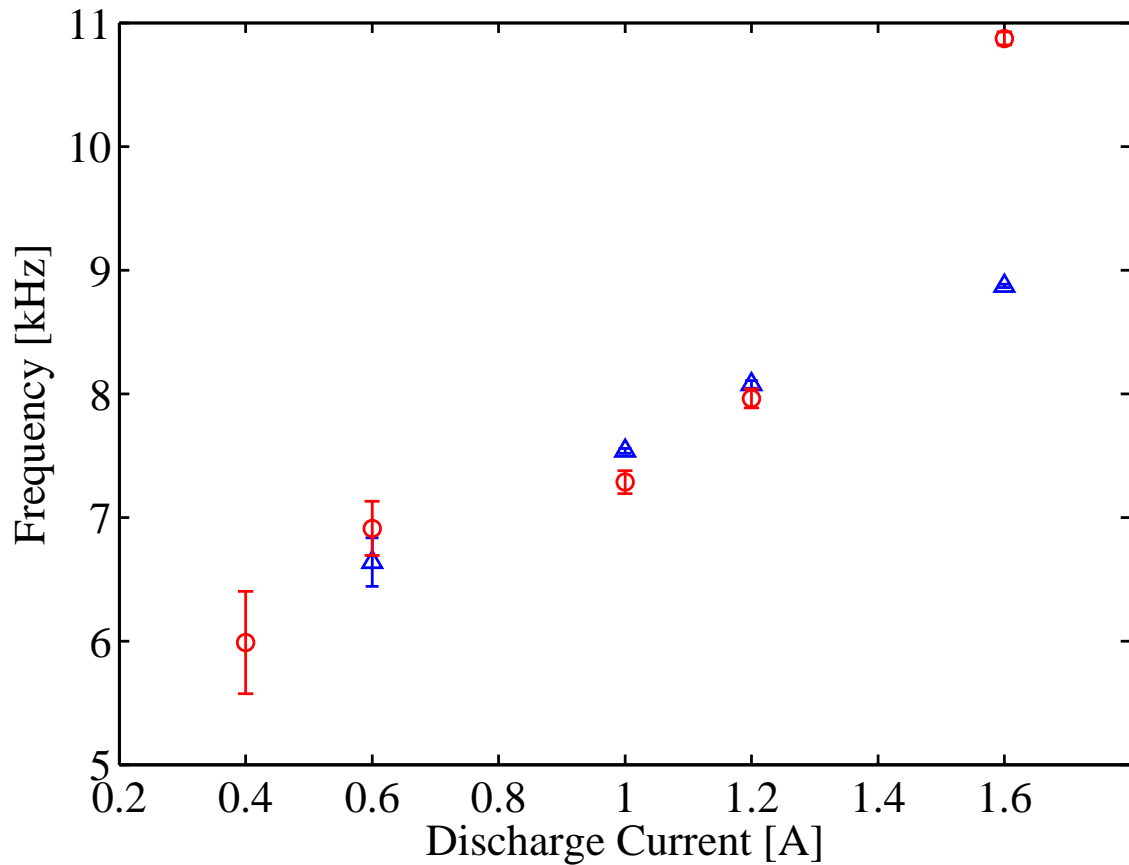
Figure 4.46: Breathing mode frequency dependence on the discharge current for the BHT-200 operating with xenon (circles) and krypton (triangles). The discharge potential and magnet current were held constant at 90 V and 1.0 A, respectively.
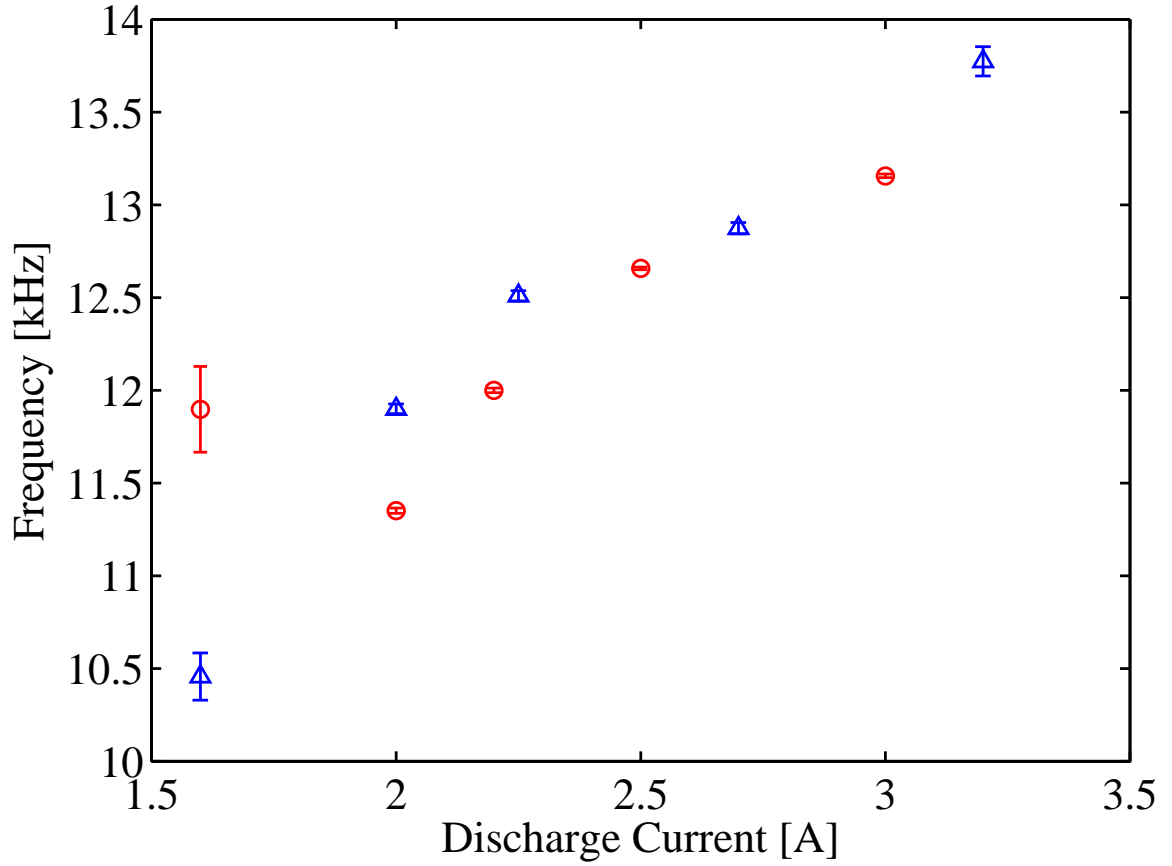
Figure 4.47: Breathing mode frequency dependence on the discharge current for the BHT-600 operating with xenon (circles) and krypton (triangles). The discharge potential and magnet current were held constant at 110 V and 1.75 A, respectively.

For the BHT-600, the breathing mode frequency dependence on the discharge current is shown in Figure 4.47. Like the BHT-200 data, at the low discharge potential, the frequency of the xenon breathing mode is nearly the same as the krypton frequency. For both thrusters, the similarities in the frequency dependence were the result of the increased mass flow rate to sustain the discharge. Similar to the xenon results, the frequency of the krypton breathing mode increased as the discharge current or mass flow was increased. Due to the increased neutral velocity, the results are in agreement with the predator/prey model and supports the description of the breathing mode where the neutral front is replenished by the increase in the mass flow rate.

Furthermore, the time-dependent current data is shown in Figure 4.48. At the low discharge current or mass flow rate, the oscillations of the breathing mode is hard to distinguish from signal noise. As the average discharge current is increased the amplitude of the oscillations increased in the current signal caused by the increase in mass flow to the ionization zone.

Magnet current to the thruster was also varied at a discharge potential of 90 V with a constant discharge current of 0.8 A for the BHT-200 with krypton. Figure 4.49 shows altering the magnet current or magnetic field does not significantly impact the breathing mode frequency. Comparable to the xenon case the frequency remained approximately constant with a net change of 6% in the range of 0.4 A to 1.0 A of magnet current. The lower krypton breathing mode frequency due to the longer ionization length was also observed throughout the magnet current test regime.
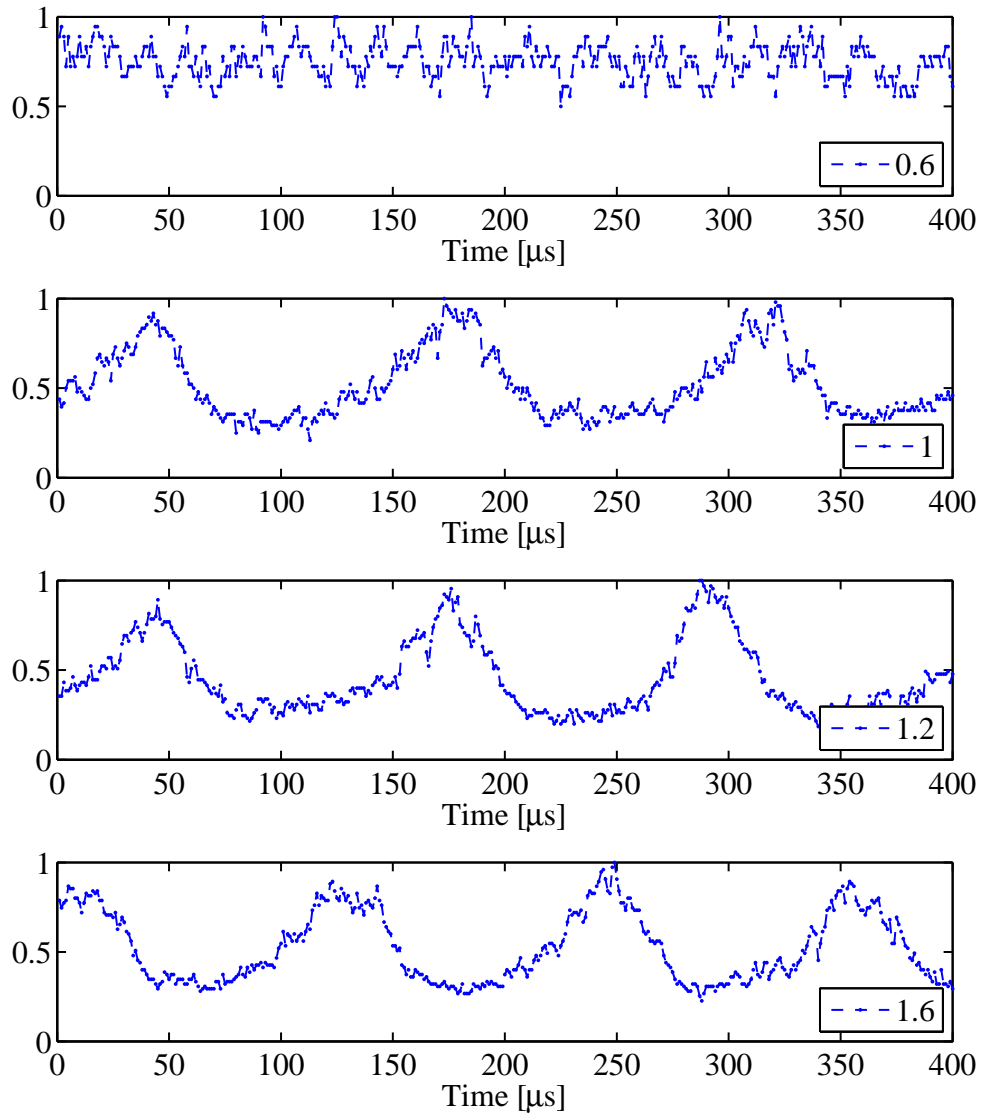
Figure 4.48:   Discharge current of BHT-200 with krypton operating at various average discharge currents (denoted in lower right corner). The discharge potential and magnet current were held constant at 90 V and 1.0 A, respectively.
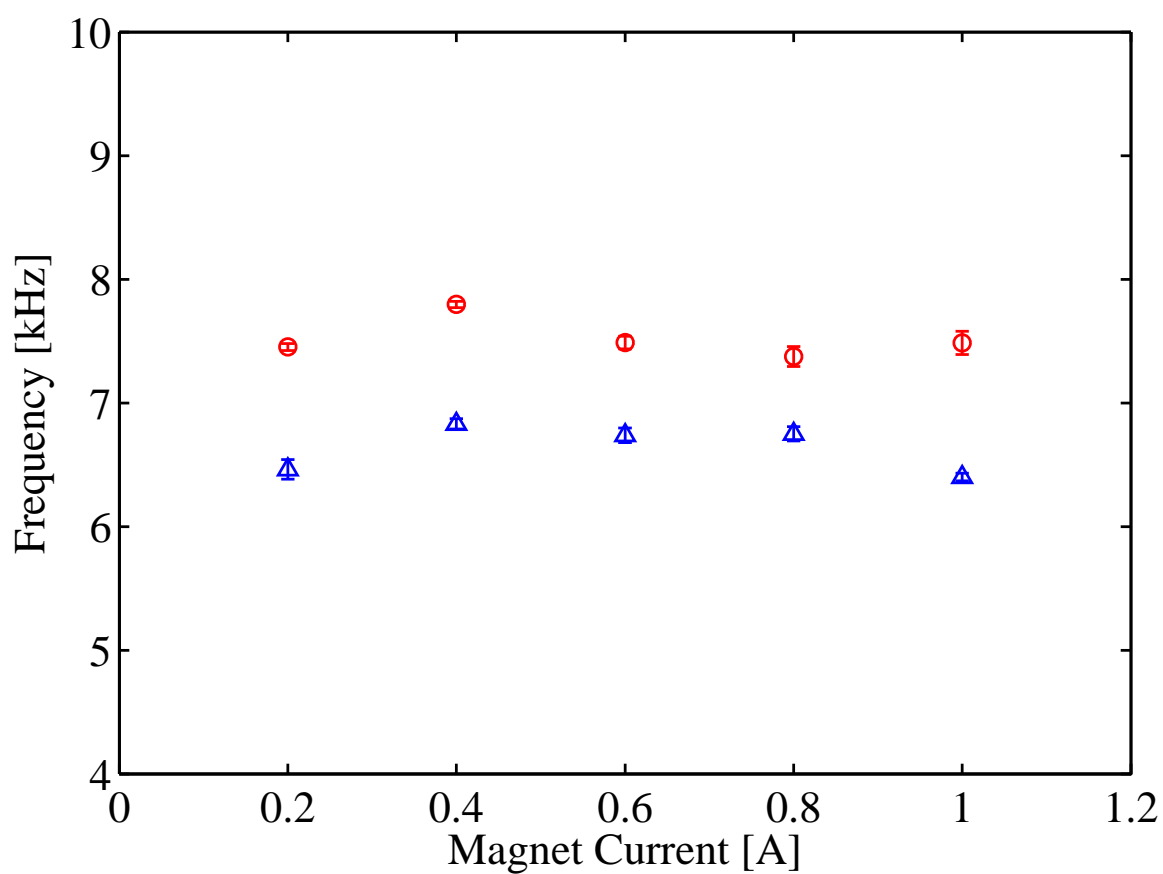
Figure 4.49: Breathing mode frequency dependence on the magnet current for the BHT-200 operating with xenon (circles) and krypton (triangles). The average discharge potential and discharge current were held constant at 90 V and 0.8 A, respectively.
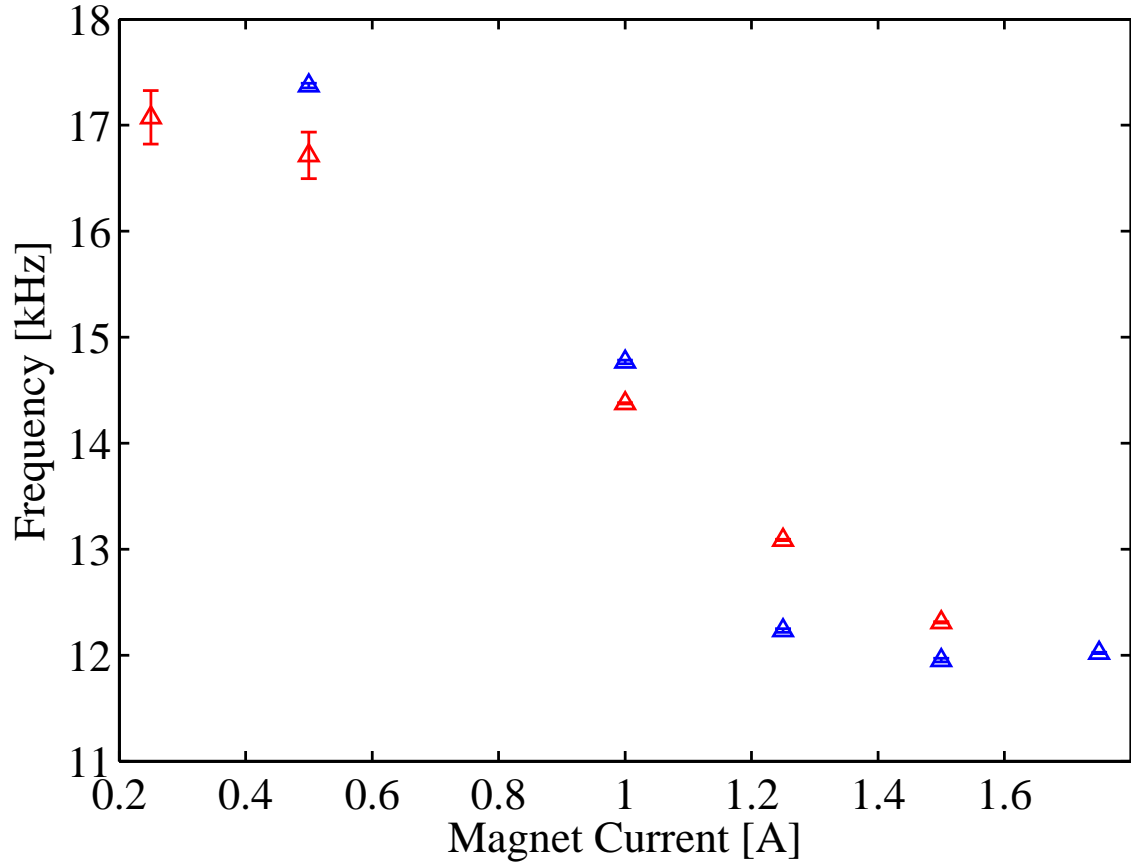
Figure 4.50:   Breathing mode frequency dependence on the magnet current for the BHT-600 operating on xenon (red) and krypton (blue) at various magnet currents with a constant discharge current of 2.0 A and discharge potential of 100 V.

However, the relationship of the magnet current and breathing mode frequency is very different for the BHT-600. In Figure 4.50, the krypton frequency shows an inverse relationship between the magnet current and the breathing mode as seen before in the xenon data. With trend for both propellants the same, it is clear the cause of the inverse relationship is the result of the different magnetic field topology. For the BHT-200, the constant breathing mode frequency for both xenon and krypton suggests the magnetic field topology did not change and had little influence in the ionization length. Conversely, the decreasing breathing mode frequency seen in the BHT-600 data for both feed gases suggest the ionization length increased with the changing magnetic field topology.

4.7 Influence of Cathode on Krypton Breathing Mode

In most studies, the frequency of the breathing mode was studied with the cathode at the self-heating mode since it is the standard operating method [28, 52, 58, 72]. This self-heating mode also provides a more efficient use of power since the cathode heating coil is not supplying the additional energy to the hollow cathode insert. However, in this section the cathode heater for the BHC-1500 was utilized to provide heating of the porous tungsten emitter and compared to the self-heating cathode results from section 4.1.

Comparison of the krypton breathing mode frequency is shown in Figure 4.51. An evaluation of the data illustrates the difference in breathing mode frequency. With the heater off, the frequency was 24 kHz; conversely, with the heater on the frequency was 31 kHz, a difference of 23%.

For the krypton case, the cause for such a variation in frequency was due to a higher number of electrons with sufficient energy to ionize the propellant. When the heater is turned on, more electrons with sufficient energy are produced at the cathode plasma. When these electron enter the ionization zone, they have a higher energy distribution which would increase the rate of ionization. The increase in the ionization rate would decrease the ionization length, resulting in the greater breathing mode frequency.

However, the frequency of the two cases does not provide any temporal insight into the breathing behavior. Figure 4.52 shows the average emission intensity of the images between the two conditions. When the cathode heater is activated, the peaks of the period tended to be narrow and well defined, while the results for the self heating mode showed more broad peaks with less definition. In other words, the thruster "breathed out" quickly when the heater was on where the higher energy electrons ionized the neutrals much more quickly and had to wait until enough neutrals replenished the ionization zone. The sudden exit of the ions is shown in the heater on data where the duration of low emission tends to be greater.
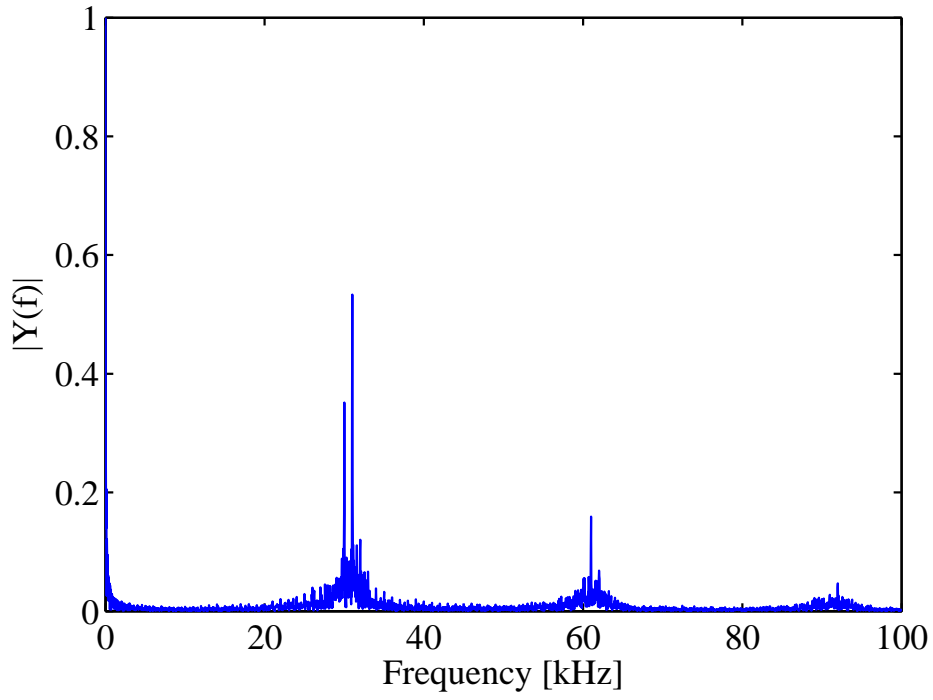
(a) Cathode heater ON
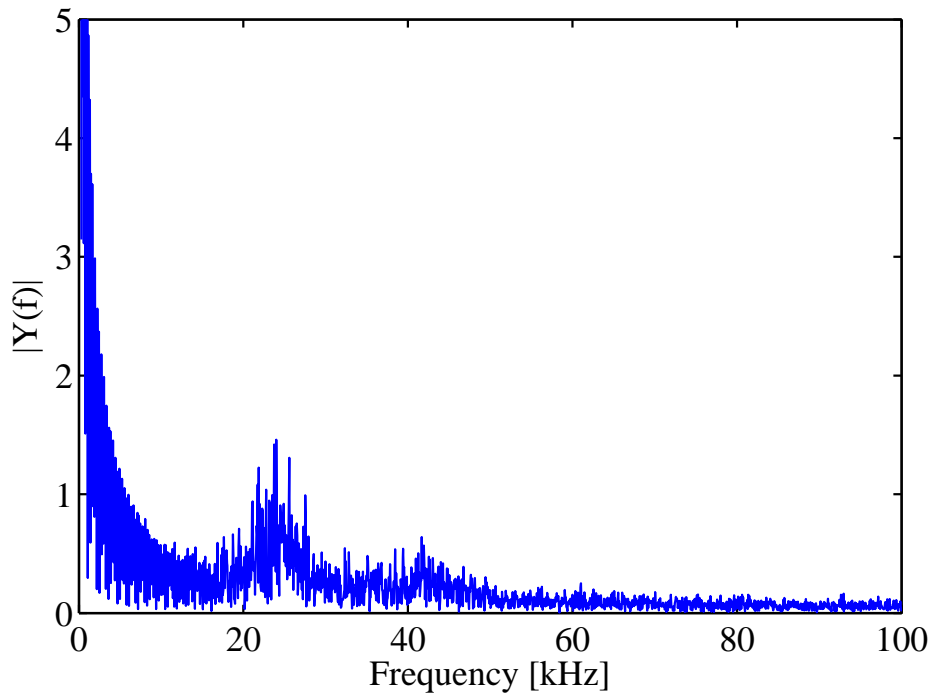
(b) Cathode heater OFF

Figure 4.51: Comparison of breathing mode frequency with the cathode heater ON (a) and the heater OFF (b). Thruster was operating at nominal conditions. $V_d = 250$ V, $I_d = 0.8$ A, $I_m = 1.0$ A, $\dot{m} = 0.94$ mg/s of krypton.
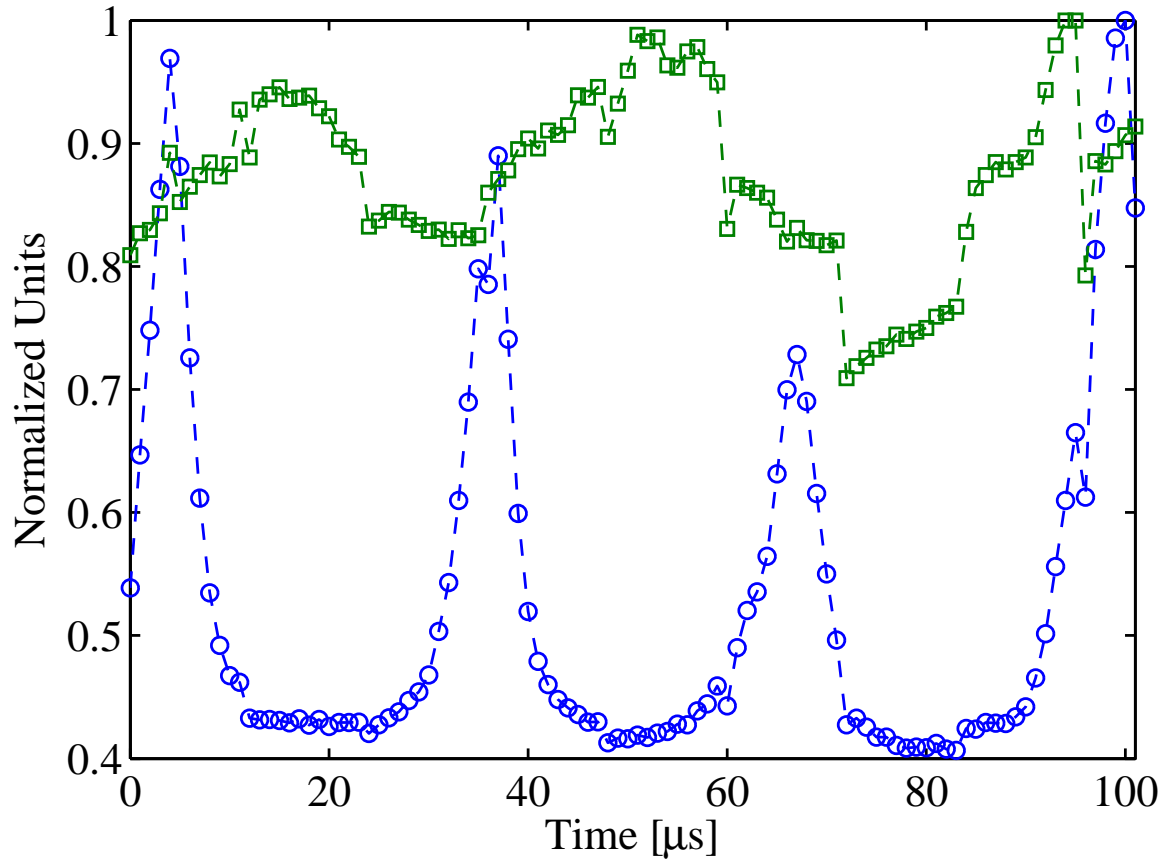
Figure 4.52: Emission intensity comparison for cathode heater ON (circles) and heater OFF (squares) with krypton. Thruster was operating at nominal conditions. $V_d = 250$ V, $I_d = 0.8$ A, $I_m = 1.0$ A, ṁ= 0.67 mg/s of krypton.

This example shows the effect of the cathode on the breathing mode. When operating at different thruster conditions, it is possible to use the cathode to either create the breathing mode oscillations or dampen them out. In the particular case where krypton is substituted for xenon, the data suggests not enough electrons with sufficient energy to ionize the discharge properly were present. By activating the cathode heater, operating the thruster with krypton similar to xenon operation is possible. Although other factors may contribute to the variations in frequency, such as the vacuum pressure, justifying such a large change at the same thruster operation is difficult [66].

4.8 Azimuthal Plasma Instabilities with Xenon

In addition to the breathing mode, the high-speed camera was capable of capturing other plasma structures, such as those traveling azimuthally. To observe these structures, the discharge potential of the thruster was significantly decreased from the nominal conditions. In this case, the discharge potential was set to 80 V for the BHT-200 while maintaining the same discharge current and magnet current. The azimuthal plasma structures become more dominant, as seen in Fig 4.53, as the discharge potential was allowed to decrease.

In these series of images, the plasma structure formed at the 5 o'clock position at $t = 1$ μs where the emission was low. In the next two frames, the plasma emission steadily increased and the plasma structure began to form a circular shape. As time progressed, the circular shape began to stretch into an oblong shape with a pointed end forming at the leading edge, traveling in the $E \times B$ direction while the rear of the structure was more blunt in shape similar to high-speed images collected by Ito and Cappelli [38]. The plasma structure continued to travel in the $E \times B$ direction, gaining in size and intensity until $t = 14$ μs when it began to decline. At $t = 24$ μs, the plasma structure, having lost most of its size and intensity, faded into the background approximately where it began.

During this operating condition, the presence of multiple plasma structures were possible within the thruster channel, as seen in Fig 4.54. In fact, most of the images of the plasma emission captured through the high-speed camera were of multiple plasma structures. In this series, two plasma structures were initially present where the larger structure on the left was nearly the same size and stationary for the first three frames. In contrast, the structure on the right moved in the counter-clockwise direction and increased in emission intensity and size until finally it was the only plasma structure within the images as seen in Fig. 4.53.

Other behaviors of the plasma structures were seen in Fig. 4.55, where the single structure in the plasma field separated into two distinct structures both rotating about

Figure 4.53: Sequential images (color enhanced) of the BHT-200 azimuthal plasma structures rotating about the center. Thruster is operated at off nominal conditions. $V_d = 80$ V, $I_d = 0.8$ A, $I_m = 1.0$ A, $\dot{m} = 0.94$ mg/s of xenon. The time between images is 1 μs with an exposure time of 750 ns. Arbitrary intensity.
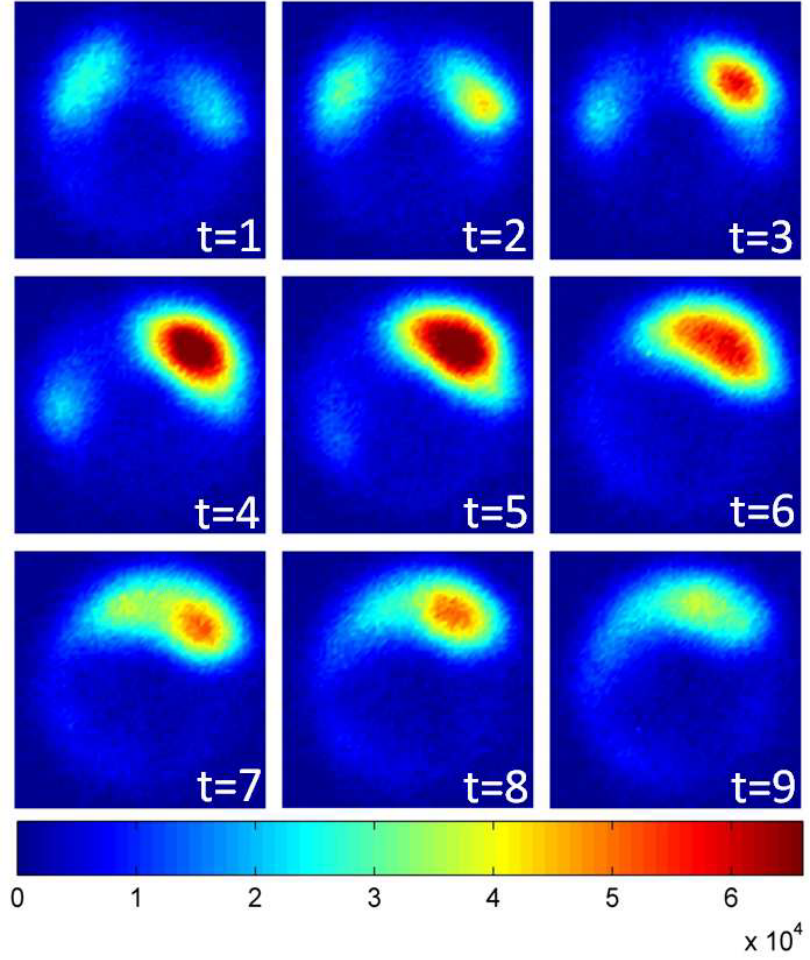
Figure 4.54:   Sequential images (color enhanced) of BHT-200 azimuthal plasma structures. The two plasma structures were rotating in the $E \times B$ direction about the center of the thruster where one plasma structure decreased in emission intensity while the other plasma structure simultaneously increased in intensity. Thruster was operating at off nominal conditions. $V_d = 80$ V, $I_d = 0.8$ A, $I_m = 1.0$ A, $\dot{m}= 0.94$ mg/s of xenon. The time between images was 1 μs with an exposure time of 750 ns. Arbitrary intensity.

the center. This phenomenon can go even further as evidenced by Fig. 4.56 where one initial plasma structure separated to form four structures.

Further investigation of the images also revealed smaller structures close to the outer walls and at the leading edge of the plasma structures. However, these smaller structures may be false since the images were created by integrating the direct emission throughout the plasma plume. Strictly speaking, the plane in which any particular small scale structures existed was difficult to determine. Other features observed in
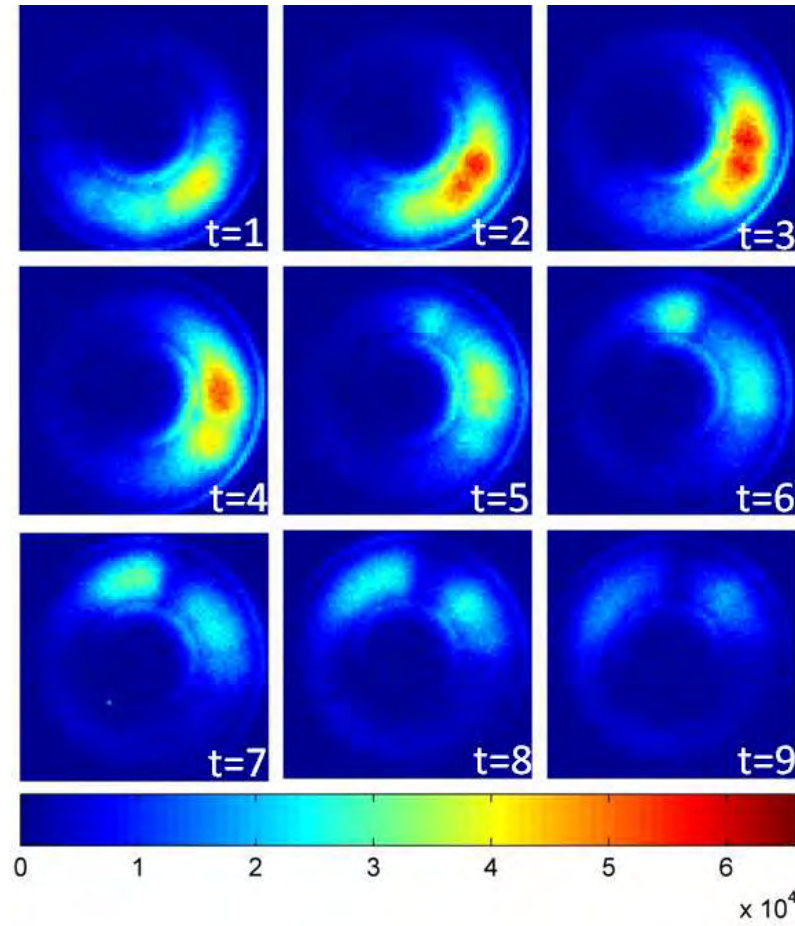
Figure 4.55: Sequential images (color enhanced) of BHT-200 azimuthal plasma structures. The initial singular plasma structure separated to form two distinct plasma structures. Thruster was operating at off nominal conditions. $V_d = 80$ V, $I_d = 0.8$ A, $I_m = 1.0$ A, $\dot{m} = 0.94$ mg/s of xenon. The time between images was 1 μs with an exposure time of 750 ns. Arbitrary intensity.
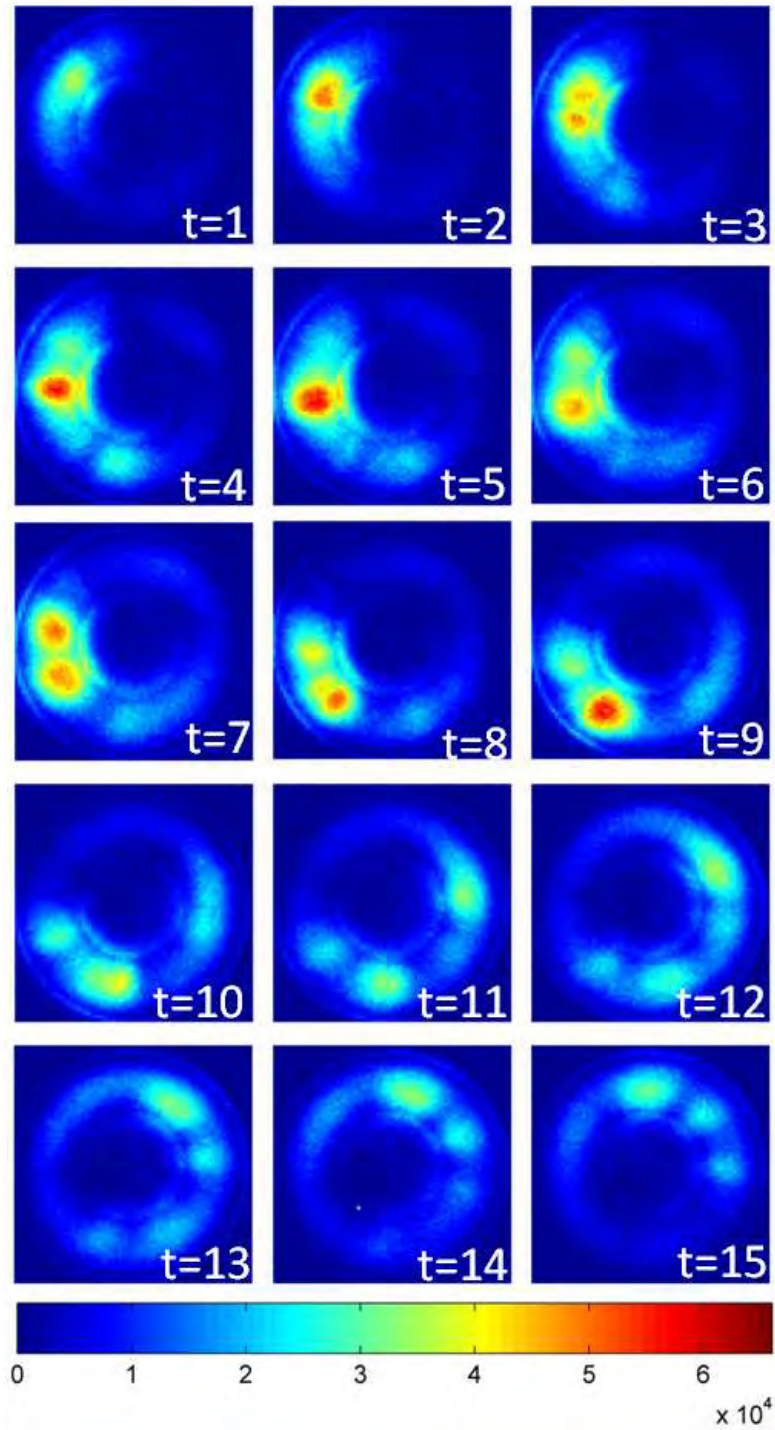
Figure 4.56:   Sequential images (color enhanced) of BHT-200 azimuthal plasma structures. The initial singular plasma structure separated to form four distinct plasma structures. $V_d = 80$ V, $I_d = 0.8$ A, $I_m = 1.0$ A, ṁ= 0.94 mg/s of xenon. The time between images was 1 μs with an exposure time of 750 ns. Arbitrary intensity.

the images include the emission of the boron nitride walls as the azimuthal plasma structures passed by.

For the BHT-600 the azimuthal modes were seen in a larger range of discharge potentials compared to the BHT-200. However, the duration of the structures are longer and are more coherent at the lower discharge potential. Figure 4.57 shows an example of the azimuthal plasma structures with the main discharge at a discharge potential of 110 V, discharge current of 2.0 A, and a magnet current of 1.75 A. In the high-speed images, details such as the emission of the ceramic wall are seen similar to the BHT-200. In addition, the images also show the outline of the anode region further inside the annulus channel which may be the result of the shallow depth of the BHT-600. The plasma jet, in the center of the image, was again observed with the BHT-600. Another interesting formation, not observed in the BHT-200 high-speed images are the *spokes* which radiate from the center plasma jet formation to the plasma ring. Furthermore, at the end of the spoke, usually a large plasma structure travels with the spoke in the $E \times B$ direction. The direction of the azimuthal plasma structures for both thrusters is identical to previous studies on the main discharge of similar devices [20, 40, 79]. However, other researchers have observed the instabilities travel in the negative $E \times B$ direction, suggesting the cause of their instability as density-gradient driven drift waves [72].

Since it was possible (and more likely) to have multiple azimuthal structures within the plasma field, it was difficult to determine the azimuthal velocity of each structure. Moreover, some of the plasma structures were only present in a few images before it dissipated and another structure formed. Therefore, the azimuthal velocity of the entire field was determined. Since the azimuthal plasma structures all traveled in the same $E \times B$ direction, an image at time, $t_{ref} + \Delta t$, was compared to the image at t_{ref}. Utilizing cross-correlation, the most likely azimuthal rate was determined for each pair of images and then converted to frequency. Of the 100 images captured for each data series, only about 30 of those images contained azimuthal plasma structures for the determination of azimuthal frequency for both the BHT-200 and BHT-600.
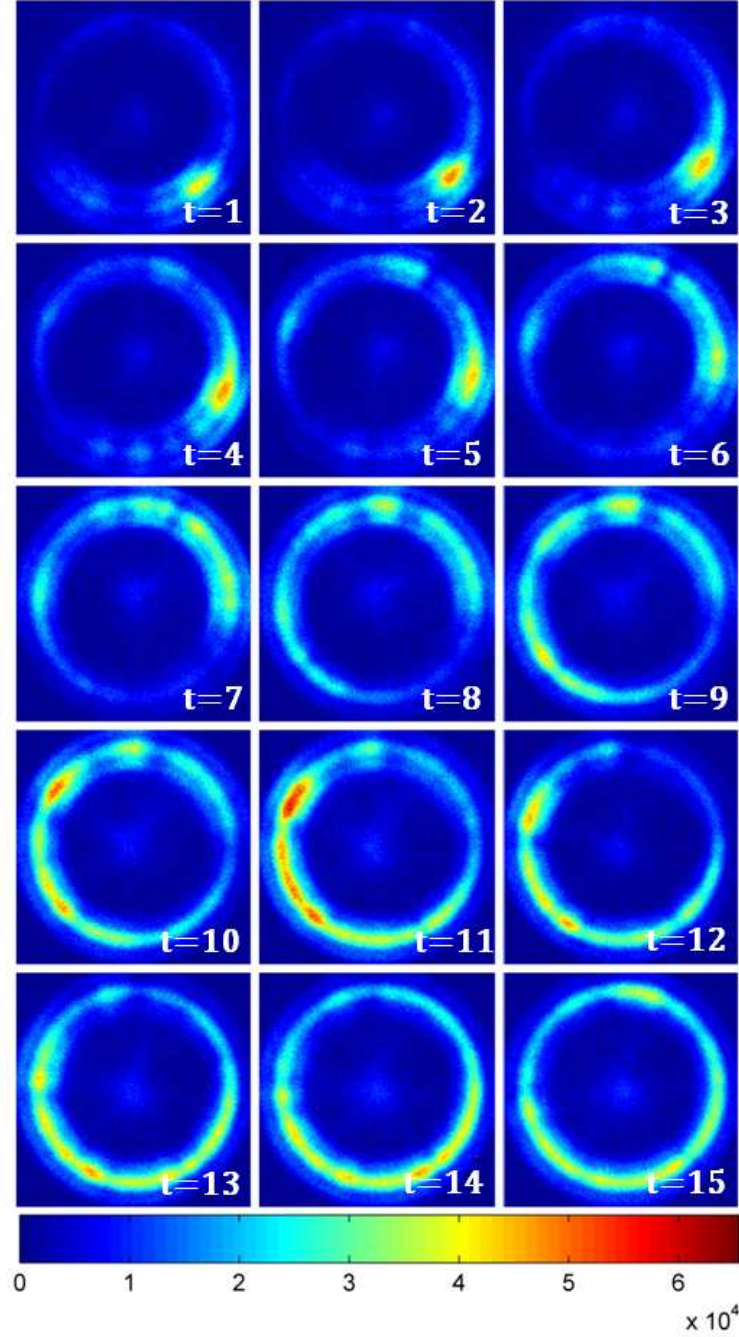
Figure 4.57: Sequential images (color enhanced) of BHT-600 azimuthal plasma structures rotating about the center. Thruster was operated at off nominal conditions. $V_d = 110$ V, $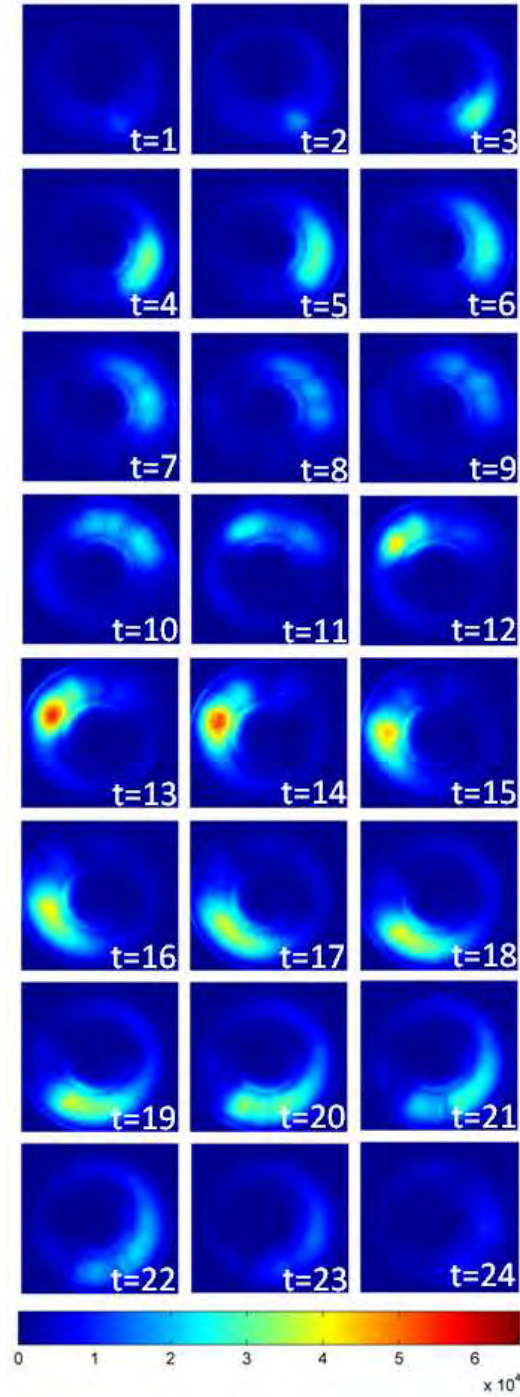I_d = 2.0$ A, $I_m = 1.75$ A, $\dot{m}= 2.33$ mg/s of xenon.. The time between images is 1 μs with an exposure time of 750 ns. Arbitrary intensity.

Additional measurements of the plasma field were taken at the lower discharge potential to determine the influence of varying thruster settings such as discharge current, discharge potential, and magnet current on the azimuthal plasma structures. A list of the different operating conditions can be seen in Table 3.3 and 3.5 and discussed in subsequent sections.

Figure 4.58, the azimuthal velocity and frequency of the BHT-200, shows the influence of the discharge potential on the azimuthal plasma structures when the discharge current and magnet current was held constant at 0.8 A and 1.0 A, respectively. At discharge potentials in the range of 80 V to 150 V, where the high-speed camera was able to detect the instabilities, the velocity of the structures increased as the discharge potential was increased.

In addition, the frequency and velocity of the azimuthal plasma structures were also calculated with a constant mass flow rate and compared to the constant discharge current case given in Figure 4.59. The constant mass flow rate has a slightly lower velocity and frequency at comparable discharge potentials, However, the trend of the two cases are very similar. A maximum difference of 20% between the constant mass flow rate case and constant discharge current case occurred.

In the case of the BHT-600, the velocity and frequency of the azimuthal plasma structures were also determined as a function of discharge potential. Figure 4.60 shows, the azimuthal plasma structures observed in the BHT-600 also increased with increasing discharge potential.

This trend of increasing frequency with increasing power is also in agreement with observations made by Esipchuk *et al.* As the electric field increases, due to the increase in discharge potential, the electron drift velocity will also increase which may cause the increase in the azimuthal plasma structures [19].

At the low discharge potential, the discharge current still provided insight to the plasma, as it did in the breathing mode oscillations. Comparing the average emission intensity of the azimuthal plasma structure seen in Figure 4.53 to the discharge cur-
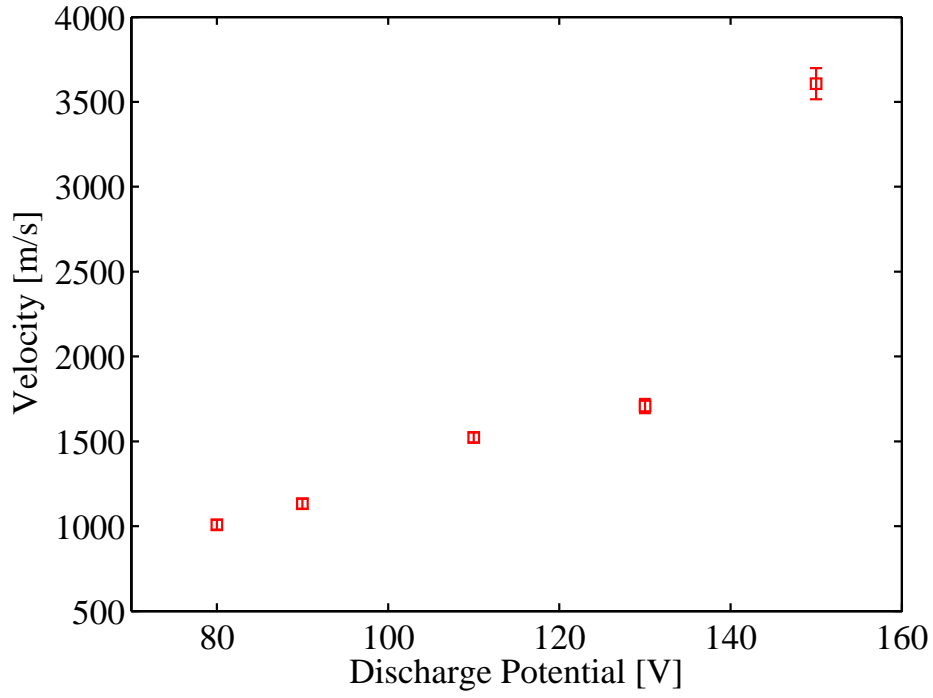
(a) Velocity of azimuthal plasma structures
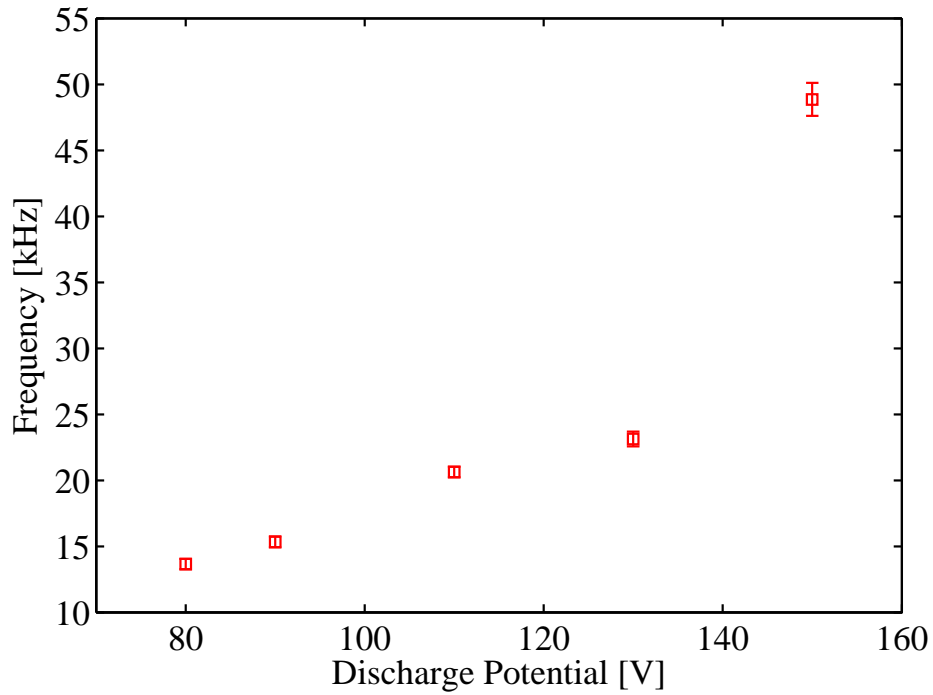
(b) Frequency of azimuthal plasma structures

Figure 4.58:   Azimuthal plasma structure velocity (a) and frequency (b) dependence on discharge potential for the BHT-200 operating with xenon. The average discharge current and magnet current were held constant at 0.8 A and 1.0 A, respectively

(a) Velocity of azimuthal plasma structures

(b) Frequency of azimuthal plasma structures

Figure 4.59: Azimuthal plasma structure velocity (a) and frequency (b) dependence on discharge potential for the BHT-200 operating with xenon. Comparison between the constant average discharge current case of 0.8 A (circles) and the constant mass flow rate case of 0.95 mg/s of xenon (squares). The magnet current for both cases was set for 1.0 A.

(a) Velocity of azimuthal plasma structures

(b) Frequency of azimuthal plasma structures

Figure 4.60:   Azimuthal plasma structure velocity (a) and frequency (b) dependence on discharge potential for the BHT-600 operating with xenon. The average discharge current and magnet current were held constant at 2.0 A and 1.75 A, respectively
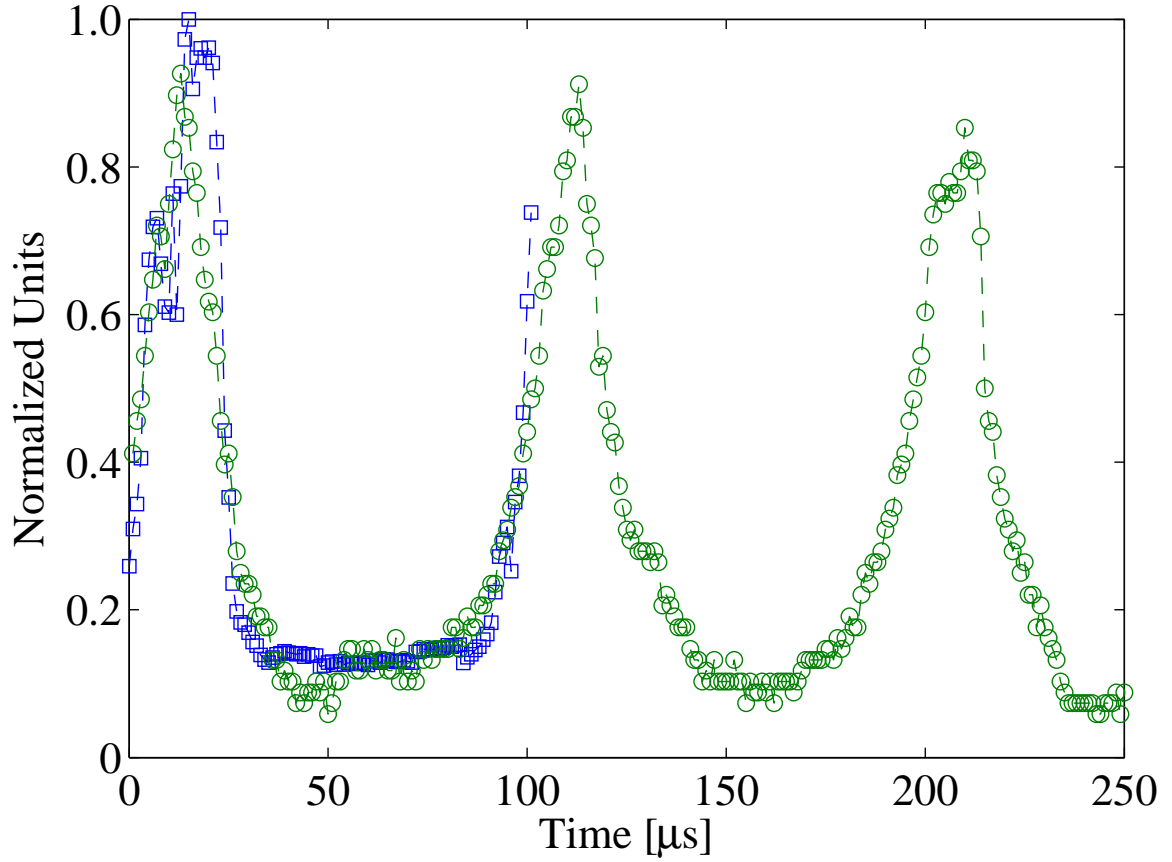
Figure 4.61: Discharge current (circles) recorded simultaneously with average direct emission intensity (square). The direct emission intensity corresponds to the periodic discharge current. Thruster was operated at off nominal conditions. $V_d = 80$ V, $I_d = 0.8$ A, $I_m = 1.0$ A, $\dot{m} = 0.94$ mg/s of xenon.

rent, both shown in Figure 4.61, two observations of the plasma emission were made. First, correlating the time of each image frame of Figure 4.53 to the corresponding time of the discharge current, the emission of the azimuthal plasma structures were only detectable when the discharge current was above 30% of the maximum value. This relationship between the emission and discharge current was also observed in the breathing mode oscillations of the previous sections.

Second, with the discharge potential set at 80 V, the discharge current and emission intensity exhibited the same pattern of periodic oscillations similar to the discharge current at 250 V which was attributed to the breathing mode. These observations suggest the azimuthal plasma structures are small regions of ionization with

mechanisms similar to those found in the predator/prey model. The rotation of the azimuthal plasma structures are the result of the neutral gas being ionized and then rapidly accelerated in the axial direction from the channel at velocities on the order of 10^4 m/s. Once the ions were depleted, the ionization shifts azimuthally to the next region of neutral gas and repeats the process [19]. Additionally, the presence of these localized structures may also suggest a coupling of the breathing mode and the azimuthal oscillations at the lower discharge potentials [72].

Moreover, as the discharge potential of the thruster was increased, the structures expanded azimuthally, reforming the ring shape seen in the breathing mode images. This observation further indicates the azimuthal plasma structures are an ionization zone within the discharge first observed by Esipchuk *et al.* Figure 4.62 shows the high-speed images of the BHT-200 plasma emission at different discharge potentials illustrating the formation of the ring shape from the azimuthal plasma structures. In addition, Figure 4.63 show the evolution of the BHT-600 from the smaller azimuthal plasma structures to the ring described by Esipchuk *et al* [19]

The effect of the discharge current or mass flow rate on the azimuthal frequencies were also studied and displayed in Figure 4.64. For the low discharge current, the main discharge of the thruster was relatively small and the emission of the plasma was also relatively weak. The data incurred in this low discharge current mode did not provide significant plasma structures in the high-speed images which may have led to the high level of standard error for those data points. However, when the discharge current was set to 0.8 A, the intensity of the emission increased significantly.

For the BHT-600, the effect of the discharge current or mass flow rate on the azimuthal plasma structures were also investigated. The velocity or frequency of the plasma structures at the low discharge current condition were difficult to capture in the high-speed images similar to the the BHT-200 results. At such low mass flow rates, the images revealed very weak plasma structures with only a few μs of duration equating to high errors at 1.6 A in Figure 4.65. However, like the BHT-200,

Figure 4.62: Sequential images (color enhanced) of the xenon azimuthal plasma structures at various discharge potentials (left) for the BHT-200 operating with xenon. The discharge current and magnet current was held constant at 0.8 A and 1.0 A, respectively. The time between images is 1 μs with an exposure time of 750 ns. Arbitrary intensity.

143
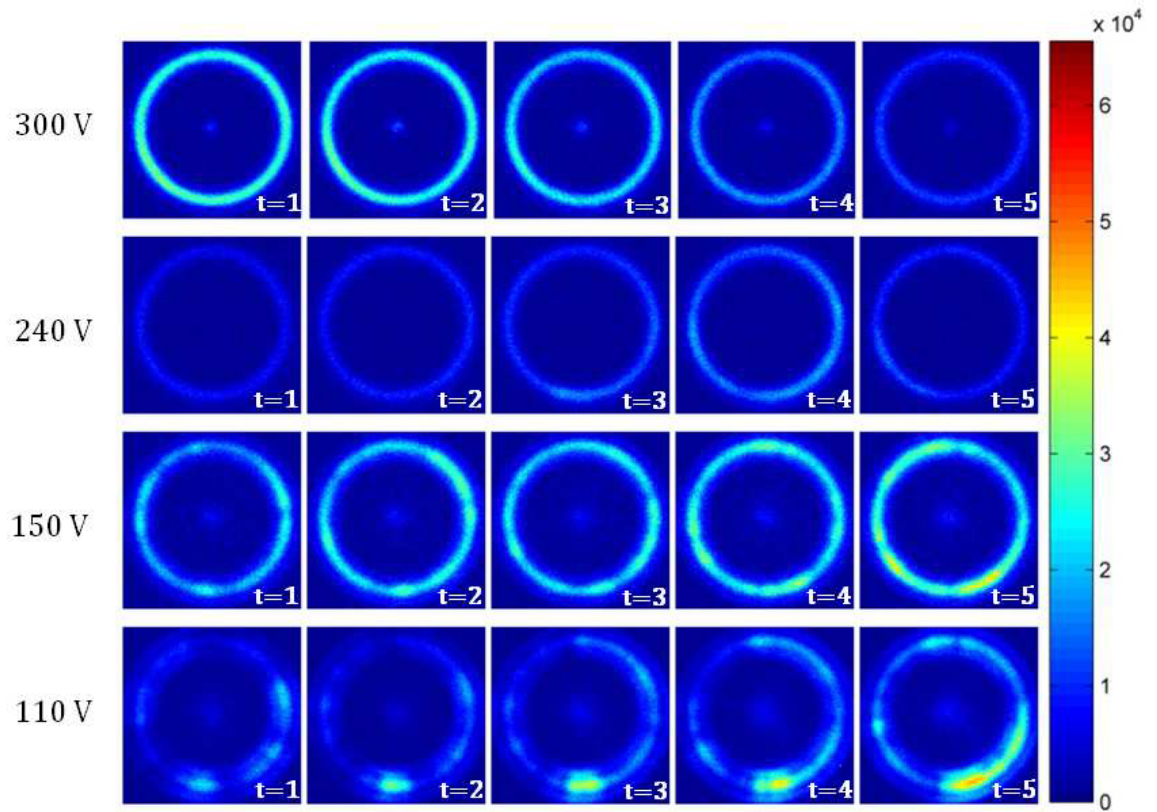
Figure 4.63:   Sequential images (color enhanced) of the xenon azimuthal plasma structures at various discharge potentials (left) for the BHT-600 operating with xenon. The discharge current and magnet current was held constant at 2.0 A and 1.75 A, respectively. The time between images is 1 μs with an exposure time of 750 ns. Arbitrary intensity.
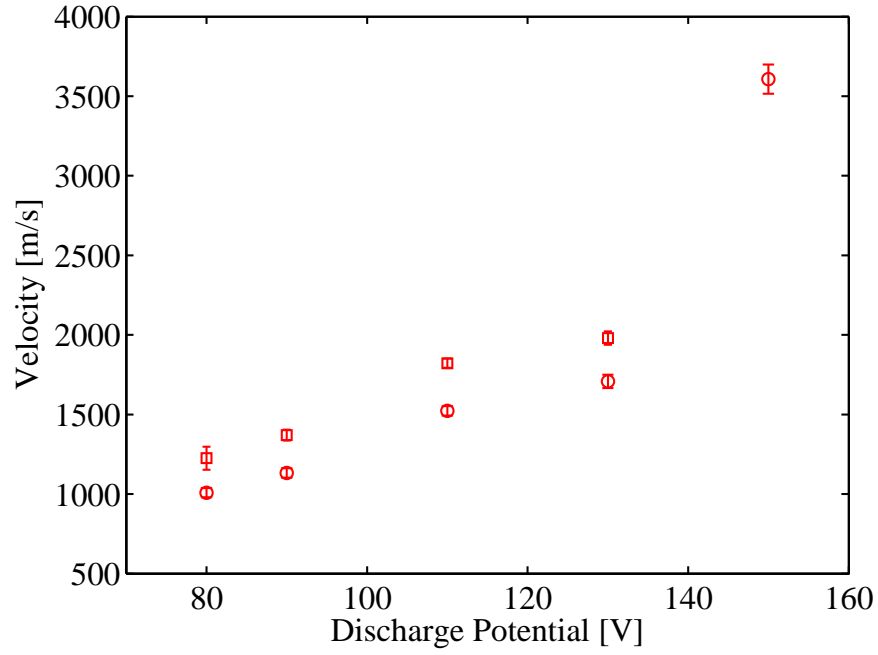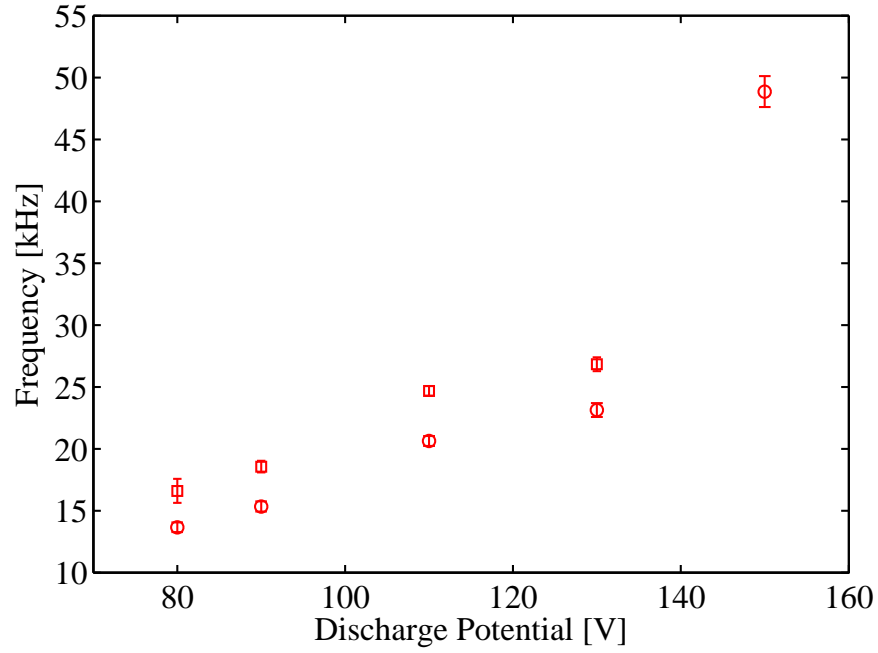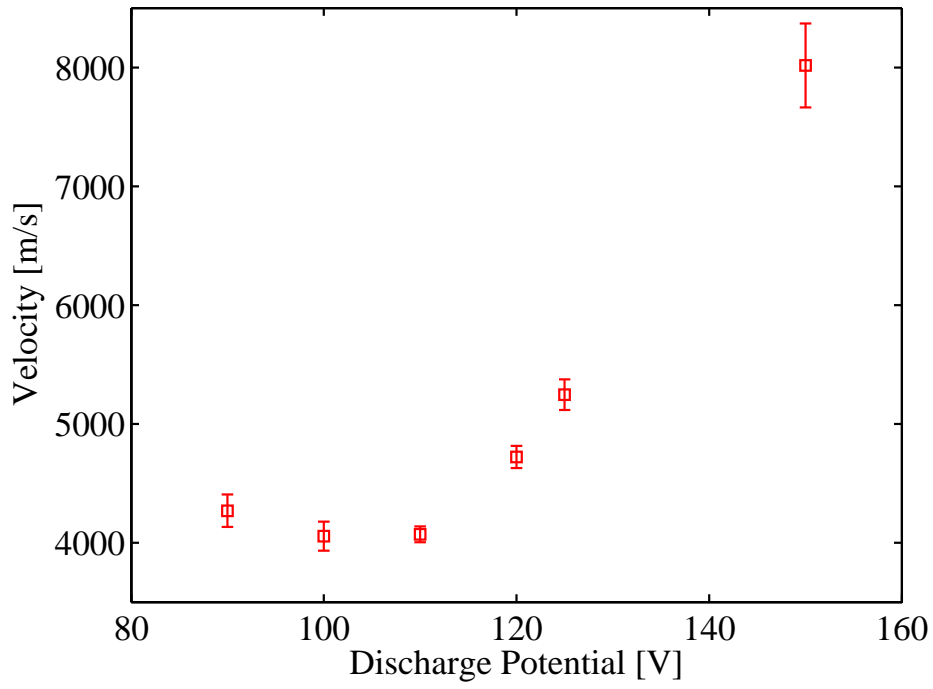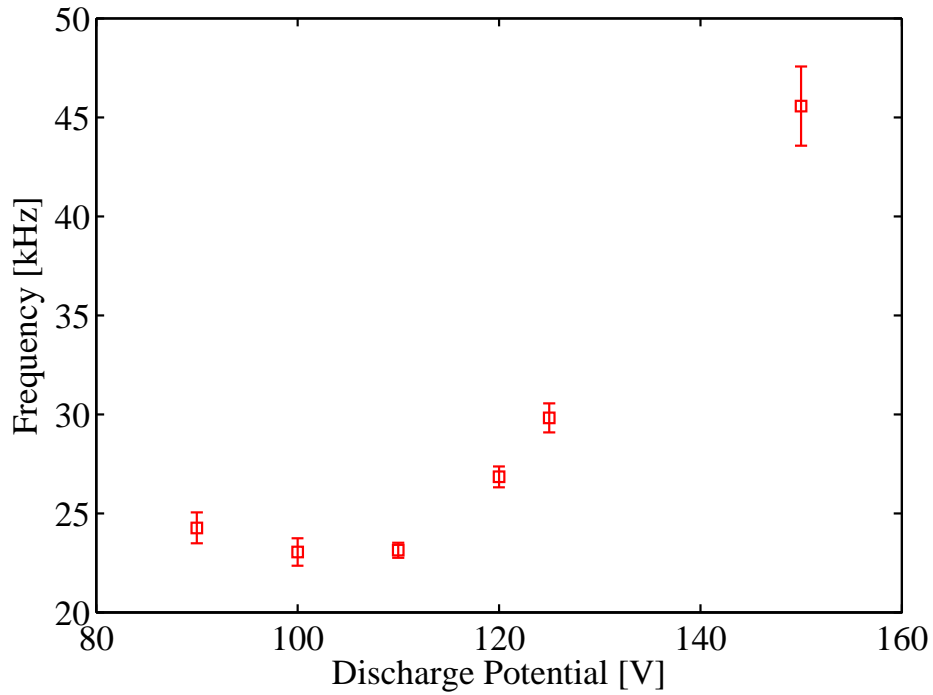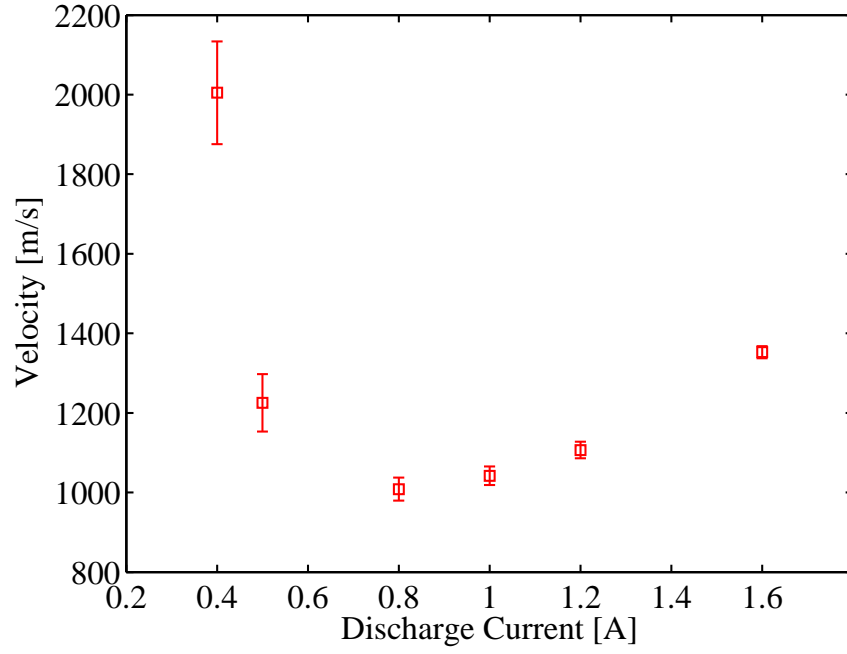
(a) Velocity of azimuthal plasma structures
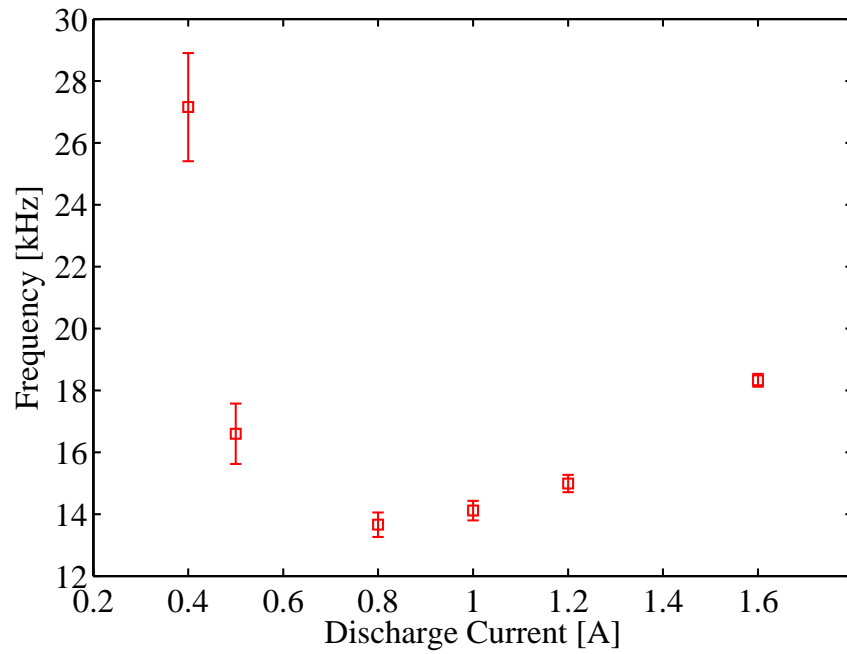
(b) Frequency of azimuthal plasma structures

Figure 4.64:   Azimuthal plasma structure velocity (a) and frequency (b) dependence on discharge current for the BHT-200 operating with xenon. The average discharge potential and magnet current were held constant at 80 V and 1.0 A, respectively

the increase in the discharge current or mass flow rate also increased the velocity of the azimuthal plasma structures. Thus at the lower discharge current or mass flow rates, the thruster did not have enough mass in the ionization region to provide enough emission for observation and the data at the low discharge current and should have minor consideration.

Dependence on the magnetic field was also examined for both thrusters. Figure 4.66 illustrates the variation in velocity and frequency of the azimuthal plasma structures as a function of the magnet current for the BHT-200 with xenon. At two different discharge potentials, 80 V and 90 V, the velocity of the azimuthal plasma structures varied as much as 50% throughout the test regime. Additionally, the trends of the velocity or frequency are nearly identical at a local minima in the range of 0.4 A and 0.6 A of the magnet current.

For the BHT-600, the influence of the magnet current on the azimuthal plasma structures is shown in Figure 4.67. The results for the BHT-600 are significantly different than those seen in the BHT-200 data. To confirm the BHT-600 result, another set of data was also taken at a higher discharge potential. From both tests, the effect of the magnet current on the velocity of the azimuthal plasma structure was inversely proportional.

The difference of results on the azimuthal plasma structures is directly related to the difference in the magnetic fields between the two thrusters [7]. For the BHT-200, the magnetic field is concentrated closer towards the nose cone. This result supports the conclusion the higher magnetic field gradient in the radial direction produces the observed behavior in the BHT-200 thruster.

Furthermore, velocity and the frequency of the azimuthal plasma structures decreased due to the increase in the magnet current. The cause of the velocity decrease is attributed to the plane location in which the azimuthal plasma structures reside. At the lower discharge potential, 100 V, the high-speed images of the BHT-600 show the the shadow of the anode highlighted by the emission of the azimuthal plasma
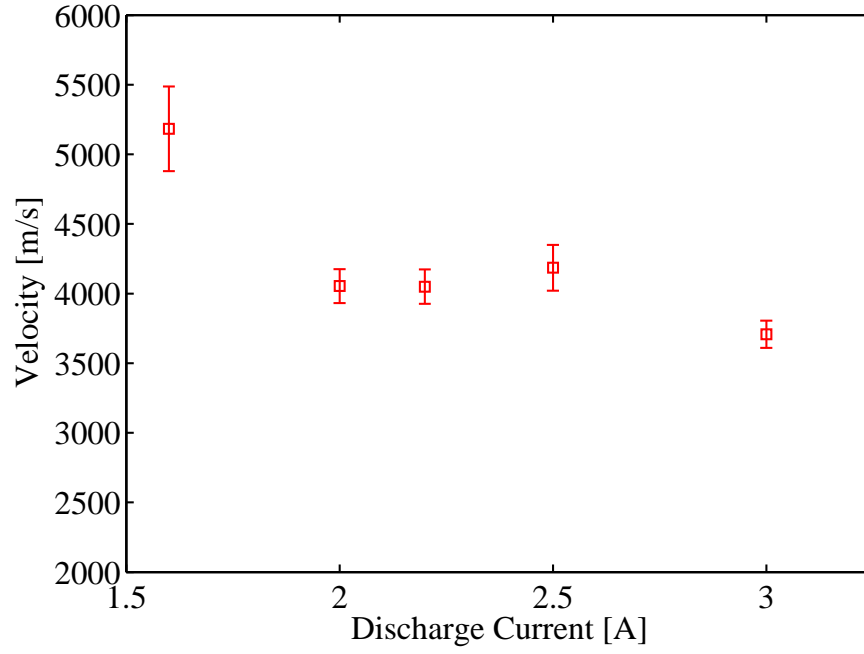
146

(a) Velocity of azimuthal plasma structures
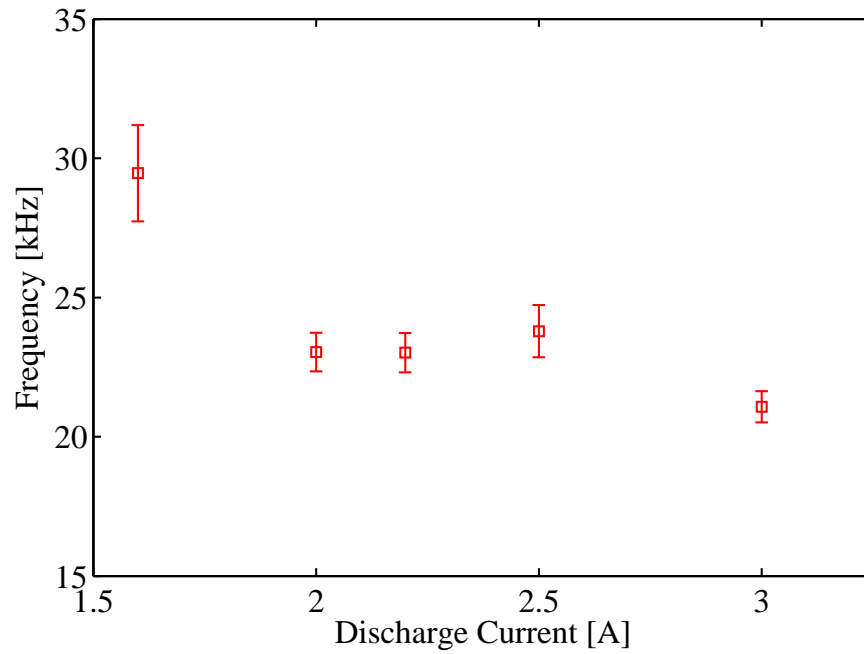
(b) Frequency of azimuthal plasma structures

Figure 4.65:   Azimuthal plasma structure velocity (a) and frequency (b) dependence on discharge current for the BHT-600 operating with xenon. The average discharge potential and magnet current were held constant at 100 V and 1.75 A, respectively

147

(a) Velocity of azimuthal plasma structures

(b) Frequency of azimuthal plasma structures

Figure 4.66: Azimuthal plasma structure velocity (a) and frequency (b) dependence on magnet current for the BHT-200 operating with xenon. The average discharge potential was held constant at 80 V (squares) and 90 V (circles) while the discharge current was held constant at 1.0 A.

(a) Velocity of azimuthal plasma structures

(b) Frequency of azimuthal plasma structures

Figure 4.67: Azimuthal plasma structure velocity (a) and frequency (b) dependence on magnet current for the BHT-600 operating with xenon. The average discharge potential and discharge current were held constant at 100 V (squares) or 90 V (circles) and 1.0 A, respectively

149

structures in Figure 4.68. However, as the magnet current is decreased, the features of the anode begin to fade and are less visible in the images. Thus, the azimuthal plasma structures are moving away from the anode region and towards the exit plane as the magnet current is decreased. The resultant higher azimuthal velocity as the magnet current is decreased is due to the increased electric field at the exit plane of the thruster. The result also corresponds to the focusing effect where the main discharge is focused by the magnetic field which forces the ionization zone towards the anode.
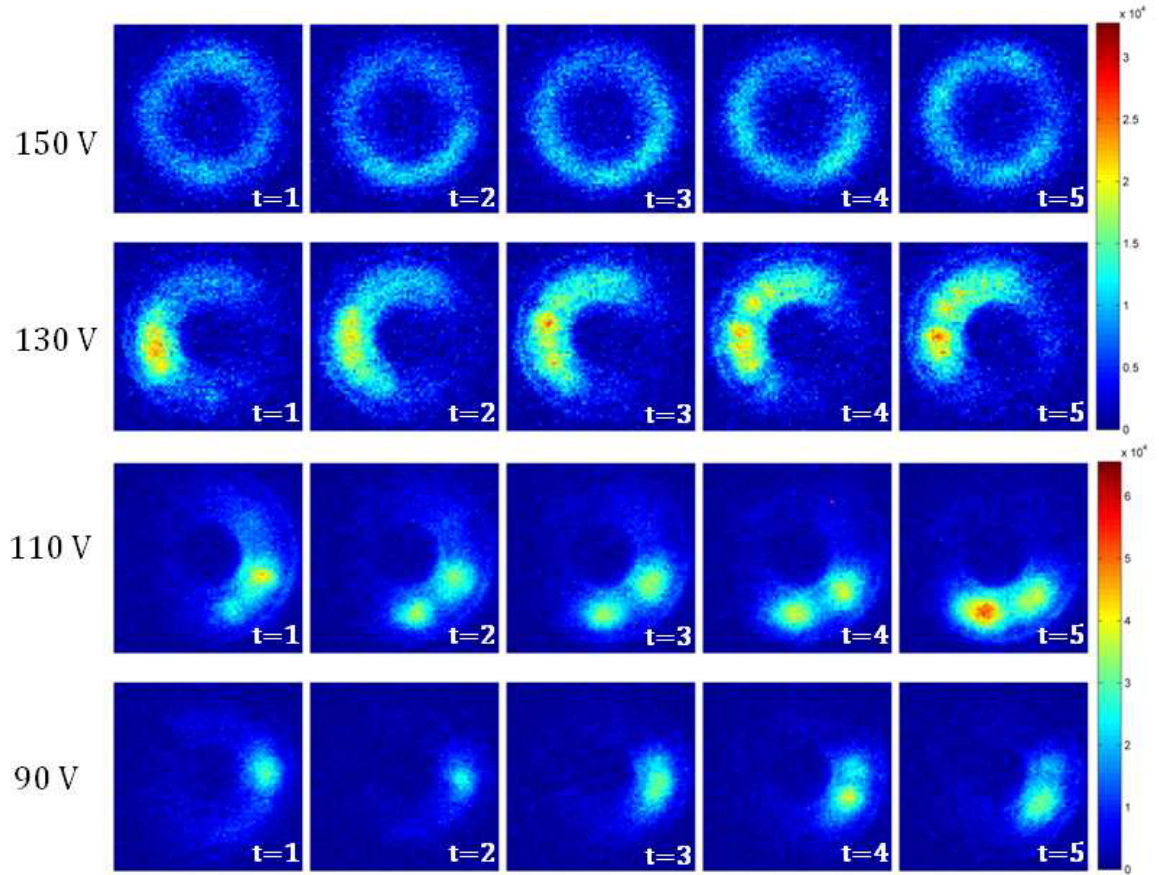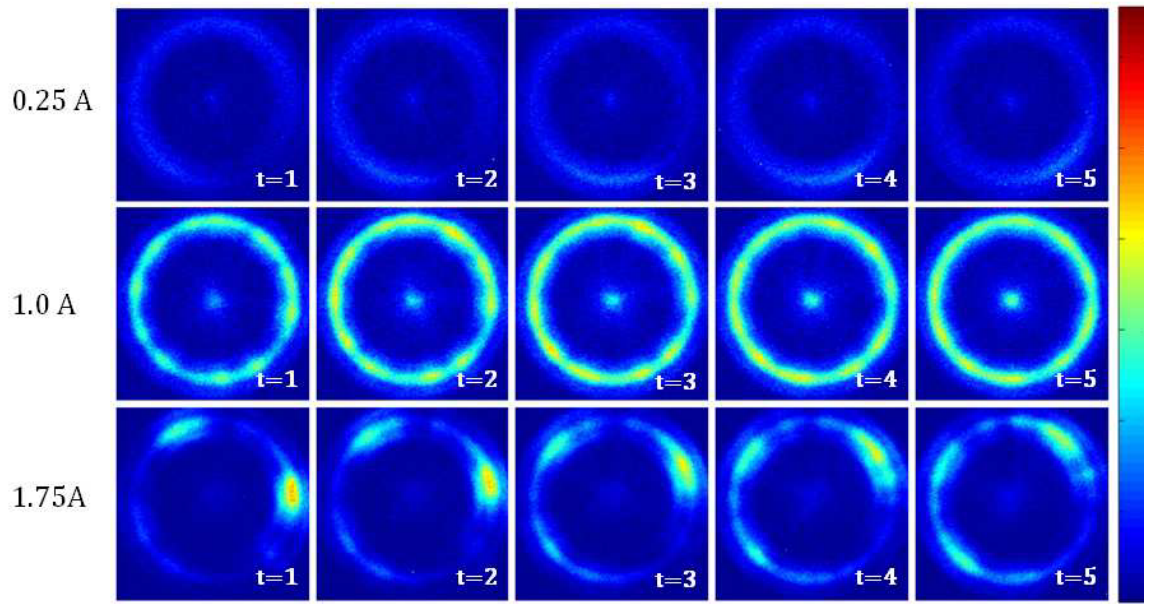
Figure 4.68: Sequential images (color enhanced) of the xenon azimuthal plasma structures at various magnet current (left) for the BHT-600. The discharge potential and discharge current was held constant at 100 V and 2.0 A, respectively. The time between images is 1 μs with an exposure time of 750 ns. Arbitrary intensity.

4.9 Azimuthal Plasma Instabilities with Krypton

The azimuthal plasma instabilities were also observed with krypton. At the low discharge potential for the BHT-200 with krypton, Figure 4.69 captures the azimuthal plasma structures rotating about the center of the thruster. As with xenon, the direction of the azimuthal plasma structure was also in the $E \times B$ direction. The high-speed images also show the emission of the ceramic insulation walls of the thruster near the azimuthal plasma structures. In the images, the main discharge of thruster also included multiple azimuthal plasma structures similar to the xenon discharge. Furthermore, the plasma structures were also observed to separate into smaller structures such as those seen at $t = 14$ to $t = 15$.

The azimuthal plasma structures were also observed in the krypton main discharge of the BHT-600. Similar to previous images, multiple azimuthal plasma structures are rotating within the main discharge in the $E \times B$ direction. A notable difference between the xenon and krypton images at the same discharge potential, discharge current, and magnet current is the lower emission intensity and the lack of a visible jet in the center of the image. This result was due to the higher ionization potential of krypton. At the lower discharge potential, not enough electrons with sufficient energy were present to either excite the neutrals or ions to provide sufficient photo emission.

The krypton azimuthal plasma structures were also observed with different thruster operating conditions similar to xenon. At various discharge potentials the azimuthal plasma structure velocity or frequency increased with increasing discharge potential as shown in Figure 4.71. For krypton, the rate of increase in velocity or frequency was greater than xenon at the same power level supporting a relationship to material properties such as atomic weight. The lighter krypton was accelerated faster than the heavier xenon by the ionization wave.

The effect of discharge potential was also observed in Figure 4.72 where the velocity of the krypton azimuthal plasma structures was greater than comparable
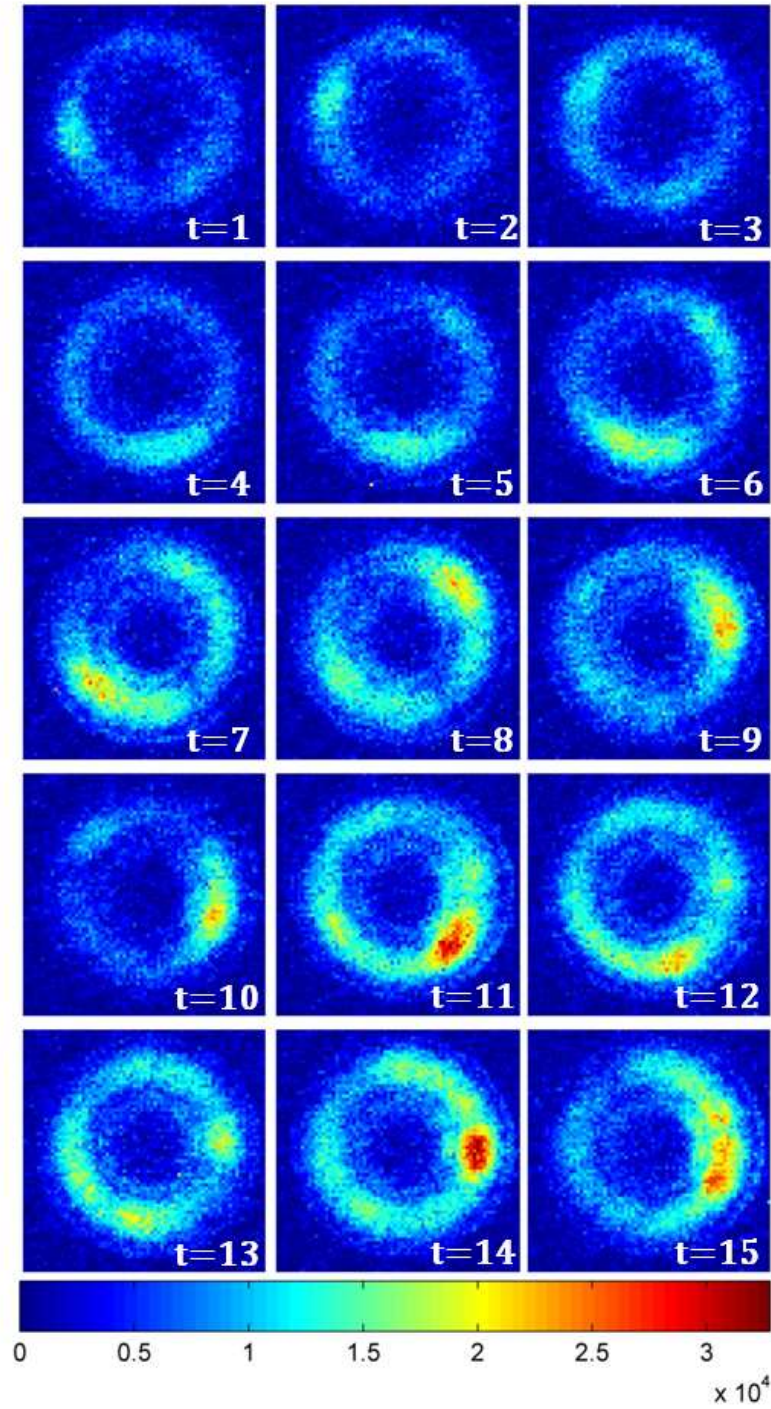
Figure 4.69: Sequential images (color enhanced) of the azimuthal plasma structures for the BHT-200 operating with krypton . The discharge potential, discharge current, magnet current and mass flow rate was held steady at 90 V, 0.8 A, 1.0 A, ṁ= 0.1.26 mg/s of krypton, respectively. The time between images is 1 μs with an exposure time of 750 ns. Arbitrary intensity.
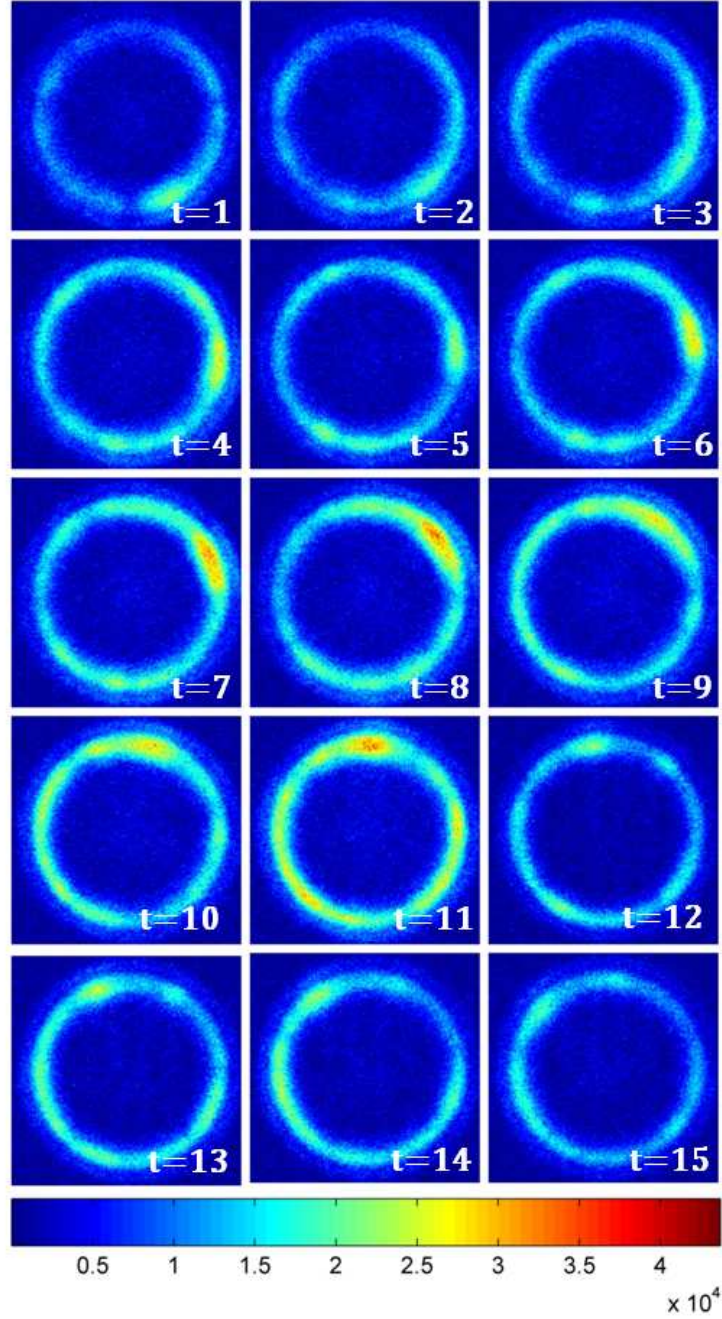
Figure 4.70:   Sequential images (color enhanced) of BHT-600 azimuthal plasma structures rotating about the center. Thruster is operated at off nominal conditions. $V_d = 110$ V, $I_d = 2.0$ A, $I_m = 1.75$ A, m= 2.32 mg/s of krypton. The time between images is 1 μs with an exposure time of 750 ns. Arbitrary intensity.
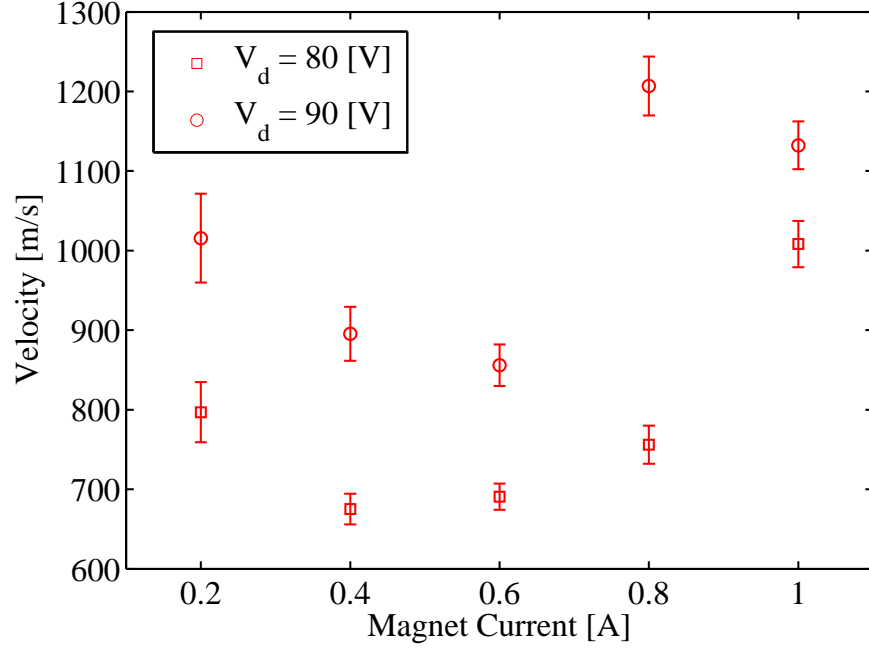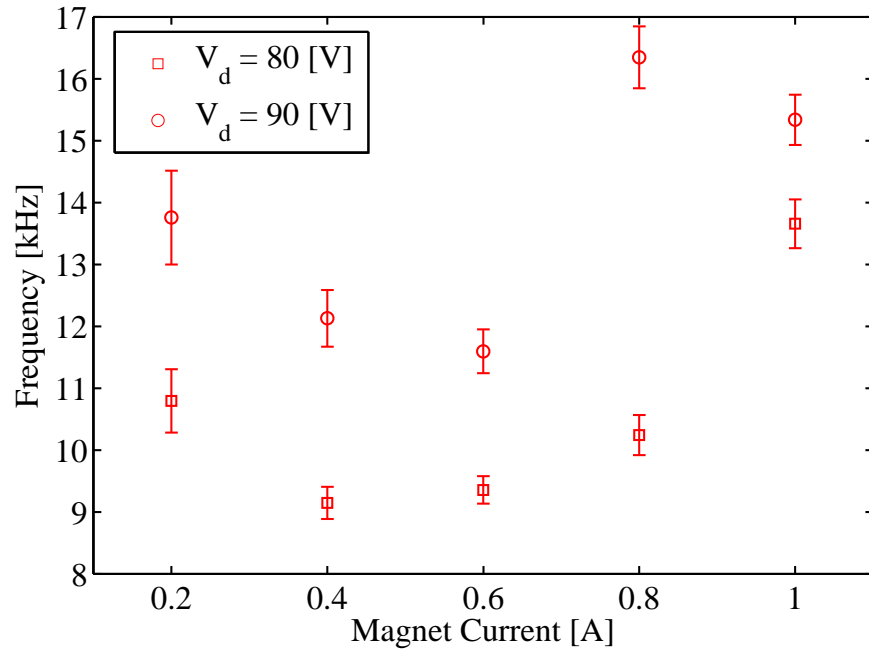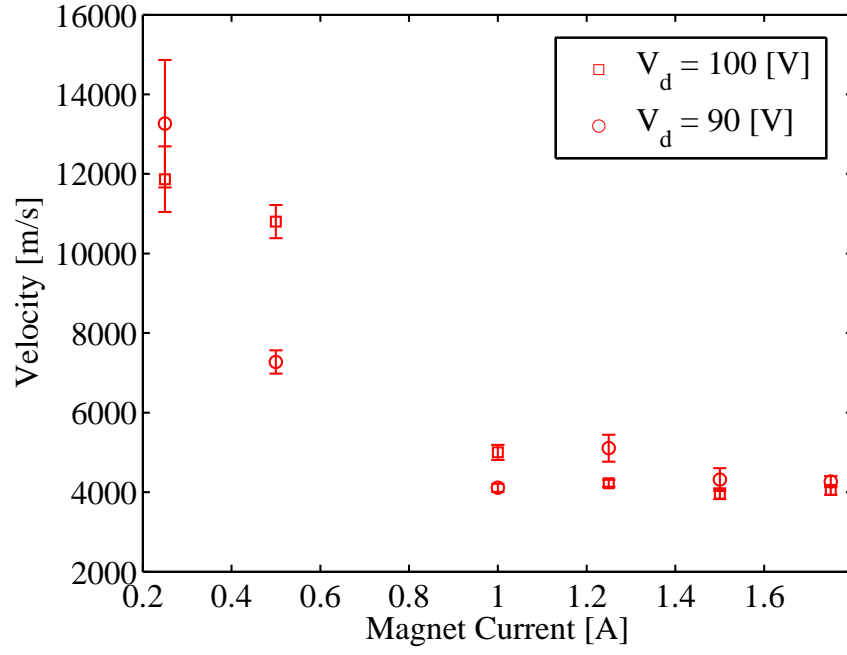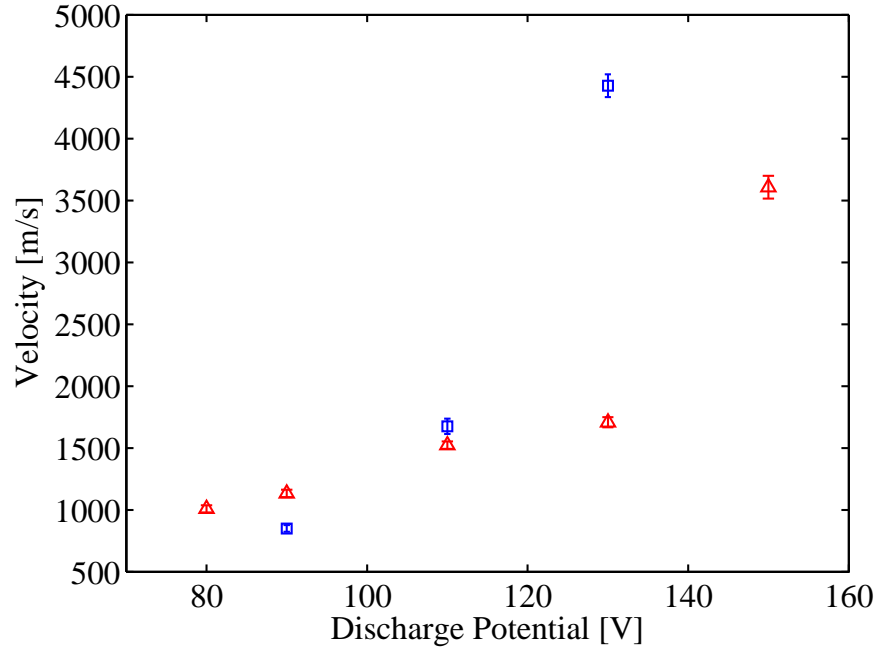
(a) Velocity of azimuthal plasma structures
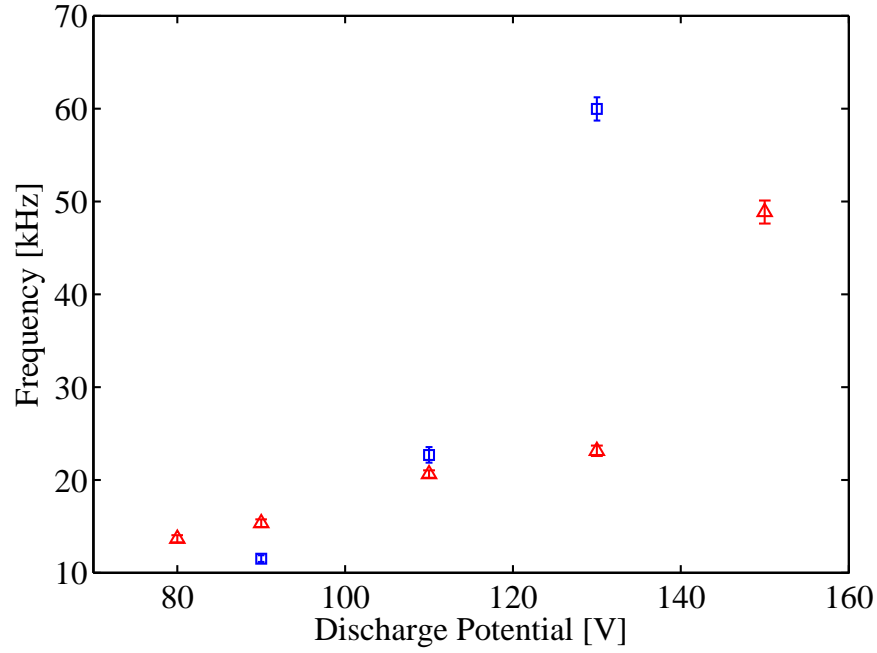
(b) Frequency of azimuthal plasma structures

Figure 4.71:   Azimuthal plasma structure velocity (a) and frequency (b) dependence on discharge potential for the BHT-200 operating with xenon (red) and krypton (blue). The average discharge current and magnet current were held constant at 0.8 A and 1.0 A, respectively

xenon values for the BHT-600. An increasing trend of the velocity or frequency was also observed for krypton. Thus for both thrusters and both propellants, the azimuthal velocity of the plasma structures increased with discharge potential.

Effects of the discharge current or mass flow rate were also examined in this study. The results on Figure 4.73 show the similarity of the krypton data to the xenon data in the ranges of discharge current examined for the BHT-200. Again, at the low discharge current, the emission from the discharge was relatively weak with few structures in the plasma field to measure. Consequently, the standard error at the low discharge current was greater at those data points. However, for both xenon and krypton, the velocity or frequency of the azimuthal plasma structure increased linearly with the discharge current after 0.8 A. The BHT-600 data shows a different trend for the velocity dependence on the discharge current. For both the krypton and xenon, a decreasing trend was observed for increasing discharge current which is shown in Figure 4.74.

Influence of the magnet current on the krypton azimuthal plasma structures for the BHT-200, illustrated in Figure 4.75, reveals similarities in trend to xenon. As the magnet current was increased, the velocity or frequency of the azimuthal plasma structures also increased. Similar results were also seen in the BHT-600 data for krypton. In addition, the comparison of krypton to xenon also show similar results in Figure 4.76. For both the xenon and krypton case, the results suggest the difference in the data was influenced by the different magnetic fields of thruster. However, the velocity and frequency data, which was collected on both thrusters and both propellants, will aid in the determination of the cause of the azimuthal instabilities.

A comparison of the measured frequencies shows the azimuthal mode observed could be either spoke instabilities, gradient-induced oscillations, or a combination of azimuthal modes [19, 40, 79]. Following the work of Janes and Lowder, who measured the rotating spoke via intrusive probes, the mechanism of the instability was observed to be ionization related. The arrival of this conclusion was based upon the correla-
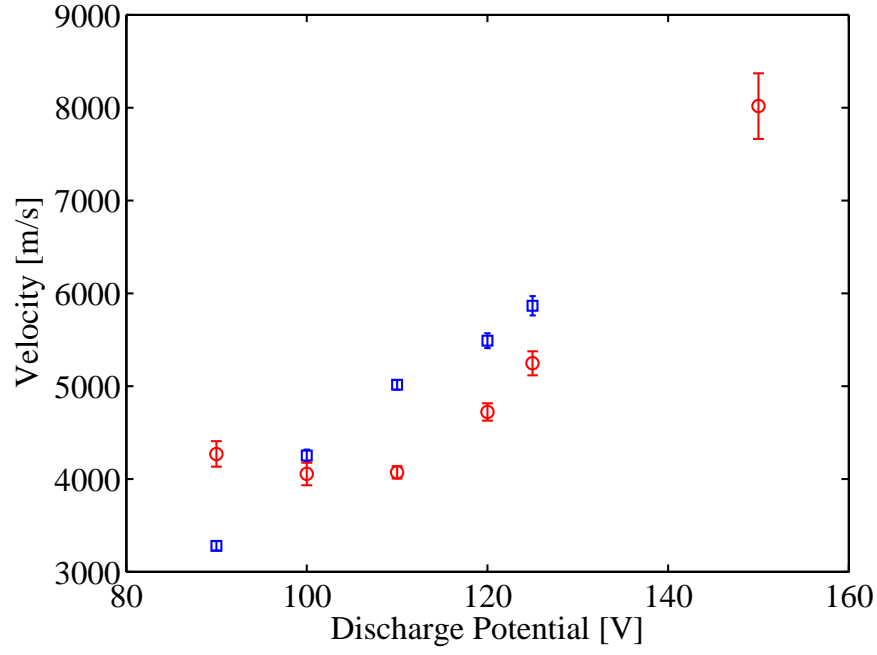
(a) Velocity of azimuthal plasma structures
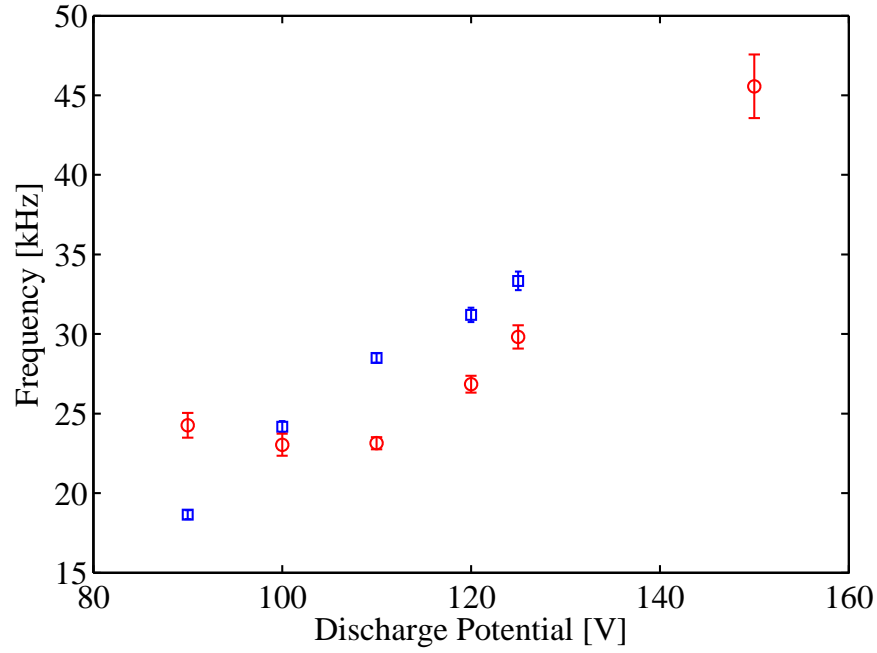
(b) Frequency of azimuthal plasma structures

Figure 4.72:   Azimuthal plasma structure velocity (a) and frequency (b) dependence on discharge potential for the BHT-600 operating with xenon (red) and krypton (blue). The average discharge current and magnet current were held constant at 2.0 A and 1.75 A, respectively.
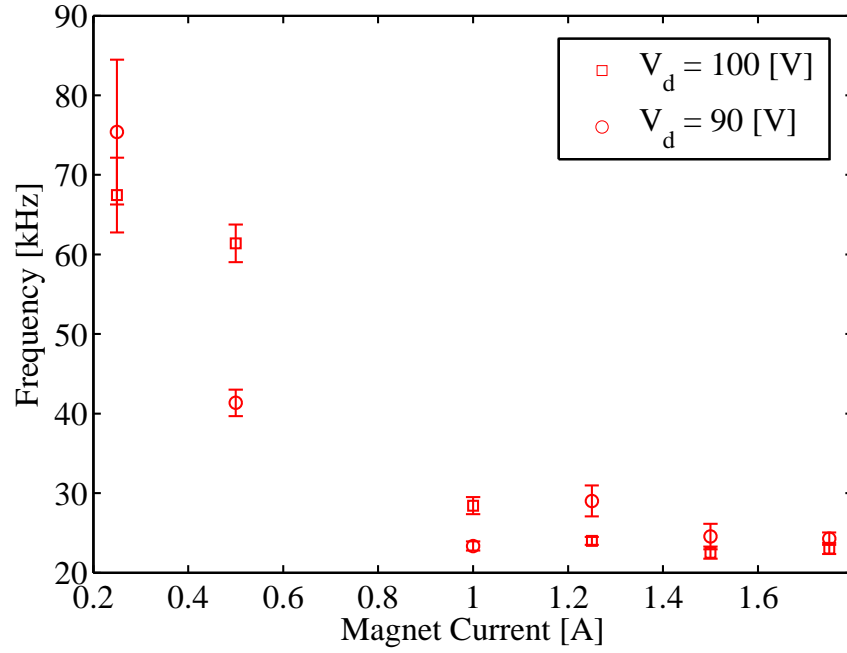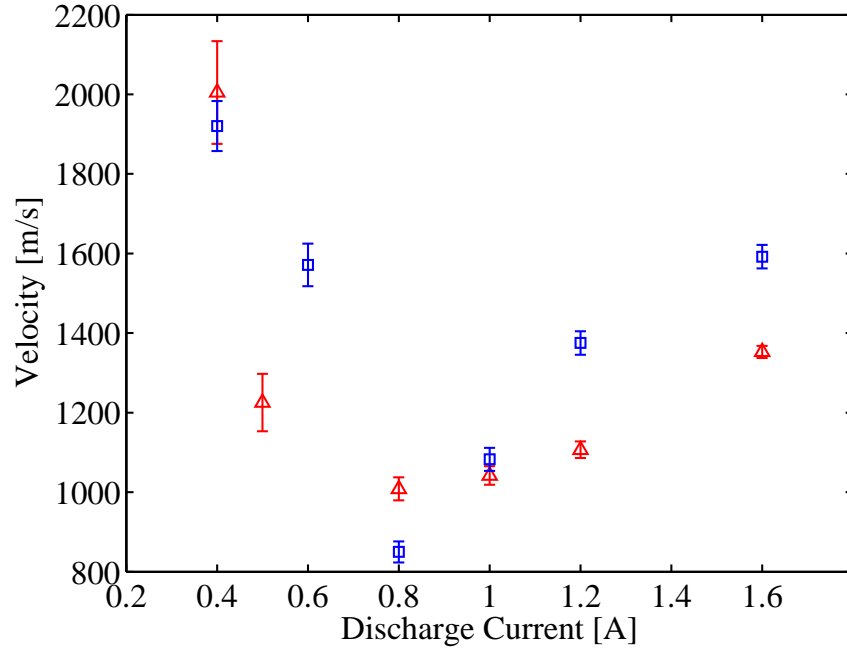
(a) Velocity of azimuthal plasma structures
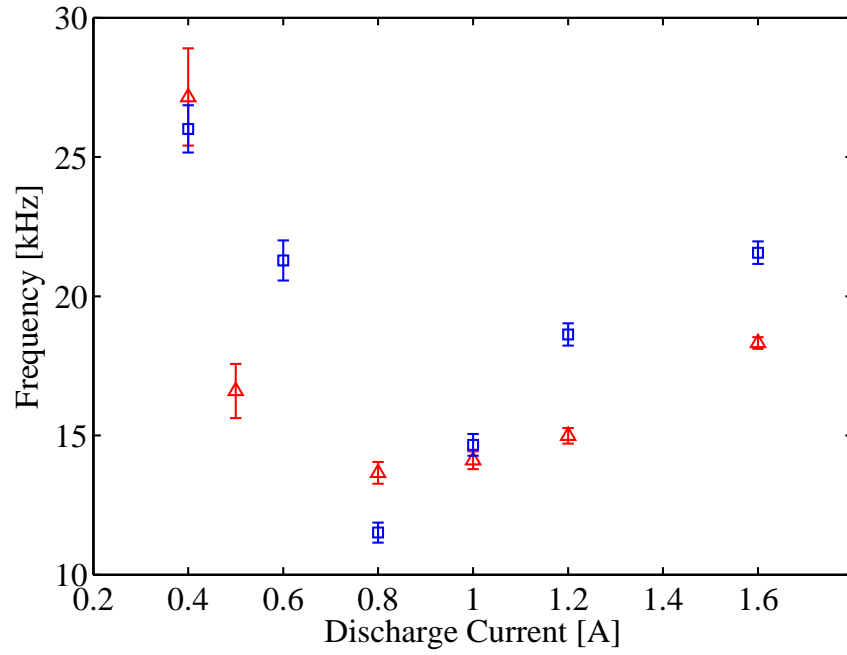
(b) Frequency of azimuthal plasma structures

Figure 4.73: Azimuthal plasma structure velocity (a) and frequency (b) dependence on discharge current for the BHT-200 operating with xenon (red) and krypton (blue). The discharge potential and magnet current were held constant at 90 V and 1.0 A, respectively.
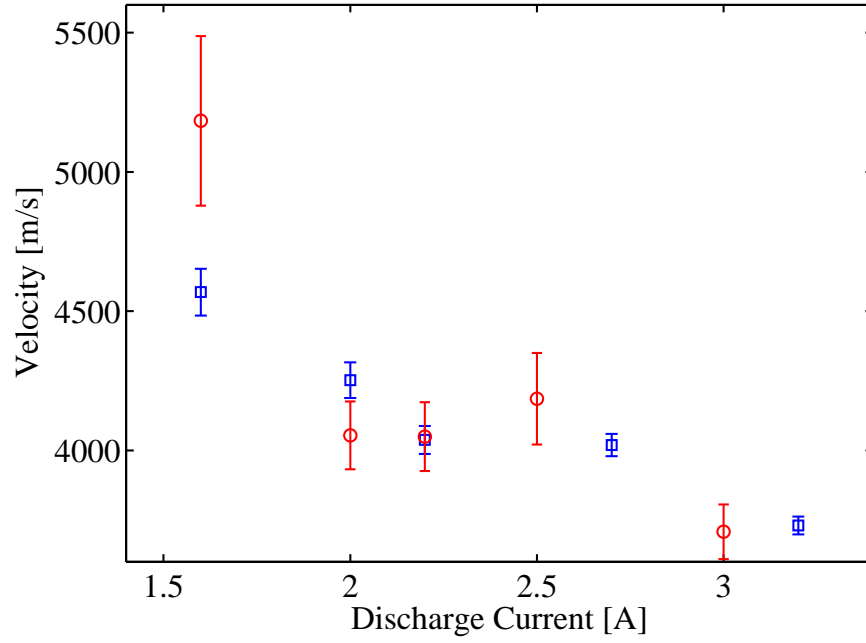
(a) Velocity of azimuthal plasma structures
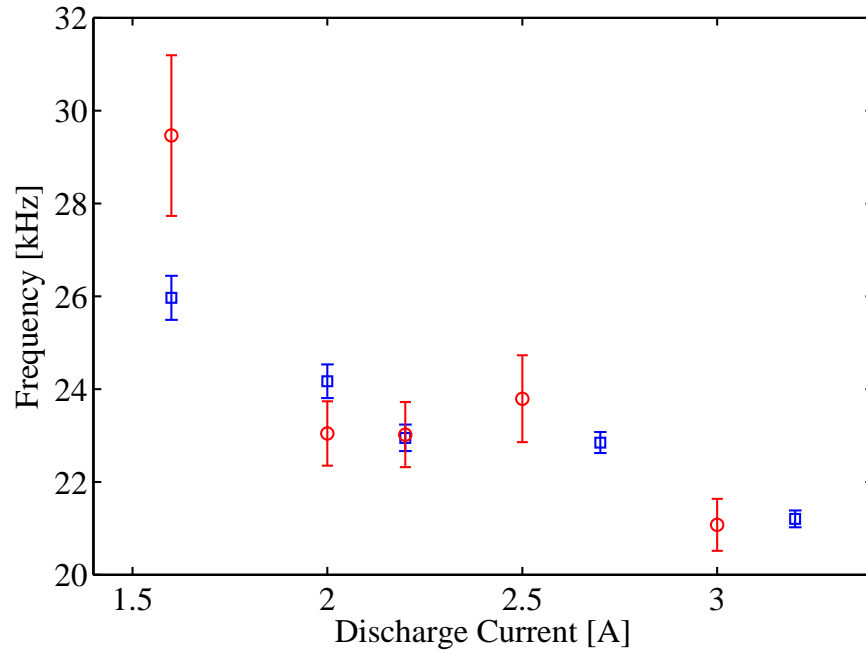
(b) Frequency of azimuthal plasma structures

Figure 4.74:   Azimuthal plasma structure velocity (a) and frequency (b) dependence on discharge potential for the BHT-600 operating with xenon (red) and krypton (blue). The average discharge potential and magnet current were held constant at 100 V and 1.75 A, respectively.
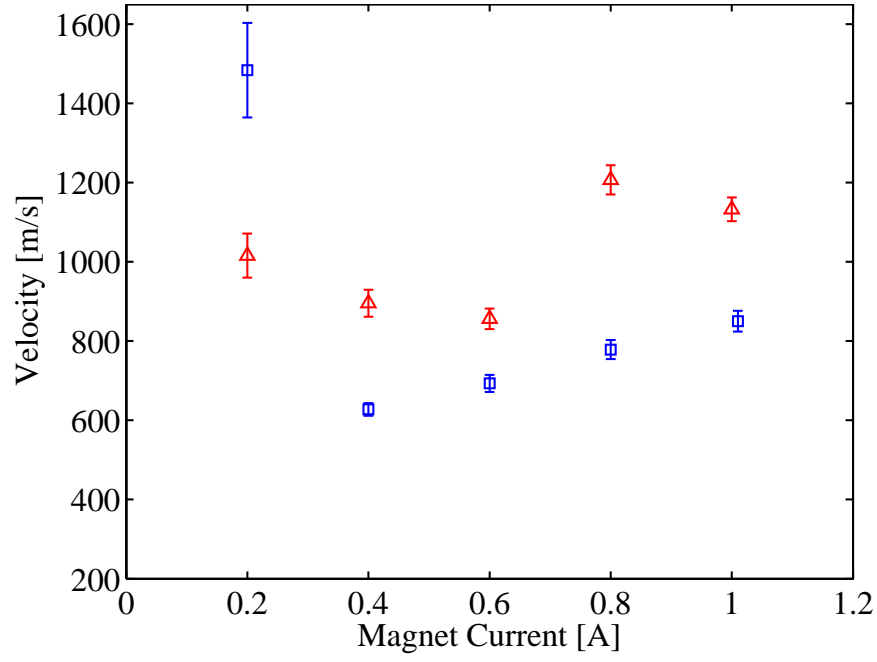
(a) Velocity of azimuthal plasma structures
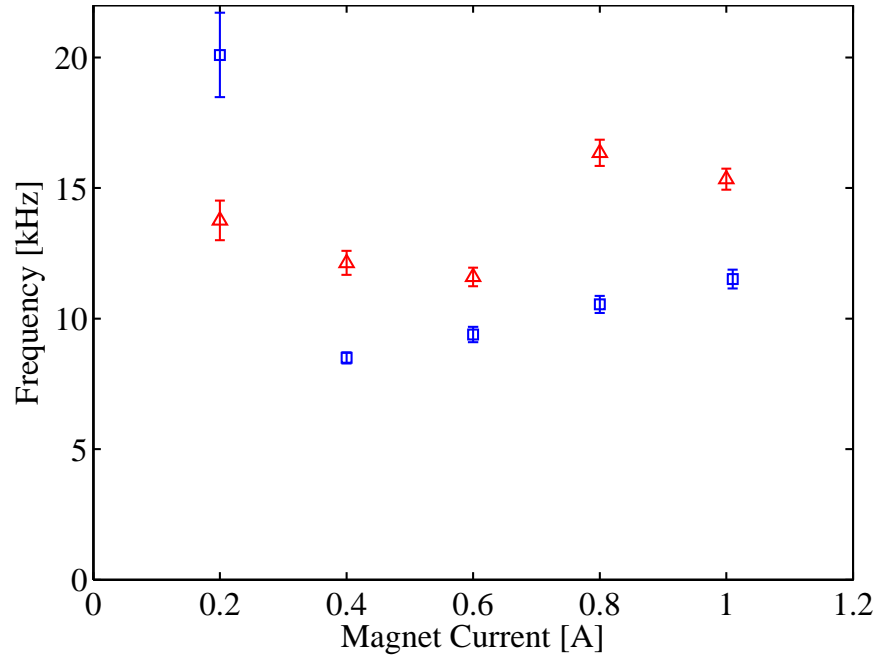
(b) Frequency of azimuthal plasma structures

Figure 4.75: Azimuthal plasma structure velocity (a) and frequency (b) dependence on magnet current for the BHT-200 operating with xenon (red) and krypton (blue). The average discharge potential and discharge current were held constant at 90 V and 0.8 A, respectively
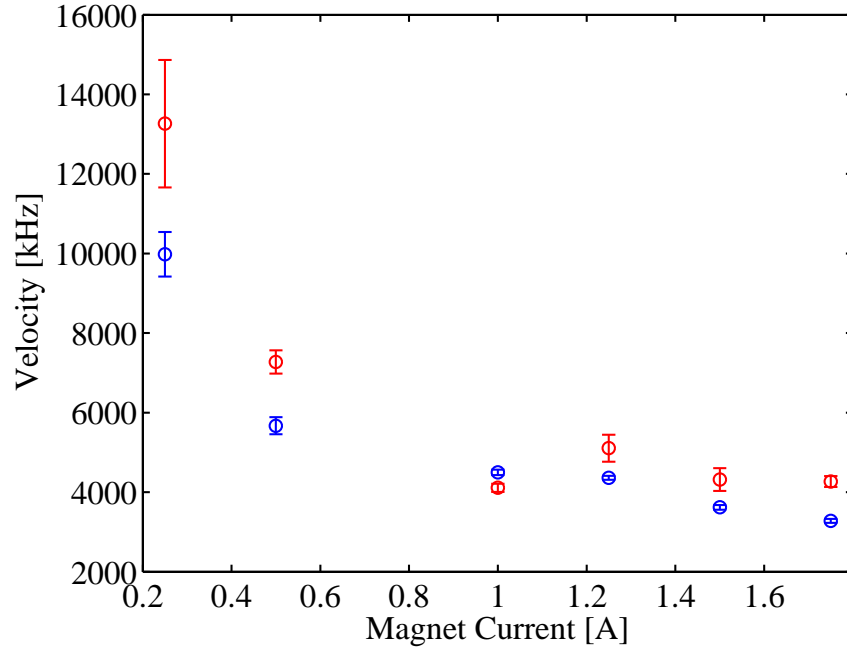
(a) Velocity of azimuthal plasma structures
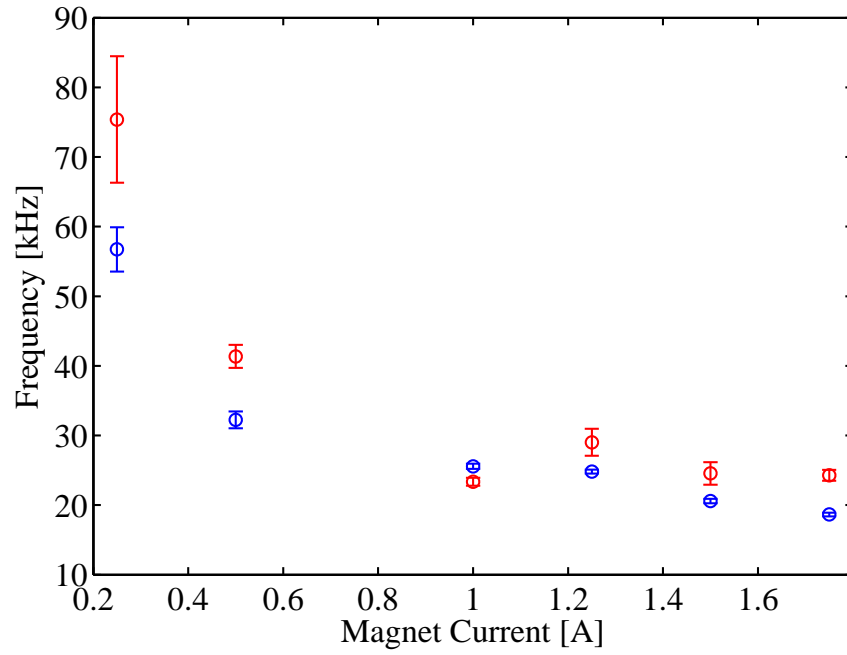
(b) Frequency of azimuthal plasma structures

Figure 4.76:   Azimuthal plasma structure velocity (a) and frequency (b) dependence on magnet current for the BHT-600 operating with xenon (red) and krypton (blue). The average discharge potential and discharge current were held constant at 100 V and 2.0 A, respectively

tion they found between the azimuthal speed of the spoke and the critical ionization velocity of the propellant which is given in Equation (2.48).

For xenon, this critical ionization velocity was 4.2 km/s. In comparison, the azimuthal velocity of the plasma structures found for the BHT-200 were within the range of 1.0 to 3.6 km/s (for a discharge potential of 80 to 150 V). For the BHT-600, the velocities were found in the range of 3.9 km/s to 7.9 km/s for a discharge potential range of 100 V to 150 V. Albeit the velocity of the azimuthal structures was close to the critical ionization velocity, the observed values varied significantly compared to the calculated u_{ci}.

The difference in velocity led to the possibility of other mechanisms which may have caused the azimuthal rotation such as gradient-induced oscillations. Unlike the spoke instabilities, these oscillations are not directly related to the ionization process, rather, they are electrostatic waves which propagate in the azimuthal direction [12, 64]. For the first mode instabilities where $k = 2\pi/\lambda = 1/r$ and choosing azimuthal propagation where $k_y = 10k_x$, the frequencies of gradient-induced oscillations were calculated in the 25 kHz - 55 kHz regime [12]. The calculated frequency for xenon was comparable to the frequencies measured for the average azimuthal plasma structures of the BHT-200 which was in the 14 kHz - 49 kHz regime Additionally, the BHT-600 was measured in the 25 kHz - 44 kHz range which was also within the calculated frequencies. The proximity of the measured velocities to the calculated velocities supports a strong correlation and promotes the conclusion the observed instabilities are caused by gradient-induced oscillations. For both types of instability, previous work shows the amplitude decreased as the discharge power was increased. [19, 40] In comparison, the direct emission measurements also exhibited the same characteristic which is given in Fig 4.62 where the increase in discharge potential to 150 V caused the plasma structures to spread azimuthally and decreased the intensity of the structures when compared to the lower discharge potential of 80 V.

One other possible cause of the azimuthal plasma structures is the magnetic striations which result from the crossed electric and magnetic field. From previous analysis, the velocity of these striations was calculated and given in Equation (2.61). Figure 4.77 and 4.78 provides the velocity profiles of the calculated magnetic striations for both xenon and krypton. Assuming the electron temperature is approximately one-tenth of the discharge potential, Figure 4.77 and 4.78 also compares the measured azimuthal velocities for both xenon and krypton to the calculated magnetic striation velocities. Employing only the estimate of electron temperatures with the corresponding azimuthal velocities, the data also suggests the cause of the azimuthal instabilities is the result of magnetic striations within the discharge.

Further evidence the observed azimuthal plasma structures are possible magnetic striation is given in the high-speed images of the main discharge. Figure 4.79 shows multiple plasma structures within the image. However, upon further investigation, the disconnected structure is separated by a dark region or striation in both the BHT-200 and BHT-600 main discharge.

Although it was not possible to determine the exact type of the oscillation utilizing the direct emission, it was possible to narrow down potential causes based on the observed frequency ranges and characteristic of the instability. More importantly, these direct emission observations presented a detailed time-dependent, 2-D image of the instability. These sequential images also provided insight into the formation of the azimuthal plasma structures with regards to their formation and dissipation throughout the discharge in addition to its confinement within the thruster channel. In addition, the main discharge was also observed to contain multiple structures with different azimuthal velocities for the first time. Some speculation as to the nature of the multiple azimuthal plasma structure include the possibility of the so-called spoke instabilities, gradient induced oscillations, and magnetic striations. From the high-speed images, features such as the so-called spokes, plasma structures from the gradient-induced oscillations, and striations were all observed in correspond to calculated values of frequency and azimuthal velocity. Although possible the observations
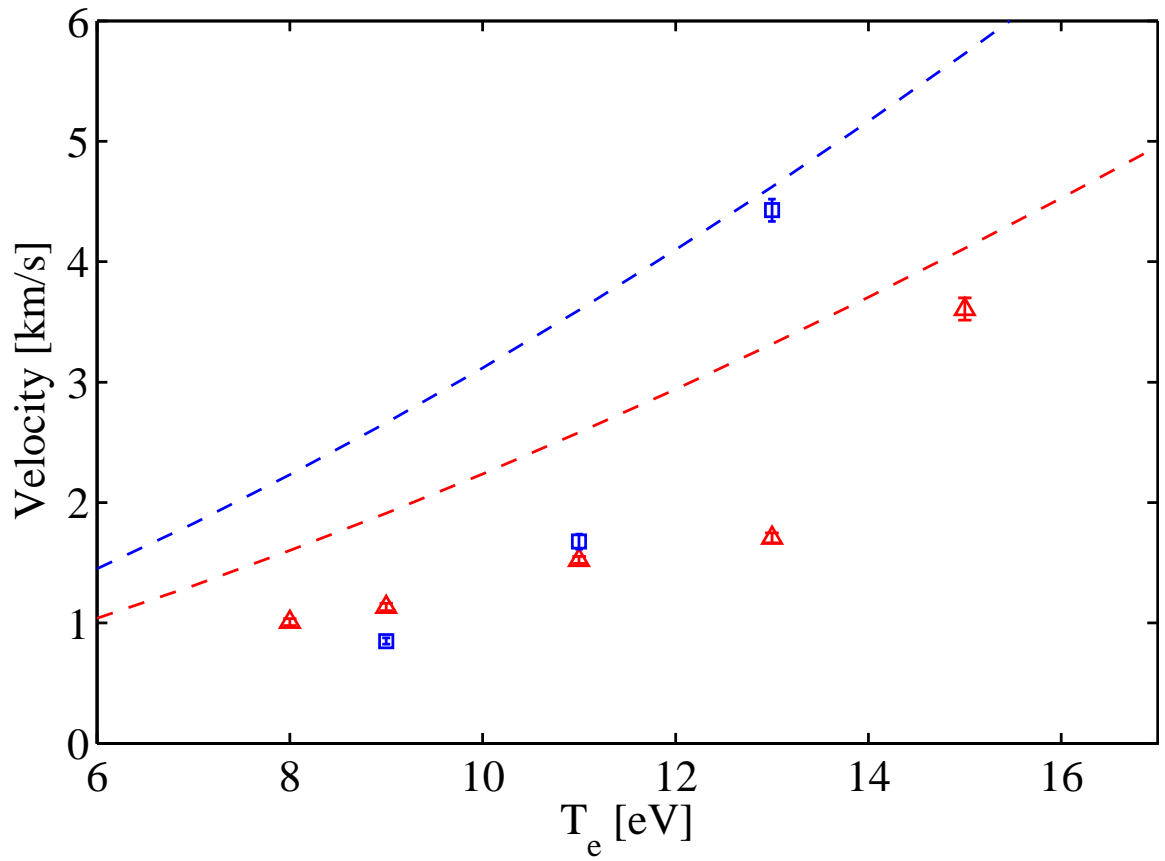
Figure 4.77:   Magnetic striation velocity dependence on electron temperature. The dashed lines represent the calculated magnetic striation velocity for xenon (red) and krypton (blue). Azimuthal plasma velocities of the BHT-200 operating with xenon (triangles) and krypton (squares) are shown with estimated electron temperature 1/10th the discharge potential.
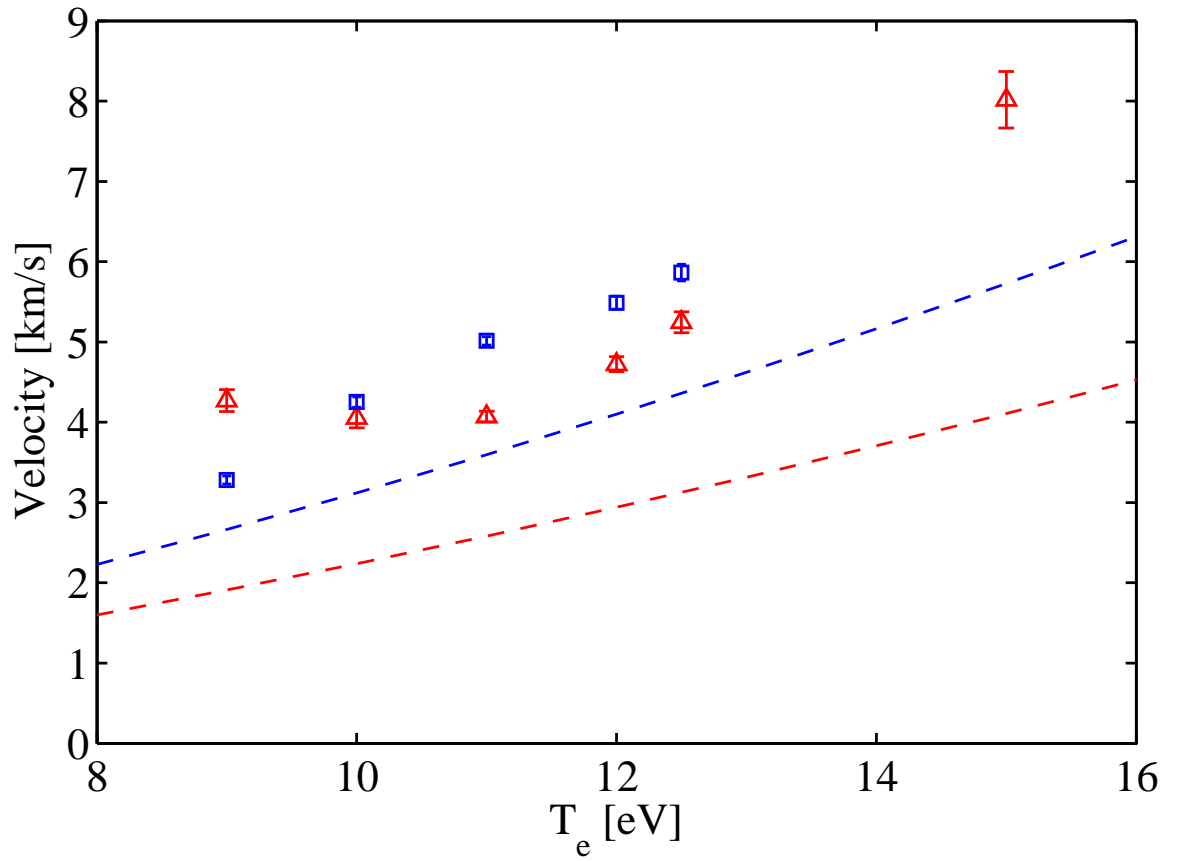
Figure 4.78: Magnetic striation velocity dependence on electron temperature. The dashed lines represent the calculated magnetic striation velocity for xenon (red) and krypton (blue). Azimuthal plasma velocities of the BHT-600 operating with xenon (triangles) and krypton (squares) are shown with estimated electron temperature 1/10th the discharge potential.
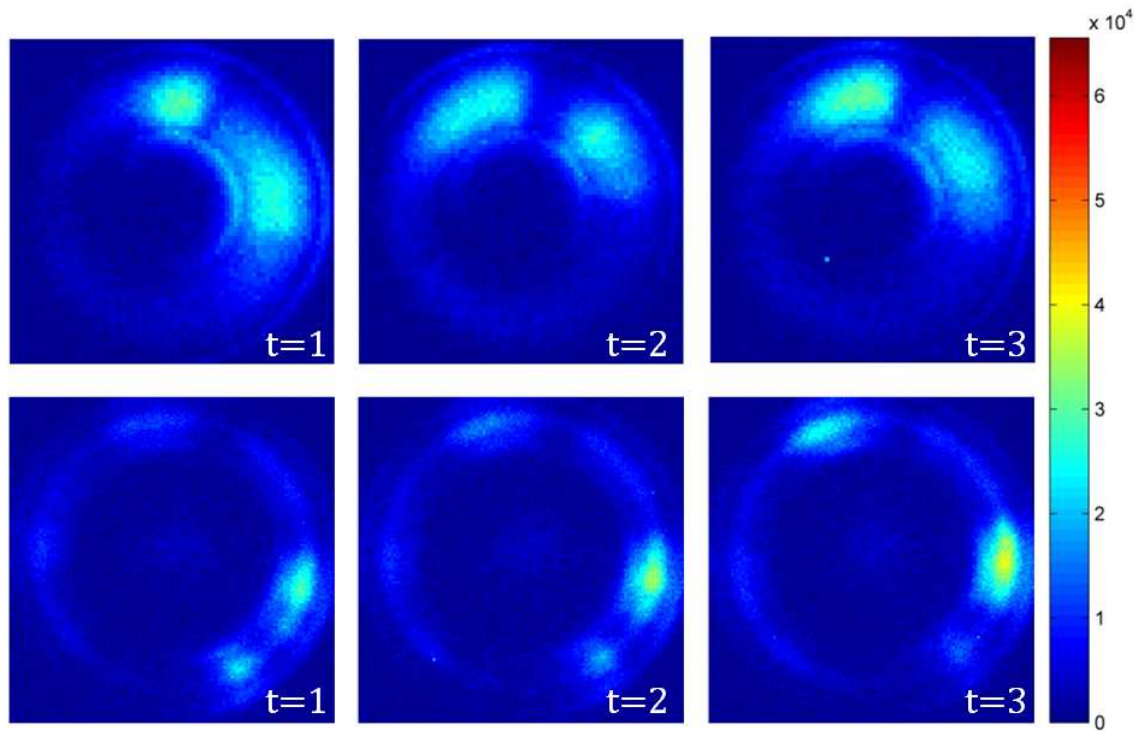
Figure 4.79: Sequential images (color enhanced) of striations within the main discharge of the BHT-200 (top) and the BHT-600 (bottom) operating with xenon. BHT-200 was operated at a discharge potential, discharge current, magnet current, and mass flow rate of 80 V, 0.8 A, 1.0 A, and 1.11 mg/s of xenon, respectively. BHT-600 was operated at a discharge potential, discharge current, magnet current, and mass flow rate of 100 V, 2.0 A, 1.75 A, and 2.26 mg/s of xenon, respectively. The time between images is 1 μs with an exposure time of 750 ns. Arbitrary intensity.

represent one type of instability, the observations are more likely the convolution of all three existing within the plasma at the low discharge potentials.

4.10 Side Views of BHT-200 and BHT-600

Side images of the BHT-200 and BHT-600 were also taken with the high-speed camera to provide spatial and time-dependent information on the main discharge of the Hall thrusters. However, due to the low emission of the plasma, the frame rate was lowered from the maximum of 1.0 Mfps to 250 kfps and 125 kfps. In addition, for both thrusters, xenon and krypton were used to determine the effects of material property.

For the BHT-200 with xenon, the high speed side images reveal the plasma front moving in and out of the exit plane of the thruster. The sequential images also illustrate the formation of the plasma jet in the center of the thruster in front of the BHT-200 nose cone, shown in Figure 4.80 at $t = 32$ and $t = 64$. The color enhanced side view images of Figure 4.81, also illustrate the development of intensity throughout the breathing mode cycle and provide a better depiction of the plasma jet. In addition, the color enhanced images, at $t = 32$, also show the asymmetry of the discharge area (left and right of the nose cone) possibly due to the azimuthal plasma structures.

Color enhanced side images of the BHT-200 krypton discharge, in Figure 4.82, also show the breathing mode of the Hall thrusters in addition to the variations in intensity at the exit plane. However, at the same thruster settings the high-speed images clearly shows a larger length (in the axial direction) of the emission as compared to xenon at the exit. Furthermore the krypton plasma jet, at $t = 32$, is not as coherent as the xenon plasma jet at $t = 32$.

In the case of the BHT-600, the side images of the thruster, shown in Figure 4.83, also reveal the oscillatory behavior of the plasma emission as it travels in the axial direction. The images also show a circular structure in the center of the image. This circular shape is actually the plasma jet seen in the BHT-200 images. However, due to the low emission, the camera was only able to image the brightest region of the jet which is the circular structure at the start of the plasma jet. The color enhanced
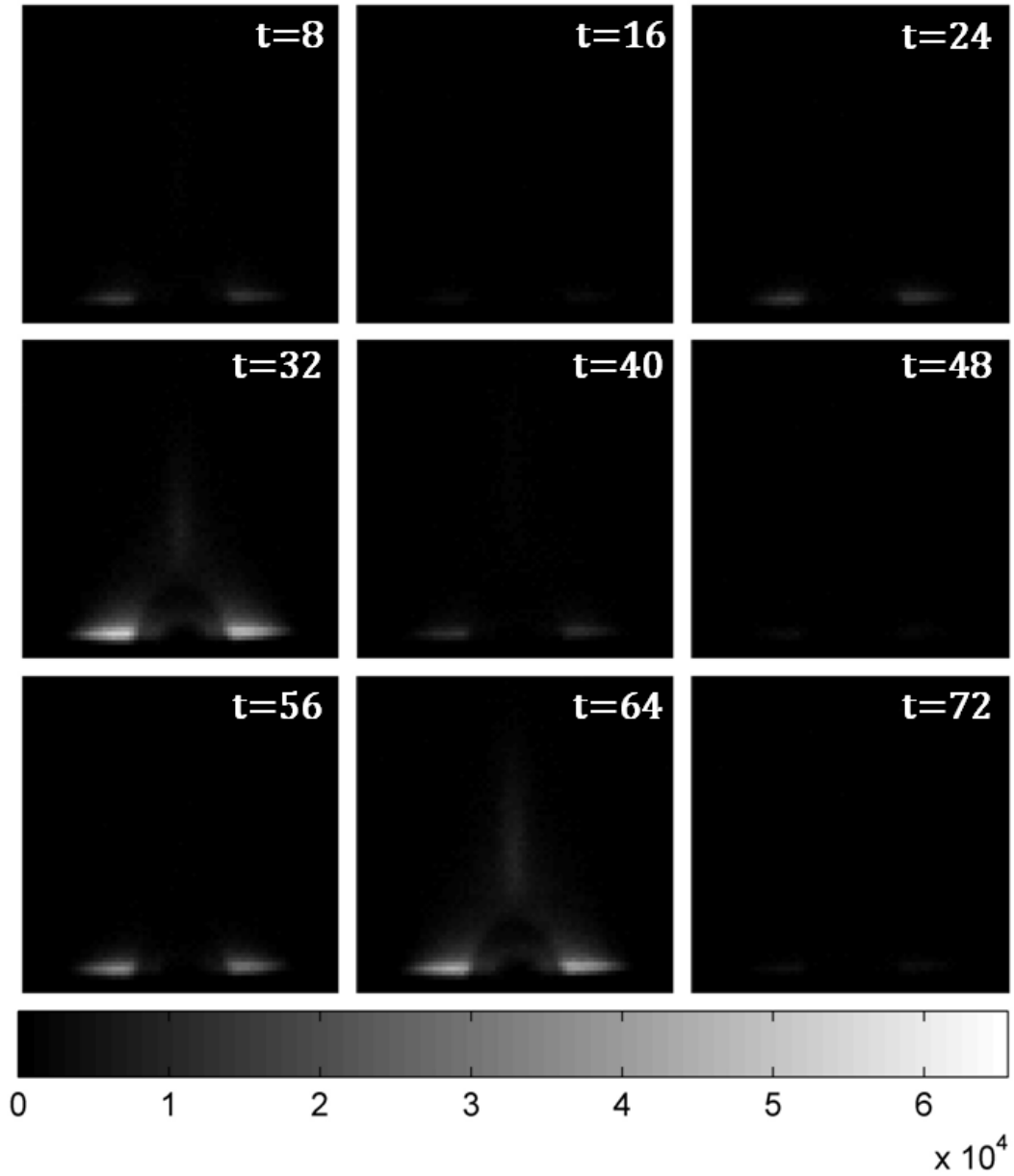
Figure 4.80: Sequential side view images (gray scale) of the main discharge for the BHT-200 with xenon. The discharge potential, discharge current, and magnet current were held steady at 250 V, 0.8 A, and 1.0 A, respectively. The time between images is 8 μs with an exposure time of 6 μs. Arbitrary intensity.
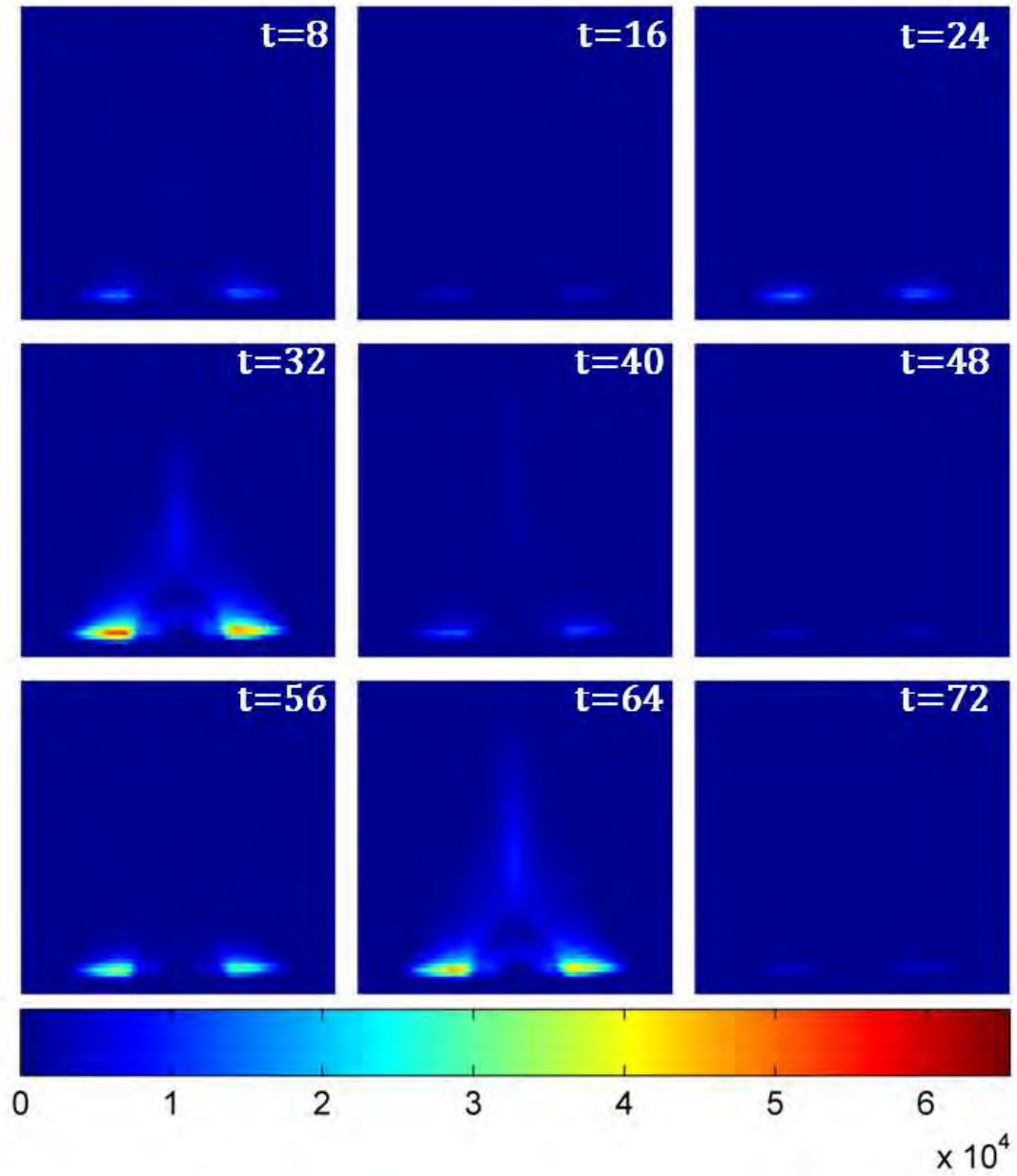
Figure 4.81: Sequential side view images (color enhanced) of the main discharge for the BHT-200 with xenon. The discharge potential, discharge current, and magnet current were held steady at 250 V, 0.8 A, and 1.0 A, respectively. The time between images is 8 μs with an exposure time of 6 μs. Arbitrary intensity.
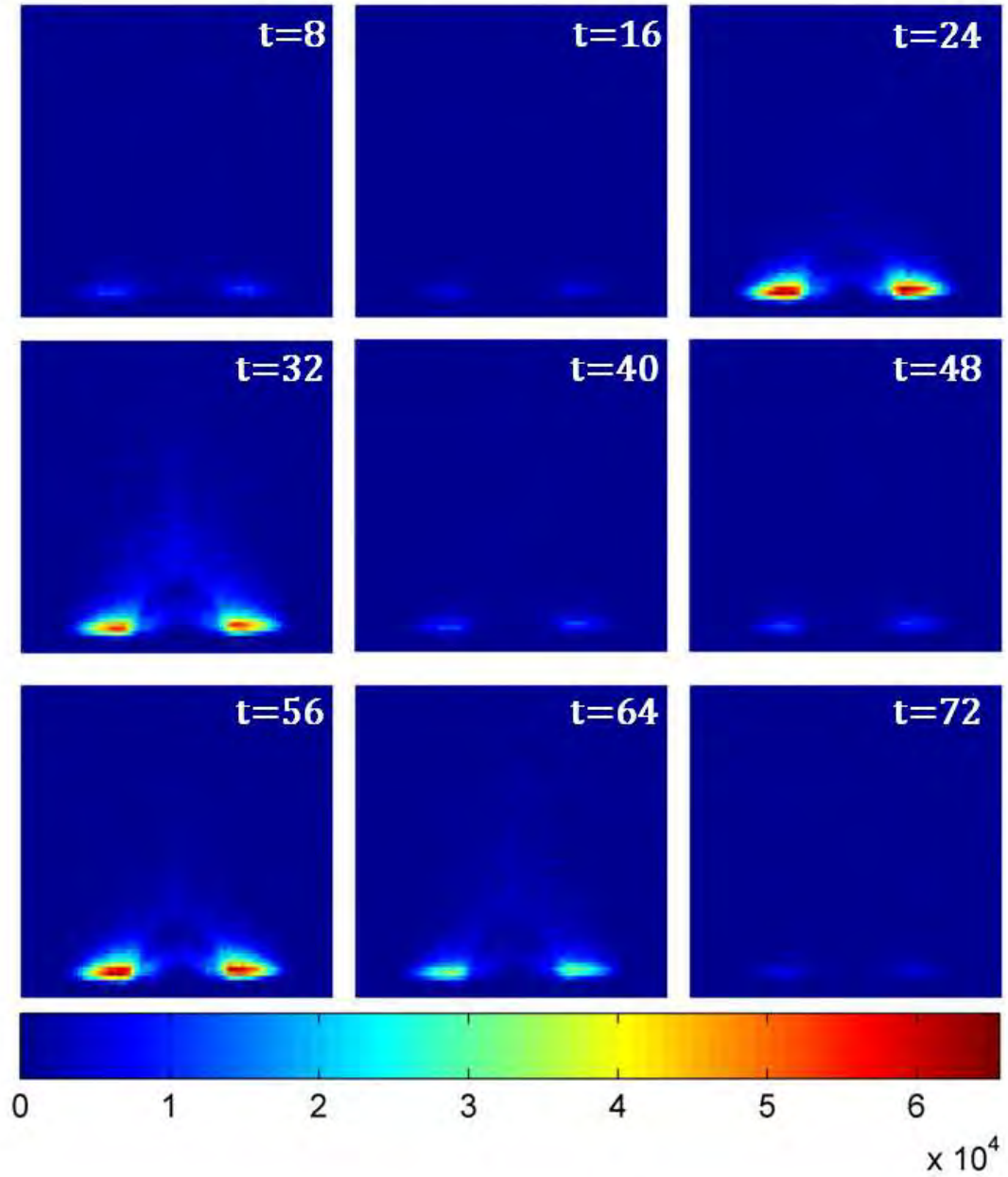
Figure 4.82: Sequential side view images (color enhanced) of the main discharge for the BHT-200 with krypton. The discharge potential, discharge current, and magnet current were held steady at 250 V, 0.8 A, and 1.0 A, respectively. The time between images is 8 μs with an exposure time of 6 μs. Arbitrary intensity.

images, Figure 4.84, reveal the level of intensity of the plasma emission near the exit plane. Here the thickness of the exit plane emission which is associated with the ionization region is clearly seen increasing and decreasing with time.

The thickness of the emission near the exit plane was also measured for different discharge potentials. Although not the same as the ionization length, L, described for the predator/prey model, this emission length, L^*, provides a good insight into the nature of the ionization region. L^* is measured from the exit plane at the thruster face since the emission inside the thruster was blocked. At various discharge potentials which also translate to different electron temperatures, L^* was measured optically and defined as intensity values 95% of the maximum.

Since the optical emission captured by the high-speed imaging is the result of radiative decay from neutral and ion excitation, the observed L^* represents a region of elevated electron temperature and electric field. This region of elevated electron temperature and electric field is proportional to the ionization length since the ionization mechanisms are mainly due to electron impact. Furthermore, measurements by Linnell and Gallimore of the electron temperature and electric field utilizing xenon and krypton have also shown elevated electron temperature and electric field near the L^* region [52].

Figure 4.85 shows the trend of L^* for both xenon and krypton in the BHT-600 discharge. For various discharge potentials the krypton L^* measured greater than the xenon L^* which provides further evidence the ionization length for krypton is larger than the ionization length for xenon. This result is also in agreement with electron temperature measurements from Linnell and Gallimore in which they found the region of elevated electron temperature for xenon and krypton began in appoximately at the same location near the exit plan. However, the region of elevated electron temperature for krypton extended further in the axial direction compared to xenon at the same discharge potential [52].
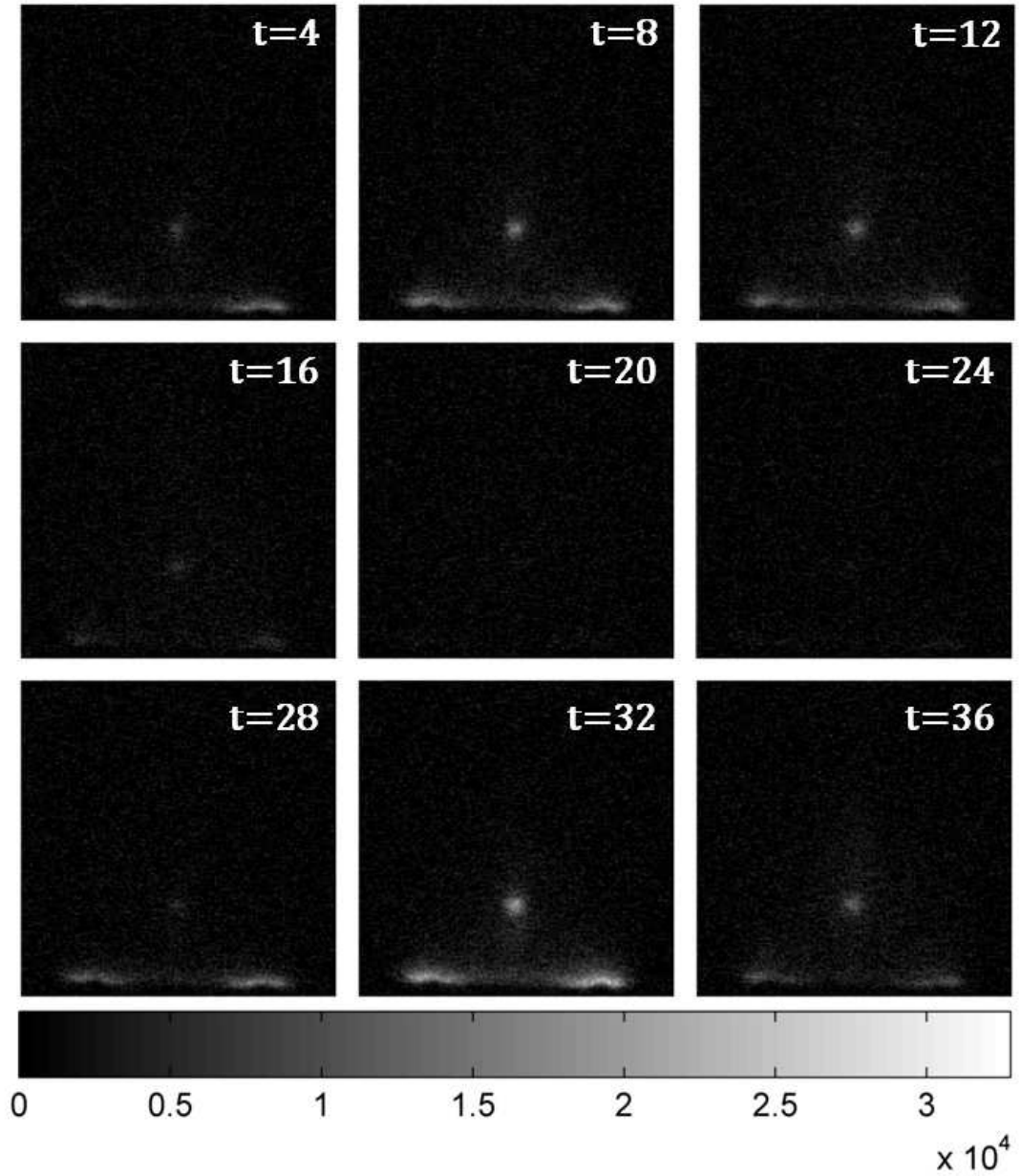
Figure 4.83: Sequential side view images (gray scale) of the main discharge for the BHT-600 with xenon. The discharge potential, discharge current, and magnet current were held steady at 250 V, 2.0A, and 1.75 A, respectively. The time between images is 4 μs with an exposure time of 2 μs. Arbitrary intensity.
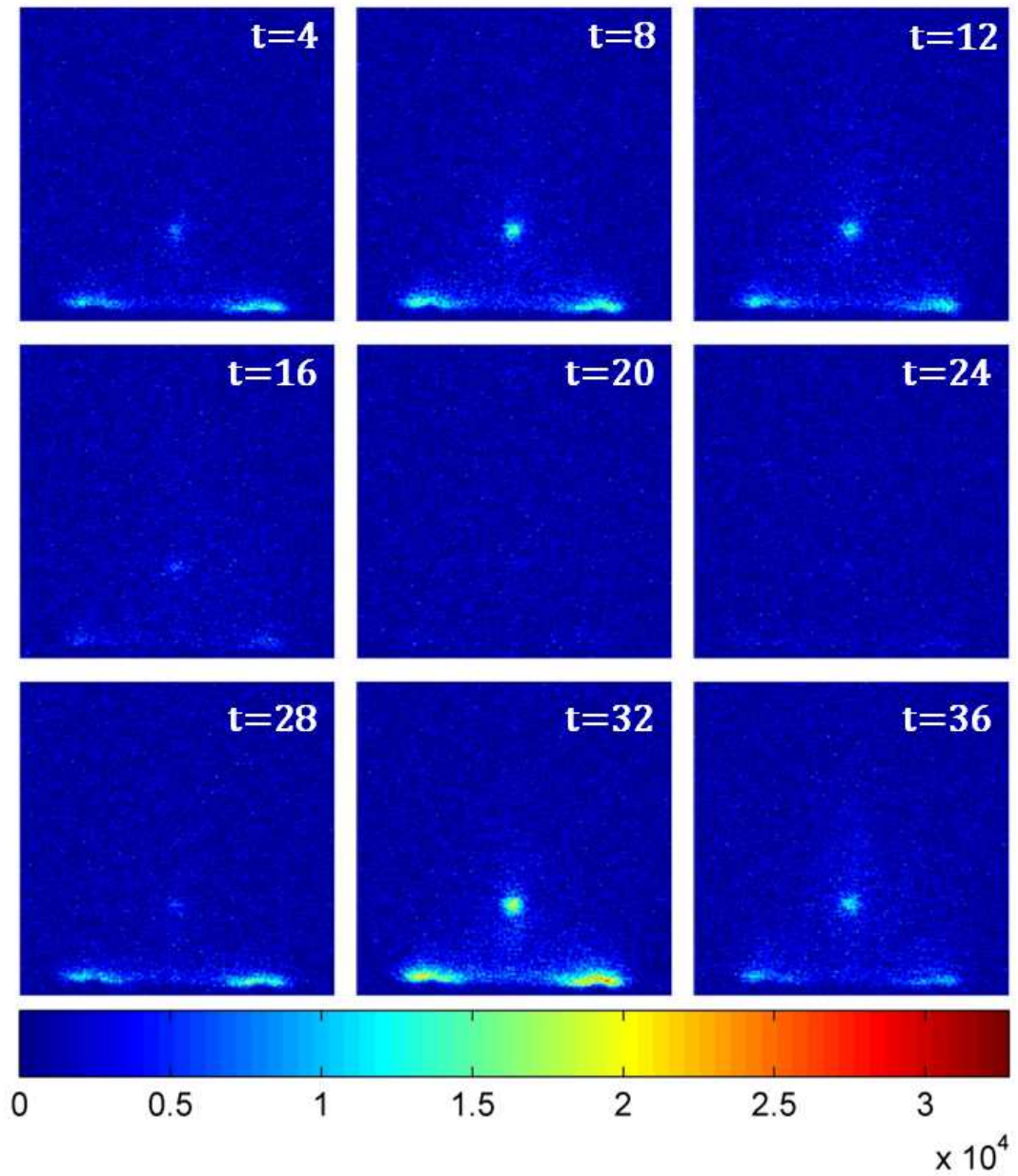
Figure 4.84:   Sequential side view images (color enhanced) of the main discharge for the BHT-600 with xenon. The discharge potential, discharge current, and magnet current were held steady at 250 V, 2.0A, and 1.75 A, respectively. The time between images is 4 μs with an exposure time of 2 μs. Arbitrary intensity.
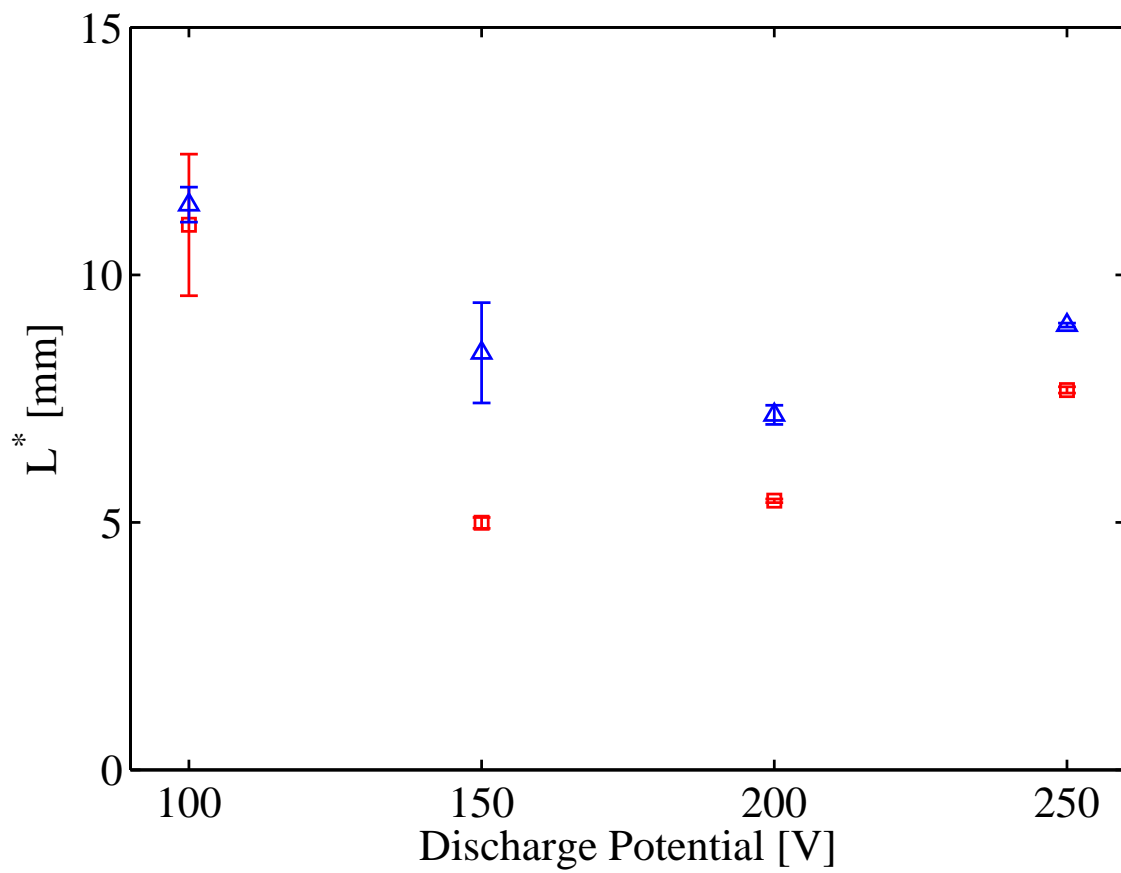
Figure 4.85:   Thickness of plasma emission near the thruster exit plane for the BHT-600 operating with xenon (squares) and krypton (triangles) at various discharge potentials. The mass flow rate and magnet current were held constant at 2.6 mg/s and 1.75 A, respectively.

With the proper time reference, given by the camera, the average velocity of the L^* wave was also calculated for xenon and krypton in the BHT-600. Since the nose cone divides the ionization ring into two parts, left side and right side, it is also possible to determine the axial wave velocity of L^* for each side. Figure 4.86 and 4.87 show the axial velocity of the emission thickness for the left and right side of the discharge channel. From the figures, the data shows the velocities on the right does not necessarily equal the velocities on the left side of the discharge channel. Further examination into the asymmetry suggests the result is due to the azimuthal plasma structure rotating within the discharge or possibly the location of the cathode. For both xenon and krypton, the difference in velocities between the left and the right sides were located at the low discharge potentials which the azimuthal plasma structures were the strongest. The velocities at various discharge potentials also corresponds to the discharge potential which the breathing mode was the strongest. For xenon, the breathing mode was the strongest at 250 V while for krypton, the strongest breathing mode was seen in the 150 V region. In the strong breathing mode regions, the velocity of L^* is close to the neutral velocity which may contribute to the movement of the emission region. At the low discharge potential of 100 V the data had significant error which is attributed to the azimuthal plasma structures. Velocity values at 100 V in Figure 4.86 and 4.87 are not representative of the L^* wave velocity.

At the lower discharge potentials, the azimuthal plasma structures were also detectable with the high-speed camera. For the BHT-200, the azimuthal plasma structures are shown in Figure 4.88 in the gray scale and the enhanced color images are presented in Figure 4.89. In the gray scale of Figure 4.88, the images show the azimuthal plasma structures traveling in the $E \times B$ direction around the nose cone of the BHT-200. The high-speed images also show the aziuthal plasma structures having a visible height nearly the length of the thruster.

In the color enhanced high-speed images, the areas of high emission intensity are shown slightly below the apex of the nose cone. This region of high intensity is also concentrated around the nose cone which is illustrated in Figure 4.90 where the
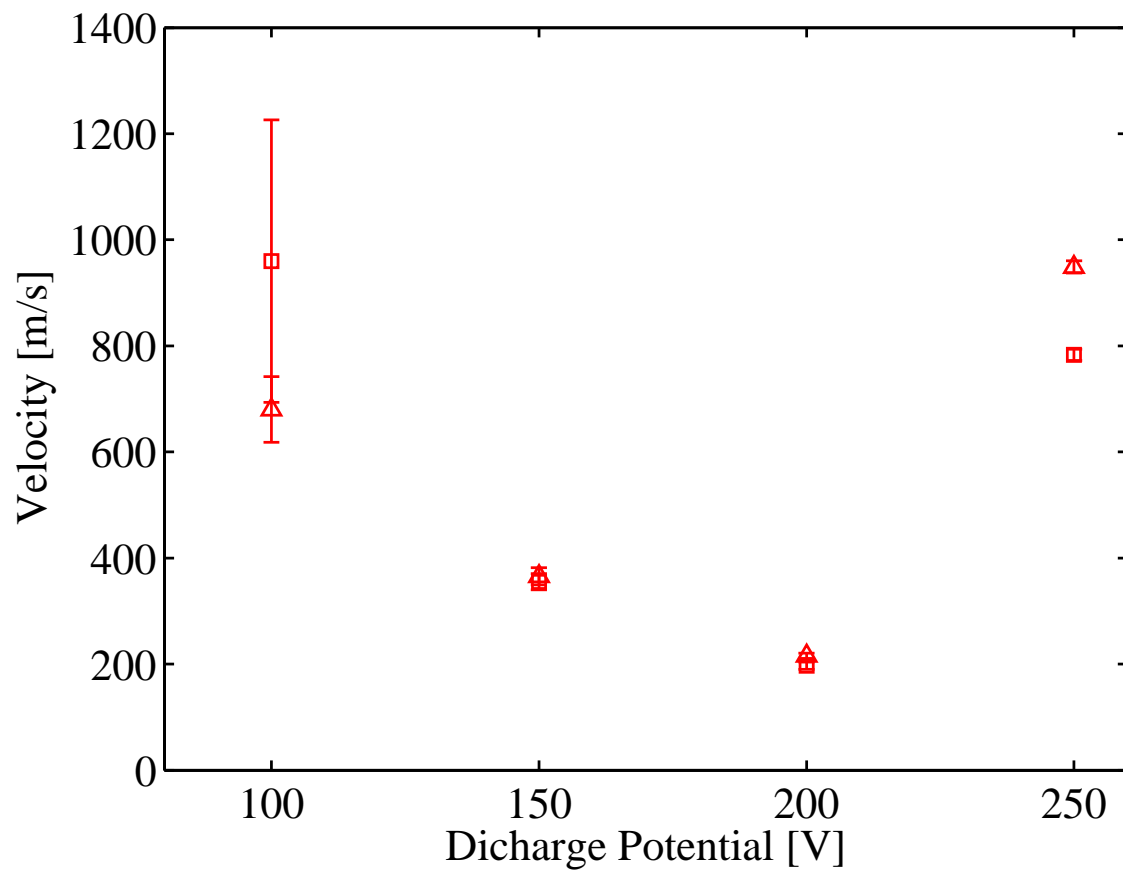
Figure 4.86:   Axial velocity of xenon plasma emission wave on the left (squares) and right (triangles) of the nose cone at the exit plan of the BHT-600. The mass flow rate and magnet current were held constant at 2.6 mg/s of xenon and 1.75 A, respectively.
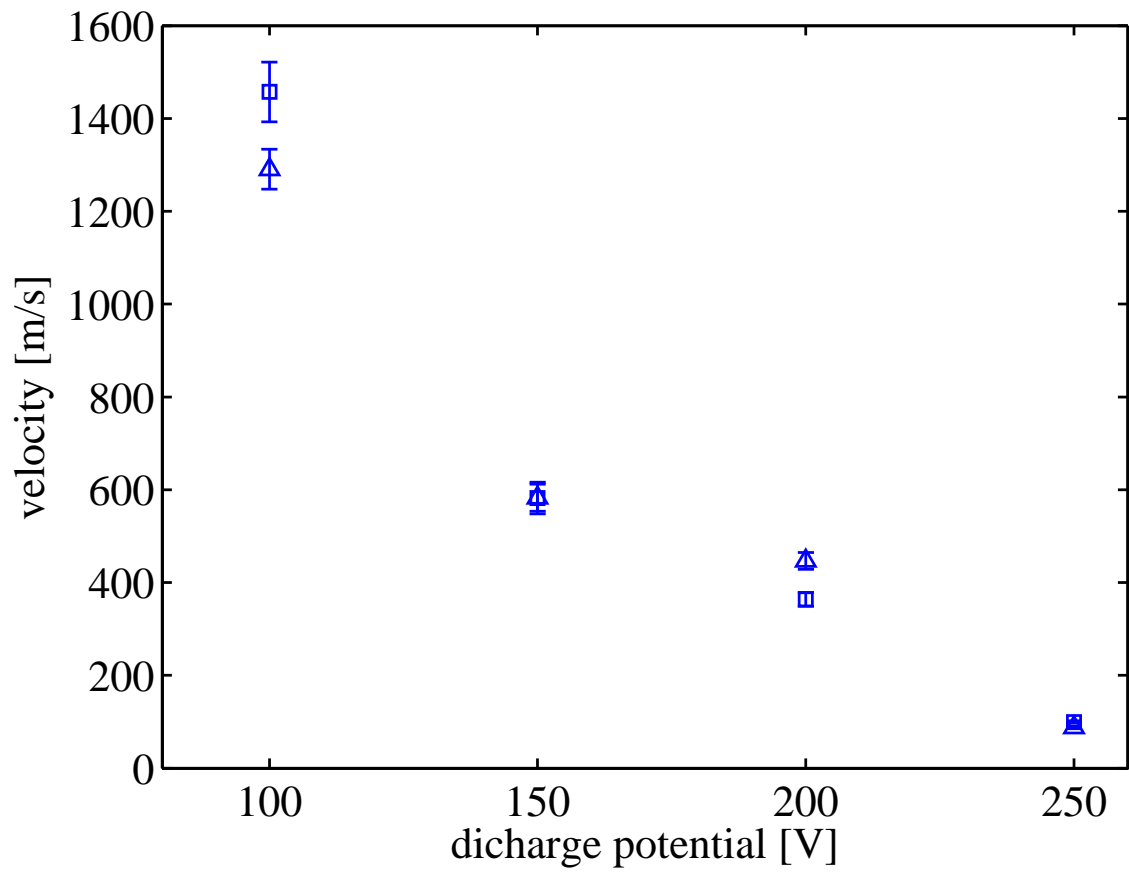
Figure 4.87: Axial velocity of krypton plasma emission wave on the left (squares) and right (triangles) of the nose cone at the exit plan of the BHT-600. The mass flow rate and magnet current were held constant at 2.6 mg/s and 1.75 A, respectively.
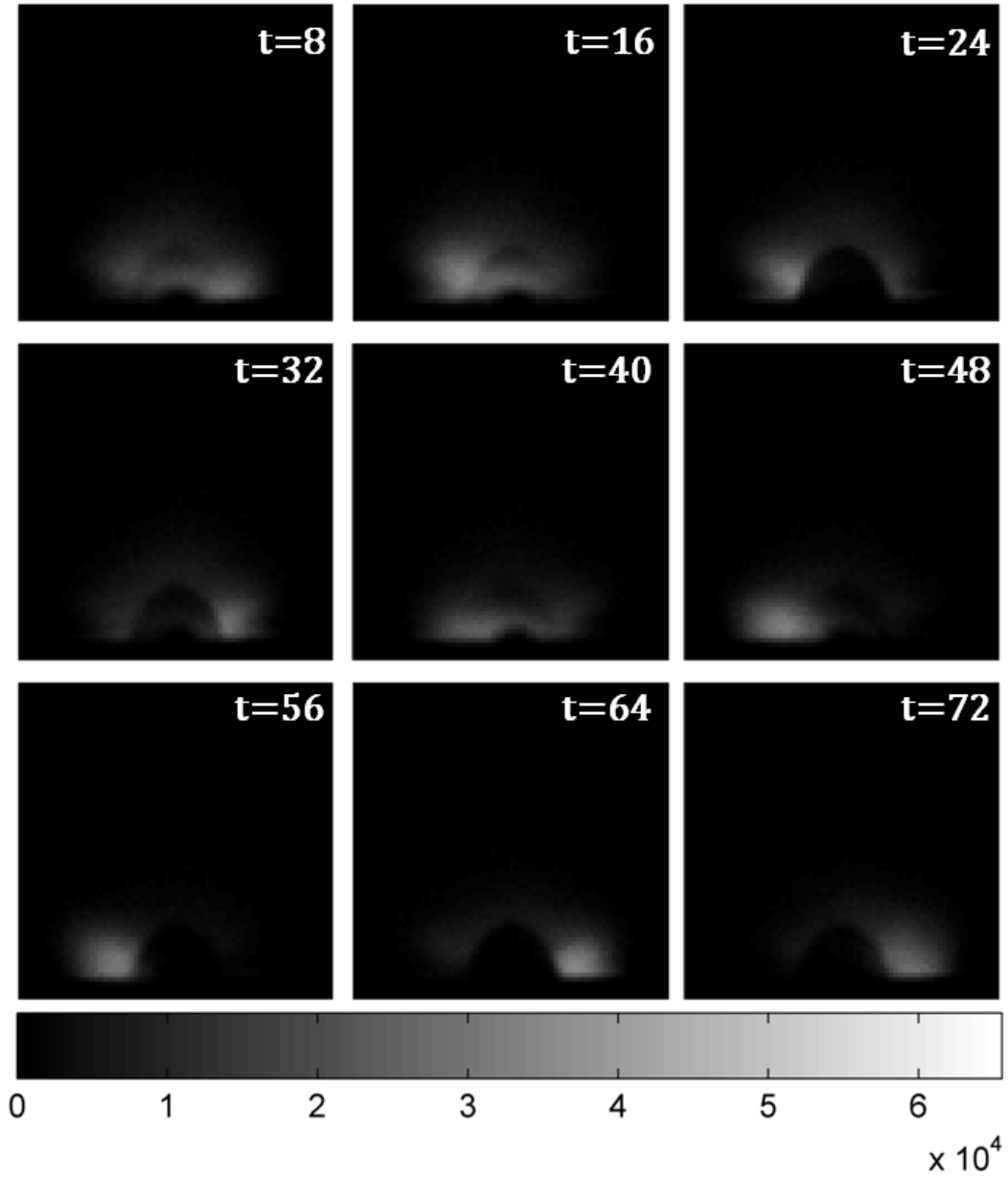
Figure 4.88:   Sequential images (gray scale) of the xenon azimuthal plasma struc-
tures in main discharge of the BHT-200. The thruster was operating at a discharge
potential, discharge current, and magnet current of 80 V, 0.8 A, and 1.0 A, respec-
tively. The time between images is 8 μs with an exposure time of 6 μs. Arbitrary
intensity.
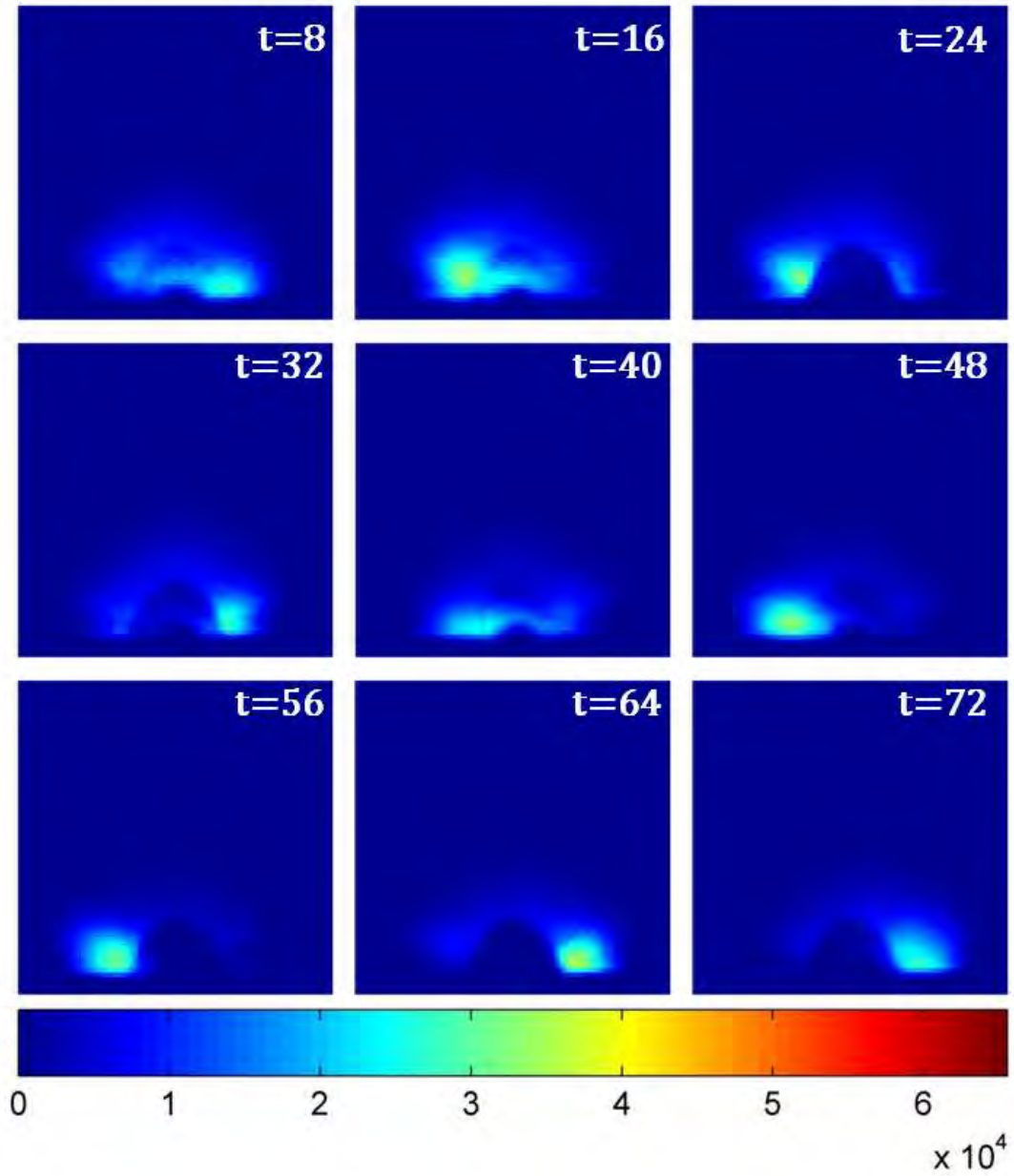
Figure 4.89: Sequential images of the xenon azimuthal plasma structures in main discharge of the BHT-200. The thruster was operating at a discharge potential, discharge current, and magnet current of 80 V, 0.8 A, and 1.0 A, respectively. The time between images is 8 μs with an exposure time of 6 μs. Arbitrary intensity.

high intensity is caused by the high electron temperature and high number densities of the plasma. Further interrogation of Figure 4.90 shows the location of the high intensity plasma coincides with the area of erosion commonly seen on the BHT-200 nose cone shown in Figure 4.91. In addition, the image shows the pattern of wear around the nose cone.

In essence, the high concentration of electron temperature and number density of excited neutrals and ions contributed to the axial erosion mechanisms previous identified by Cheng. The high speed images demonstrate the erosion of the nose cone is not just due to collisions of ions and neutrals traveling in the axial direction. Rather, the erosion of the nose cone has contributions from the azimuthal direction similar to a lathe removing material [7].

Azimuthal plasma structures were also observed from the side view of the BHT-600. The high-speed images, in Figure 4.92, show the areas of high intensity traveling in the $E \times B$ direction as previously mentioned. The perspective of the images presents the azimuthal plasma structures as a spoke with the center anchored to the plasma jet in the center of the image. As the plasma rotates in the series of images, several spoke structures are observed rotating concurrently.

In the side images of the both Hall thrusters, the breathing mode oscillations and the azimuthal plasma instabilities were examined. The oscillations and instabilities were also visualized in the main discharges of xenon and krypton which were very similar in characteristics. For the BHT-600, the optical emission thickness provided by the breathing mode, at the exit plane, was measured for xenon and krypton. The results provide evidence the krypton ionization length was larger than xenon at the same discharge potential.

Azimuthal plasma structures for the BHT-200 were also presented in this section. Visualization of the thruster from the side found the plasma structures could also contribute to the erosion of the nose cone. In the images of the BHT-600, the spoke structures were also observed to rotate in the $E \times B$ direction. The center of the
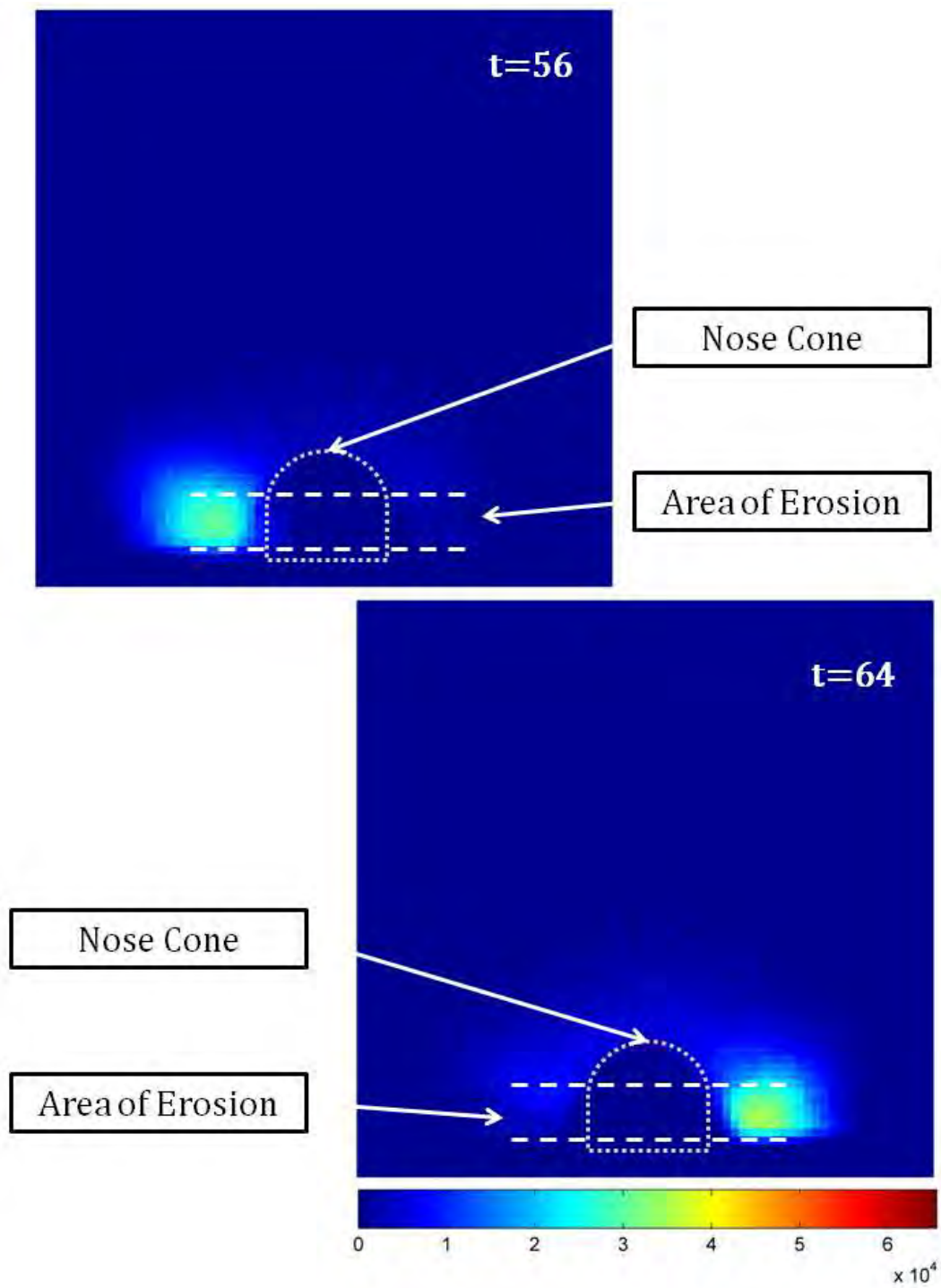
Figure 4.90: Sequential images of the xenon azimuthal plasma structures in main discharge of the BHT-200. The thruster was operating at a discharge potential, discharge current, and magnet current of 80 V, 0.8 A, and 1.0 A, respectively. The exposure time of the images are 6 μs. Arbitrary intensity.
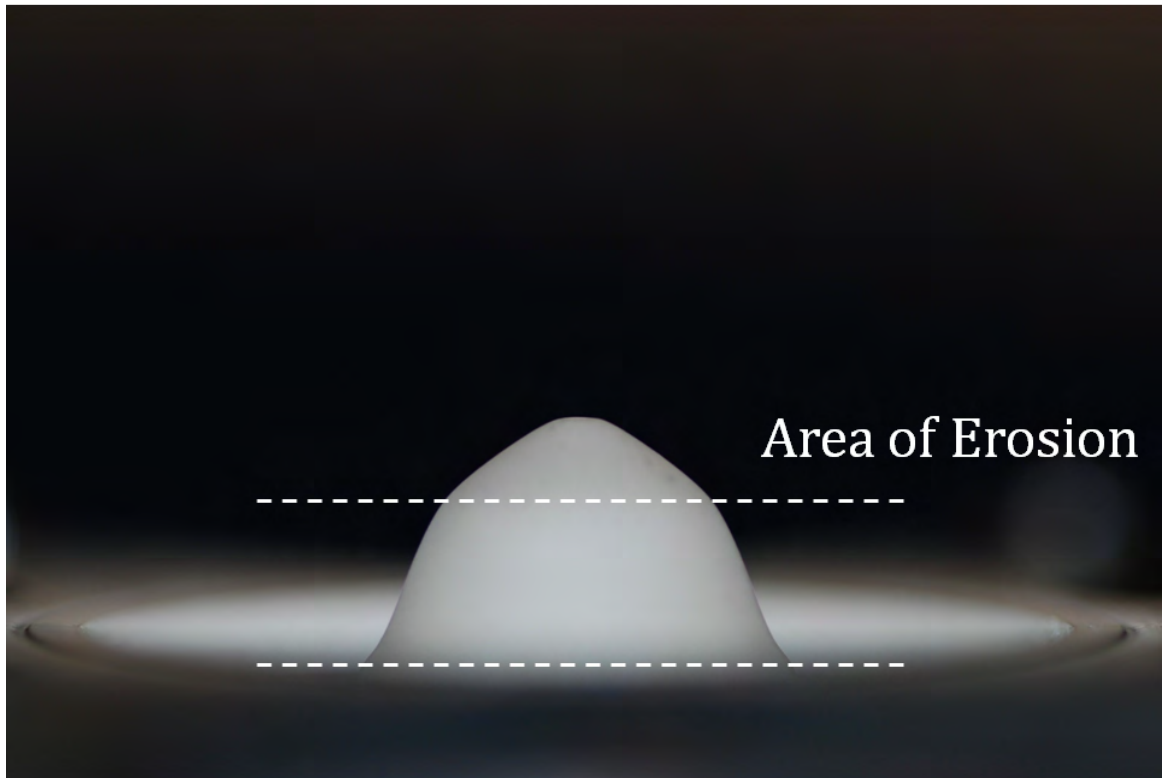
Figure 4.91:   Image of BHT-200 with area of erosion on the nose cone highlighted.
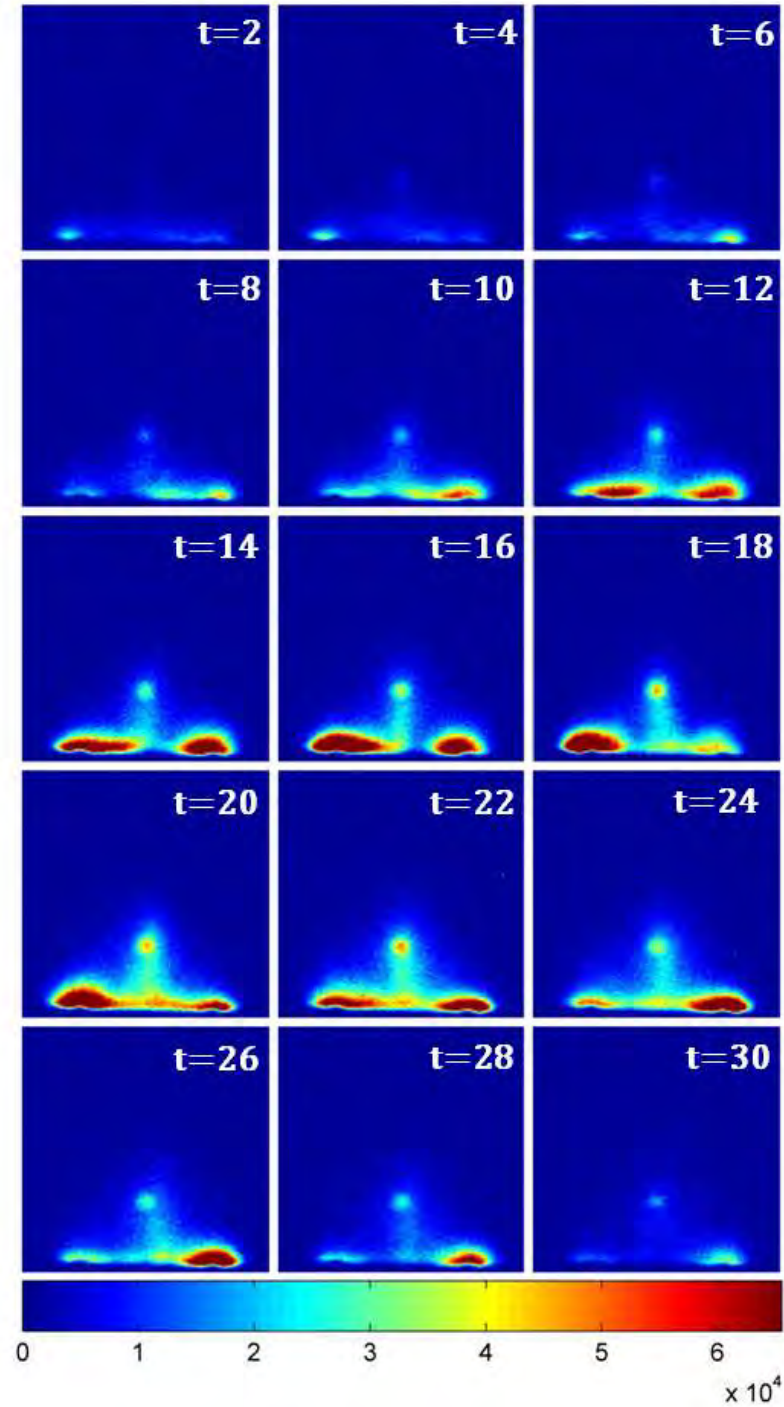
F

Figure 4.92: Sequential images of the xenon azimuthal plasma structures in main discharge of the BHT-600. The thruster was operating at a discharge potential, discharge current, and magnet current of 100 V, 2.0 A, and 1.75 A, respectively. The time between images is 2 μs with an exposure time of 1 μs. Arbitrary intensity.

spoke was located near the plasma jet in the center of the thruster several millimeters away from the exit plane. In addition, the images revealed several spokes could exist simultaneously within the discharge at low discharge potentials.

V. Summary and Recommended Future Work

Various instabilities and oscillations within the main discharge of Hall thrusters were observed over the decades. The frequencies of these fluctuations can range anywhere from the low kHz regime to the MHz regime depending on the cause or nature of the oscillation or instability. Experimental methods to characterize the oscillations or instabilities within the main discharge have usually included some type of intrusive technique which disrupts or alters the plasma plume. In this study, the characteristics of the plasma were observed using non-intrusive techniques to quantify the different oscillations and instabilities of the Hall thruster discharge. A comparison of two different thrusters, the BHT-200 and BHT-600, was made to identify any similarities or differences in a low power and a medium power thruster. In addition, the interest of an alternative propellant has also increased, due to the increasing cost of xenon. The alternative propellant used in this study was krypton and the oscillations and instabilities of the krypton discharge were also compared to those of xenon.

Utilizing an ultra-high speed camera, which was capable of recording up to one Mfps, two types of plasma instabilities were observed since the high-speed images provided time-dependent, two-dimensional information. The first type of oscillation was detected moving in the axial direction of the thruster while the second type was captured moving in the azimuthal direction. These observations were made for both the low power, BHT-200, and the medium power, BHT-600, thrusters. Xenon and krypton were used for both thrusters and the discharge of both types of propellants demonstrated the oscillations and instabilities were found in both the axial and azimuthal direction.

5.1 *Breathing Mode*

At the nominal or design operating conditions of the Hall thrusters, the main discharge experiences a very steady oscillation primarily in the axial direction. Further study of these oscillations through numerical modeling have shown they are a result of periodic depletion and replenishment of neutrals at the thruster exit which were

186

termed the breathing mode by Boeuf and Garrigues and the predator/prey model by Fife *et al.* In the high-speed images of the main discharge for the BHT-200, the intensity of the plasma emission has also demonstrated this oscillatory behavior in the frequency range of 40 kHz for xenon and 25 kHz for krypton at the nominal operating condition. For the BHT-600 operating at nominal conditions, the results show the oscillations of the emission intensity were in the 48 kHz regime for xenon and 35 kHz regime for krypton.

Analysis of the breathing mode shows the frequency of xenon is greater than the frequency of krypton at comparable discharge potentials.

Based on the predator/prey model the difference in frequency between xenon and krypton was largely due to the difference in ionization lengths. For krypton, having a smaller cross section compared to xenon, the residence time for ionization was greater which resulted in the longer ionization zone as compared to the xenon. Since the ionization length was inversely proportional to the frequency, the krypton breathing mode frequency should be lower than comparable xenon breathing mode frequency. Indeed, this result was verified by the measured breathing mode frequencies of both propellants utilized in both thrusters. In addition, high-speed imaging from the side view of the thruster confirms the optical emission near the exit plane was longer for krypton than xenon. Although the observed region was not the ionization zone, the optical emission still provided some insight since the captured emission was largely the result of radiative decay from the excited ions and neutrals. The high optical emission intensity also suggests this region has elevated electron temperatures which coincides with measurements made by Linnell and Gallimore. This region of elevated electron temperatures coincides with the ionization zone and provides some measure of the ionization length.

Operating conditions of the Hall thruster, such as the discharge potential, discharge current, and magnet current were also altered to determine the effects on the breathing mode frequency. Reductions in the discharge potential, from the nominal,

showed a similar decrease in the breathing mode frequency for both the BHT-200 and BHT-600. Xenon spectra data from the BHT-200, in conjunction with the CRM and HPHall simulations, suggests the electron temperature of the ionization zone declined with the decrease in discharge potential. This result supports the predator prey model where Fife *et al* states the frequency of the breathing mode was dependent on the ionization rate which is directly proportional to the electron temperature. Physically, this reduction in electron temperature increased the residence time of the neutrals. Thus, it took longer to ionize the neutrals which decreased the rate of ion depletion in the ionization region.

The discharge current, controlled by the mass flow rate, was also varied to determine its effects on the breathing mode. For both thrusters, the effect of increasing the discharge current or mass flow rate for both feed gases resulted in an increase in the breathing mode frequency. Again, the results from this study supports the predator/prey model where the increase in the mass flow rate increased the neutral velocity. Furthermore, as the ions are accelerated out of the ionization zone, the neutral front is now replenished at a higher rate. Since the ionization zone is replenished at a higher rate, the frequency of the breathing mode is increased.

The magnet current, which controls the magnetic field topology, had different effects on the breathing mode frequency for the low power and medium power thrusters. For the BHT-200, the breathing mode frequency was nearly constant for both xenon and krypton at the various magnet currents tested. This suggests the magnetic field topology did not affect the ionization length for either propellants. Conversely, the variation in the magnetic field topology had a significant effect on the BHT-600 breathing mode frequency. In the case of xenon and krypton, the magnet current and breathing mode frequency was inversely proportional suggesting the increase in magnet current increased the ionization length through the manipulation of the magnetic field topology. Although it is not entirely clear the cause for the difference between the two thrusters, the magnetic field profile have been shown to be very different by Cheng.

The operating condition of the hollow cathode also influenced the amplitude and frequency of the breathing mode. In the krypton case, the difference in having the cathode heater on versus allowing the cathode to sustain self-heating changes the nature of the breathing mode. By having the cathode heater on, the electron number density with sufficient energy was also increased which allowed for a more dominant breathing mode oscillation and increased the frequency of the oscillation.

5.2 Azimuthal Modes

The other mode observed in this study was the azimuthal plasma emission resembling a small disk-like or tear-drop like structures in the high-speed images. These azimuthal plasma structures were captured rotating in the $E \times B$ direction similar to the observations made by previous researchers. However, the time-dependent, two-dimensional images provide a detailed illustration of the plasma structures expanding upon previous descriptions. Furthermore, the images reveal multiple structures within the discharge of the Hall thruster where simple intrusive probes could not determine such detail.

Although possible to detect azimuthal non-uniformity in all of the images from the low to the high discharge potentials, the azimuthal plasma structures were more dominant in the low discharge regime for both the BHT-200 and BHT-600. For both thrusters, the multiple azimuthal plasma structures were observed to have different azimuthal velocities and were observed either separating or combining into each other. Since the plasma structures would form and dissipate quickly in the images it was difficult to calculate velocities for individual structures. However, the bulk azimuthal velocity of the plasma field was calculated. The results for the BHT-200 showed the azimuthal velocity of the plasma field varied from 1.0 km/s to 3.6 km/s for xenon and 0.8 km/s to 4.5 km/s for krypton in the discharge potential range from 80 V to 150 V and 90 V to 130 V, respectively. For the BHT-600, the azimuthal velocity ranged from 4.0 km/s to 8.0 km/s for xenon at a discharge potential range of 90 V to 150 V.

In the case of krypton, the azimuthal velocities in the BHT-600 ranged from 3.2 km/s to 5.8 km/s in the 90 V to 130 V range of discharge potentials.

The effect of the discharge current on the azimuthal plasma structures was not as clearly defined. In the BHT-200 case, both xenon and krypton had a similar trend of decreasing and increasing azimuthal velocities. However, at the lower discharge current, the thruster was not operating consistently. Thus, the measured values may be considered less accurate. At higher discharge potentials for the BHT-200, both propellants showed an increasing trend with increasing current or mass flow rate. The results of the BHT-600 clearly shows an inverse trend with increasing discharge current or mass flow rate. A possible reason for the difference could reside in the different magnetic field profiles. As the mass flow rate is increased the ionization zone could have moved further out of the discharge channel into a lower magnitude magnetic field. Conversely, for the BHT-200 the increase in the mass flow rate could have moved its ionization zone outward to a higher magnetic field.

Variations in the magnet current also show similar results to the discharge current. For the BHT-200, an increase in the magnet current increased the velocity for xenon and krypton while an increase in the magnet current for the BHT-600 resulted in a decrease in velocity. In the case of the BHT-200 magnetic field, as the magnet current was increased the magnitude of the magnetic field also increased near the ionization zone which cause the increase. In contrast, as the magnet current was increased for the BHT-600 the concentration of the magnetic field moved further in towards the anode and was weaker near the ionization zone which was near the thruster exit plane. Again, due to the difference in the magnetic field topology, the BHT-200 and BHT-600 did not have the same trend.

Side views of the thrusters showed some unique features of the azimuthal plasma structure. For the BHT-200 the area of highest emission intensity coincided with the areas of erosion on the nose cone. This circular erosion mechanism caused by these regions of high densities and electron temperature may be a significant contributer

to the erosion of the nose cone. The result suggests new modeling techniques need implementation in determining the lifetime characteristics of Hall thrusters.

The side views also provide details with regards to the spoke instabilities. In the images, multiple spokes are seen rotating about the center of the thruster where the center of the spokes meet at the start of the plasma jet and extends out towards the discharge channel. Each spoke was also observed connecting to the plasma structures observed earlier.

In summary, the direct emission of the main discharge of two Hall thrusters and two types of propellants were analyzed in this study. High-speed images of the plasma emission show two types of instabilities with one traveling in the axial direction while the other traveled in the $E \times B$ direction. Variations of the thruster parameters was shown to affect both types of instabilities leading to possible active or passive control of the instability. By closely investigating these oscillations and instabilities, improved numerical models and simulations can be created contributing to the advancement of Hall thruster design. Additionally, this research satisfies the objectives at the beginning of this document. Using high-speed imaging techniques, the operational modes and instabilities, up to 500 kHz, of the Hall thruster were captured. This non-intrusive method also provided time-dependent information about the main discharge measuring velocity and frequency of the plasma instabilities and oscillations. With the spatial resolution of the images, a method was developed to the two-dimensional characteristics of the plasma instabilities which have not been done before. Furthermore, variations of the thruster parameters such as discharge potential, discharge current, and magnet current was examined to determine their effects on the plasma instabilities. Lastly, based on velocity, frequency, and spatial behavior, this study provided possible causes of the azimuthal plasma instabilities.

5.3   Recommendations for Future Work

Future work can increase the value of this study in several areas. One of the first recommendations is the measurement of electron temperature. In this study, the

collection optics collimated too much of the plume and were not focused enough on the region of interest. New optics should be installed before the fiber optic line to narrow the field of view, which should provide a better estimate of the electron temperature within the ionization zone. Furthermore, the HPHall model needs more experimental data at different operating conditions (i.e. discharge potential, discharge current, etc) to provide more accurate data for the CRM.

Since the ultra-high speed camera did not have any optical filters, the resultant images were from multiple species of xenon or krypton. In the future, optical filters should be installed to separate species. Two obstacles prevented the optical filters from inclusion in this study. The first, was the optical filters which were required to separate the xenon neutrals and ions. Since the filters were not part of the standard optical wavelengths, they required a custom build from the manufacturer. With a custom build, the time for delivery was not able to meet the time requirements of this study. Second, even if the optical filters were delivered, there may not be enough emission signal to the camera at the desired sampling rate. Thus, an intensifier would be required to make this work.

The analysis of the azimuthal plasma structure was a good first iteration to determine the velocities and frequencies. However, the cross-correlation method was time and computationally intensive. Efforts are already underway in conjunction with the math department to develop a faster algorithm which would not only provide the bulk velocity, but also the individual velocities of the individual plasma structures. In addition, characterizations of the shape and and residence time of the plasma structures would also give significant insight as to the nature of the instabilities.

Bibliography

1. *S. H. HPV-2, IS-CCD Spectral Response, 2006-02-03.*

2. Albarede, L., S. Mazouffre, Andre Bouchoule, and M. Dudeck. "Low-Frequency Electron Dynamics in the Near Field of a Hall Effect Thruster". *Physics of Plasmas*, 13, 2006.

3. Albarede, Luc, Vanessa Vial, Alexey Lazurenko, Andre Bouchoule, and Michel Dudeck. "Low Frequency Dynamical Behavior of the Plasma at the Exit Plane of a Hall Effect Thruster". *Rarefied Gas Dynamics*, 1113–1118, 2005.

4. Boeuf, J. P. and L. Garrigues. "Low frequency oscillations in a stationary plasma thruster". *J. Appl. Phys*, 84(7):3541–3554, July 1998.

5. Bohnert, Alex M. *Thermal Characterization of a Hall Effect Thruster*. Master's thesis, Air Force Institute of Technology, Wright-Patterson AFB, OH, March 2008.

6. Boniface, C., L. Garrigues, G. J. M. Hagelaar, and J. P. Boeuf. "Anomalous Cross Field Electron Transport in a Hall Effect Thruster". *Applied Physics Letters 89*, 2006.

7. Cheng, Shanon Yun-Ming. *Modeling of Hall Thruster Lifetime and Erosion Mechanisms*. Ph.D. thesis, Massachusetts Institute of Technology, 2007.

8. Chesta, Enrico, Cheryl M. Lam, Nathan B. Meezan, Daniel P. Schmidt, and Mark Cappelli. "A Characterization of Plasma Fluctuations within a Hall Discharge". *IEEE T. Plasma. Sci.*, 29(4):582, August 2001.

9. Chiu, Y., S. Austin, B. L. Willliams, R. A. Dressler, and G. F. Karabadzhak. "Passive optical diagnostic of Xe-propelled Hall thrusters. I. Emission cross section". *Journal of Applied Physics*, 99, 2006.

10. Chiu, Y., B. W. Ticknor, B. A. Fritz, J. R. Winick, M. K. Scharfe, D. Bromaghim, J. Cline, R. A. Dressler, C. Freeman, V. Hruby, and L. Johnson. "Near-Infrared Radiance from the Discharge of a BHT-200 Thruster Plasma: Chamber Measurements and Collisional Radiative Model". *57th Joint Army Navy NASA Air Force (JANNAF) Propulsion Meeting, Colorado Springs, CO.* 2010.

11. Choueiri, E. Y. "Fundamental Difference between the Two Hall Thruster Variants". *Phys. Plasmas*, August 2001.

12. Choueiri, E. Y. "Plasma oscillations in Hall thrusters". *Phys. Plasmas*, 8(4):1411–1426, 2001.

13. Choueiri, E. Y. "A Critical History of Electric Propulsion: The First 50 Years (19061956)". *J. Propul. Power*, 20(2):193, March-April 2004.

14. Choueiri, Edgar Y. "Characterization of Oscillations in Closed Drift Thrusters". *30th AIAA/ASME/SAE/ASEE Joint Propulsion Conference; Indianapolis, IN*, 1994.

15. Darnon, F., L. Garrigues, J. P. Boeuf, Andre Bouchoule, and M. Lyszyk. "Spontaneous Oscillations in a Hall Thruster". *IEEE T. Plasma. Sci.*, 27(1):98, February 1999.

16. Darnon, F., C. Kadlec-Philippe, A. Bouchoule, and M. Lyszyk. "Dynamic Plasma and Plume Behavior of SPT Thrusters". *34th AIAA/ASME/SAE/ASEE Joint Propulsion Conference and Exhibit, Cleveland, OH*, July 1998.

17. Darnon, F., M. Lyszyk, and A. Bouchoule. "Optical Investigation on Plasma Oscillations of SPT Thrusters". *American Institute of Aeronautics and Astronautics, Washington, DC*, AIAA-97-3051, 1997.

18. Dressler, R. A., Y. Chiu, O. Zatsarinny, K. Bartschat, R. Srivastava, and L. Sharma. "Near-Infrared Collisional Radiative Model for Xe plasma electrostatic thrusters: the role of metastable atoms". *Journal of Physics D: Applied Physics*, 42, 2009.

19. Esipchuk, Y. B., A. I. Morozov, G. N. Tillin, and A. V. Trofimov. "Plasma oscillations in a closed-drift accelerators with an extended acceleration zone". *Sov. Phys. Tech. Phys.*, 18(7):928, 1974.

20. Esipchuk, Y. V. and G. N. Tillin. "Drift Instability in a Hall-current plasma accelerator". *Sov. Phys. Tech. Phys.*, 21:417, 1976.

21. Fife, J. M., Manuel Martinez-Sanchez, and James Szabo. "A Numerical Study of Low-Frequency Discharge Oscillations in a Hall Thrusters". *American Institute of Aeronautics and Astronautics, Washington, DC*, AIAA-97-3052, 1997.

22. Fife, John Michael. *Hybrid-PIC Modeling and Electrostatic Probe Survey of Hall Thruster*. Ph.D. thesis, Massachusetts Institute of Technology, Cambridge, MA, 1998.

23. Fridman, Alexander A. and Lawrence A. Kennedy. *Plasma Physics and Engineering*. Taylor and Francis Books Inc., New York, NY, 2004.

24. Goebel, Dan M. and Ira Katz. *Fundamentals of Electric Propulsion: Ion and Hall Thrusters*. John Wiley and Sons Inc., Hoboken, NJ, 2008.

25. Gorshkov, O. A., A. S. Koroteev, B. A. Arkipov, V. M. Murashko, N. A. Anfimov, V. I. Lukyashenko, V. Kim, and G. A. Popov. "Overview of Russian Activities in Electric Propulsion". *37th AIAA/ASME/SAE/ASEE Joint Propulsion Conference & Exhibit, Salt Lake City, Utah*, July 2001.

26. Gurnett, D.A. and A. Bhattachajee. *Introduction to Plasma Physics*. Cambridge University Press, New York, NY, second edition, 2005.

27. Hargus, W. A. "Laser-Induced Fluorescence of Neutral Xenon on the Near Field of a 200 W Hall Thruster". *41st AIAA Jount Propulsion Conference, Tuscon, AZ*, 2005.

28. Hargus, W. A. and C. S. Charles. "Near Exit Plane Velocity Field of a 200-Watt Hall Thruster". *Journal of Propulsion and Power*, 24(1), 2008.

29. Hargus, W. A. and C. S. Charles. "Near-Plume Laser-Induced Fluorescence Velocity Measurements of a Medium Power Hall Thruster". *Journal of Propulsion and Power*, 26(1):135–141, 2010.

30. Hargus, W. A. and M. R. Nakles. "Low Power Hall Effect Thruster Discharge Plasma Oscillation Characterization". 2008.

31. Hargus, William A. *Investigation of the Plasma Accelaration Mechanism within a Coaxial Hall Thruster*. Ph.D. thesis, Stanford Univeristy, 2001.

32. Hargus, William A. and Christopher S. Charles. "Near Plume Laser Induced Fluorescence Velocity Measurements of a 600 W Hall Thruster". *44th AIAA/AS-ME/SAE/ASEE Joint Propulsion Conference and Exibit*, July 2008.

33. Hargus, William A., Nathan B. Meezan, and Mark A. Cappelli. "A Study of a Low Power Hall Thruster Transient Behavior". *International Electric Propulsion Conference*, 351–358. 1997.

34. Hargus, William A., Michael R. Nakles, Rachel Tedrake, and Bruce Pote. "Effect of Anode Current Fluctuations on Ion Energy Distributions within a 600 W Hall Effect Thruster". *44th AIAA/ASME/SAE/ASEE Joint Propulsion Conference and Exibit*, July 2008.

35. Hargus, William A. and Bruce Pote. "Examination of a Hall Thruster Start Transient". *38th AIAA Joint Propulsion Conference and Exibit*, July 2002.

36. Hruby, V., J. Monheiser, B. Pote, J. Rostler, J. Kolencik, and C. Freeman. "Development of low power Hall thrusters". *30th AIAA Plasma Dynamics and Lasers Conference and Exhibit, Norfolk, VA*. 1999.

37. Hutchinson, I.H. *Principles of Plasma Diagnostics*. Cambridge University Press, New York, 2002.

38. Ito, Tsuyohito and Mark A. Cappelli. "High Speed Images of Drift Waves and Turbulence in Magnetized Microplasmas". *IEEE T. Plasma. Sci.*, 36(4):1228, August 2008.

39. Ito, Tsuyohito, Nicolas Gascon, W. Scott Crawford, and Mark A. Cappelli. "Experimental Characterization of a Micro-Hall Thruster". *Journal of Propulsion and Power*, 23(5):1068–1074, September-October 2007.

40. Janes, G.S. and R.S. Lowder. "Anomalous Electron Diffusion and Ion Acceleration in a Low-Density Plasma". *Phys. Fluids*, 9(6):1115–1123, 1966.

41. Jankovsky, Robert S., David T. Jacobson, Lee S. Mason, Vincent K. Rawlin, Maris A. Mantenieks, David H. Manzella, Richard R. Hofer, and Peter Y. Peterson. "NASA's Hall Thruster Program". *37th Joint Propulsion Conference and Exibit*, July 2001.

42. Kadomtsev, B. B. and A. V. Nedospasov. "Instability of the Positive Column in a Magnetic Field and the 'Anamolous' Diffusion Effect". *Jounal of Nuclear Energy, Part C*, 1:230–235, 1960.

43. Kapulkin, Alexander and Mauricio M. Guelman. "Low-Frequency Instability in Near-Anode Region of Hall Thruster". *IEEE Transactions on Plasma Science*, 36(5):2082–2087, October 2008.

44. Karabadzhak, G. F., Y. Chiu, and R. A. Dressler. "Passive optical diagnostic of Xe propelled Hall thrusters. II. Collisional-radiative Model". *Journal of Applied Physics*, 99, 2006.

45. Katsonis, K., M. Cornille, A. Siskos, and M. Tanguy. "Low Temperature Validation of a Xe Plasma C-R Model". *4th International Spacecraft Propulsion Conference, Cagliari, Sardinia, Italy*. 2004.

46. Keidar, Michael and Isak I. Beilis. "Electron Transport Phenomena in Plasma Devices with E X B Drift". *IEEE Transactions on Plasma Science*, 34(3):804–814, June 2006.

47. Kim, Vladimir, Garri Popov, Boris Arkhipov, Vyacheslav Murashko, Oleg Gorshkov, Anatoly Koroteyev, Valery Garkusha, Alexander Semenkin, and Sergi Tverdokhlebov. "Electric Propulsion Activity in Russia". *IEPC*, October 2001.

48. Lazurenko, A., T. Dudok de Witt, C. Cavoit, V. Krasnoselskikh, A. Bouchoule, and M. Dudeck. "Determination of the Electron Anomalous Mobility Through Measurements of Turbulent Magnetic Field in Hall Thrusters". *Physics of Plasmas*, 14, 2007.

49. Lazurenko, Alexey, Vladimir Krasnoselskikh, and Andre Bouchoule. "Experimental Insight Into High-Frequency Instabilities and Related Anomalous Electron Transport in Hall Thrusters". *IEEE Transactions on Plasma Science*, 36(5):1977–1988, October 2008.

50. Linnell, J. A. *An evaluation of Krypton propellant in Hall thrusters*. Ph.D. thesis, University of Michigan, 2007.

51. Linnell, J. A. and A. D. Gallimore. "Internal Plasma Potential Measurements of a Hall Thruster using Plasma Lens Focusing". *Physics of Plasmas*, 13, 2006.

52. Linnell, J. A. and A. D. Gallimore. "Internal plasma potential measurements of a Hall thruster using xenon and krypton propellant". *Phys. Plasmas*, 13, 2006.

53. Litvak, Andrei A. and Nathan J. Fisch. "Resistive Instabilities in Hall Current Plasma Discharge". *Physics of Plasmas*, 8(2):648–651, February 2001.

54. Liu, D., R. E. Huffman, R. D. Branam, and W. A. Hargus. "Ultra-High Speed Imaging of Hall Thruster Discharge Oscillation with Krypton Propellant". *IEEE Transactions of Plasma Science*, (to be published).

55. Lobbia, R. B. and A. D. Gallimore. "A Method of Measuring Transient Plume Properties". *44th AIAA/ASME/SAE/ASEE Joint Propulsion Conference and Exhibit*. 2008.

56. Lobbia, R. B. and A. D. Gallimore. "Two-Dimensional Time-resolved Breathing Mode Plasma Fluctuation Variation with Hall Thruster Discharge Settings". *31st International Electric Propulsion Conference, Ann Arbor, Michigan*. 2009.

57. Lobbia, R. B. and A. D. Gallimore. "High-speed dual Langmuir probe". *Review of Scientific Instruments*, 81, 2010.

58. Lobbia, R. B. and A. D. Gallimore. "Temporal Limits of a rapidly swept Langmuir probe". *Physics of Plasmas*, 17, 2010.

59. Lobbia, R. B. and A.D. Gallimore. "Fusing Spatial and Temporally Seperated Single-point Turbulent Plasma Flow Measurements into Two-Dimensional Time-resolved Visualization". *12th International Conference on Information Fusion, Seattle, WA*, 2009.

60. Lobbia, R. B., Liu T. M., and A. D. Gallimore. "Correlating time-resolved optical and langmuir probe measurements of Hall thruster dynamics". *JANNAF 6th Modeling and Simulation/ 4th Liquid Propulsion/ 3rd Spacecraft Propulsion Joint Subcommittee Meeting, Orlando, FL*. 2008.

61. Manzella, D. H. "Stationary Plasma Thruster Plume Emissions". *International Electric Propulsion Conference*. 1997.

62. Manzella, David H. "Stationary Plasma thruster Ion Velocity Distribution". *30th AIAA/ASME/SAE/ASEE Joint Propulsion Conference*, June 1994.

63. Matlock, T. S., W. A. Hargus, C. W. Larson, and M. R. Nakles. "An Inversion Method for Reconstructing Hall Thruster Plume Parameters from Line Integration Measurements". *43rd AIAA/ASME/SAE/ASEE Joint Propulsion Conference, Cincinnati, OH*. 2007.

64. Morozov, A. I., Y. V. Epsinchuck, A. M. Kaulkin, V. A. Nevrovskii, and V. A. Smirnov. "Effect of the magnetic field on a closed-electron-drift accelerator". *Sov. Phys. Tech. Phys.*, 17(3):482, 1972.

65. Nakles, M. R., R. R. Barry, C. W. Larson, and W. A. Hargus. "A Plume Comparison of Xenon and Krypton Propellant on a 600 W Hall Thruster". *31st International Electric Propulsion Conference, Ann Arbor, MI*. 2009.

66. Nakles, M. R. and W. A. Hargus. "Background Pressure Effects on Internal and Near-field Ion Velocity Distribution of a Medium-Power Hall Thruster". *44th AIAA Joint Propulsion Conference, Hartford, CT*. 2008.

67. Nedospasov, A. V. "Striations". *Soviet Physics Uspekhi*, 11(2):174–187, 1968.

68. Pagnon, D., F. Darnon, S. Roche, S. Bechu, L. Megne, A. Bouchoule, M. Touzeau, and P. Lasgorceix. "Time Resolved Characterization of the Plasma and the Plume of a SPT Thruster". *35th AIAA/ASME/SAE/SEE Joint Propulsion Conference and Exibit, Los Angeles, CA*. 1999.

69. Pekarek, L. "Ionization Waves (Striations) in a Discharge Plasma". *Soviet Physics Uspekhi*, 11(2):188–208, Semptember-October 1968.

70. Raitses, Y., E. Merino, J. B. Parker, and N. J. Fisch. "Operation and Plume Measurements of Miniaturized Cylindrical Hall Thrusters with Permanent Magnets". *45th AIAA/ASME/SAE/ASEE Joint Propulsion Conference & Exhibit, Denver, CO*. 2009.

71. Rotter, John E. *An Analysis of Multiple Configurations of Next-Genertion Cathodes in a Low Power Hall Thruster*. Master's thesis, Air Force Institute of Technology, 2950 Hobson Way, WPAFB, OH, March 2009.

72. Smith, A.W. and Mark A. Cappelli. "Time and Space-correlated plasma potential measurements in the near field of a coaxial Hall plasma discharge". *Phys. Plasmas*, 16, 2009.

73. Sommerville, J. D., L. B. King, Y. Chiu, and R. A. Dressler. "Ion-Collsional Emission Excitation Cross Sections for xenon Electric Thruster Plasmas". *Journal of Propulsion and Power*, 24(4):880–888, 2008.

74. Stuhlinger, Ernest. *Ion Propulsion for Space Flight*. McGraw-Hill Book Company, New York, 1964.

75. Vial, V., S. Mazouffre, M. Prioul, D. Pagnon, and A. Bouchoule. "CCD Images of Hall Effect Thruster Plume Dynamics After Ultrafast Current Ignition". *IEEE Transactions on Plasma Science*, 33(2):324–325, April 2005.

76. Vincenti, W. G. and Charles H. Kruger. *Introduction to Physical Gas Dynamics*. Krieger Publishing Company, Malabar, FL, 1986.

77. Wilbur, Paul J., Robert G. Jahn, and Frank C. Curran. "Space Electric Propulsion Plasmas". *IEEE Transactions on Plasma Science*, 19(6):1167–1179, December 1991.

78. Yang, J., S. Yokota, R. Kaneko, and K. Komurasaki. "Diagnosing on Plasma Plume from xenon Hall thruster with collisional-radiative model". *Physics of Plasmas*, 17, 2010.

79. Yoshikawa, S. and D.J. Rose. "Anomalous Diffusion of a Plasma across a Magnetic Field". *Phys. Fluids*, 5(3):334, March 1962.

REPORT DOCUMENTATION PAGE

Form Approved
OMB No. 0704–0188

1. REPORT DATE (DD–MM–YYYY)	2. REPORT TYPE		3. DATES COVERED (From — To)
15–09–2011	Doctoral Dissertation		Aug 2008 — Sep 2011

4. TITLE AND SUBTITLE

Two-Dimensional, Time-Dependent Plasma Structures of a Hall Effect Thruster

5a. CONTRACT NUMBER

5b. GRANT NUMBER

5c. PROGRAM ELEMENT NUMBER

6. AUTHOR(S)

Liu, David, Captain, USAF

5d. PROJECT NUMBER

5e. TASK NUMBER

5f. WORK UNIT NUMBER

7. PERFORMING ORGANIZATION NAME(S) AND ADDRESS(ES)

Air Force Institute of Technology
Graduate School of Engineering and Management (AFIT/EN)
2950 Hobson Way
WPAFB OH 45433-7765

8. PERFORMING ORGANIZATION REPORT NUMBER

AFIT/DS/ENY/11-04

9. SPONSORING / MONITORING AGENCY NAME(S) AND ADDRESS(ES)

Mr. Michael Huggins
Air Force Research Laboratory
Space and Missile Division (AFRL/RZS)
5 Pollux Drive
Edwards AFB, CA 93524
DSN 525-5230

10. SPONSOR/MONITOR'S ACRONYM(S)

AFRL/RZS

11. SPONSOR/MONITOR'S REPORT NUMBER(S)

12. DISTRIBUTION / AVAILABILITY STATEMENT

Approval for public release; distribution is unlimited.

13. SUPPLEMENTARY NOTES

This material is declared a work of the U.S. Government and is not subject to copyright protection in the United States.

14. ABSTRACT

The Hall thruster is a type of electric propulsion utilized by satellites to perform a wide variety of missions ranging from station keeping, orbital maneuvers, and even deep space propulsion. In order to accommodate the multitude of missions it also has a wide assortment of sizes and power configurations which can range from approximately an inch in diameter at 20 W to a couple of feet in diameter at 1.5 kW. Additionally, this electro-static device provides high specific impulse without the added weight penalty associated with conventional chemical thrusters. It supplies this high specific impulse by ionizing a gas such as xenon or krypton and then accelerating it through the electric field to speeds on the order of kilometers per second depending on the thruster size and power. Although the steady-state outputs such as thrust and specific impulse are measurable, other transient mechanisms within the main discharge are still not well understood.

15. SUBJECT TERMS

Hall thrusters, breathing modes, plasma instabilities, optical emission

16. SECURITY CLASSIFICATION OF:			17. LIMITATION OF ABSTRACT	18. NUMBER OF PAGES	19a. NAME OF RESPONSIBLE PERSON
a. REPORT	b. ABSTRACT	c. THIS PAGE			Branam, Richard, LtCol, USAF
U	U	U	UU	226	19b. TELEPHONE NUMBER (include area code) (937) 255–3636, ext 6163; david.liu@afit.edu

Standard Form 298 (Rev. 8–98)
Prescribed by ANSI Std. Z39.18